

UNIVERSITY OF EAST ANGLIA

JOHN INNES CENTRE

**Viruses in motion:
maturation of an insect virus-like
particle – a nanomachine**

ROGER CASTELLS GRAELLS

Thesis submitted to the University of East Anglia
for the degree of Doctor of Philosophy

2019

This copy of the thesis has been supplied on condition that anyone who consults it is understood to recognise that its copyright rests with the author and that use of any information derived there-from must be in accordance with current UK Copyright Law. In addition, any quotation or extract must include full attribution.
Copyright © R. Castells Graells, 2019.

Als meus pares i germans,

*«A Man would do nothing, if he waited until he could do it so well
that no one would find fault with what he has done»*
Cardinal Newman

*«What is a scientist after all?
It is a curious man looking through a keyhole,
the keyhole of nature, trying to know what's going on»*
Jacques-Yves Cousteau

*«If you really want this, you have to work really hard,
take advantage of all opportunities, but don't give up»*
Jane Goodall

«El saber no ocupa lloc i és una herència que ningú et podrà prendre»
Núria Brisa Vilalta

This last quote translates to: *«Knowledge does not take space and it is a heritage
that you can keep forever because no one can take it from you»*
This is a piece of advice that our family has given us since childhood.
It encouraged us to constantly learn and enjoy the search for knowledge.

Abstract

Virus-like particles (VLPs) are particles that lack the infectious genome of the parent virus but retain the ability to self-assemble. Transient expression of viral coat proteins in a variety of systems can be used to synthesize VLPs that are morphologically indistinguishable from the virus from which they have been derived. In this thesis, I have used VLPs to study virus maturation mechanisms.

The main focus of this thesis has been the study of the maturation of *Nudaurelia capensis* omega virus (N ω V), an insect virus. N ω V has a pH-controlled maturation mechanism that involves a precise autocatalytic cleavage within the capsid protein that is accompanied by a dramatic decrease in the diameter of the particles. I used insect cell and plant-based transient expression of the N ω V coat protein to produce procapsids and showed that reduction in pH results in cleavage of the coat protein and the concomitant decrease in particle diameter. Mature VLPs purified from plants had a structure indistinguishable from the authentic virus at 2.7 Å resolution, as determined by cryo-electron microscopy (cryo-EM). However, the plant-produced VLPs showed the formation of strong interactions between the subunits of N ω V, probably representing covalent crosslinks, that limited their dynamic properties. Given the fact that insect cells did not present this difficulty, we used them to make the VLPs for cryo-EM analysis of intermediates in the process of maturation. These analyses revealed the conformational changes in the structure of the particles that accompany maturation, such as the formation of the cleavage site and the closure of the pores of the particle.

The culmination of this thesis is represented by a movie of the maturation process of N ω V. This movie provides, for the first time, high-resolution information about the large conformational changes and protein rearrangements occurring during the maturation of this virus.

Keywords: *Nudaurelia capensis* omega virus, virus maturation, autocatalytic cleavage, virus-like particle, cryo-electron microscopy

Resum (abstract in Catalan)

Les partícules similivíriques (VLPs), acrònim de l'anglès *Virus-Like Particles*, són partícules que no tenen el material genètic viral però que conserven la capacitat d'autoassemblar-se. Per sintetitzar les VLPs es poden utilitzar diversos sistemes mitjançant els quals es produeixen les proteïnes de la càpsida del virus. Aquestes partícules són morfològicament idèntiques als virus originals dels quals han estat derivades. En aquesta tesi he utilitzat les VLPs per estudiar els mecanismes de maduració dels virus.

L'objectiu principal d'aquesta tesi ha estat l'estudi del procés de maduració de *Nudaurelia capensis* omega virus (N ω V), un virus d'insecte. N ω V té un mecanisme de maduració, que està controlat pel pH, que implica una segmentació autocatalítica de la proteïna de la càpsida del virus i va acompanyada d'una reducció del diàmetre de les partícules. En aquesta tesi vaig utilitzar cèl·lules d'insectes i plantes per tal de produir la proteïna de la càpsida de N ω V i generar partícules, conegudes com a procàpsides. Endemés vaig demostrar que la reducció en el pH dóna lloc a la segmentació de la proteïna de la càpsida i a la reducció del diàmetre de les partícules. Mitjançant criomicroscopia electrònica (cryo-EM) vaig obtenir, a una resolució de 2.7 Å, l'estructura de partícules que havien estat madurades en plantes i vaig veure que tenien una estructura idèntica als virus autèntics. Tot i això, les VLPs extretes de plantes tenien interaccions fortes entre les seves subunitats, probablement degut a enllaços covalents, i això va limitar les seves propietats dinàmiques. Tenint en compte que les cèl·lules d'insecte no presentaven aquesta dificultat, les vam utilitzar per obtenir les estructures dels intermedis en el procés de maduració mitjançant anàlisis amb cryo-EM. Aquestes anàlisis van revelar els grans canvis conformacionals en l'estructura de les partícules que ocorren durant la maduració, com ara la formació del punt de segmentació i el tancament dels porus de la partícula.

La conclusió d'aquesta tesi està representada per una pel·lícula del procés de maduració de N ω V. Aquesta pel·lícula proporciona, per primera vegada, informació d'alta resolució sobre els grans canvis conformacionals i els reordenaments de proteïnes que es produeixen durant la maduració d'aquest virus.

Paraules clau: *Nudaurelia capensis* omega virus, maduració viral, segmentació autocatalítica, partícules similivíriques, criomicroscopia electrònica

Acknowledgements

First and foremost, I would like to thank George P. Lomonossoff, for being a great, encouraging, awesome, funny, enthusiastic and inspirational supervisor. His lessons, advice and discussions, together with his always open door, have been crucial in this PhD journey. George has the magic power to always find solutions and opportunities for any challenge. It has been a joy to do science in his lab and to discover the amazing world of viruses. I am also very grateful for all the opportunities to attend conferences, workshops, visits to collaborators and all the events that have allowed me to learn, network and realize that lots of science can happen over some food and drinks. I have also enjoyed the freedom to explore and develop new ideas and carry on science communication projects, including the use of 3D printing technologies. Finally, I want to thank him for teaching me how to *romper pelotas!*

I am also very grateful to my committee members: Rob Field, for all his wisdom, support and invaluable advice and Keith Saunders, the super RA, for guiding my first steps in the virology world with the turnip crinkle virus project and for always being ready to help and engage in fruitful discussions.

I would also like to thank Jack Johnson for introducing me to the N ω V system. Thank you very much for your ideas, discussions, support, deep structural biology knowledge and infinite enthusiasm. Your drive to solve the structures for the N ω V maturation movie has been key to developing this challenging project. Also, thank you very much for welcoming me at The Scripps Research Institute and sunny California.

Thanks to all the collaborators that have contributed to making this project a reality. First, I want to thank Neil Ranson and Emma Hesketh from the Astbury Centre at the University of Leeds for amazing cryo-EM data, training and advice for the processing of the cryo-EM structures. Thanks also to the PhD students and postdocs from the Astbury Centre, Matt, Becky, Charlotte, Dan, Dave, Josh and Shawn for sharing their experience. Thanks to Tatiana Domitrovic from the Federal University of Rio de Janeiro (Brazil) for all the help, advice and support in the experiments to characterize the N ω V VLPs and also for great discussions. Thanks to Tsutomu Matsui from the Stanford Synchrotron Radiation Lightsource (USA) for the SAXS experiments and all his advice and detailed structural biology knowledge on the N ω V maturation process.

To Alison Smith, Brendan Fahy, Sophien Kamoun, Ben Petre and Vladimir Nekrasov for excellent rotation projects that provided fantastic tools and experiences.

I have enjoyed a lot being in the Lomonossoff lab during these years and I want to thank all the current and former members, for creating a nice, supportive and enthusiastic environment. In particular, Alberto, for showing me new techniques and

interesting experiments; Albor, for how to be patient; Daniel, for life experience and experiment troubleshooting; Eva and Hadrien, for always finding solutions, for great discussions, for plenty of advice on experiment planning and thesis “planification”; Inga, for trying new experiments with the BY2 cells; Inma, for unmeasurable advice and taking care of us in the office 124; Jojo, for introducing me for the first time to the lab and for all the useful tips to start and pursue a PhD; Keith, for being a super RA, as mentioned above; Marina, Mim, Sachin, Anna, Sung and Yulia, for all their help and experience. Thank you so much for everything, you are amazing!

Big thanks also to Dave Lawson, “the structures master”, for all his invaluable structural biology experience and help with structural biology analysis. Cryo-EM has been a steep learning curve and Dave has been fundamental to integrate all the new knowledge and set up the cryo-EM server to perform the data analysis.

To the Biological Chemistry Department, with special mention to Monica, Lesley, Nidda and Judith, for introducing me to the insect cell expression system and gel filtration columns, Jorge, for encouraging discussions, Sarah, Naomi, Liz and Jenna, for helping with all the administration, conferences and travels.

To the photography and bioimaging platform, Andrew, Elaine, Grant, Jake, Kim and Phil, and the staff from the John Innes Centre, including horticultural services, media kitchen, stores and library, which makes the life and research of the scientists easier.

To Tom Dendooven, Javier Cifuentes and Daniel Bollschweiler for sharing their vast cryo-EM knowledge, for always being ready to help and for teaching me about Belgian beers.

To Frank, Mauricio and Noor for engaging scientific discussions and life advice.

To my fellow friends and colleagues, Abraham, Adam, Alba, Ana, Ariadna, Estela, Isabel, Javi, Lola, Marc, Matt, Mattia, Miguel, Neftaly, Nuno, Pablo, Pilar, Roland, Sophie, Sibyl, Sylvain, Vanessa and all the other students and friends with whom I shared this PhD journey in Norwich. Especially, thanks to Juan Carlos for his comradery in the lab along these years and all his wisdom.

Josep, Pablo, Virgínia, Cristina, Melissa, Abi, Carmen, Antonio, Vicky, Mihai, Dimitra and all the other great friends that I met during the summer science internships. Martí, Roger, Lambert, Pau, Aleix, Laia and to all the “biotecs” from the Universitat Autònoma de Barcelona. (UAB), the BUSS Program and the Amgen Scholars Program.

To the “Metòdics”, Carla, Helena and Jordi, for all the fun, support and wisdom.

To the “Altercat” members, Albert, David, Miki, Òscar, Toni, Xavi, for all the years having fun, playing music together, recording a CD and getting our music into Spotify!
Viu, viu, viu i somriu! Viu, viu, viu que és estiu! Viu, viu, viu i gaudiu!

To my appreciated high school teacher, Vicenç Sebastià, for making biology an enjoyable subject and for providing advice, opportunities and support for many years. Thank you very much for sharing your passion about science!

To Bettina Bölter, Josep Maria Casacuberta, Carme Garcia, Simon Krattinger, Salvador Lladó, Toni Miras, Pere Puigdomènech, Inga Sjuts, Anna Maria Solanas, Justine Sucher, Cristina Vives and many other teachers, supervisors and mentors that, during these years in Barcelona, Cerdanyola del Vallès, Terrassa, Munich, Zurich and Norwich, have shared their time, knowledge and enthusiasm and have motivated me to embark in the enjoyable journey of science.

I want to thank the Youth and Science Program from Catalunya-La Pedrera Foundation for all the scientific opportunities provided over the years and for the scholarships to attend science summer camps during three summers.

Thanks to my music teachers, Albert, Dani, Francesc, Guim, Lluís, Xavi and many others, for all the enthusiasm and values that they have taught me such as perseverance, teamwork and creativity.

I would like to thank the John Innes Foundation, for funding such an incredible Rotation PhD Programme and Steph Bornemann for running it. I am very grateful for all the opportunities provided and for helping me to develop my career as a scientist.

Special thanks to OpenPlant and Colette Matthewman for believing in our 3D printing project and awarding us with the OpenPlant Fund, which has allowed the production of over 1000 models of molecules, proteins and viruses that have been distributed among scientists and teachers around the world for educational purposes.

If you have managed to read until this sentence of the acknowledgments, it means that you are ready to read the whole thesis, good job!

If you are looking for your name, the following sentence is for you. Thank you very much to everyone who has contribute to this journey and that has not been mentioned yet! :)

Last but not least, I want to thank all my family. Especially, a big thank you to my Mum and Dad, Núria and Pere Ramon, and to my brothers, David and Xavier, for all their love, immeasurable support, patience and motivation along all these years. There are not enough words to express my gratitude towards them. I also want to thank my grandparents, Josep Maria, Núria B. and Núria R.; and my aunt Amàlia for all their love, experience and life lessons. *Moltes gràcies a tots, sou únics i us estimaré sempre!*

Table of Contents

ABSTRACT	I
RESUM (ABSTRACT IN CATALAN)	II
ACKNOWLEDGEMENTS	III
LIST OF FIGURES	XI
LIST OF TABLES	XV
1. INTRODUCTION	1
1.1. General introduction	1
1.2. Virus-like particles (VLPs)	5
1.2.1. Plant-based virus-like particles	6
1.2.2. Insect cell-based virus-like particles	7
1.3. Cryo-electron microscopy and the resolution revolution	8
1.3.1. Cryo-EM of viruses	10
1.4. Small angle X-ray scattering (SAXS)	12
1.4.1. SAXS of viruses	12
1.5. Virus maturation	13
1.6. <i>Nudaurelia capensis</i> omega virus (N ω V)	15
1.6.1. N ω V genome	15
1.6.2. N ω V life cycle	16
1.6.3. N ω V structure and maturation	18
1.6.4. N ω V conformational changes and kinetics	21
1.6.5. The gamma peptide and its lytic activity	21
1.6.6. Applications and engineering of N ω V	24
1.6.7. The N ω V “movie”	24
1.7. Thesis outline and objectives	25
2. MATERIALS AND METHODS	27
2.1. Molecular cloning	27
2.1.1. DNA constructs	27
2.1.2. Plasmids used	27
2.1.3. Transformation of <i>Escherichia coli</i>	27
2.1.4. Transformation of <i>Agrobacterium tumefaciens</i>	28
2.1.5. Bacterial storage conditions	28

2.1.6. Plasmid and DNA isolation and purification	28
2.1.7. Restriction digests	28
2.1.8. DNA ligation	28
2.1.9. Site-directed mutagenesis	29
2.1.10. Polymerase Chain Reaction (PCR)	29
2.1.11. Agarose gel electrophoresis	29
2.1.12. DNA sequencing	29
2.2. Transient expression of proteins in <i>Nicotiana benthamiana</i>	30
2.2.1. Plant material and growth conditions	30
2.2.2. Agroinfiltration solution preparation	30
2.2.3. Small-scale protein extraction	30
2.2.4. Large-scale particle extraction	31
2.3. Transient expression of proteins in insect cells culture	32
2.3.1. Insect cells growth conditions	32
2.3.2. Insect cells infection	32
2.3.3. Large-scale particle extraction	32
2.4. <i>Nudaurelia capensis</i> omega virus VLPs purification	33
2.4.1. Protein dialysis	33
2.4.2. Protein concentration	33
2.5. Protein analysis	33
2.5.1. Polyacrylamide gel electrophoresis	33
2.5.2. Western blotting and immunodetection	34
2.6. Protein quantification	34
2.6.1. BCA assay kit	34
2.6.2. Spectrophotometry	34
2.7. Liposome preparation and membrane disruption assay	35
2.8. Transmission electron microscopy	36
2.8.1. Negative staining of virus-like particles samples	36
2.8.2. Negative staining of leaf section samples	36
2.8.3. Imaging conditions	37
2.9. Cryo-electron microscopy	37
2.9.1. Preparation of samples	37
2.9.2. Imaging conditions	37
2.9.3. Data processing and 3D reconstruction	37
2.10. Software	38

5. BACK TO THE INSECTS	102
5.1. Introduction	102
5.2. Results	103
5.1.1. Expression of N ω V WT coat protein in insect cells	103
5.1.2. N ω V conformational changes under TEM	104
5.1.3. Cryo-EM of the N ω V procapsid (pH 7.6): The initial assembly	106
5.1.4. SAXS analysis to study the conformational changes of N ω V VLPs as a function of pH	115
5.1.5. The time-dependent pH 5.6 intermediate	118
5.1.6. The conditions for the intermediates to perform the cryo-EM studies	119
5.3. Discussion	121
6. N ω V, "THE MOVIE"	122
6.1. Introduction	122
6.2. Results	123
6.2.1. Cryo-EM structure of N ω V intermediate (pH 6.25): the initial stage of compaction	123
6.2.2. Cryo-EM structure of N ω V intermediate (pH 5.9): half-way in the maturation	128
6.2.3. Cryo-EM structure of N ω V intermediate (pH 5.6): formation of cleavage site and autoproteolysis start	134
6.3. Summary of cryo-EM structures for the maturation movie	140
6.4. Analysis of the transitions at the 6- and 5-fold axis	142
6.5. Quaternary conformational changes to direct the maturation	145
6.6. The multiple roles of γ peptides: breaking and building bonds	147
6.7. Formation of the cleavage site	149
6.8. The movie of N ω V, a simple yet structurally sophisticated nanomachine	151
6.9. Discussion	152
7. GENERAL DISCUSSION	154
7.1. On the importance of having different expression systems	155
7.2. Maturation in the original host	156
7.3. The role of RNA in N ω V maturation	156
7.4. The maturation of the N ω V movie	157
7.5. N ω V conformational changes: a model to design and engineer nanomachines	159
7.6. Final conclusion	160
REFERENCES	161
ACRONYMS AND ABBREVIATIONS	172

APPENDIX 1 – TABLE OF PRIMERS	A1
APPENDIX 2 – SEQUENCES	A2
APPENDIX 3 – CRYO-EM DATA ACQUISITION REPORTS	A4
APPENDIX 4 – MOVIES	A12
APPENDIX 5 – 3D PRINTING	A13
APPENDIX 6 – PUBLICATIONS	A15



List of Figures

Figure 1.1 Structures of icosahedral viruses solved with X-ray crystallography methods.	4
Figure 1.2 Summary of the transient expression process of proteins in plants using pEAQ vectors.	7
Figure 1.3 Structures of viruses solved with cryo-electron microscopy.	11
Figure 1.4 Views on the X-ray structure of the N ω V mature capsid from authentic virions.	15
Figure 1.5 Lepidopteran larvae midgut pH profile.	16
Figure 1.6 Cleavage of the coat protein during maturation.	17
Figure 1.7 Tetravirus crystallographic structures.	18
Figure 1.8 Ribbon representation of N ω V capsid coat protein and autoproteolytic cleavage site.	19
Figure 1.9 N ω V asymmetric unit.	20
Figure 1.10 The four coat proteins subunits of N ω V in the mature capsid form.	20
Figure 1.11 The gamma peptide in the subunits of N ω V in the capsid form.	22
Figure 1.12 Inside view of N ω V capsid with gamma peptides highlighted.	23
Figure 3.1 Plasmid map of the pEAQ- <i>HT</i> expression vector with the N ω V coat protein gene inserted.	42
Figure 3.2 Time-course analysis of the expression of N ω V coat protein in <i>N. benthamiana</i> .	43
Figure 3.3 Sucrose gradient step in the purification of N ω V WT VLPs from <i>N. benthamiana</i> .	45
Figure 3.4 TEM image of N ω V VLPs from <i>N. benthamiana</i> , extracted and dialysed at pH 7.6.	47
Figure 3.5 Leaf section of <i>N. benthamiana</i> infiltrated with pEAQ- <i>HT</i> (EV control).	48
Figure 3.6 Leaf section of <i>N. benthamiana</i> infiltrated with pEAQ- <i>HT</i> N ω V.	49
Figure 3.7 Close up of a leaf section of <i>N. benthamiana</i> infiltrated with pEAQ- <i>HT</i> N ω V.	50
Figure 3.8 Measurements of N ω V VLPs in a leaf section of <i>N. benthamiana</i> .	51
Figure 3.9 Time course incubation at pH 5.0 of wild-type N ω V VLPs produced in plants.	53
Figure 3.10 Maturation curve of N ω V WT VLPs produced in plants.	53
Figure 3.11 Comparison of the kinetics of cleavage between N ω V VLPs from plants and insect cells.	54
Figure 3.12 Stability of the N ω V WT VLPs over time at pH 7.6.	55
Figure 3.13 Membrane lytic activity of N ω V VLPs produced in <i>N. benthamiana</i> and <i>S. frugiperda</i> .	57
Figure 3.14 Initial kinetics of liposome dye release at pH 7.6 induced by mature N ω V VLPs.	57
Figure 3.15 Maturation curve of N ω V VLPs produced in plants and incubated at different pHs.	59
Figure 3.16 Lytic activity of N ω V VLPs from plants with different percentages of cleavage.	60

Figure 3.17 Correlation between lytic activity and percentage of cleaved subunits in N ω V VLPs.	60
Figure 3.18 N ω V VLPs capsids matured <i>in vitro</i> from procapsid produced in plants.	61
Figure 3.19 N ω V VLPs capsids extracted at pH 5.0 from plants.	62
Figure 3.20 N ω V VLPs capsids matured in the plant and extracted at pH 7.6.	63
Figure 4.1 Cryo-EM micrograph of N ω V WT capsid VLPs matured <i>in planta</i> .	69
Figure 4.2 Representative 2D averages of the N ω V WT capsid VLPs.	70
Figure 4.3 2.7 Å resolution structure of N ω V capsid by cryo-EM.	71
Figure 4.4 Cryo-EM structure of N ω V capsid VLP coloured by radius.	72
Figure 4.5 View down a 5-fold axis of the N ω V capsid VLP cryo-EM structure.	73
Figure 4.6 View of the model build in the density map at the cleavage site.	74
Figure 4.7 Surface representation generated from the fitted model in the N ω V WT capsid VLP cryo-EM map.	75
Figure 4.8 Comparison of the structure from the quasi-equivalent subunits of N ω V capsid.	75
Figure 4.9 Inside view of the atomic model of the N ω V capsid matured in plants.	76
Figure 4.10 Cross sections of the cryo-EM map of the N ω V capsid VLP with RNA density.	78
Figure 4.11 Cryo-EM micrograph of N ω V procapsid VLPs.	79
Figure 4.12 Representative 2D averages of the N ω V procapsid VLPs.	80
Figure 4.13 8.2 Å resolution structure of N ω V procapsid by cryo-EM.	82
Figure 4.14 Sucrose gradient step in the purification of N ω V N570T VLPs from <i>N. benthamiana</i> .	83
Figure 4.15 Low pH triggers the cleavage for the N ω V WT coat protein but not for the N ω V N570T.	85
Figure 4.16 SAXS profile of N ω V WT and N570T VLPs at different pHs.	86
Figure 4.17 TEM image of N ω V VLPs intermediates produced in plants and purified at pH 5.7.	90
Figure 4.19 2D classification of the N ω V pH 5.7 intermediate VLPs.	92
Figure 4.20 3D classes from the pH 5.7 dataset.	92
Figure 4.21 Comparison of the cryo-EM structures of the N ω V VLPs intermediates at pH 5.7.	93
Figure 4.22 Summary of the cryo-EM structures obtained from plant-produced N ω V VLPs.	95
Figure 4.23 Side by side comparison of N ω V WT VLPs produced in plants and insects.	97
Figure 5.1 Sucrose gradient step in the purification of N ω V VLPs produced in insect cells.	103
Figure 5.2 TEM images of N ω V VLPs incubated pH 7.6, left, and at pH 5.0, right.	105
Figure 5.3 Cryo-EM micrograph of N ω V procapsid VLPs.	107
Figure 5.4 2D classes obtained in the 2D classification step of the N ω V procapsid VLPs.	108
Figure 5.5 3D classification of the N ω V procapsids VLPs.	108
Figure 5.6 4.9 Å resolution structure of N ω V procapsid VLP by cryo-EM.	109
Figure 5.7 Cryo-EM map of the N ω V procapsid displaying the protein and RNA shell densities.	110

Figure 5.8 Views of the N ω V procapsid cryo-EM structure to display the porosity of the particle.	112
Figure 5.9 Inside view of the cryo-EM density map of the N ω V procapsid VLP with a fitted model.	113
Figure 5.10 Model generated from the fitted model in N ω V procapsid cryo-EM map.	113
Figure 5.11 Comparison of the structure from the subunits of N ω V procapsid.	114
Figure 5.12 Scattering curves of the SAXS data from N ω V VLPs incubated at different pHs.	116
Figure 5.13 Close view at the scattering curves of the SAXS data for N ω V VLPs incubated at different pHs.	117
Figure 5.14 Scattering curves of the SAXS data from N ω V VLPs incubated at pH 5.60 for different times.	118
Figure 5.15 Scattering curves of the SAXS data from the intermediates of N ω V VLPs.	119
Figure 5.16 Representation of the calculated diameters, from the SAXS data, for the N ω V VLPs at different pHs.	120
Figure 6.1 Cryo-EM micrographs of N ω V VLPs at pH 6.25.	124
Figure 6.2 Representative 2D classes averages of N ω V VLPs at pH 6.25.	125
Figure 6.3 3D classes from the of N ω V VLPs at pH 6.25.	126
Figure 6.4 4.8 Å resolution structure of N ω V intermediate (pH 6.25) by cryo-EM.	127
Figure 6.5 Cryo-EM micrographs of N ω V VLPs at pH 5.9.	128
Figure 6.6 Representative 2D classes averages of N ω V VLPs at pH 5.9.	129
Figure 6.7 3D classes from the pH 5.9 dataset.	130
Figure 6.8 3.9 Å resolution structure of N ω V intermediate (pH 5.9) by cryo-EM.	131
Figure 6.9 Surface representation generated from the fitted model in the N ω V intermediate (pH 5.9) cryo-EM map.	132
Figure 6.10 Comparison of the structure from the quasi-equivalent subunits of N ω V intermediate (pH 5.9).	133
Figure 6.11 Cryo-EM micrographs of N ω V VLPs at pH 5.6.	134
Figure 6.12 Representative 2D classes averages of N ω V VLPs at pH 5.6.	135
Figure 6.13 3D classes from the pH 5.6 dataset.	136
Figure 6.14 Comparison of the four intermediate cryo-EM structures from N ω V VLPs at pH 5.6.	137
Figure 6.15 Comparison of the cryo-EM structures of intermediate 4 at pH 5.6 and capsid N ω V VLPs.	138
Figure 6.16 Successive stages in the maturation of N ω V VLPs.	141
Figure 6.17 6-fold axis view from three maturation stages of N ω V VLPs.	143
Figure 6.18 5-fold axis view from three maturation stages of N ω V VLPs.	144
Figure 6.19 Side view of the subunit A of N ω V across different points in the maturation.	145
Figure 6.20 Side view of the subunit C of N ω V across different points in the maturation.	146
Figure 6.21 Structure and distribution of the γ peptides in N ω V VLP.	148

Figure 6.22 Arrangement of the residues, from subunit A, that participate in the cleavage site in the procapsid and capsid N ω V VLP structures.	150
Figure 6.23 N ω V, “the movie”.	151
Figure 7.1 The N ω V movie structure snapshots.	158

List of Tables

Table 2.1 PCR mix and protocol for colony PCR	29
Table 2.2 List of antibodies	34
Table 2.3 List of media, buffers and soil used for experiments with bacteria, plants and insect cells.	39
Table 7.1 Summary of cryo-EM structures produced in this thesis.	140

Chapter 1

Introduction

This thesis presents results of a study of the maturation process of an insect virus, *Nudaurelia capensis* omega virus (N ω V), from a structural point of view. This study combines the use of structural biology tools, such as cryo-electron microscopy (cryo-EM) and small angle X-ray scattering (SAXS) as applied to virus-like particles (VLP) produced in insect cells and plants. The following introduction will present key ideas and concepts in the history of virology, structural biology and VLPs, essential for this work. It will be followed by an overview of the expression systems and their value for producing proteins of interest, like VLPs. Techniques used to study the structure of virus particles, like cryo-EM and SAXS will be briefly introduced. Finally, the previous work on the insect virus, *Nudaurelia capensis* omega virus (N ω V) and virus maturation, will be reviewed to introduce the main goals and hypothesis of this thesis.

1.1. General introduction

Viruses are extraordinary macromolecular structures able to infect countless types of organisms around the globe. Over millions of years, viruses have been evolving to hijack replication machineries to multiply their nucleic acids (Theze et al., 2011). In the oceans, for example, they are the most abundant biological entities and it is possible to find millions of virus particles in just one millilitre of seawater (Bergh et al., 1989; Suttle, 2007). In fact, it is estimated that there are more viruses on Earth than stars in the Universe (Moelling, 2012).

Viruses can be defined as infectious intracellular parasites that have a genome made of DNA or RNA. This genome encodes the viral components that will be synthesised in the host cell and that will self-assemble into new virus particles. These particles, which can have a variety of structures, protect and transmit the genome to other cells or organisms to start new infections (Flint et al., 2015).

Herculean efforts have been made for the last hundred years in order to visualize viruses and understand their intricate structures and the mechanisms involved, for

example, in the assembly, maturation and replication of the virus particles (Johnson, 2010; Lomonosoff, 2018; Lustig and Levine, 1992; Mettenleiter et al., 2018).

In the 1930s, after the development of the electron microscope, the first viruses were visualized by Ernst Ruska, Helmut Ruska and colleagues (Kruger et al., 2000; Ruska, 1987). Subsequently, the first micrographs of viruses, from ectromelia virus and tobacco mosaic virus (TMV), were published (von Borries et al., 1938; Kausche et al., 1939; Mettenleiter et al., 2018).

Another breakthrough in virology happened with the *in vitro* assembly of TMV. To demonstrate the self-assembly process, the viral coat protein was mixed with the viral RNA, which triggered the formation of infectious particles (Fraenkel-Conrat and Williams, 1955). Furthermore, bacteriophage and TMV were used to demonstrate that the nucleic acid molecules from viruses, DNA or RNA, were the components that had infective activity (Fraenkel-Conrat et al., 1957; Gierer and Schramm, 1956; Hershey and Chase, 1952).

In 1978 the structures of tomato bushy stunt virus at 2.9 Å resolution (Harrison et al., 1978), an icosahedral virus; and of tobacco mosaic virus at 2.8 Å resolution (Bloomer et al., 1978), a helical virus, were published. These were some of the early high-resolution structures of viruses achieved using X-ray crystallography. For the first time it was possible to analyse in great detail the structures of the coat protein subunits and the architecture of the virus particles. Afterwards, the structures of viruses such as southern bean mosaic virus (Abad-Zapatero et al., 1980), human common cold virus (Rossmann et al., 1985), poliovirus (Hogle et al., 1985), black beetle virus (Hosur et al., 1987), bean-pod mottle virus (Chen et al., 1989) and others, were solved (see Figure 1.1), providing a better understanding of the structure, functions and protein-nucleic acid interactions of viruses. Furthermore, these structures revealed that proteins from different viruses, infecting very different hosts, could have common folds, like the jelly-roll motif frequently observed in icosahedral viruses, even when the amino acid sequences were not conserved (Rossmann and Johnson, 1989).

Viruses were also used in the early cryo-electron microscopy (cryo-EM) studies (Adrian et al., 1984). Initially, cryo-EM only provided low resolution models and it was sometimes referred as blob-ology (Smith and Rubinstein, 2014). However, some labs combined virus crystallography and cryo-EM to get more information about the structure of viruses and were able to build new models and even to map interactions of the nucleic acids with the subunits of the particle (Cheng et al., 1994; Johnson, 2013; Wang et al., 1992). Recently, in the 2010s, there has been a revolution in cryo-EM, thanks

to improvements in microscopes, detectors and software, that has allowed the generation of atomic resolution models, lots of them of viruses, which has been considered a resolution revolution (Kuhlbrandt, 2014; Liu et al., 2010; Smith and Rubinstein, 2014). In 2017, the Nobel Prize in Chemistry was awarded to Jacques Dubochet, Joachim Frank and Richard Henderson for their work in developing cryo-EM (Cressey and Callaway, 2017).

Viruses can be used and engineered to develop nanoparticles and have demonstrated great potential for applications in nanobiotechnology and biomedicine (Lee and Wang, 2006; Lomonosoff and Evans, 2014; Steele et al., 2017). Some of the recent developments include drug delivery (Czapar and Steinmetz, 2017), bio-imaging (Leong et al., 2010), gene delivery (Azizgolshani et al., 2013) and vaccines (Marsian and Lomonosoff, 2016). In addition to engineering existing naturally occurring viruses, recently computationally-designed icosahedral particles with virus-like properties have been generated. These synthetic nucleocapsids are able to carry their own mRNA, are resistant to nucleases and can be custom-designed, offering a new range of possibilities in nanotechnology (Butterfield et al., 2017).

Despite the great advances achieved in virology and structural biology in the last century, some of them described above, the complex mechanisms used to generate particles are still unknown. In this thesis I present a thorough study of the maturation mechanism of an insect virus. Using cryo-EM we have been able to reveal the process by which N ω V virus particles transition from an immature form, known as procapsid, to a mature and infectious stage, known as capsid. In order to study all the stages in the maturation process I have produced N ω V virus-like particles (VLPs) using plants and insect cells. The definition, properties, uses and production of VLPs are described in the following section.

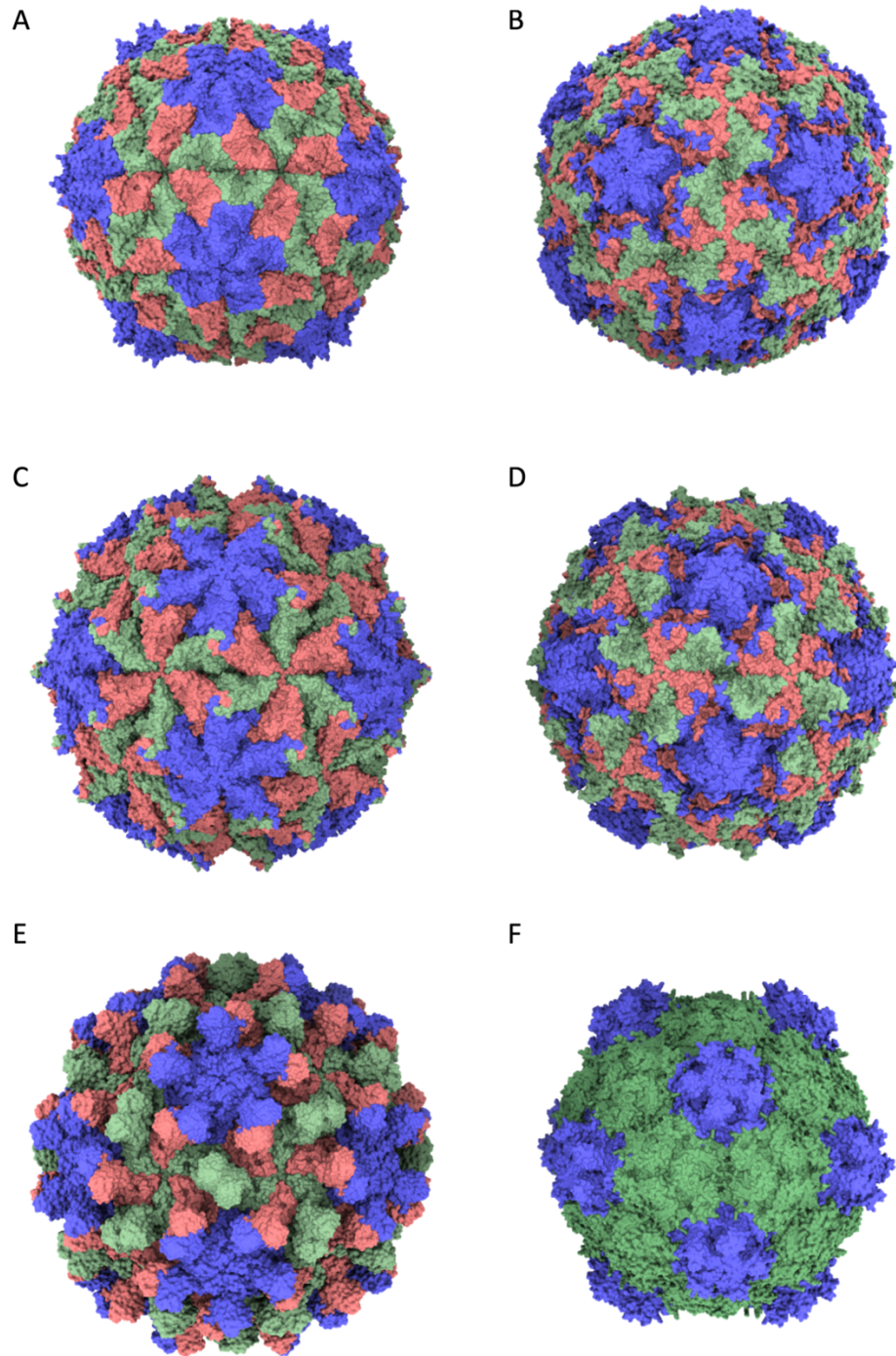


Figure 1.1 | Structures of icosahedral viruses solved with X-ray crystallography methods. The study of the structure of viruses allowed, for the first time, to identify similarities in different viruses that were not based on the amino acid sequence but on the folding of the coat proteins. Some of the first structures of viruses include: southern bean mosaic virus (pdb 4sbv) (a), human rhinovirus (pdb 4rhv) (b), black beetle virus (pdb 2bbv) (c), poliovirus (pdb 2plv) (d), tomato bushy stunt virus (pdb 2tbv) (e), bean-pod mottle virus (pdb 1bmV) (f). Image generated using ChimeraX (Goddard et al., 2018).

1.2. Virus-like particles (VLPs)

A virus-like particle (VLP) is a particle that mimics the morphology and structure of a virus but that lack its infectious genome. This non-infectivity makes them suitable for a broad range of biomedical and nanotechnological applications (Marsian and Lomonosoff, 2016; Steele et al., 2017). When the virus coat proteins are expressed recombinantly, these are able to establish interactions and self-assemble into particles that usually resemble the structure of the original virus (Hesketh et al., 2015; Marsian et al., 2017). These particles can retain the native conformation of their immunogenetic and therefore elicit potent immune responses, which provide protective immunity (Marsian and Lomonosoff, 2016; Marsian et al., 2019). These properties make VLPs ideal vaccine candidates and there have already been several successful studies; influenza (D'Aoust et al., 2008), bluetongue virus (Thuenemann et al., 2013) and poliovirus type 3 (Marsian et al., 2017). In many cases, expression of the coat proteins (CP) alone, in the absence of nucleic acid, allows VLP formation (Hesketh et al., 2015). However, this is not always the case, as some viruses, such as *Ageratum* yellow vein virus, can not generate VLPs when only its CP is expressed (Hesketh et al., 2018).

The ability to retain the original morphological features, makes VLPs a powerful tool for structural studies (Hesketh et al., 2015). They are especially beneficial in circumstances where it is difficult to isolate the original virus or when it could be a threat for health and safety or to the environment. Therefore, VLPs allow the study of the structure of virus particles without the inconvenience of handling an infectious entity, making them safe to use. In addition, in some instances, they can provide extra information as some of the characteristics of viruses have only been identified when produced recombinantly as VLPs. This is because some processes involved in particle formation occur rapidly in the original cellular environment, making them difficult to detect. Furthermore, viruses obtained after the infection are the end product of sometimes complex processes, including maturation. Using the baculovirus protein expression system to produce VLPs of an insect virus, for example, it was possible to generate an immature form of a virus that otherwise had been isolated only in the mature form as an infectious virus (Agrawal and Johnson, 1995; Kearney and Johnson, 2014).

Several expression systems have been developed to produce these virus proteins recombinantly; for example, bacteria, yeast, insect cells, mammalian cells, and plants (Kadri et al., 2013; Masavuli et al., 2017; Peyret and Lomonosoff, 2013; Saunders et al., 2009).

In this thesis I have explored the use of plants and insect cells for the production of VLPs from an insect virus. These expression systems are briefly described in the following sections to provide the reader with an overview of the technologies and the advantages and limitations that they present.

1.2.1. Plant-based virus-like particles

About thirty years ago, plants started to be used for the production of heterologous proteins from humans and animals and were thought of as a cheaper way to produce pharmaceuticals. However, the long times required for the stable transformation of plants, the labour-intensive processes and, generally, the low yields, did not make them very attractive for the demanding processes of the pharmaceutical industry (Lomonosoff and D'Aoust, 2016).

Plant-based expression systems evolved and new technologies appeared, such as the transient transformation of plant tissues with *Agrobacterium tumefaciens* (Peyret and Lomonosoff, 2015). With transient expression systems, it was then possible to produce a protein of interest in a matter of days. One of the systems developed was the CPMV-*Hypertrans* (CPMV-*HT*) based on a modified version of the CPMV RNA-2, which provided enhanced translation of the target gene that yielded high levels of heterologous expression of proteins in plants (Sainsbury and Lomonosoff, 2008; Sainsbury et al., 2010). This expression system resulted in a set of plasmids, the pEAQ (Easy and Quick) vectors. These plasmids provided a platform for the easy and quick production of high yields of recombinant proteins, without the need of viral replication, through agroinfiltration of leaves (see Figure 1.2) (Peyret and Lomonosoff, 2013; Sainsbury et al., 2009).

These innovations were a paradigm shift that revolutionized the plant-based expression field and made it a strong contender for the manufacture of pharmaceutical and biotechnological products (Arntzen, 2015; Lomonosoff and D'Aoust, 2016; Ma et al., 2003). To date, several antibodies (Rosenberg et al., 2013), enzymes for replacement therapies (Zimran et al., 2011), VLPs (Castells-Graells et al., 2018; Peyret et al., 2015; Thuenemann et al., 2013) and vaccines (D'Aoust et al., 2008; Marsian and Lomonosoff, 2016; Marsian et al., 2017) have been produced successfully in plants.

In human therapeutics production, an advantage of plants is the safety that they provide regarding mammalian viral infections, which has been a source of contamination for other expression systems. In some instances, contamination in mammalian cells bioreactors can represent a risk for human health (Zimran et al., 2011).

The plant species used for the production of VLPs in this thesis is *Nicotiana benthamiana*, a wild relative of tobacco. This plant, which comes from desert areas in Australia, is regularly used for transient expression of proteins because it has a fast growth rate, it is easy to handle and infiltrate, and has a defective RNA silencing system (Bally et al., 2018; Goodin et al., 2008). These properties allow for the production of high yields of proteins, in some instances, up to one gram of protein of interest per kilogram of plant leaves (Lomonossoff and D'Aoust, 2016).

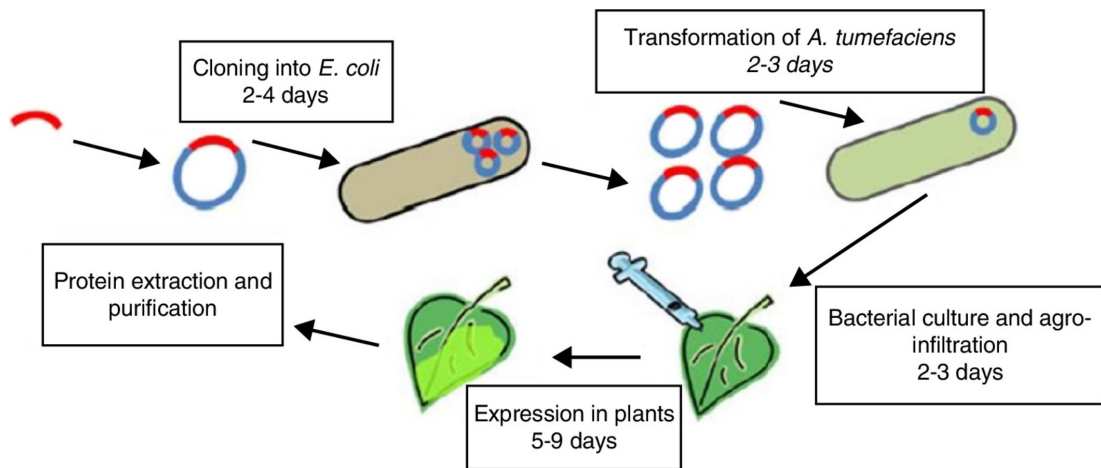


Figure 1.2 | Summary of the transient expression process of proteins in plants using pEAQ vectors.

The gene sequence for the protein of interest, like the coat protein of a virus, is inserted in a vector that is amplified in *Escherichia coli*. Then *A. tumefaciens* are transformed with the plasmid, selected, grown in culture and then agro-infiltrated in the intercellular space of *N. benthamiana* leaves. *A. tumefaciens* will transfer the gene of interest to the plant cells and it is then expressed. After 2 to 10 days of the infiltration, the leaves are harvested and the protein is extracted and purified. Image from Peyret and Lomonossoff (2013).

1.2.2. Insect cell-based virus-like particles

Insect cells are another widely used expression system that can generate large amounts of a desired protein when used with a recombinant baculovirus, containing the sequence for the protein of interest (Kretzschmar et al., 1996; van Oers et al., 2015). Multiple virus particles have been produced using insect cells (Agrawal and Johnson, 1995; Roosien et al., 1990; Saunders et al., 2009; Urakawa et al., 1989), which have been used in applications such as vaccine production (Metz et al., 2013) and structural biology studies (Bothner et al., 1999).

As each expression system has specific properties, it is appropriate to test the production of the protein of interest with multiple systems. There have been several

proteins that have been generated using different expression systems. Variances in the solubility and yield of the proteins have been observed across the different systems (Avesani et al., 2014).

In this thesis, NoV VLPs were produced both in plants and insect cells and several differences were observed that are described in the following chapters. It is noteworthy that VLPs of other viruses have already been generated with both of these expression systems, namely, poliovirus (Marsian et al., 2017; Urakawa et al., 1989), CPMV (Saunders et al., 2009) and bluetongue virus (French et al., 1990; Thuenemann et al., 2013). When compared with plants, insect cells have the limitation that they are usually more expensive to maintain and they are vulnerable to contaminations (Avesani et al., 2014). However, insect cells can also offer some advantages in the purification steps and in the properties of the particles as described in the following chapters.

In this section I have described some of the properties that make VLPs suitable for a broad range of applications. Structural biology, one of the main themes in this thesis, has made use of VLPs in order to understand better the architecture and the molecular mechanism associated with virus particle maturation (Johnson and Chiu, 2000). In the following section I describe the evolution and current state of cryo-electron microscopy, the main tool used in structural studies of the VLPs presented in this thesis. I also briefly discuss small angle X-ray scattering (SAXS), the technology used to establish the optimal conditions to do the cryo-EM analysis in this study.

1.3. Cryo-electron microscopy and the resolution revolution

Structural biologists aim to obtain high-resolution structures of macromolecules with the assumption that function is determined by structure. Traditionally, X-ray crystallography and nuclear magnetic resonance (NMR), were the best tools to achieve near-atomic resolution structures. X-ray crystallography, for example, was used to obtain most of the high resolution structures of proteins (Kendrew et al., 1960) and macromolecular complexes, i.e. viruses (Chen et al., 1989; Helgstrand et al., 2004; Hosur et al., 1987) and protein complexes (Ghilarov et al., 2019; Lawson et al., 1991; Perutz et al., 1960).

However, some macromolecular structures were too big or disordered to determine their structure with these techniques. Electron microscopy offered the possibility to solve this challenge by taking images of randomly oriented molecular complexes that were used to calculate a 3D map of the particle. Still, this methodology

presented limitations such as the radiation damage suffered by the samples and associated loss in resolution. In the 1980s, the development of methods for the preparation and imaging of specimens under cryogenic conditions, in a thin layer of vitreous ice, offered new possibilities and led to the method of cryo-electron microscopy (cryo-EM) (Dubochet et al., 1982). Briefly, cryo-EM is a technique based in the use of a transmission electron microscope (TEM) to generate 2D images of specimens that have been frozen in a hydrated state under conditions that generate vitreous ice. These images can be combined to generate 3D reconstructions that can result in the generation of high-resolution macromolecular structures (Bai et al., 2015; Nogales and Scheres, 2015). To build the three-dimensional structures, thousands and even millions of images of single particles are extracted from the cryo-EM micrographs and processed with computational tools (Scheres, 2012).

In the early days, cryo-EM provided low resolution structures of macromolecules (Smith and Rubinstein, 2014). These structures could be combined with high-resolution crystal structures to solve complexes and answer biological questions (Cheng et al., 1994; Wang et al., 1992). Over the past years, multiple advances in cryo-EM, including the introduction of direct electron detectors (McMullan et al., 2014; Ruskin et al., 2013), have allowed the determination of near-atomic-resolution structures of macromolecules (Kuhlbrandt, 2014; Smith and Rubinstein, 2014). Some of the early near-atomic resolution structures included viruses (Wolf et al., 2010; Zhang et al., 2008) and smaller structures, like the mitochondrial ribosome subunit (Amunts et al., 2014). Cryo-EM is expanding fast and is one of the leading tools in the structural biology field; recently this technology has been proven to be critical for the structural study of pathogens, sometimes in time-critical conditions as with the emergence of the Zika virus (Sirohi et al., 2016). Furthermore, it is increasing the number of structures of protein complexes being determined to resolutions that reveal aspects of the architecture and the molecular basis of their mechanism of action (Alushin et al., 2014; Pei et al., 2019).

For the study of proteins smaller than 100 kDa, which in some cases can be difficult or impossible to resolve with cryo-EM, protein cages that act as imaging scaffolds have been designed. These scaffolds display the target protein in well-defined and symmetric orientations and have allowed the visualization of proteins of 17- and 26-kDa at near-atomic detail by cryo-EM (Liu et al., 2018, 2019a). Subsequently, the use of cryo-EM is expanding to proteins and macromolecular assemblies with a broad range of sizes and complexity.

1.3.1. Cryo-EM of viruses

In 2010, a human adenovirus was one the first viruses from which the atomic structure was obtained by cryo-EM single-particle reconstruction (Liu et al., 2010). Viruses usually have symmetrical structures, which benefits the 3D reconstructions and makes them very popular specimens in cryo-EM single-particle analysis (Figure 1.3). Solving the structures of viruses can reveal various mechanisms, like assembly, particle dynamics, nucleic acid packaging and cellular interactions (Johnson and Chiu, 2000). This information can then be used to develop diagnostics, design new vaccines or transform viruses in nanotechnological tools (Earl and Subramaniam, 2016; Liu et al., 2016; de Ruiter et al., 2019).

Recently a *de novo* cryo-EM reconstruction of cowpea mosaic virus (CPMV), a plant-infecting virus, was determined that provided new information about virus assembly and genome encapsidation (Hesketh et al., 2015, 2017). Moreover, high resolution cryo-EM structures have been achieved for plant viruses that are a risk for agriculture and food safety, including the geminivirus, *Ageratum* yellow vein virus (Hesketh et al., 2018), and the comovirus, broad bean stain virus (Lecorre et al., 2019). Likewise, in the case of animal viruses, the cryo-EM structures of several strains of norovirus will help to develop antivirals and vaccine formulations (Jung et al., 2019) and the structure of an adeno-associated virus will guide future developments in the design of gene therapies (Tan et al., 2018). Cryo-EM is also very powerful for difficult structures of large viruses, such as *Sulfolobus* turreted icosahedral virus (Veesler et al., 2013), which infects an archaeon isolated from extreme environments, or the paramecium bursaria chlorella virus 1, which has particles of 190 nm in diameter with over 6000 coat proteins (Fang et al., 2019). Recent studies have characterized the internal organization and packaging of virus genomes, which is vital to understand virus assembly, genome packaging and infection (Ilca et al., 2019; Liu et al., 2019b).

In the present thesis multiple structures from different conformations of the capsid subunits within NoV VLPs, have been revealed by cryo-EM. These structures provide a unique dynamic and detailed view of the maturation process (see Chapters 4, 5 and 6 for further details).

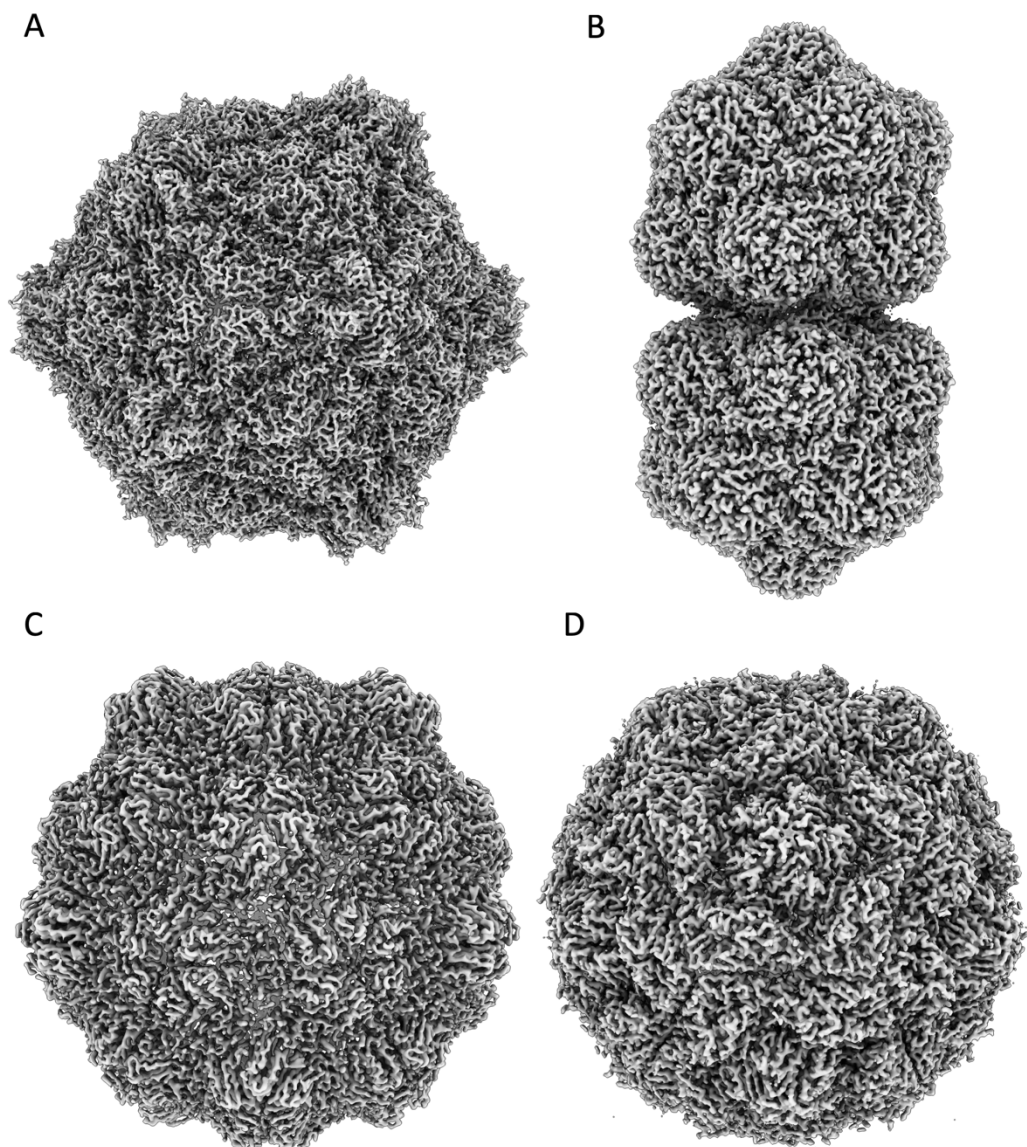


Figure 1.3 | Structures of viruses solved with cryo-electron microscopy. Cryo-EM maps of several viruses with different symmetries and resolutions. (a) cowpea mosaic virus (emd-3952), (b) *Ageratum* yellow vein virus (emd-4174), (c) Atlantic cod nervous necrosis virus (emd-4899), (d) poliovirus type 3 (emd-3747). Image generated using ChimeraX (Goddard et al., 2018).

1.4. Small angle X-ray scattering (SAXS)

Small angle X-ray scattering (SAXS) is a biophysical technique that offers complementary information to X-ray crystallography and electron microscopy. It is based on the analysis of the scattering, at small angles, from X-rays that scattered from a sample. SAXS allows the determination of the shape, size, conformation, aggregation, unfolding, and assembly state of macromolecular structures in solution. However, the resolution range is low (about 50 to 10 Å) compared with other techniques (Putnam et al., 2007).

Combined with other structural techniques, SAXS can contribute to the creation of models of dynamic molecular machines that act in diverse processes such as replication, secretion, assembly and also the large conformation changes of particles as in the case of the N ω V maturation process (Matsui et al., 2010a; Putnam et al., 2007). Usually, the characterization of multiple states in SAXS is more straightforward if the different states are separated and treated as homogeneous samples. In some cases, changes in the buffer conditions can be enough to direct the population of particles to a single conformation. However, it is also possible to determine mixed conformational states, especially if an atomic-resolution structure is available to calculate the theoretical scattering (Putnam et al., 2007).

1.4.1. SAXS of viruses

SAXS has been used to study the maturation of several viruses where the large-scale conformational changes can be controlled by changing the pH. The maturation of these viral capsids induces changes in the SAXS scattering curve that can be correlated with changes in the structure and size of the particle (Putnam et al., 2007). HK97 bacteriophage, for example, undergoes conformational changes during maturation converting the prohead into the expanded mature head state (Lee et al., 2004). These changes have been studied combining several techniques including SAXS, X-ray crystallography and cryo-EM.

For N ω V VLPs it has been possible to identify progressive changes in the SAXS pattern for the procapsid, intermediate stages and capsid; generated by changes of pH. Furthermore, using time-resolved SAXS it was possible to identify intermediates that are dependent on pH and also on the elapsed time since the start of the maturation process. This provided new mechanistic insights on the reorganization and autocatalysis taking place at the subunits (Canady et al., 2001; Matsui et al., 2010a).

1.5. Virus maturation

Large macromolecular protein assemblies are initially built with weak protein-protein interactions inside the cells. These fragile contacts are beneficial as they allow the proper positioning of the subunits and avoid kinetic traps (Caspar, 1980; Katen and Zlotnick, 2009; Zlotnick, 2003). The intracellular space is favourable for weak interactions, which are needed to activate and deactivate cellular functions. However, virus particles also have an extracellular phase, which requires additional stability. To overcome this challenge, virus particles can go through a series of steps during and after the assembly process that allow them to go from initial weak interactions, that allow proper assembly of the particles, to a series of intermediates where the particles gain stability and, usually, infectivity. This transition is known as virus maturation (Johnson, 2010).

Virus maturation is a common mechanism in bacteriophages and animal viruses, including HIV, herpes viruses and N ω V, involving a transition from an initial non-infectious procapsid to a more stable and robust structure, the infectious virion (Steven et al., 2005; Veesler and Johnson, 2012). This process usually involves reorganizations in the quaternary structure of the virus particle that contribute to the protection of the viral genome and formation of the infectious virion. This restructuring can represent substantial changes in the physicochemical properties of the virus, including shape, size and surface charge. The study of the dynamics and mechanisms of these changes can provide fundamental information on virus function, protein assemblies and protein-protein interactions (Lee et al., 2004). Maturation can be driven by different triggers, including nucleic acid packaging, pH-dependent changes and proteases. Acidic pH can drive both expansion of the capsid as in HK97 (Lee et al., 2004) or compaction of the particle as in the case of N ω V (Canady et al., 2000; Matsui et al., 2010a). In maturation processes where there is proteolytic activity, this contributes to trigger structural changes rather than to degrade or eliminate a component and it is usually controlled by a viral protease (Steven et al., 2005). In the case of N ω V, the proteolytic activity that activates infectivity is a maturation-dependent autocatalytic cleavage within the capsid protein that generates a lytic peptide. This peptide stays associated with the particle and is able to lyse cell membranes during the infection process (Banerjee and Johnson, 2008; Domitrovic et al., 2012; Veesler and Johnson, 2012).

Maturation can also be understood as a programmed process in viruses that has been evolving towards a greater sophistication for particle survival in the harsh

extracellular environment. The maturation mechanisms are diverse between different virus families and there are already some examples of cryo-EM structures that have looked at intermediates in the process, such as the HK97 first expansion intermediate, that has been imaged to 9.3 Å. This structure provided insightful information regarding the maturation process of the bacteriophage and it was speculated that enriched inter-subunit interactions may contribute to the stability of the intermediates along the maturation (Veesler et al., 2012). Despite the great advances in the study of virus maturation, many details are still unknown as the study of maturation outside the cellular environment can be challenging. Therefore, models where the maturation could be studied as a continuous system *in vitro* would be ideal.

In 1996, the first paper about the crystal structure of N ω V, a tetravirus which has a maturation mechanism that can be controlled by pH changes, was published (Munshi et al., 1996). This was the first of multiple studies that have examined the maturation process of this virus for over 20 years, making it an excellent model system to study maturation *in vitro* (Domitrovic et al., 2013; Kearney and Johnson, 2014). Despite the intensive efforts to study the different maturation intermediates, it has not so far been possible to obtain the high-resolution structures necessary to get a deep understanding of the maturation process. However, in the past years there has been a “resolution revolution” in the field of cryo-electron microscopy (Kuhlbrandt, 2014) which has presented a new opportunity to study maturation. In the following sections, I describe the biology of N ω V, the previous known structural data and the approach followed in this thesis to solve, for the first time, high-resolution structures of the different steps in the maturation process of N ω V using cryo-electron microscopy.

1.6. *Nudaurelia capensis* omega virus (N ω V)

Nudaurelia capensis omega virus (N ω V) belongs to the *Tetraviridae*, a family of viruses with non-enveloped T=4 capsids (see Figure 1.4) and single-stranded positive-sense RNA genomes that infect one order of insects, the Lepidoptera (moths and butterflies) (Hanzlik and Gordon, 1997; Speir and Johnson, 2008).

The natural hosts of N ω V are the larvae of the pine emperor moth (*Nudaurelia cytherea capensis*), a member of the *Saturniidae* family that is originally from South Africa (Hendry et al., 1985). N ω V is part of the genus *Omegatetravirus*, which also includes *Helicoverpa armigera* stunt virus (HaSV), a virus original from Australia that also infects a moth. Actually, the initial research on tetraviruses was motivated by the possibility to use them as biocontrol agents against pest insect species (Christian et al., 2005; Grace and Mercer, 1965).

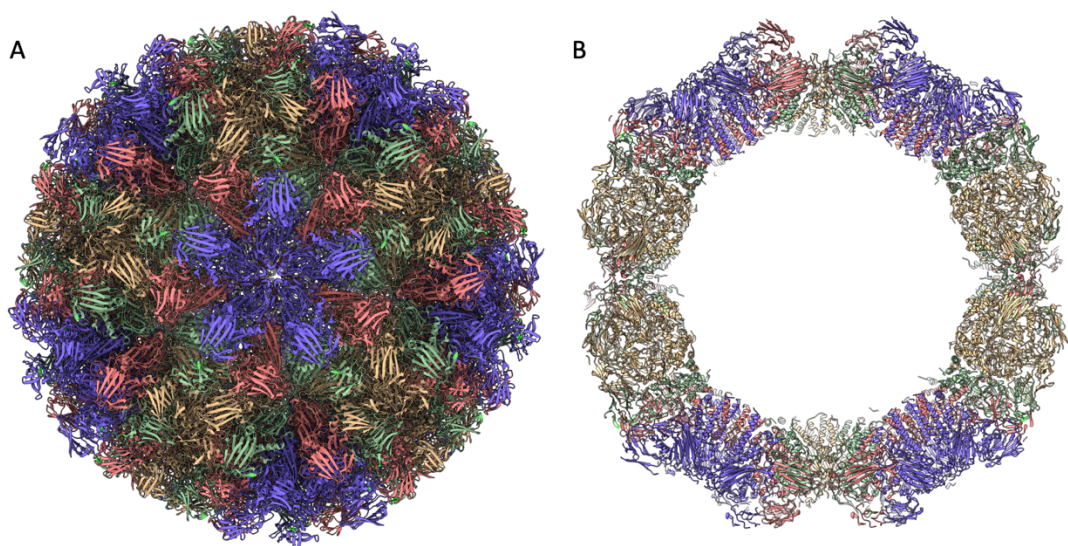


Figure 1.4 | Views on the X-ray structure of the N ω V mature capsid from authentic virions. N ω V has a T = 4 icosahedral capsid with 240 copies of a single coat protein. Ribbon representation of the surface of the full capsid (a) and of a section (b). Structures obtained from PDB entry 1OHF (Helgstrand et al., 2004). Images generated using ChimeraX (Goddard et al., 2018).

1.6.1. N ω V genome

N ω V has a single-stranded positive-sense bipartite RNA genome. RNA-1 (~5.3 kb) encodes for the RNA-dependent RNA polymerase (RdRP) while RNA-2 (~2.5 kb) encodes the capsid protein (Agrawal and Johnson, 1992).

1.6.2. NøV life cycle

NøV is transmitted from insect to insect through ingestion, after which it infects and proliferates in the cells of the midgut. After the start of the infection, the larvae become flaccid and usually die in a few days (Brooks et al., 2002; Walter et al., 2008). It has been reported, in similar viruses infecting *Saturniidae*, that the particles initially form inclusion bodies inside the cells of the gut, then they are dispersed in the cytoplasm and finally the cell membrane from the gut cells breaks and the particles are released (Grace and Mercer, 1965).

It has been proposed that inside the cells, the particles are initially assembled at a relatively neutral pH, allowing for the formation of the procapsids. Later, with apoptosis, there is a drop in the pH that triggers the maturation of the particles. Then the particles are released to the midgut, which has an alkaline pH in lepidopteran larvae (see Figure 1.5) (Dow, 1992). Finally, this alkaline pH triggers conformation changes in the mature particles, which involve the lytic peptide, favouring the disruption of lipid membranes and the propagation of the infection (Domitrovic et al., 2012; Penkler et al., 2016).

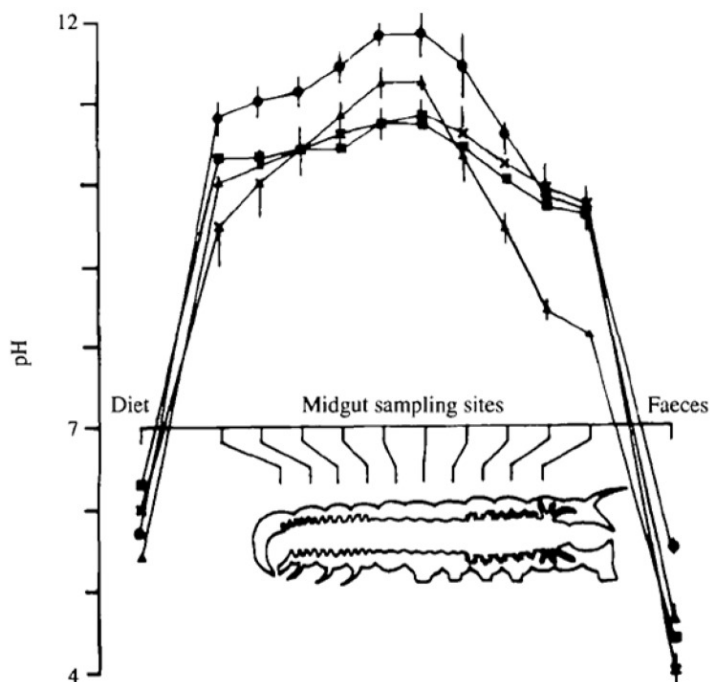


Figure 1.5 | Lepidopteran larvae midgut pH profile. The midgut is the environment where the virus infection occurs. Its highly alkalinity promotes the activity of the lytic peptide from the virus, which contributes to the propagation of the infection. Image from Dow (1992).

It has not been possible to establish a cell line with infectious N ω V virus. However, when the coat protein of N ω V is produced in expression systems, such as insect cells, it assembles into stable intermediate VLPs (known as procapsid) of 48 nm in diameter, that are porous at neutral pH (pH 7.6) (Agrawal and Johnson, 1995). These particles go through a major *in vitro* maturation process, when they are exposed to acidic conditions (pH 5.0), which also triggers an autocatalytic cleavage. The resulting particles are 41 nm in diameter and they are morphologically indistinguishable from the authentic virus (Canady et al., 2000). This autocatalytic cleavage between residues Asn570 and Phe571 results in two polypeptides, β and γ , of 62- and 8-kDa respectively, which remain as part of the mature particle (see Figure 1.6). The residues involved in the formation of the cleavage site are further described in section 1.6.3.

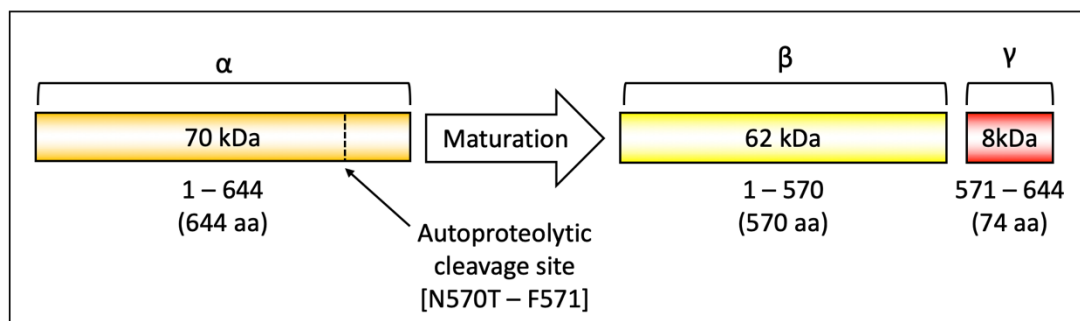


Figure 1.6 | Cleavage of the coat protein during maturation. Schematic representation of the α peptide (full coat protein) and the cleavage site between residues N570 and F571. The subunit cleavage starts at pH 5.5 and generates the β peptide that will maintain the structure of the virus and the γ peptide, which stays in contact with the capsid and is able to lyse cell membranes.

When isolated from *N. capensis* larvae, N ω V was found to be mostly in the mature capsid form, with the cleaved peptides. However, in some extractions it has been possible to also detect low levels of the uncleaved coat protein (70 kDa) (Walter et al., 2008).

As mentioned previously, it is likely that the maturation process, induced by a change in pH *in vitro*, is mimicking maturation in a virus infection. HaSV VLPs, which are similar to N ω V, were produced in yeast cells and it was observed that, in apoptotic cells, the population of procapsid VLPs shifted towards capsid VLPs (Tomasichio et al., 2007). This suggested that apoptosis, which also happens in late stages of insect cell infection (Brooks et al., 2002), decreases the pH in the cells causing the maturation of N ω V. Following maturation, the infectious particles are released from the host cells and the infection propagated.

1.6.3. NωV structure and maturation

The structure of the NωV capsid, from authentic virus purified from infected larvae, at 2.8 Å resolution was determined by X-ray crystallography (Helgstrand et al., 2004; Munshi et al., 1996). The structures of other tetraviruses have been documented and there are atomic models based on X-ray crystallography for HaSV (PDB entry 3S6P) and providence virus (PrV) (PDB entry 2QQP) (Speir et al., 2010). The tetravirus capsids share a similar structural organization; the viruses are composed of 240 copies of the coat protein arranged in icosahedral capsids with a triangulation number $T = 4$ (see Figure 1.7) (Caspar and Klug, 1962; Helgstrand et al., 2004; Munshi et al., 1996; Speir et al., 2010).

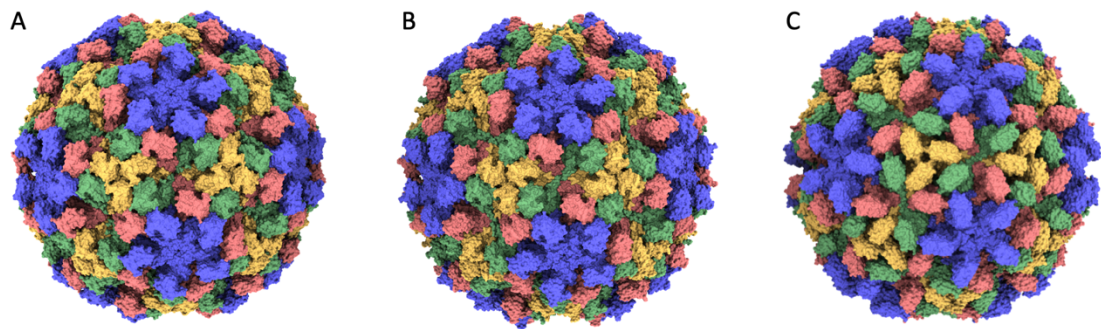


Figure 1.7 | Tetravirus crystallographic structures. Side by side comparison of the structures of NωV (pdb 1ohf) (a), HaSV (pdb 3s6p) (b) and PrV (pdb 2qqp) (c) (Helgstrand et al., 2004; Munshi et al., 1996; Speir et al., 2010). NωV and HaSV nearly have a 70% of sequence identity and their structures are almost indistinguishable. Image generated using ChimeraX (Goddard et al., 2018).

The full-length N ω V coat protein has 644 amino acids and is composed of a single Ig domain (~100 residues), a jellyroll β -barrel domain and a helical domain (see Figure 1.8). The N and C termini from the coat protein face the interior of the capsid and have positively charged domains (primarily, residues 1–45 and 625–644) that interact with the RNA (Kearney and Johnson, 2014) and contribute with the stabilization of the genome.

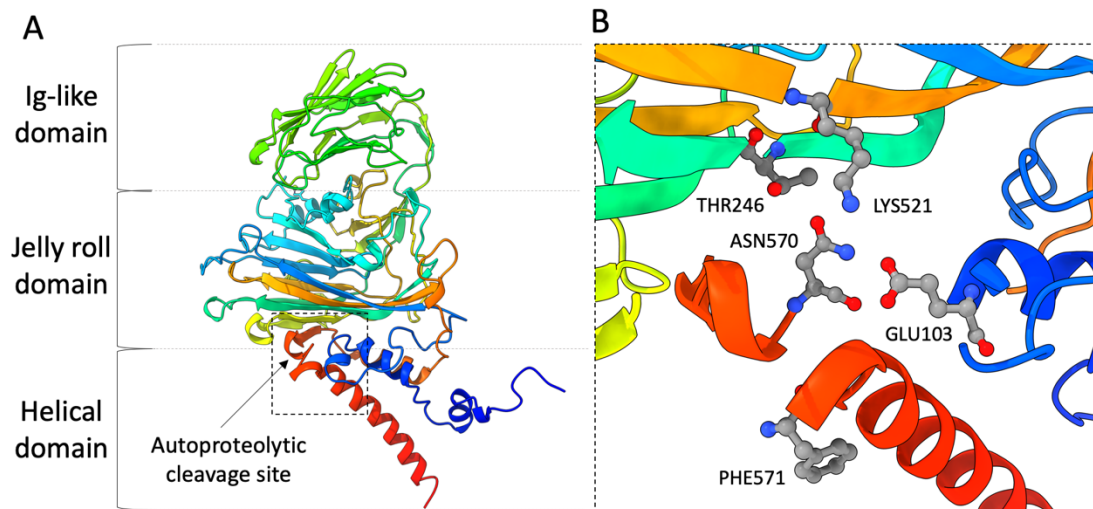


Figure 1.8 | Ribbon representation of N ω V capsid coat protein and autoproteolytic cleavage site. Side view of the A subunit of the N ω V capsid coat protein. The rainbow colouring of the protein starts with blue at the N-terminus and ends with red at the C-terminus. The structure displayed is after autoproteolytic cleavage has occurred. The autoproteolytic event, between residues Asn570-Phe571 of the helical domain (indicated with an arrow), takes place during maturation (a). To form the cleavage site it is believed that Glu103 and Thr246 or Lys521 form the hydrogen bonds with the side chain of Asn570 to move it to the optimal location and then start the autoproteolytic cleavage (b) (Taylor, 2005). In the active site, the catalytic dyad consists of Asn570 and the acidic residue, Glu103. This type of proteolytic enzyme is classified as an asparagine peptide lyase (Rawlings et al., 2011). Structure obtained from PDB entry 1OHF (Helgstrand et al., 2004; Munshi et al., 1996). Images generated using ChimeraX (Goddard et al., 2018).

The icosahedral asymmetric unit contains four subunits, all with the same amino acid sequence, which are labelled as A (blue), B (red), C (green) and D (yellow) (see Figure 1.9). The A subunits form the pentamers at the 5-fold axis and also trimers with the B and C subunits at the quasi 3-fold axis. Three D subunits form trimers in a similar way and are adjacent to the icosahedral 3-fold axis (see Figure 1.4). The N- and C-terminal portions from the different subunits have conformational polymorphism. These

differences have effects on the quaternary structure and result in regions formed by the same sequence performing different roles, which are dictated by the quasi-equivalent subunit where they are positioned (see Figure 1.10) (Kearney and Johnson, 2014).

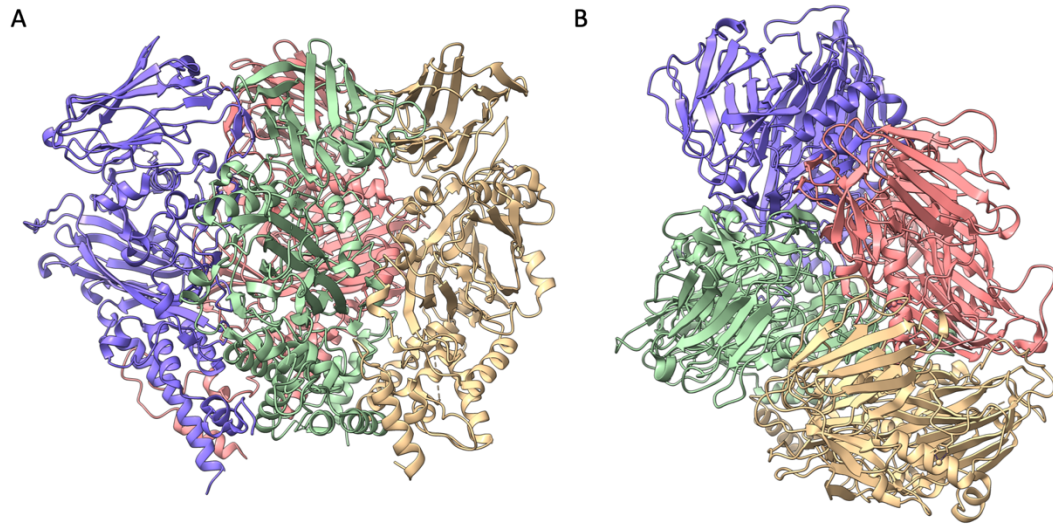


Figure 1.9 | N ω V asymmetric unit. Side view (a) and top view (b) of the asymmetric unit of N ω V. Subunit A (blue), B (red), C (green) and D (yellow). Structure from PDB entry 1OHF (Helgstrand et al., 2004). Images generated using ChimeraX (Goddard et al., 2018).

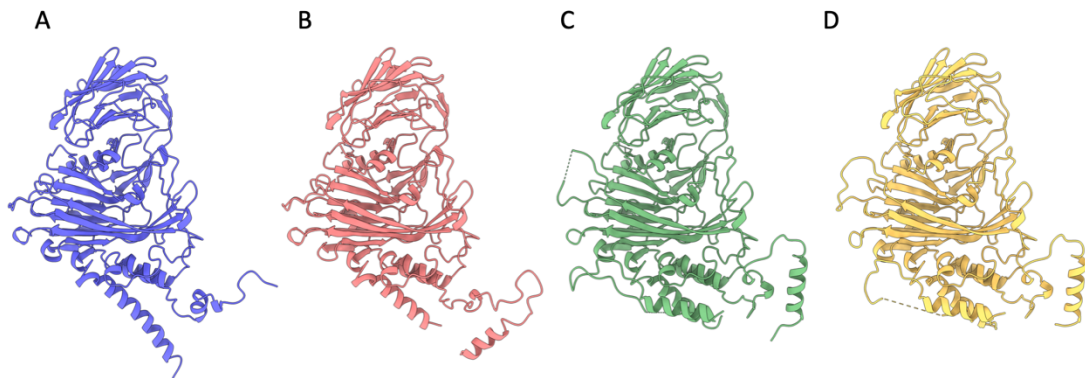


Figure 1.10 | The four coat proteins subunits of N ω V in the mature capsid form. Side by side comparison of the N ω V subunits (a, b, c, d). There is conformational polymorphism in the helical domain, the alpha helices display different arrangements. Structures from PDB entry 1OHF (Helgstrand et al., 2004). Images generated using ChimeraX (Goddard et al., 2018).

1.6.4. N ω V conformational changes and kinetics

During the maturation of N ω V, the large conformational changes occur very quickly (Matsui et al., 2010a). Furthermore, N ω V has intermediate capsid states at pH values between 7.6 and 5, such as pH 5.8 and 5.5 (Canady et al., 2001). These conformational changes are reversible if no more than 10% of the subunits have been cleaved or in a mutant in which the Asn570 at the cleavage site is replaced with a Thr; this generates particles with the expected morphology but that are cleavage defective (Canady et al., 2001; Taylor et al., 2002).

Additional experiments, to study the cleavage kinetics of the maturation when this is induced by incubation of the particles at pH 5.0, found that after 30 minutes of initiating the maturation, nearly 50% of the subunits are cleaved while the completion of the cleavage in the remaining subunits requires several hours (Matsui et al., 2009). This was followed by time-resolved cryo-EM experiments where the structures of N ω V VLPs were resolved at 3 minutes, 30 minutes and 4 hours after initiating the maturation at pH 5.0. Difference maps between the different timepoints and the fully matured capsids were computed and showed that at 3 minutes, the cleavage sites for the A and D subunits were already formed. At 30 minutes there were fewer differences in the density map for the B subunit but there was still a remarkable difference density for the C subunit. Finally, at four hours, subunits A, B and D had no difference in density while the subunit C still had some difference. These results indicated that A and D subunits cleaved first, followed by B and finally the C subunits cleaving at the slowest pace (Matsui et al., 2010b).

1.6.5. The gamma peptide and its lytic activity

Viruses have developed multiple mechanisms to enter and escape cells. Lytic peptides have proven to be a very effective mechanism which allows non-enveloped animal viruses to enter cells (Banerjee and Johnson, 2008). The mechanisms by which these lytic peptides work are not fully understood and several model systems are being used to gain more insights about their function, particularly in regards to the gamma peptide of flock house virus (Bajaj et al., 2016; Banerjee et al., 2009). These peptides can be involved in several cell entry-related events, including the interaction and disruption of host membranes to facilitate the delivery of the viral genome inside the cells (Banerjee and Johnson, 2008).

For N ω V, experiments combining liposomes loaded with a self-quenching dye, buffers at different pH and N ω V VLPs at different stages in the maturation; have shown

that the maximum lytic activity occurs at basic pHs (pH 8 and above) and that it is necessary for the gamma peptide to be cleaved. Therefore, procapsid VLPs, which are not cleaved, do not lyse the liposomes (Domitrovic et al., 2012). Additionally, experiments on the time-resolved lysis of liposomes provided new insights on the lytic peptides that participate in the lysis of the membranes. As discussed above, cleavage and generation of the lytic peptide is a process that takes time and follows an order in the different subunits (Matsui et al., 2010b); therefore lysis experiments were performed at different times after initiating the maturation. The experiments showed that in less than 30 minutes full lytic activity was achieved (Domitrovic et al., 2012). However, at this time less than 50% of the subunits are cleaved and these correspond to cleavage of the A and D subunits (Matsui et al., 2010b). The gamma peptide in the D subunits is inserted in the capsid while in the A subunit forms a pentameric helical bundle within the shell (see Figure 1.11 and Figure 1.12). This suggested that lytic activity came from the gamma peptide from the A subunit and could be ejected through the pentamer (Domitrovic et al., 2012).

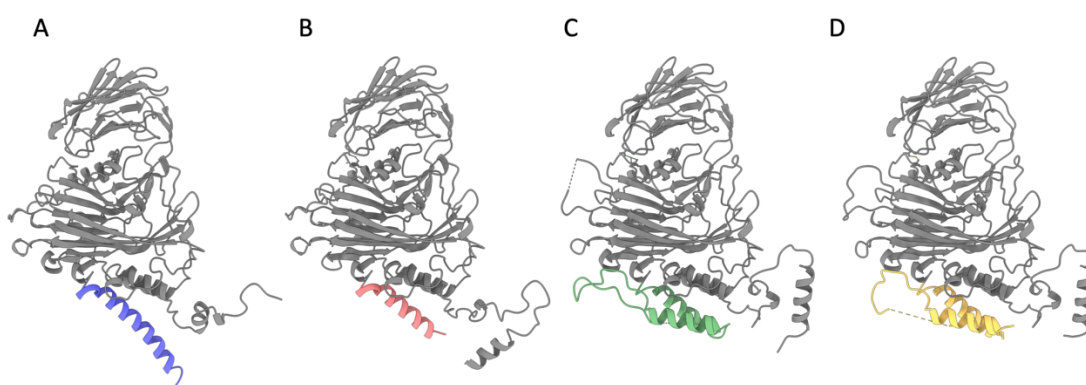


Figure 1.11 | The gamma peptide in the subunits of N ϕ V in the capsid form. Side by side comparison of the four subunits with the gamma peptide highlighted in colour in each subunit (a, b, c, d). The γ peptide displays different conformations across the subunits. The structure for the gamma peptides of A and B subunits, is only visible the residues from 571 to approximately 590. For the C and D subunits there is an additional part of the gamma peptide visible between residues 608 to 641. Structures obtained from PDB entry 1OHF (Helgstrand et al., 2004). Images generated using ChimeraX (Goddard et al., 2018).

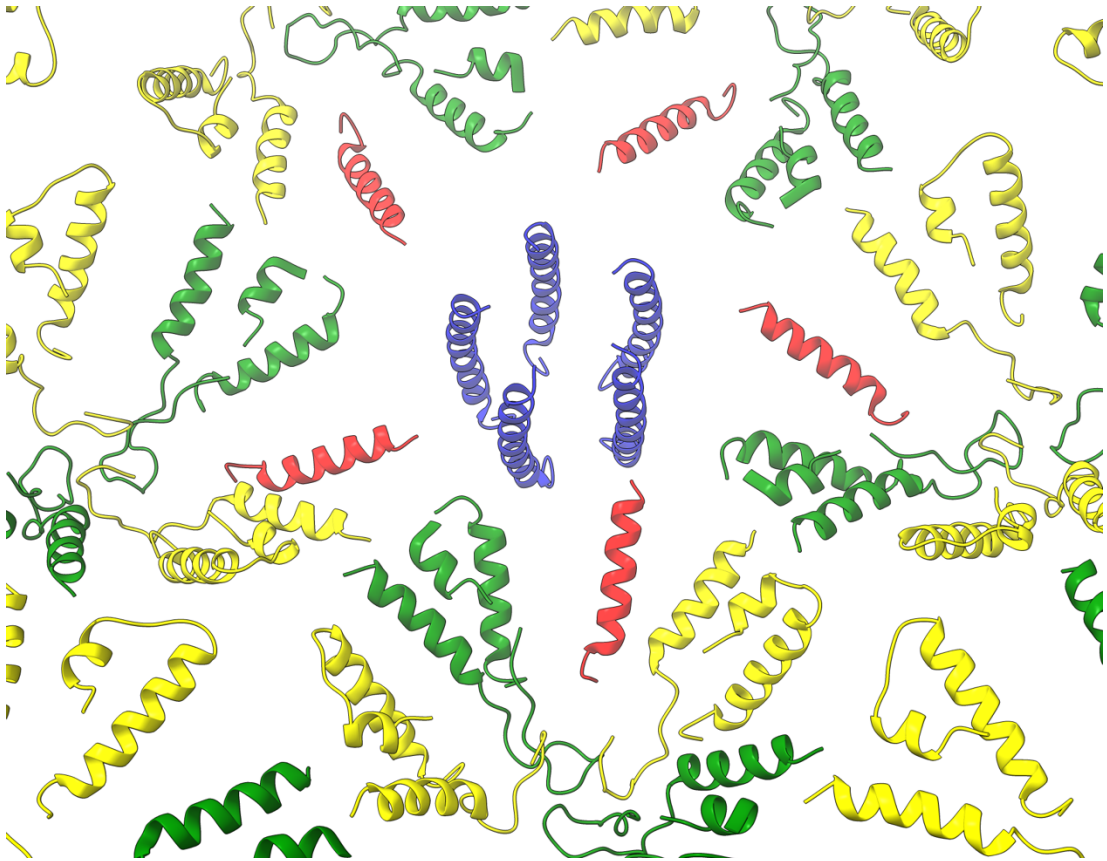


Figure 1.12 | Inside view of N ω V capsid with gamma peptides highlighted. N ω V capsid inside view of only the gamma peptides sequences for subunit A (blue), B (red), C (green) and D (yellow). The gamma peptide in the A subunit forms a pentameric helical bundle within then shell and has been proposed that it has lytic activity. Structures obtained from PDB entry 1OHF (Helgstrand et al., 2004). Image generated using ChimeraX (Goddard et al., 2018).

1.6.6. Applications and engineering of N ω V

N ω V is an excellent model for the study of pH-induced conformational changes in macromolecular assemblies. A better understanding of the intermediate stages of maturation of this virus can lead to the development of new strategies to disrupt the viral life cycle by targeting subunit interfaces with drugs. The interruption of the conformational changes could block the cleavage and the maturation process (Speir and Johnson, 2008). Therefore, it can be of interest for biomedical applications. Furthermore, it has been shown that the Ig domains of N ω V can be modified to carry specific chemical tags and maybe alter its tropism. For example, a (His)₆ tag was inserted into the GH loop of the surface-exposed Ig-like domain of the capsid protein. The produced His-tagged VLPs were able to bind to paramagnetic nickel beads, making this GH loop a potential place for the introduction of new modifications for biotechnological applications (Maree et al., 2006). In addition, the lytic peptide of N ω V has already been used to facilitate the entry of quantum dots into cells (Safi et al., 2017). The ability to precisely control the dynamics of nanoparticles like N ω V will provide novel tools to develop dynamic nanomachines.

1.6.7. The N ω V “movie”

As described in sections 1.6.2 and 1.6.3, N ω V capsid proteins are able to assemble into virus-like particles (VLPs) that maintain the structure and capacity to mature under pH changes (Agrawal and Johnson, 1995; Kearney and Johnson, 2014). Although the structure of the capsid stage was solved at 2.8 Å resolution (Helgstrand et al., 2004; Munshi et al., 1996), no other high-resolution information is available for the other stages in the maturation process.

Since N ω V has a maturation process that can be controlled and that has progressive intermediates, it should be possible to isolate the different stages in the maturation and get their structures. These structures would provide a new view on the architecture and large-conformational changes involved in the maturation of this virus, as well as their driving forces, and would fundamentally new insights for non-enveloped animal viruses (Kearney and Johnson, 2014).

The final goal would be to solve the different structures and then combine them, like frames, to generate the complete “movie” of the maturation process of N ω V.

1.7. Thesis outline and objectives

The main aim of this thesis was to elucidate the details of the maturation process of N ω V to near-atomic resolution. This virus has progressive series of intermediates during its maturation that are determined by pH, which makes it an ideal model for structural and biochemical studies. The overall objective was to reveal the structures of the different stages through the transitions to gain a unique view of the dynamics and processes driving the formation of fully mature virus particles. To do so, the goal was to produce and characterize N ω V VLPs at different stages in the maturation process in order to undertake cryo-electron microscopy (cryo-EM) analysis and to ultimately generate a model of virus maturation at a near-atomic level.

To achieve the overall aim of the project I explored the use of plants to produce N ω V procapsid VLPs. Previous research had shown that plants are suitable for the fast and cheap production of VLPs (Marsian and Lomonosoff, 2016; Thuenemann et al., 2013). The unique properties that N ω V VLPs have in terms of dynamics and structure made them a good candidate to be pursued as a new plant-produced nanoparticle. The objective was to express the coat protein of N ω V in plants, characterize the formation of N ω V VLPs and demonstrate the potential use of plants as a platform to produce dynamic nanoparticles. Together with collaborators, I characterized the properties of the plant-produced VLPs including their ability to break lipid membranes with their lytic peptide (see Chapter 3). The study of N ω V to produce dynamic virus-like particles as protein-based nanomaterials could allow the development of future applications which require mobile as opposed to static structures, for example, nanomachines with controlled motion.

The final goal of this thesis was to combine the biochemical and structural studies to build a high-resolution movie of the N ω V maturation process and reveal the structural changes that the virus undergoes to achieve the final mature and infectious stage. These results would provide a model for the understanding of viral dynamics and the process of particle maturation for non-enveloped animal viruses. However, from SAXS and cryo-EM analysis I found that the plant-produced particles presented limitations in their dynamics, which made the study of the structure of the maturation intermediates (see Chapter 4) problematic. Because of this, I decided to produce N ω V VLPs in insect cells, to compare them with those produced in plants, and I discovered that the maturation of plant-derived particles was hampered by cross-linking of the subunits during purification. Therefore, I switched to the insect cell-produced VLPs to proceed with the

structural characterization of the maturation process (see Chapter 5). I solved the structure of the procapsid and multiple intermediates in the maturation process, analysed and compared the conformational changes across the structures and, finally, built the “movie” of the N ω V maturation (see Chapter 6).

Chapter 2

Materials and methods

2.1. Molecular cloning

2.1.1. DNA constructs

The DNA sequence of N ω V, which was provided by J. E. Johnson (The Scripps Research Institute, USA), was codon optimized for *N. benthamiana* and ordered for synthesis from GeneArt (Life Technologies) with the flanking restriction sites AgeI and XhoI. Moreover, a Kozak consensus sequence (TAACA) was added at the start of the coding sequence.

2.1.2. Plasmids used

For the production of recombinant proteins in plants, it was used the pEAQ-*HT* vector, which contains a multiple cloning site for the insertion of the gene of interest, the suppressor of gene silencing P19 and the kanamycin resistance enabled by nptII (Sainsbury et al., 2009). The gene inserted in pEAQ-*HT* was originally synthesized by GeneArt and was delivered in the pMA plasmid, which contained ampicillin resistance. Further details on this construct are provided in Chapter 3.

For the production of recombinant protein in insect cells, it was used the pFastBac 1 vector for the Bac-to-Bac[®] Baculovirus Expression System (Invitrogen). The plasmid with the N ω V inserted sequence was kindly provided by Tatiana Domitrovic, from Universidade Federal do Rio de Janeiro (UFRJ).

2.1.3. Transformation of *Escherichia coli*

One Shot[®] TOP10 chemically competent *Escherichia coli* (Life Technologies) were used for propagation of the plasmids and were transformed as per manufacturer's instructions. Briefly, cell aliquots were mixed with 10-50 ng of plasmid DNA, incubated on ice for 30 min, followed by a 30 s heat shock at 42 °C and then 2 min incubation on ice. Cells were allowed to recover in SOC medium for 1 hour at 37 °C and 225 rpm, after which they were plated on agar plates containing the appropriate antibiotics and were

incubated overnight at 37 °C. To identify transformed colonies, colony PCR was used with appropriate primers (see Appendix 1). Positive colonies were grown in 5 ml of LB medium containing the appropriate antibiotics and were incubated overnight at 37 °C and 225 rpm.

2.1.4. Transformation of *Agrobacterium tumefaciens*

Agrobacterium tumefaciens strain LBA4404 (Hoekema et al., 1983) electrocompetent cells were transformed by electroporation at 2500 V (Electroporator 2510, Eppendorf). 50 ng of plasmid DNA were used for electroporation of 40 µl of cells in an electroporation cuvette. Cells were then immediately incubated in 800 µl of SOC media for 1 hour at 28 °C and shaking at 200 rpm, then were plated on LB agar containing 50 µg/ml rifampicin and 50 µg/ml kanamycin and incubated overnight at 28 °C.

2.1.5. Bacterial storage conditions

The clones of *E. coli* and *A. tumefaciens* were grown in liquid culture overnight and then were pelleted. The pellet was resuspended in 1 ml of growing media supplemented with glycerol to a final concentration of 25% (v/v). The mixtures were frozen in liquid nitrogen and then stored at -80 °C.

2.1.6. Plasmid and DNA isolation and purification

The QIAprep® Spin Miniprep Kit (Qiagen) was used to isolate and purify the plasmids from bacteria, QIAquick® PCR purification kit (Qiagen) for DNA purification from PCR reactions and QIAquick® Gel Extraction Kit for DNA extraction and purification from agarose gels. The kits were used according to the manufacturer's instructions. Purified DNA samples were stored at -20 °C.

2.1.7. Restriction digests

Restriction enzymes, from New England Biolabs (NEB) and Promega, were used with the appropriate buffers following manufacturer's instructions.

2.1.8. DNA ligation

Quick Ligase (NEB) and T4 Ligase (NEB) were used to ligate DNA fragments following manufacturer's instructions. For ligations of inserts into plasmids, a 3:1 insert to plasmid molar ratio was used. DNA was quantified using a UV-Vis spectrophotometer (NanoDrop™).

2.1.9. Site-directed mutagenesis

The N570T point mutation was introduced in the sequence of the N ω V coat protein. This mutation avoids the cleavage of the coat protein at Asn570-Phe571 which occurs in the WT VLPs at low pHs. This mutation was introduced into the plasmid using the GeneArt Site-directed mutagenesis system (Invitrogen), following manufacturer's instructions. The sequences of the primers used are included in Appendix 1.

2.1.10. Polymerase Chain Reaction (PCR)

For cloning, Phusion high-fidelity polymerase (Roche) was used to amplify the DNA fragments following manufacturer's instructions. The list of primers used can be found in Appendix 1.

For colony PCR, the DNA template was substituted with bacterial cells picked off, with a pipette tip, from a single colony. For the positive colonies, the picked off cells were also used to inoculate 5 ml of culture that was then grown overnight. For example, for the pEAQ vector, C1 and C3 primers, listed in Appendix 1, were used.

Table 2.1 | PCR mix and protocol for colony PCR

PCR Mix		PCR protocol		
Component	Volume	Temperature	Time	Cycles
2x Go Taq Green MM	10 μ l	95 $^{\circ}$ C	5 min	31 X
DNA template	1 μ l	95 $^{\circ}$ C	1 min	
10 μ M forward primer	0.5 μ l	58 $^{\circ}$ C	45 s	
10 μ M reverse primer	0.5 μ l	72 $^{\circ}$ C	1 min/kb	
dH ₂ O	8 μ l	72 $^{\circ}$ C	5 min	
		10 $^{\circ}$ C	∞	

2.1.11. Agarose gel electrophoresis

To analyse PCR fragments, restriction fragments and ligations, agarose gel electrophoresis was used. Gels had 0.8 - 1.2 % (w/v) agarose dissolved in TBE buffer. The molecular weight marker used was HyperLadder I (Bioline). The gel was stained with ethidium bromide.

2.1.12. DNA sequencing

Sequencing samples, such as plasmids, were prepared following manufacturer's instructions. Sequencing was performed out by Eurofins Genomics.

2.2. Transient expression of proteins in *Nicotiana benthamiana*

2.2.1. Plant material and growth conditions

Nicotiana benthamiana plants were grown in Nicotiana soil mix (see Table 2.3), watered daily and kept at 25 °C. Supplemental lighting, with 400W sodium lamps, was provided to maintain a 16 hours photoperiod. Plants were agroinfiltrated 3-4 weeks after pricking out the seedlings.

2.2.2. Agroinfiltration solution preparation

To grow the agrobacteria for the infiltration solution, 2× YT liquid medium was prepared with appropriate antibiotics for the selection of the *Agrobacterium* strain (rifampicin 50 µg/ml for LBA4404) and expression plasmid (kanamycin 50 µg/ml for pEAQ-based plasmids). The culture was usually inoculated in the afternoon and grown overnight. The following day it was subcultured into a bigger volume of medium, using the same concentration of antibiotics as before, and it was grown overnight. The volume of the culture depends on the number of plants used in the experiment. Usually, to infiltrate 3 leaves of one *N. benthamiana* plant (approximately 10 g of fresh weight tissue), 5 ml of infiltration solution is enough. Afterwards, the cultures were centrifuged at 3,260 × g for 10 min at room temperature to pellet the cells. The supernatant was discarded and the pelleted cells were gently resuspended in the MMA buffer (see Table 2.3) to an OD₆₀₀ of 0.4. Then the agro-suspension solution was incubated at room temperature for 0.5–3 h to allow the bacterial culture to adapt to the buffer conditions. Finally, using a blunt-ended syringe, the solution was infiltrated into the leaf intercellular spaces of *N. benthamiana*, as described in Thuenemann et al. (2013).

2.2.3. Small-scale protein extraction

For protein expression tests and time course experiments, small-scale extractions were used. The agroinfiltrated tissue was harvested and a cork-borer was used to take six leaf disks, each one from a different leaf, from infiltrated areas. The six disks, approximately 110-130 mg of fresh weigh material, were transferred into 2 ml screw-cap tubes and were immediately frozen in liquid nitrogen and then stored at -80 °C. For the grinding step, the tubes were transferred to dry ice and then the leaf disks were ground using a pre-cooled metallic pestle, to make sure that the leaf tissue stayed frozen during the grinding. After the tissue became powder, it was mixed with 200 µl of extraction buffer (50 mM Tris, 250 mM NaCl, pH 7.6) + 100 µl of protein loading buffer

(see Table 2.3) and then it was immediately boiled for 20 minutes. The boiled samples were centrifuged at 16,000 x g for 30 minutes and the supernatant was kept and analysed on SDS-PAGE gels.

2.2.4. Large-scale particle extraction

To obtain large amounts of recombinant protein for further characterization and analysis, large-scale protein extractions were set up. Agroinfiltrated leaves of *N. benthamiana* were harvested at 2 to 10 days post infiltration. The plant tissue was weighted and grinded in two and a half volumes of the suitable extraction buffer using a waring blender. The crude extract was then filtered using two layers of Miracloth (Millipore) and then the filtrate was spun at 15,000 x g for 20 minutes at 11 °C. The supernatant was recovered and further purified using a sucrose cushion, as described in Peyret (2015).

The composition of the extraction buffers is specified in each results chapter. For example, to purify N ω V VLPs in the procapsid form, the extraction buffer composition was 50 mM Tris, 250 mM NaCl, pH 7.6. On the other hand, to purify N ω V VLPs in the capsid form, the extraction buffer composition was 50 mM NaOAc, 250 mM NaCl, pH 5.0.

To prepare the single sucrose cushion, the supernatant was transferred into the ultracentrifuge tube (UltraClear 25 x 89 mm) and then 5 ml of 30% (w/v) sucrose solution were layered at the bottom of the tube. The sucrose solutions had the same composition as the buffer used for the initial extraction. The tubes were centrifuged at 166,880 x g (30,000 rpm) for 3 hours at 11 °C using a SureSpin 630/36 ultracentrifuge swing-out rotor (Sorvall). Afterwards, the supernatant was discarded and 400 μ l of the same buffer used for the initial extraction were added to the pellet to resuspend it overnight at 4-8 °C on a shaking platform.

The resuspended pellet was spun at 12,000 xg for 30 minutes at 11 °C in order to remove insoluble material. The clarified supernatant was transferred on top of a 10-40% (w/v) continuous sucrose gradient that was prepared using ultracentrifuge tubes (UltraClear 14 x 89 mm) and a gradient maker (Gradient Master™, Model 108, BioComp Instruments). The sucrose had the same composition of the buffer used for the extraction. The sucrose gradient was centrifuged at 273,800 x g (40,000 rpm) for 1 hour and 15 minutes at 11 °C using a TH641 ultracentrifuge swing-out rotor (Sorvall). The gradient was fractionated from the bottom or top of the tube, specified in each experiment, or the opalescent bands were directly recovered by making a hole on the side of the tube.

To remove sucrose, buffer exchange and concentrate the samples, centrifugal filters (Amicon®, Merck) with a molecular weight cut-off (MWCO) of 100 kDa, were used. For the buffer exchange 10 mM Tris, 250 mM NaCl, pH 7.6 or 10 mM NaOAc, 250 mM NaCl, pH 5.0 were used, depending on the composition and pH of the initial extraction buffer. The concentrated VLPs were stored in the fridge at 4 °C.

2.3. Transient expression of proteins in insect cells culture

2.3.1. Insect cells growth conditions

Spodoptera frugiperda cells (Sf21 cell line) were grown in an incubator with shaking at 26 °C. The cell culture media was Sf-900™ II SFM (Life Technologies) supplemented with 10 % of Fetal bovine serum (Gibco®, Thermo Fisher Scientific).

2.3.2. Insect cells infection

Sf21 cells were infected with recombinant baculoviruses when the insect cells culture had a concentration of 2 to 3 x 10⁶ cells x ml⁻¹. The baculovirus stocks were generated as per manufacturer's instructions. Briefly, the pFastBac vector, containing the N ω V coat protein sequence, was transformed into *E. coli*, DH10Bac strain, which had the baculovirus shuttle vector (bacmid) and a helper plasmid. Then a transposition reaction allowed for the generation of the recombinant bacmid. This recombinant bacmid DNA was transfected into Sf21 cells using the FuGENE® HD Transfection Reagent (Promega). The transfection allowed the generation of the viral stock, which was amplified and used to infect insect cell cultures and express the recombinant protein.

2.3.3. Large-scale particle extraction

To obtain large amounts of recombinant protein for further characterization and analysis, large-scale protein extractions were set up. Insect cells transiently expressing the coat protein of N ω V were harvested at 3 to 5 days post infection. The infected insect cell culture was spun at 500 x g for 10 minutes at 11 °C. The supernatant was discarded and the pelleted cells were resuspended in 25 ml of 50 mM Tris, 250 mM NaCl, pH 7.6 buffer for every 50 ml of initial cell culture. Nonidet P-40 (NP-40) was added to a final concentration of 0.5 % (v/v) (from a 10 % stock). It was mixed gently to avoid too much foam. Then the mixture was incubated for 15 minutes on ice. It was important to shake the mixture every 5 minutes during the incubation in order to break all the cells and release the VLPs. Afterwards, the mixture was spun for 10 minutes at 10,000 x g; the

supernatant was recovered and the pellet was discarded. To prepare the single sucrose cushion, the supernatant was transferred into the ultracentrifuge tube (UltraClear 25 x 89 mm) and then 3 ml of 30% (w/v) sucrose solution were layered at the bottom of the tube. The sucrose solutions had the same composition as the buffer used for the initial extraction. The sucrose cushion was centrifuged at 166,880 x g (30,000 rpm) for 3 hours at 11 °C using a SureSpin 630/36 ultracentrifuge swing-out rotor (Sorvall). Then the supernatant was discarded and 400 µl of the same buffer used for the initial extraction were added to the pellet to resuspend it overnight at 4 - 8 °C on a shaking platform.

The resuspended pellet was spun at 12,000 x g for 30 minutes at 11 °C in order to remove insoluble material. The clarified supernatant was treated following the same procedure described in section 2.2.4. The concentrated VLPs were stored at 4 °C.

2.4. *Nudaurelia capensis* omega virus VLPs purification

2.4.1. Protein dialysis

For the dialysis of protein samples, the Spectra-Por® Float-A-Lyzer® G2 with a MWCO of 100- and 1000- kDa were used. The samples were dialyzed overnight and between two and three changes of the dialysis buffer were done in order to favour the complete buffer exchange.

2.4.2. Protein concentration

Amicon® Ultra Centrifugal Filters (Merck) with a molecular weight cutoff (MWCO) of 100 kDa were used for buffer exchange and protein concentration.

2.5. Protein analysis

2.5.1. Polyacrylamide gel electrophoresis

Protein samples were mixed with protein loading buffer (2:1 ratio) (see details in Table 2.3) and denatured by boiling for 10 minutes. Boiled samples were loaded on precast polyacrylamide gels (4-12 % Bis-Tris) and were resolved with MOPS SDS or MES SDS buffer (Life Technologies) for 30 - 50 minutes at 200 V, depending on the required range of molecular weight separation. To visualize the protein bands, the gels were stained with InstantBlue (Expedeon Ltd). When needed, protein bands of interest from stained polyacrylamide gels were identified by Mass Spectrometry by the John Innes Centre Proteomics facility.

2.5.2. Western blotting and immunodetection

The proteins from the SDS gels were transferred to a nitrocellulose membrane using either the semi-dry blotting process (Trans-Blot® Turbo™ Transfer System, Bio-Rad) with the 10-minute protocol for high-molecular weight proteins or the wet electroblotting system (Mini Trans-Blot® Electrophoretic Transfer Cell, Bio-Rad) running for 1 hour at 100 V on ice to keep the system constantly cooled. After transfer, the membranes were blocked with western blot blocking buffer and agitation for 1 hour at room temperature or overnight at 4 - 8 °C. Then they were incubated with the appropriate primary antibody for 1 hour and then washed three times for 5 minutes each time with western blot washing buffer. Afterwards, the HRP-conjugated secondary was added for 30 - 45 minutes and was followed by three washes with western blot washing buffer and three washes with PBS buffer only. Antibodies used in this project are listed below in Table 2.2 and the buffer compositions are defined in Table 2.3.

To detect bound HRP-conjugated antibody, Immobilon Western Chemiluminescent HRP substrate (Millipore) was used as per manufacturer's instructions. Protein bands were visualised with an ImageQuant LAS 500 (GE Healthcare) CCD camera imaging system, which recorded the chemiluminescence.

Table 2.2 | List of antibodies

Name	Target	Species	HRP	Source
N ω V polyclonal Ab	N ω V coat protein	Rabbit	no	Tatiana Domitrovic, Federal University of Rio de Janeiro
Ab6721	Rabbit IgG	Goat	yes	Abcam

2.6. Protein quantification

2.6.1. BCA assay kit

In order to define the protein concentration of VLP samples, the BCA Protein Assay Kit (Thermo Scientific) was used following manufacturer's instructions.

2.6.2. Spectrophotometry

Protein concentration and purity was estimated by spectrophotometry (NanoDrop™) using A280 and A260/280 ratio.

2.7. Liposome preparation and membrane disruption assay

In collaboration with Tatiana Domitrovic (Federal University of Rio de Janeiro), we tested the lytic activity of the plant-produced N ω V VLPs. Briefly, liposomes composed of 1,2-dioleoyl-sn-glycero-3-phosphocholine (Avanti Polar Lipids, Inc.) and containing sulforhodamine B (SulfoB; Invitrogen/Molecular Probes), a fluorescent dye, were prepared as previously described (Odegard et al., 2009).

For the membrane disruption assays, the liposome suspensions in 10 mM HEPES buffer (pH 7.0) were diluted 100 X in the assay buffers: 100 mM Tris, 250 mM NaCl (adjusted to pH 7.5 - 9.5) or 100 mM NaOAc, 250 mM NaCl (adjusted to pH 5.0 - 7.0). The different buffer conditions used are further described in Chapter 3. To start with the assay, the fluorescence intensity from the liposome suspension was measured with a Cary Eclipse fluorescence spectrophotometer (Varian). An excitation wavelength of 535 nm and an emission wavelength of 585 nm were used. After a few seconds, when the reading was stable, the N ω V procapsids or capsids were added to the liposome suspension to the required final concentration and incubated for 5 to 20 min at room temperature. During the incubation, the fluorescence intensity variations were recorded. Finally, Triton X-100 was added to the liposome suspension to a final concentration of 0.1% to determine 100% dye release. The analyses are described in Chapter 3 and the calculations were performed as previously described (Domitrovic et al., 2012).

2.8. Transmission electron microscopy

2.8.1. Negative staining of virus-like particles samples

Negative staining EM grids were generated by applying 3 μ l of sample (\sim 0.1 to 1 mg/ml) on to carbon-coated 400 mesh cooper grids (EM Resolutions). Prior to applying the sample, grids were glow-discharged for 20 seconds at 10 mA (Leica EM ACE200). Excess liquid was blotted away with filter paper and then the grid was stained with 2% (w/v) uranyl acetate (UA) for 30 seconds, excess liquid was removed with filter paper and it was allowed to air-dry.

2.8.2. Negative staining of leaf section samples

Negatively stained leaf sections were prepared by Elaine Barclay (Bioimaging facility, John Innes Centre). The protocol followed and provided by Elaine is as follows. Plant leaves were cut into 1 mm² fragments and fixed overnight in a solution of 2.5% (v/v) glutaraldehyde in 0.05 M sodium cacodylate, pH 7.3. The fixative was washed out by three successive 10-minute washes in 0.05 M sodium cacodylate and then the fixed samples were placed in a tissue processor (Leica EM TP) to proceed with the remaining steps automatically. Then there was a post-fixation step in 1% (w/v) osmium tetroxide in 0.05 M sodium cacodylate for one hour at room temperature. The osmium fixation was followed by three 15-minute washes in distilled water before beginning 30-minute ethanol dehydration series in 10%, 30%, 50%, 70%, and 95% (v/v) ethanol. Finally, there were two incubations in 100% (v/v) ethanol, each for an hour. Once dehydrated, the samples were gradually infiltrated with LR White resin (London Resin Company) by successive changes of 1:1, 2:1 and 3:1 resin to ethanol ratios, for at least one hour each and at room temperature. Then 100% resin was used for a 16 hours infiltration and then another one was done with fresh resin for another 8 hours. The samples were then removed from the tissue processor and were transferred into gelatine capsules full of fresh LR White resin and were incubated at 60°C for 16 hours to allow polymerization.

Finally, the samples, imbedded in resin blocks, were sectioned with a diamond knife using an ultramicrotome (Leica EM UC6). Ultrathin sections of approximately 90 nm were placed on 200 mesh copper palladium grids (Agar Scientific Ltd) which had previously been coated with pyroxylin and carbon. For contrast staining, the sections were stained with 2% (w/v) uranyl acetate for 1 hour and with 1% (w/v) lead citrate for 1 minute, washed in distilled water and air dried.

2.8.3. Imaging conditions

Grids were viewed using a FEI Tecnai G2 20 TWIN TEM (FEI UK Ltd) at 200 kV and imaged using an AMT XR-60 digital camera to record TIF files (John Innes Centre). Later on, the grids were viewed with a FEI Talos 200C TEM (FEI UK Ltd) at 200 kV and imaged using a OneView 4k x 4k digital camera (Gatan) to record DM4 files (John Innes Centre).

2.9. Cryo-electron microscopy

2.9.1. Preparation of samples

Cryo-EM grids were prepared by applying 3 μ l of sample (\sim 0.2 to 0.4 mg/ml) to 400 mesh grids with a supporting carbon lacey film. The lacey carbon was coated with an ultra-thin carbon support film, less than 3 nm thick (Agar Scientific, UK). Prior to applying the sample, grids were glow-discharged for 30 seconds at 10 mA (easiGlow, Ted Pella). Excess liquid was blotted away by the pads from the Vitrobot Mk IV. Then the sample was vitrified by flash-freezing it in liquid ethane, cooled by liquid nitrogen.

2.9.2. Imaging conditions

NoV data was collected by Dr. Emma Hesketh and Dr. Charlotte Scarff on a FEI Titan Krios EM at 300 kV (Astbury Biostructure Laboratory, University of Leeds). The exposures were recorded using EPU automated acquisition software on a FEI Falcon III direct electron detector. Micrographs were collected at 1.065 \AA /pixel. The data acquisition reports for each dataset are provided in Appendix 3.

2.9.3. Data processing and 3D reconstruction

Movie stacks were motion-corrected and dose-weighted using MOTIONCOR2 (Zheng et al., 2017). CTF estimation was performed using GCTF (Zhang, 2016) and particles were picked using RELION (Scheres, 2012; Zivanov et al., 2018). The autopicking was performed using 2D templates generated after an initial run without reference templates (Laplacian). Subsequent data processing was carried out using the RELION 2.1/3.0 pipeline (Kimanius et al., 2016; Scheres, 2012; Zivanov et al., 2018).

The details for the processing of each one of the datasets are provided in Chapters 4, 5 and 6 together with the cryo-EM maps.

2.10. Software

- The BLAST function of the NCBI to look for nucleotide and protein information.
- Benchling to manage the information about the vectors.
- Fiji to handle and analyse gel and electron microscope images.
- Microsoft Office software to prepare the figures.
- Chimera and ChimeraX (Goddard et al., 2018) to make the figures of the protein structures.

Table 2.3 | List of media, buffers and soil used for experiments with bacteria, plants and insect cells.

Name	Composition
<i>Media for bacteria culture</i>	
Luria Bertani (LB)	10 g·L ⁻¹ tryptone, 5 g·L ⁻¹ yeast extract, 5 g·L ⁻¹ NaCl. pH adjusted to 7.0 with 1 M NaOH
LB agar	As LB, with Lab M No.1 agar added to a final concentration of 1.5%
SOC	20 g·L ⁻¹ tryptone, 5 g·L ⁻¹ yeast extract, 0.58 g·L ⁻¹ NaCl, 0.19 g·L ⁻¹ KCl, 2.03 g·L ⁻¹ MgCl ₂ , 2.46 g·L ⁻¹ MgSO ₄ ·7H ₂ O, 3.6 g·L ⁻¹ glucose
2x YT	16 g·L ⁻¹ tryptone, 10 g·L ⁻¹ yeast extract, 5 g·L ⁻¹ NaCl. pH adjusted to 7.4 with 5 M NaOH
<i>Media for insect cells culture</i>	
Sf-900TM II SFM	Commercial medium with undisclosed composition (Life Technologies)
<i>Soil for plant growth</i>	
Nicotiana soil mix	Peat supplemented with 2.5 g·L ⁻¹ dolomite limestone, 1.3 g·L ⁻¹ base fertiliser, 2.7 g·L ⁻¹ Osmocote®, 0.3 g·L ⁻¹ Exemptor®, 0.25 g·L ⁻¹ wetter
<i>Buffers</i>	
MMA	10 mM MES buffer, pH 5.6; 10 mM MgCl ₂ ; 100 µM acetosyringone
Phosphate-buffered saline (PBS)	140 mM NaCl, 15 mM KH ₂ PO ₄ , 80 mM Na ₂ HPO ₄ , 27 mM KCl, pH 7.2
Tris/Borate/EDTA (TBE)	10.8 g·L ⁻¹ Tris-HCl, 5.5 g·L ⁻¹ Boric, 2 mM EDTA
Western blot (WB) transfer buffer	3.03 g·L ⁻¹ Tris-HCl, 14.4 g·L ⁻¹ glycine, 20 % (v/v) methanol
WB blocking buffer	5 % (w/v) dry milk, 0.1% (v/v) Tween-20, in PBS
WB washing buffer	0.1 % (v/v) Tween-20, in PBS
Protein loading buffer (SDS gels)	4x NuPAGE LDS sample buffer (Invitrogen) and β-mercaptoethanol (3:1 ratio)

Chapter 3

Production and characterization of *Nudaurelia capensis* omega virus VLPs in plants

3.1. Introduction

This chapter presents the successful expression and characterization of recombinant N ω V VLPs in plants. N ω V VLPs have been previously produced in insect cells (Agrawal and Johnson, 1995), but this is the first time that their production has been attempted in plants. Previous research has demonstrated that plants are an excellent platform to recombinantly produce a broad range of VLPs, including nonenveloped single-stranded positive-sense RNA animal viruses (Marsian and Lomonosoff, 2016; Marsian et al., 2017, 2019; Saunders et al., 2009). This suggested that plants could also be a viable approach to produce N ω V VLPs.

The aim of the research reported in this chapter was to study the expression of the N ω V coat protein in *N. benthamiana*, to find the best conditions for expression, assembly and purification and to compare the properties of these particles with the ones produced in insect cells (Agrawal and Johnson, 1995; Matsui et al., 2009; Taylor et al., 2002). Particularly, this chapter focuses on properties like the autoproteolytic and lytic activity of the particles to analyse the effects of the plant expression on the dynamics and biological activity of the VLPs. Furthermore, this chapter reveals new insights into the effect that plant-based expression has for the production of some viral coat proteins, this is further described in Chapter 4.

3.2. Results

3.2.1. Expression of N ω V WT coat protein in plants

To produce N ω V VLPs it is only necessary to express the coat protein of the virus (Agrawal and Johnson, 1995). This protein self-assembles into procapsids that are able to undergo a maturation process, which is pH-dependent, that results in autoproteolytic cleavage of the coat protein (Canady et al., 2000).

The sequence information for the N ω V coat protein was provided by our collaborator, Prof. Jack Johnson, from The Scripps Research Institute. This allowed us to use the same amino acid sequence as that employed for the previous studies with insect cells, enabling direct comparisons to be made, as multiple sequences of this virus can be found in the GenBank database (du Plessis et al., 2005). The selected sequence was codon-optimized to be used in *N. benthamiana*, ordered for gene synthesis and cloned into the pEAQ-*HT* vector (see Figure 3.1), a system that allows for the rapid testing of the expression of the protein of interest in plants (Sainsbury et al., 2009). The sequence inserted into the plasmid was verified (see Chapter 2).

When starting a project, small-scale transient expression of the new molecule is a quick and easy approach to check for the feasibility of large-scale production. Therefore, to test the expression of N ω V coat protein, plants were transiently transformed with the pEAQ-*HT*-N ω V-WT by infiltration of agrobacterium suspensions containing this vector. Leaf discs were collected 0 to 12 days post infiltration (dpi), frozen in liquid nitrogen and stored at -80 °C. All the discs were processed at the same time and the total protein was extracted, as described in Chapter 2. The negative control was material from plants infiltrated with the pEAQ-*HT*-EV (empty vector), which was usually sampled in the middle of the time course. The protein extracts were run in gradient SDS-PAGE gels and the proteins were then transferred to a nitrocellulose membrane. The immunodetection was done using a polyclonal antibody for the N ω V coat protein (see Figure 3.2).

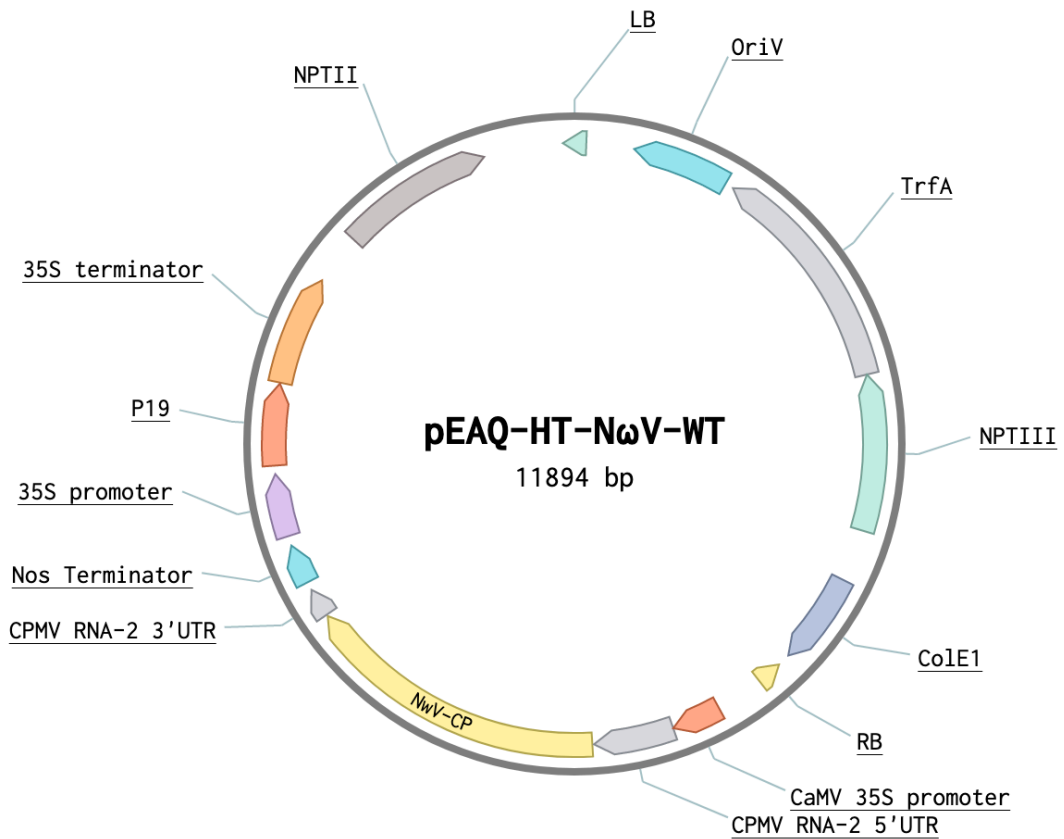


Figure 3.1 | Plasmid map of the pEAQ-HT expression vector with the N ω V coat protein gene inserted.

The synthetic gene, encoding the codon-optimized N ω V coat protein sequence (N ω V-CP), was inserted into the multiple cloning site (MCS) between the two CPMV RNA-2 untranslated regions (UTRs). The CPMV RNA-2 5'UTR contains the *HT* mutations that increases translational efficiency (Sainsbury and Lomonossoff, 2008; Sainsbury et al., 2009). These UTRs are flanked by the CaMV 35S promoter and the nos terminator. Additionally, the vector has the P19 suppressor of silencing sequence to increase the availability of transgene transcript and contains essential elements for its replication and selection in *E. coli* and *A. tumefaciens*.

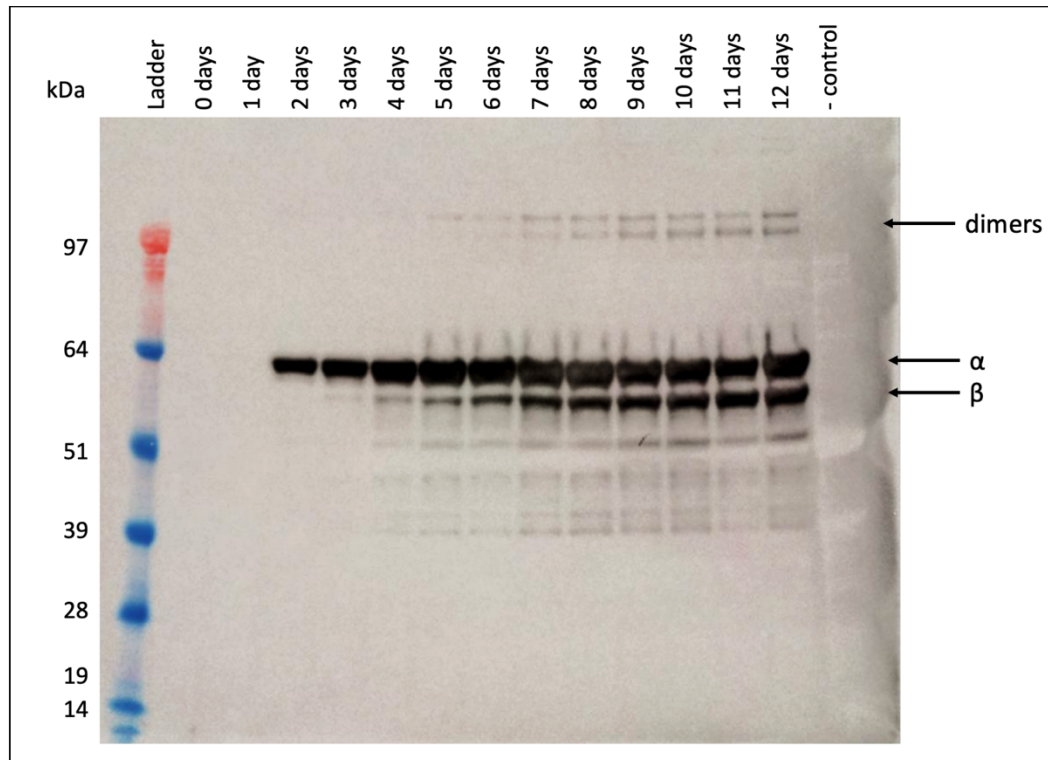


Figure 3.2 | Time-course analysis of the expression of N ω V coat protein in *N. benthamiana*. Samples were collected 0 to 12 dpi from leaves that were expressing pEAQ-*HT*-N ω V-WT. The negative control (- control) was from leaf material infiltrated with the pEAQ-*HT*-EV (empty vector). The protein was detected using a polyclonal antibody for the N ω V coat protein. Expression of the N ω V coat started to be detected 2 dpi and the cleavage started to appear between 3 and 5 dpi and accumulated overtime. Ladder = SeeBlue Plus 2 pre-stained protein standard.

Plants agroinfiltrated with pEAQ-*HT*-N ω V-WT started expressing a protein of an approximate molecular weight of 70 kDa at 2 dpi, according to the western blot results from the protein extracts. This was consistent with the expected size for the full-length coat protein (α peptide) of N ω V, which is of 70 kDa. However, after 3 to 5 dpi a lower molecular weight band of about 62 kDa appeared. This smaller protein was the correct size to be the β peptide, which is the product of the autoproteolytic cleavage of the α peptide when there is maturation of the particles. This indicated that the N ω V coat protein was produced in plants and over time there was processing of the protein. The accumulation of the β peptide increased overtime. This suggested that the coat proteins were either assembling into VLPs and then maturing inside the plant or that some protease was degrading the coat protein. Additionally, higher molecular weight bands of around 150 kDa were observed in some of the extracts, which could correspond to dimers of the coat protein that have either resisted the denaturation process used to run

the SDS gel or are covalently linked (see Chapter 4). When the sample was purified from the plant extract (see details in section 3.2.2), the high molecular bands (~150 kDa) and the 70 and 62 kDa bands were also confirmed to be related to the N ω V coat protein by mass spectrometry of tryptic digests.

To conclude, it is important to note that the cleavage results described in this chapter are different from what it has been previously observed in insect cells, where only the α peptide was extracted after recombinant expression (Agrawal and Johnson, 1995). This suggests that in plants cleavage occurs *in vivo* inside the plant overtime. At this stage it was hypothesized that the maturation was driven by changes in the pH of the environment where the particles accumulated inside the plants. However, it could be also triggered by other factors like RNA encapsidation, a possibility further discussed at the end of this chapter.

Summary of section 3.2.1: N ω V coat protein can be transiently expressed in plants and a fraction of the α peptide is cleaved after it started to accumulate in the cells, suggesting a process of *in vivo* maturation of the N ω V VLPs inside the plant leaves over time.

3.2.2. Purification of N ω V WT VLPs expressed in plants

N ω V VLPs were extracted from plant material using the 50 mM Tris, 250 mM NaCl, pH 7.6 extraction buffer, to preserve any procapsids present in the sample. Then the plant extract was clarified and further purified using a single sucrose cushion centrifugation, as described in Chapter 2. To further purify the N ω V VLPs and reduce the amount of plant protein contaminants, the samples were run through a continuous 10 to 40% (w/v) sucrose gradient (see Figure 3.3). These gradients facilitate the separation of heterogeneous sample based on the properties, such as size, of each component. This was very convenient, because VLPs are large assemblies of proteins and were expected to run in different fractions than the other plant proteins. Furthermore, this technique has been previously used to separate particles with different sizes (Taylor et al., 2002), which was useful in order to be able to separate heterogeneous populations of particles and aggregates.

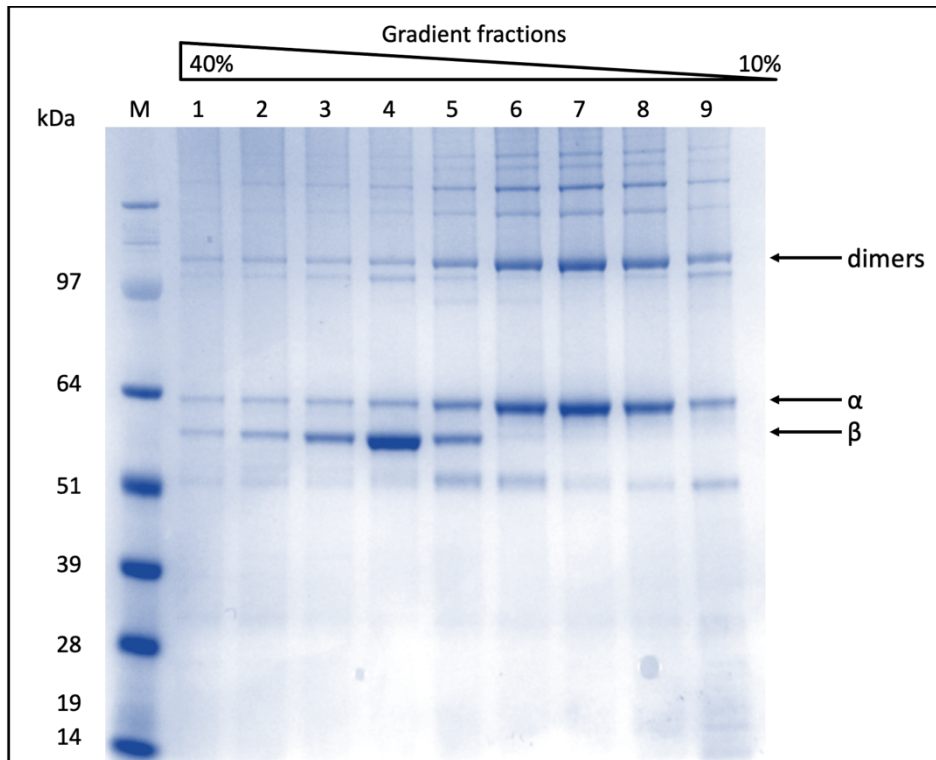


Figure 3.3 | Sucrose gradient step in the purification of N ω V WT VLPs from *N. benthamiana*. The resuspended material from the previous pelleting step was run through a continuous 10 to 40 % (w/v) sucrose gradient. The fractions were collected from the bottom of the tube, being the first collected fraction labelled as 1. These fractions were separated in a 4 to 12 % SDS-PAGE stained with InstantBlue. Across the gradient the fractions contain different concentrations and ratio of cleaved and uncleaved protein. The cleaved protein (fraction 4) corresponds to mature particles and sediments in lower fractions than the uncleaved procapsid (fractions 6 and 7). M = SeeBlue Plus 2 pre-stained protein standard.

The particles were separated in the gradient during the ultracentrifugation and were analysed with SDS-PAGE gels stained with InstantBlue (see Figure 3.3). In the gel it was observed that the β peptide, the cleaved version of the coat protein, accumulated in the lower fractions of the gradient, while the uncleaved protein advanced less in the gradient. The cleaved protein corresponds to the form of the coat protein found in mature N ω V capsids, which have a smaller diameter than the procapsid containing the uncleaved coat protein. Previous research with insect cells also reported that capsids moved further down in gradients than procapsids (Taylor et al., 2002). These results suggested that the particles were able to mature inside the plants, as proposed in the previous section, and that it was possible to separate the different populations of particles, procapsids and capsids, by sucrose gradient. Using other gradients, such as

iodixanol, it was also possible to isolate mature N ω V capsids directly from plant extracts at pH 7.6. As described in previous research, it is possible to combine different kinds of gradients in order to isolate particles with different properties (Brillault et al., 2017; Marsian et al., 2017; Peyret, 2015; Thuenemann et al., 2013). These results demonstrated that the expression of N ω V VLPs in plants was successful. Recovered purified yield of N ω V VLPs was found to range from 0.1 to 0.25 mg of protein per gram of fresh weight infiltrated leaf tissue. This was very encouraging as this yield was sufficient to carry on further experiments.

In the following sections the modifications in buffers and procedures that have been employed for the purification and isolation of particles at different stages of the maturation process are described. Furthermore, as shown in section 3.2.1, the ratio of cleaved and uncleaved protein changes depending on the time that the extraction was done after the infiltration. This indicated that in order to get populations of mainly procapsids, the time that the VLPs spend in plants should be short (3 to 4 dpi); on the other hand, to get populations enriched for mature capsids, a longer incubation time in plants (6 to 12 dpi) is necessary.

Summary of section 3.2.2: The initial sucrose cushion is a valuable step to concentrate the VLPs; however, it also results in the accumulation of plant contaminants and additional purification steps are required. Multiple ultracentrifugation steps help to concentrate the VLPs and then separate them from the plant contaminants using procedures like the sucrose gradients described in this section. Furthermore, this gradient procedure allowed the separation of capsids and procapsids from the plant extract; indicating that the maturation that occurs in plants over time yields heterogeneous populations of particles. In conclusion, for the production of N ω V VLPs in plants they are important both the conditions of the extraction and the time that the particles spend inside the plants.

3.2.3. Characterization of N ω V WT VLPs

3.2.3.1. Transmission-electron microscopy of purified N ω V procapsid VLPs

Procapsids were isolated from the peak fractions of the sucrose gradient, as described in the previous section (see section. 3.2.2), and used for TEM analysis. The details of the preparation of the grids are provided in Chapter 2. Briefly, the purified sample was loaded on a grid, the excess of sample was then removed with filter paper and finally it was stained with 2% (w/v) uranyl acetate.

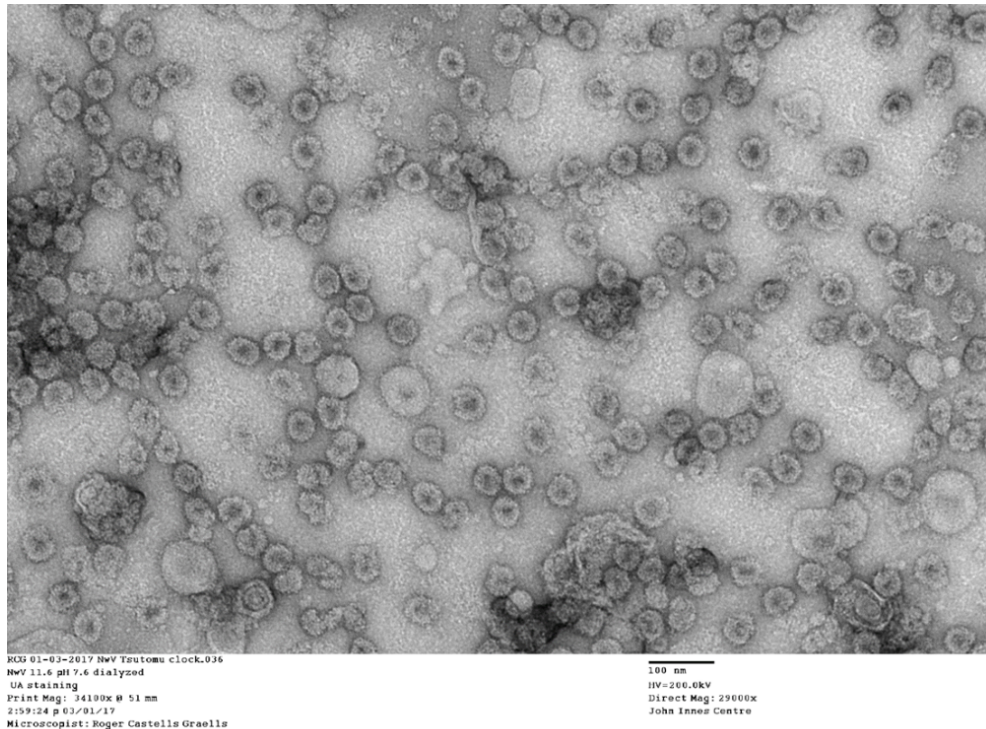


Figure 3.4 | TEM image of N ω V VLPs from *N. benthamiana*, extracted and dialysed at pH 7.6. The particles were stained with 2% (w/v) uranyl acetate (UA) and visualized by TEM. The VLPs have a spherical shape and some imperfections due to their flexibility. Their diameter is ~45-50 nm. The 100 nm scale bar is provided in the figure caption generated by the microscope software.

The TEM images demonstrate that the N ω V coat protein expressed in plants is able to self-assemble in VLPs. The N ω V VLPs have the shape expected for this virus and the correct diameter of ~48 nm. The particles are porous and the stain is able to penetrate to the centre of the particles. These procapsids display flexibility and the heterogeneity in their morphology may be induced by the uranyl acetate as it has a low pH (4.2 - 4.5) and these particles are pH sensitive. Therefore, these images showed the first plant-made N ω V VLPs and they present a similar morphology as previously reported for the insect cell-produced procapsid VLPs (Taylor et al., 2002). The confirmation of the presence of plant-produced N ω V VLPs by TEM represented a major step forward in my project as it was essential in order to be able to perform the structural analysis (see Chapter 4).

Summary of section 3.2.3.1: In plants it is possible to successfully express and assemble N ω V procapsid VLPs. The particles display the characteristic features and size expected for this virus. As mentioned in section 3.2.2, it was also possible to obtain N ω V capsid VLPs directly from the plant extracts. In this thesis three different ways to obtain capsids have been explored, which are described in the following sections. The TEM images for all the N ω V capsid VLPs are presented in section 3.2.4.

3.2.3.2. Leaf sections of infiltrated plant material

It was anticipated that the N ω V coat protein would be expressed in the cytoplasm of the plant cells, as the coat protein did not contain any secretion signal, and we wanted to find out if the particles ended up accumulating in the cytoplasm, in some other compartment from the cell or released to the apoplast. To explore the distribution of the particles within the plant leaves we performed thin sections of plants transiently expressing the N ω V coat protein and also of controls infiltrated with empty vector (EV).

For this experiment, I prepared the plants and the transient transformations, then Elaine Barclay, from the bioimaging facility at John Innes Centre, performed the fixation, embedding and sectioning of leaf fragments. Finally, I imaged the sections with the TEM.

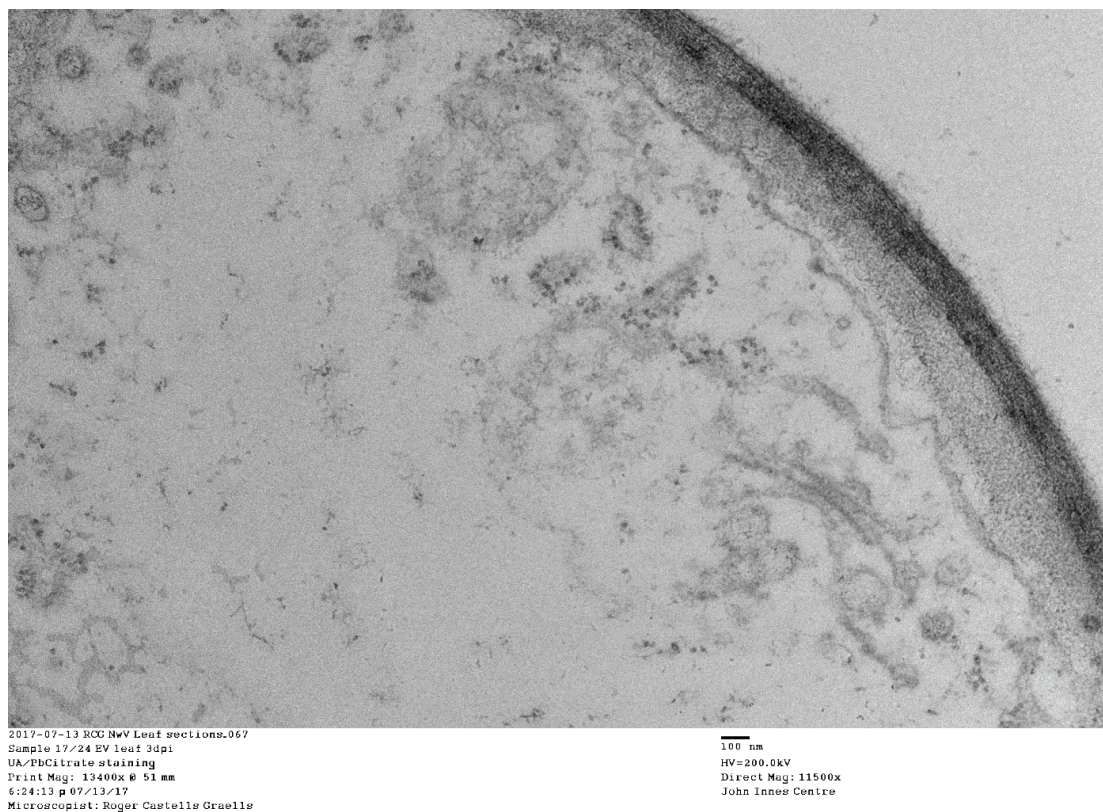


Figure 3.5 | Leaf section of *N. benthamiana* infiltrated with pEAQ-HT (EV control). On the right side of the image it is possible to observe a dark line, which corresponds to the cell wall. On the left of this line there are several structures from the inside of the plant cell. The ~20 nm spherical structures could correspond to ribosomes. The leaf fragment was fixed 3 days after being infiltrated with the pEAQ-HT empty vector and was stained with UA/Lead citrate (LC). A 100 nm scale bar is provided in the figure caption generated by the microscope software.

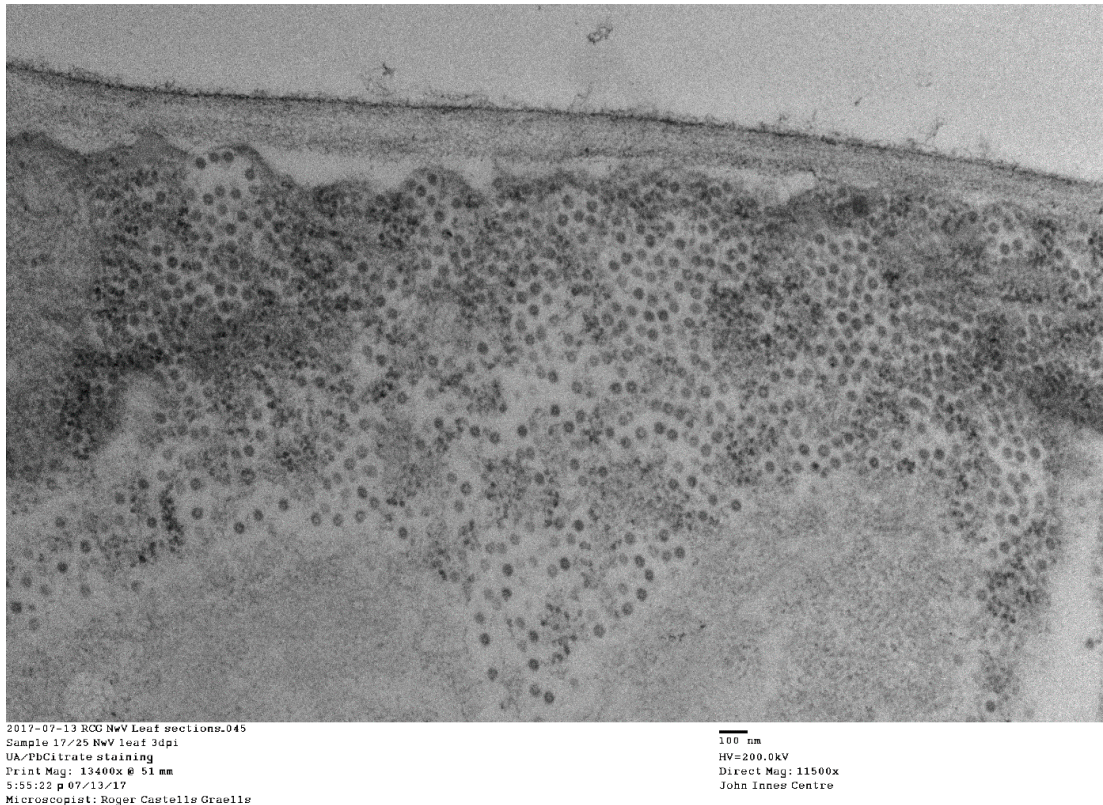


Figure 3.6 | Leaf section of *N. benthamiana* infiltrated with pEAQ-HT N ω V. On the top side of the image it is possible to observe a dark line, which corresponds to the cell wall. Below this line there is an accumulation of hundreds of spherical structures with a diameter of \sim 40 to 50 nm which corresponds to N ω V VLPs accumulating in the cytoplasm of the cell. The leaf fragment was fixed 3 days after being infiltrated with the pEAQ-HT-N ω V-WT vector and was stained with UA/LC. A 100 nm scale bar is provided in the figure caption generated by the microscope software.

The first two images (Figure 3.5 and Figure 3.6) were taken at the same magnification (11,500 x) in an area near the cell wall in order to compare the EV control and the N ω V construct. In the second image (Figure 3.6) it was possible to see structures resembling N ω V VLPs that were not present in the EV control. These strongly suggested the accumulation of N ω V VLPs in the cytoplasm of the plant cells. Furthermore, it was hypothesized that the smaller structures (\sim 20 nm) observed in the EV control, were ribosomes. These structures were also present in the sample expressing the N ω V construct but they were mixed with the high density of N ω V VLPs.

Further images were taken of smaller areas of the plant cell at higher magnification in order to characterize the N ω V VLPs inside the cells.

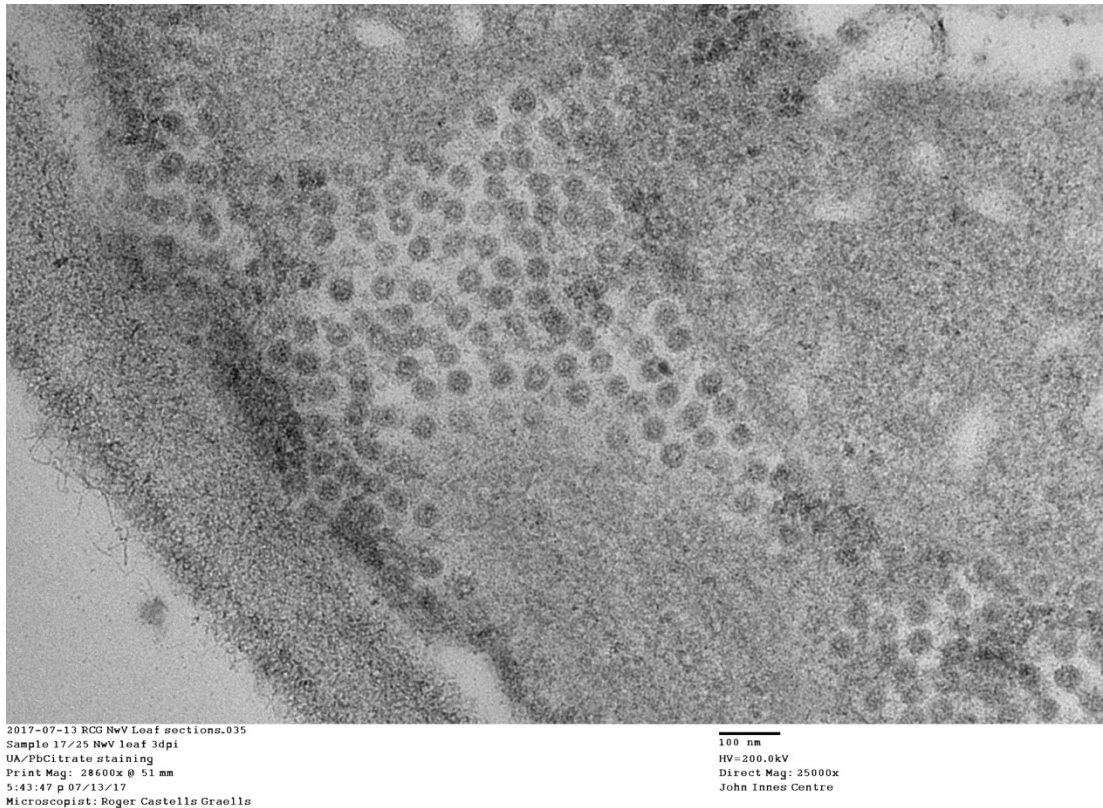


Figure 3.7 | Close up of a leaf section of *N. benthamiana* infiltrated with pEAQ-*HT* NwV. Close up image of the leaf section where it was possible to see the accumulation of NwV VLPs in the cytoplasm of the cell. The layer observed in the left side of the image corresponds to the cell wall. The leaf was fixed 3 days after being infiltrated with the pEAQ-*HT*-NwV-WT vector. Stained with UA/LC. A 100 nm scale bar is provided in the figure caption generated by the microscope software.

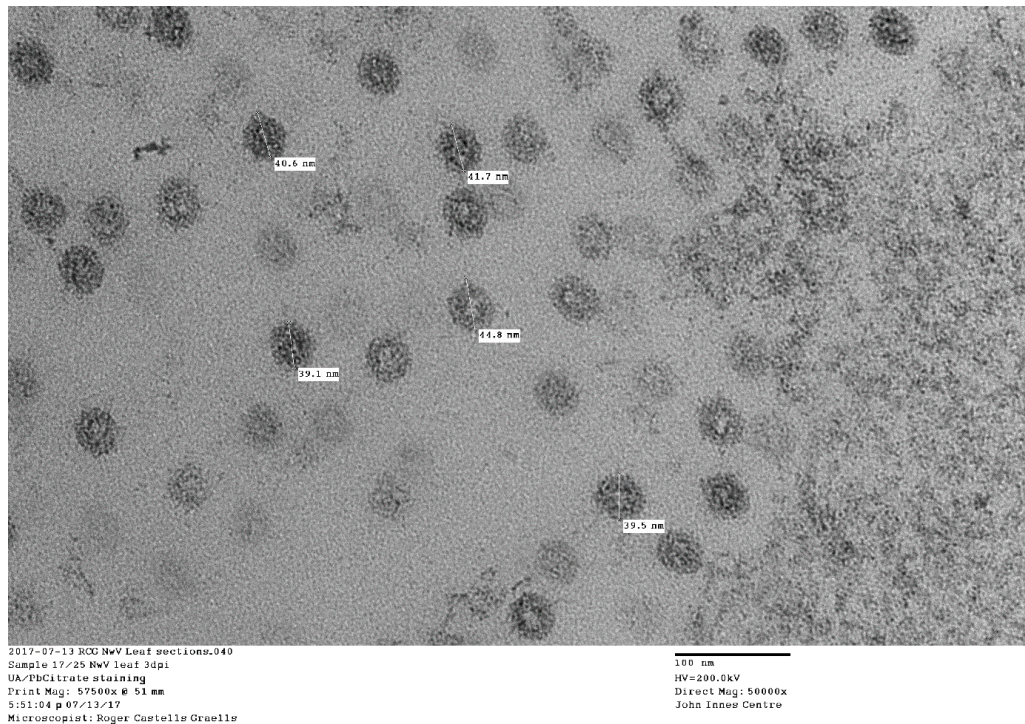


Figure 3.8 | Measurements of N ω V VLPs in a leaf section of *N. benthamiana*. N ω V VLPs in the cytoplasm of the plant cell measured using a 50,000 x magnification. The particles presented slight differences in diameter (~39 to 45 nm). The leaf was fixed 3 days after being infiltrated with the pEAQ-*HT*-N ω V-WT vector. Stained with UA/LC. A 100 nm scale bar is provided in the figure caption.

The leaf sections reveal the accumulation of numerous N ω V VLPs in the cytoplasm of the plant cell (see Figure 3.7). Measurements performed with the TEM images indicate that the observed particles have a diameter of approximately 40 to 45 nm, which is the expected range for the particles and can include both procapsids (~48 nm) and capsids (~42 nm) (see Figure 3.8). It is important to note that these samples were sections of leaves, so there could be variations in the size of the particles determined by the region of the particle where it had been cut. The presence of particles in the apoplast was not observed, suggesting that at this stage all the particles were still inside the cells. In the negative control it was not possible to observe the presence of VLPs, however some smaller spherical structures of around 20 nm were present and it was hypothesized that those could be ribosomes from the plant cell. Therefore, it is possible to conclude that the N ω V coat protein is able to assemble in VLPs inside the plants cells which then can be purified, as shown in section 3.2.2.

Summary of section 3.2.3.2: When N ω V coat protein is transiently expressed in plant cells is able to form particles. The N ω V VLPs accumulate in the cytoplasm and stay inside the cells in the early days of expression.

3.2.3.3. Autocatalytic cleavage assay: a comparison between the insect cell- and plant-produced VLPs

N ω V procapsids (uncleaved) can transition to the capsid conformation when pH is lowered from neutral to acid conditions (Canady et al., 2000). The conformational change then leads to activation of the autocatalytic site of each capsid protein. The autoproteolysis of the capsid protein α (70 kDa) occurs between residues Asn570 and Phe571 and generates the β (62 kDa) and γ (8 kDa) peptides. Previous research (Matsui et al., 2009) measured the kinetics of cleavage for N ω V WT VLPs produced in insect cells and showed that at pH 5.0 the half-life of the cleavage is of 30 min. In order to check the cleavage kinetics of the plant-produced particles, I performed the autocatalytic cleavage assays with plant-produced N ω V procapsid VLPs and monitored the extent of cleavage by SDS-PAGE. This experiment was important in order to better understand the properties of the plant VLPs and to see how they performed in comparison to the insect cells-produced VLPs.

I performed the following experiment at the John Innes Centre and I also repeated it with the collaboration of Prof. Tatiana Domitrovic, from the Universidade Federal do Rio de Janeiro (UFRJ). The experiments and analysis from this section of the thesis are presented in agreement with Tatiana Domitrovic, who plotted the results obtained and compared them with previous insect cells data that she had access to.

For the cleavage assay reactions, it was important to control the pH to start the maturation. For this experiment, for example, 1 volume of N ω V procapsids resuspended in 10 mM Tris-HCl, 250 mM NaCl, pH 7.6 buffer was mixed with 9 volumes of the lower-pH buffer (100 mM NaOAc, 250 mM NaCl, pH 5.0). The reactions were incubated at room temperature and stopped by adding the protein loading buffer and then immediately freezing the mixture with liquid nitrogen. The SDS-PAGE analysis was used to visualize the formation of β protein and to quantify cleavage by band densitometry analysis, as previously described (Matsui et al., 2009).

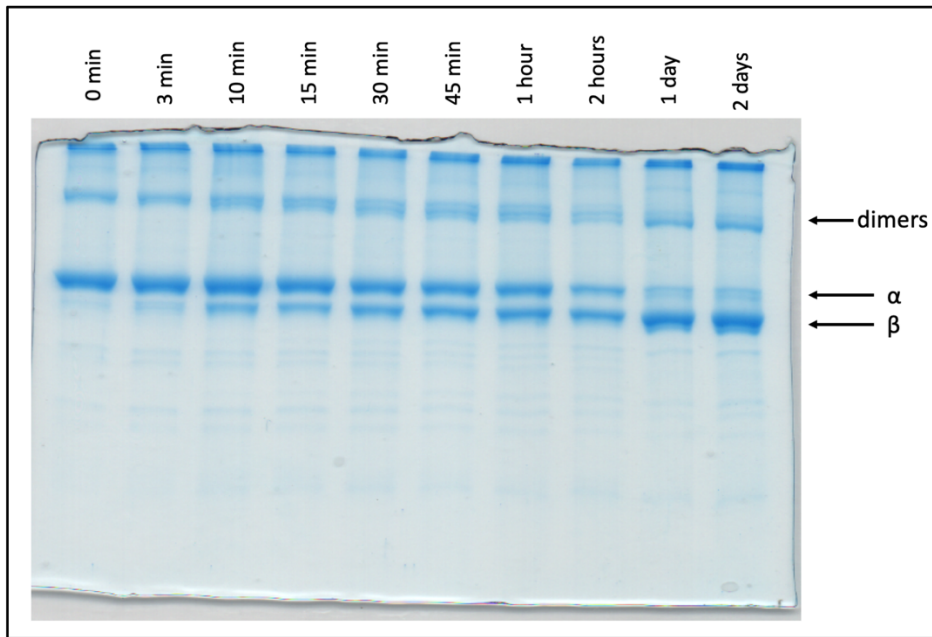


Figure 3.9 | Time course incubation at pH 5.0 of wild-type NwV VLPs produced in plants. SDS gel of the NwV procapsid VLPs incubated for different times at pH 5.0. After 3 to 10 min it was possible to detect autoproteolytic cleavage with the generation of the β peptide. At the same time that the cleavage of the α peptide progressed, it was possible to see also a shift in the high molecular weight band, indicating that the dimers of the coat protein also undergo cleavage (see Chapter 4).

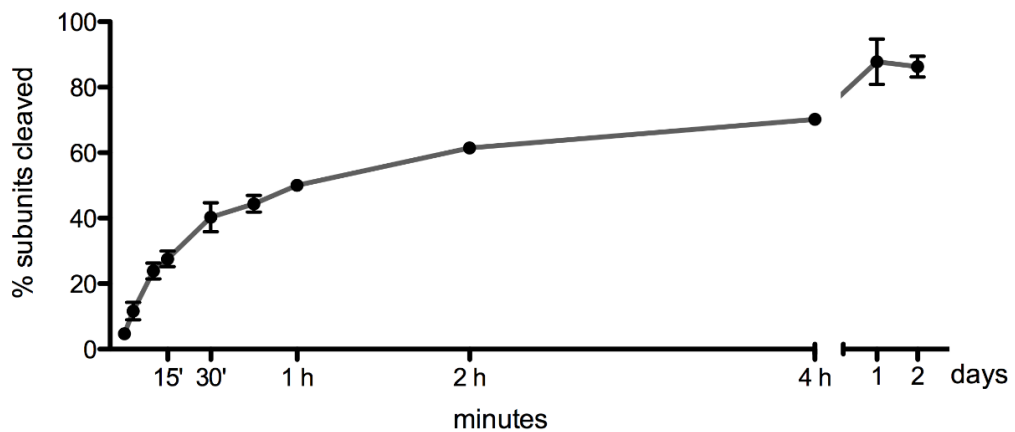


Figure 3.10 | Maturation curve of NwV WT VLPs produced in plants. The fraction of subunits cleaved was determined by band densitometry of the SDS-PAGE gel image using the software ImageJ. A square of fixed size was used to delimit the gel area containing α and β proteins. Each time point was measured individually and the program retrieved the density of each protein band. The sum of α and β signals corresponded to 100%. Therefore, the extent of cleavage corresponds to the % of β density in relation to the total density of each time point. In the first two hours, over 60 % of the subunits were cleaved and cleavage progressed in the following hours.

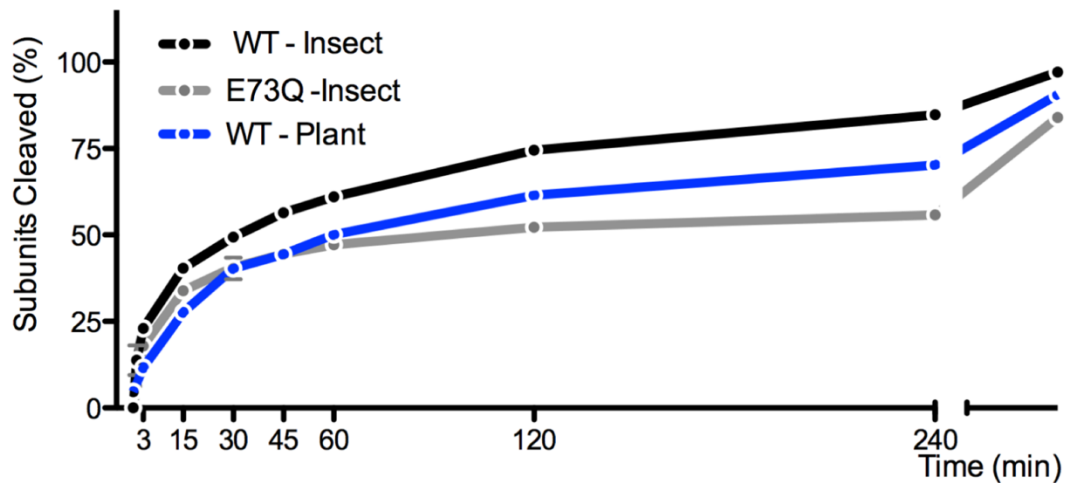


Figure 3.11 | Comparison of the kinetics of cleavage between N ω V VLPs from plants and insect cells. The kinetics of cleavage for the different N ω V VLPs follows a similar pattern. The 50 % of initial cleavage is achieved approximately between the first 30 to 60 min after incubating the particles at pH 5.0. Compared with N ω V WT VLPs produced in insect cells, the plant ones have a slower rate of cleavage. However, plant VLPs cleaved faster than the insect produced E73Q, a mutation that results in slower cleavage rates (Matsui et al., 2009). Note that all particles end up with similar percentage of cleaved subunits over time.

The autocatalytic cleavage assays demonstrated that the N ω V WT procapsid VLPs produced in plants were able to mature and cleave the coat protein after incubating the particles at pH 5.0. Half of the subunits were cleaved after 45 to 60 minutes of dropping the pH. Furthermore, when the kinetics were compared with previous data from insect cells, the plant-produced particles had a similar profile but the overall rate of cleavage was slower, nearly doubling the amount of time required for the cleavage, but being faster than mutations known to interfere the cleavage rates in insect produced particles. This difference might be due to post-translational modifications characteristic of the expression system that could affect the structure and the dynamics of the particles.

Additionally, in the SDS gel (see Figure 3.9) it was observed that the high molecular weight bands, shifted in size during the cleavage process, suggesting that these dimers of N ω V coat protein were also able to cleave.

Summary of section 3.2.3.3: N ω V procapsid VLPs produced in plants are able to undergo autoproteolytic cleavage when they are incubated at pH 5.0. The kinetics of the cleavage, when compared with insect cells-produced VLPs, have a similar profile but occur at a somewhat slower rate. The formation and activity of the cleavage site depends on capsid conformational state; therefore, the fact that there was cleavage suggested that there was authentic formation of mature particles.

3.2.3.4. Stability assay of N ω V at a neutral pH

In the previous section I described the cleavage induced by the change in pH, which was a product of the autoproteolysis activity of N ω V VLPs. Cleavages can be also produced as a process of non-specific degradation of proteins, therefore, it was worth investigating the stability of the coat protein over time at room temperature. To investigate how N ω V procapsids behaved over time when incubated in the original buffer (pH 7.6), I collected samples at different time points using the same procedure described in the autocatalytic cleavage assay (see section 3.2.3.3).

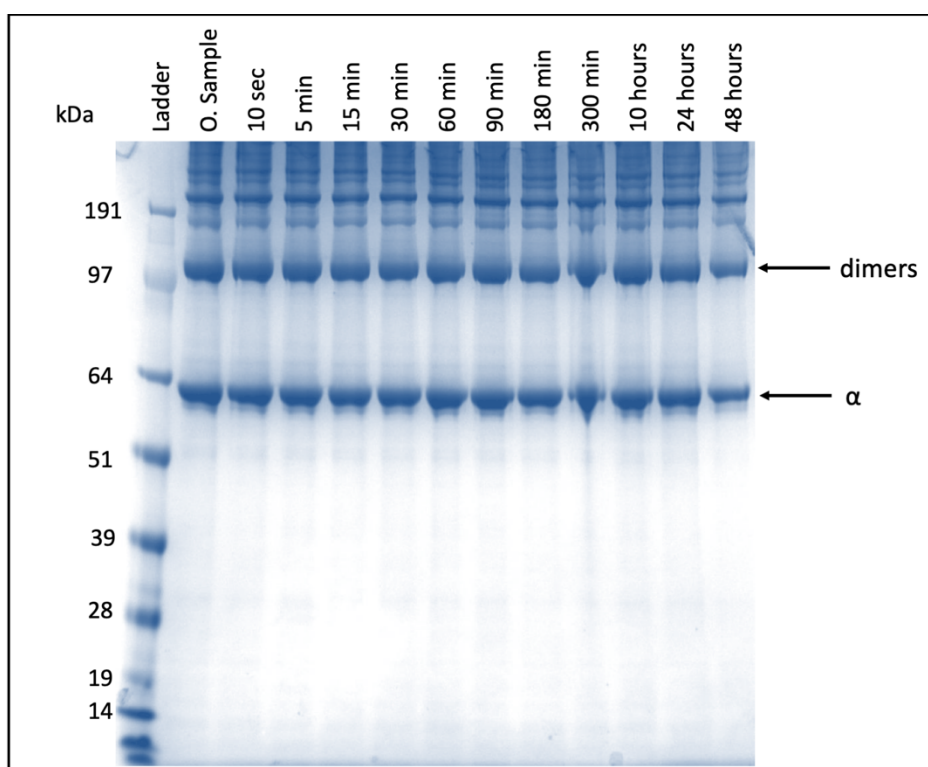


Figure 3.12 | Stability of the N ω V WT VLPs over time at pH 7.6. The N ω V WT VLPs were incubated at pH 7.6 and at room temperature. Samples were collected at different time points. During the incubation, no major changes in the profile of the protein were observed in the SDS gel, as it stayed in the form of full coat protein (α peptide). O. sample = original sample. Ladder = SeeBlue Plus 2 pre-stained protein standard.

Summary of section 3.2.3.4: There was no degradation or cleavage observed when the particles were kept at neutral pH and at room temperature. Together with the results from section 3.2.3.3, indicated that the cleavage previously observed was a product of the autoproteolytic activity of N ω V at low pH rather than non-specific cleavage over time.

3.2.3.5. Membrane disruption assay: lytic activity of the N ω V VLPs

During the infection cycle, N ω V needs to interact and penetrate the membranes from the midgut cells of the *N. capensis* larvae in order to start the infection. To do so, it uses the lytic peptide (γ) that is generated as a product of the autoproteolytic cleavage during maturation. Using membrane disruption assays it has been possible to measure the ability of N ω V VLPs produced in insect cells to perforate membranes (Domitrovic et al., 2012, 2013). In order to investigate if the plant-produced N ω V VLPs would have the lytic activity after maturation, as this would be crucial to validate the structural relevance and biological activity of these particles, we performed membrane disruption assays.

We performed the following first set of experiments in collaboration with Tatiana Domitrovic, from the UFRJ, using the plant-produced VLPs that I prepared at the John Innes Centre. The experiments were later repeated by T. Domitrovic and Jonas Siqueira, from UFRJ. Furthermore, T. Domitrovic, plotted the results and compared them with insect cell-produced N ω V VLPs. The experiments and analysis from this section are presented with the kind permission of the collaborators. The membrane disruption assay details are described in Chapter 2.

Briefly, N ω V VLPs matured *in vitro* were mixed with liposome preparations at different pHs (from 5.0 to 9.0). The increase in absorbance produced by the release of the self-quenching dye enclosed in the liposomes was measured to quantify the dye release and the lytic activity of the N ω V VLPs.

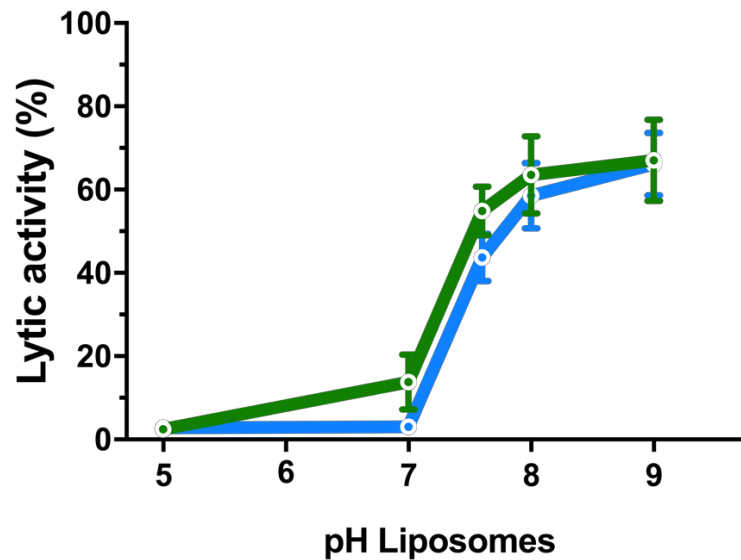


Figure 3.13 | Membrane lytic activity of N ω V VLPs produced in *N. benthamiana* and *S. frugiperda*. Lytic activity of mature N ω V VLPs expressed in plants (green line) and insect cells (blue line) against DOPC liposomes under different pH conditions (from 5.0 to 9.0). End point values were measured after 10 minutes incubations with liposome preparations. At acidic pHs there was no disruption of the liposomes. At basic pHs, lytic activity was detected by the lysis of the liposomes. Standard deviations from at least two experiments are shown as error bars.

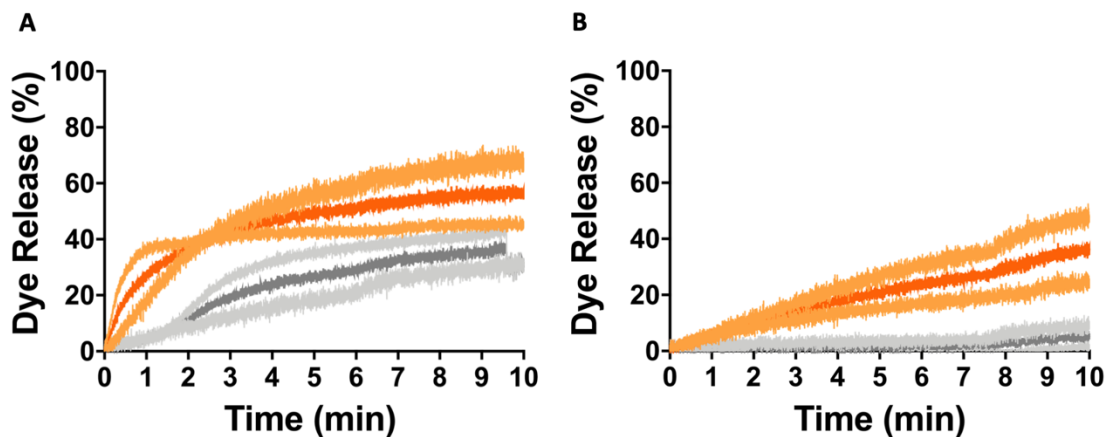


Figure 3.14 | Initial kinetics of liposome dye release at pH 7.6 induced by mature N ω V VLPs. Dye release induced by N ω V VLP produced in plants (a) and in insect cells (b). Two N ω V VLP concentrations were tested, 2 μ g / mL (grey) and 20 μ g / mL (orange). The plant-produced VLPs induced an increased initial rate of liposome lysis, which was also correlated with the concentration of VLPs. Standard deviations from at least two experiments are shown as dashed thin lines.

The results from the membrane disruption assays (see Figure 3.13) demonstrated that N ω V VLPs, from both plants and insect cells, are biologically active when they are in the form of mature capsids. Plant-produced N ω V VLPs presented membrane lytic activity under alkaline conditions (>pH 7.0) with maximum lytic activity occurring at pH 8.0 and pH 9.0, likewise insect derived N ω V VLPs. Under acidic conditions, there was no rupture of the liposomes. It has been suggested that this is because the midgut of the insect that this virus infects has alkaline conditions; therefore, the virus may have evolved in order to have the lytic activity in the range of >pH 7.0 (Domitrovic et al., 2012).

Furthermore, we noticed that the plant-produced N ω V VLPs gave an increased initial rate of liposome lysis when compared with insect cells ones (see Figure 3.14). This could be a consequence of differences in the particle dynamical properties caused by differences in RNA content and inter-subunit crosslinks (further details in Chapter 4) of the plant-derived N ω V particles. A similar effect has been observed for the closely related tetravirus HaSV. In that case, the lytic activity of the virion was compared with the insect cells-produced HaSV VLPs, which contained cellular RNA. Both particles presented similar pH dependent lytic activity, but the virion had a slower rate of liposome lysis than the VLP (Penkler et al., 2016).

Summary of section 3.2.3.5: Plant-produced mature N ω V VLPs have membrane lytic activity under alkaline conditions. Their initial rate of liposome lysis is higher than insect cells VLPs; this may be due to differences in the particle dynamical properties.

3.2.3.6. N ω V cleaving intermediates and their lytic activity

In order to further investigate the effect that different pHs have on the maturation of N ω V, procapsids were incubated for two days at different pHs (from 5.0 to 7.6). The amount of cleavage and lytic activity of the incubated particles was quantified using the methods described in sections 3.2.3.3 (autocatalytic cleavage assay) and 3.2.3.5 (membrane disruption assay).

These experiments were also performed together with Tatiana Domitrovic, from UFRJ. The results are reproduced with her kind permission.

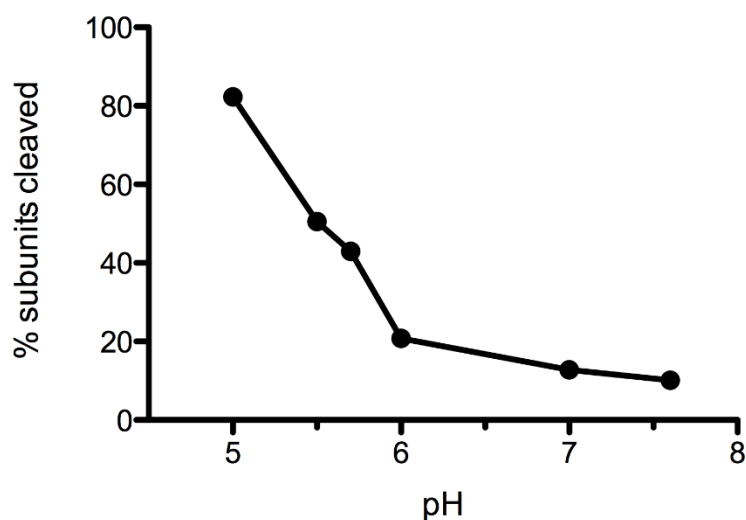


Figure 3.15 | Maturation curve of N ω V VLPs produced in plants and incubated at different pHs. Subunits cleaved as a function of pH, estimated from the densitometry of the bands from the SDS gel. The cleavage increases with the acidity, with the highest rate of cleavage at pH 5.0. The particles were incubated for two days at different pHs (from 5.0 to 7.6).

Figure 3.15 showed that cleavage started to be noticeable at pH values below 6.0. At pH 5.7 and 5.5 the number of subunits cleaved was around 50%, suggesting that at this pH there may be an intermediate in the maturation process. This partial cleavage of the total coat proteins could be a consequence of the structure of the particle and the charge of the residues at this pH range (more details about N ω V intermediates are provided in Chapters 4, 5 and 6).

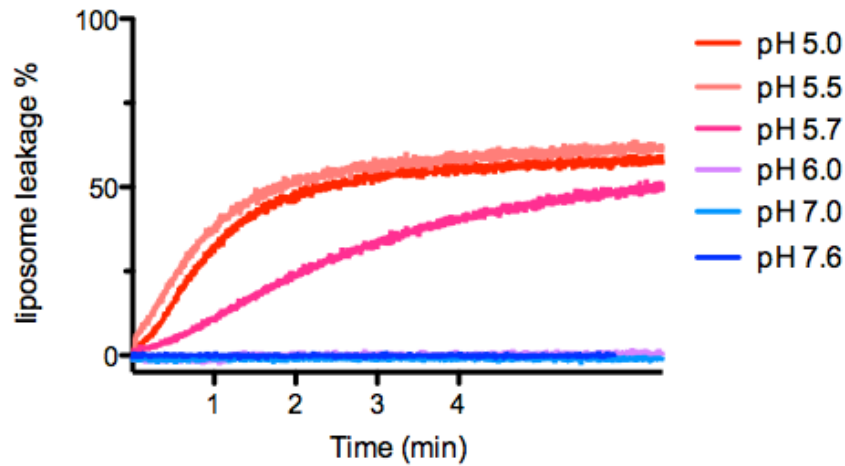


Figure 3.16 | Lytic activity of NwV VLPs from plants with different percentages of cleavage. Liposome leakage induced by NwV VLPs that were incubated for two days at different pHs (from 5.0 to 7.6). The measurements were performed with the DOPC liposomes under pH 7.6 conditions. Lytic activity was detected for particles that were incubated at pH 5.7 and below.

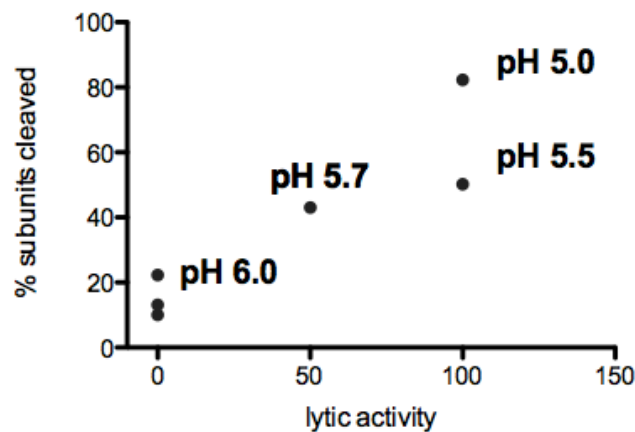


Figure 3.17 | Correlation between lytic activity and percentage of cleaved subunits in NwV VLPs.

The particles incubated from pH 6 to 7.6 did not have lytic activity (Figure 3.16). At pH 5.7 they presented 50 % lytic activity with around 40 % of cleaved subunits. At pH 5.5, over half of the subunits in the particles, which would correspond to subunits A and D (Matsui et al., 2010b), were cleaved and the lytic activity achieved 100 %, the same as the fully matured particles at pH 5.0 (Figure 3.17).

Summary of section 3.2.3.6: Plant-produced NwV VLPs can present intermediate cleavage states when are incubated at pH 5.5 or 5.7. The lytic activity of the particles is influenced by the number of cleaved subunits, achieving the higher rates at pH 5.5 and 5.0.

3.2.4. Production and isolation of N ω V capsids *in vitro* and *in vivo*

The aim of the previous sections was to characterise the properties and maturation of the N ω V procapsids produced in plants. These procapsids were matured to capsids by reducing the pH to 5.0, *in vitro*, which resulted in the compaction and cleavage of the subunits in the particles. In this section I describe the effect that the timing of the maturation has on the structure and purification of the N ω V VLPs in plants.

3.2.4.1. *In vitro* maturation of the N ω V VLPs after extraction

This is the maturation process that has been mainly described so far. The N ω V VLPs were extracted as procapsids at pH 7.6 and then the pH was reduced to 5.0 *in vitro* to initiate particle maturation. For the TEM analysis, the details are provided in Chapter 2. Briefly, N ω V VLPs, incubated for 5 minutes at pH 5.0, were loaded on a grid, the excess of sample was then removed with filter paper and finally it was stained with 2% (w/v) uranyl acetate (Figure 3.18, right image).

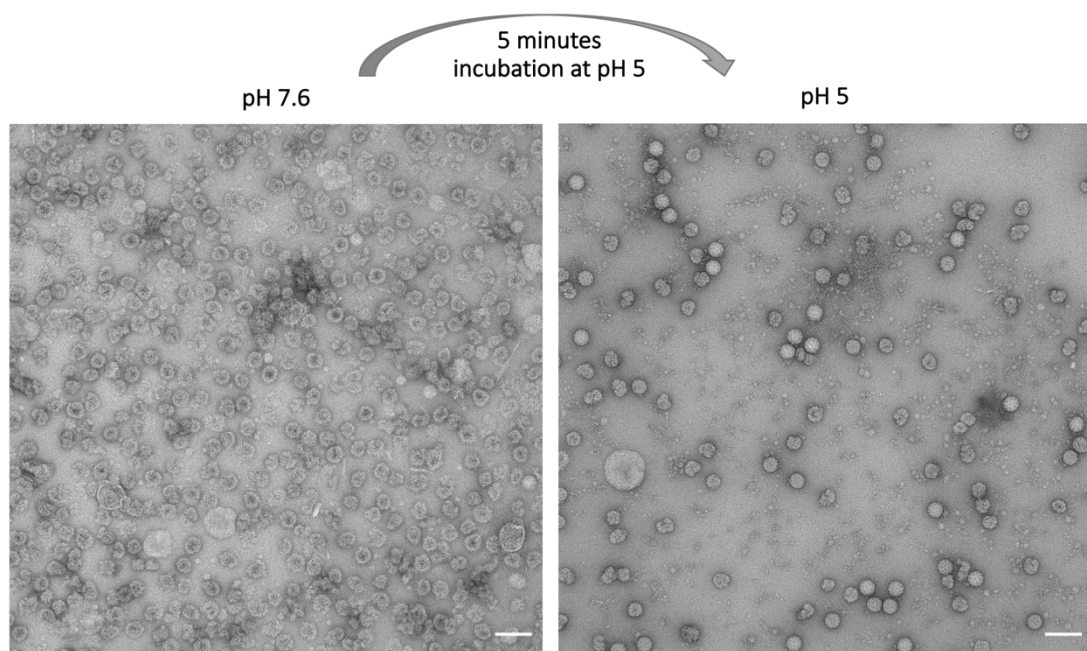


Figure 3.18 | N ω V VLPs capsids matured *in vitro* from procapsid produced in plants. The procapsids (pH 7.6), left image, were observed as porous and fragile and of an approximate size of ~45-50 nm. With the pH drop and transition to the capsid stage (pH 5.0), right image, a part of the population of particles became less porous, more homogeneous and of an approximate size of ~40-43 nm. However, there were also misshapen and broken particles, which might be particles unable to properly transition to the capsid form. The VLPs were stained with 2 % (w/v) UA. Magnification: 45,000 x. The scale bar is 100 nm.

3.2.4.2. *In vitro* maturation of the NωV VLPs during extraction

Another procedure to obtain capsids is to extract the VLPs from the plant using a buffer at pH 5.0 (50 mM NaOAc, 250 mM NaCl, pH 5.0). The protocol followed the same steps as in section 3.2.2, with the difference that the extraction buffer was at pH 5.0 instead of 7.6. As capsids are more resistant to proteases than procapsids (Bothner et al., 2005), the goal was to generate the capsid form early in the purification in order to reduce the action of proteases and other degradation mechanisms present in the plants. The particles produced with this procedure (Figure 3.19) looked more homogenous in contrast with the ones presented in the previous section and displayed similar features as NωV capsid VLPs produced in insect cell (Taylor et al., 2002)

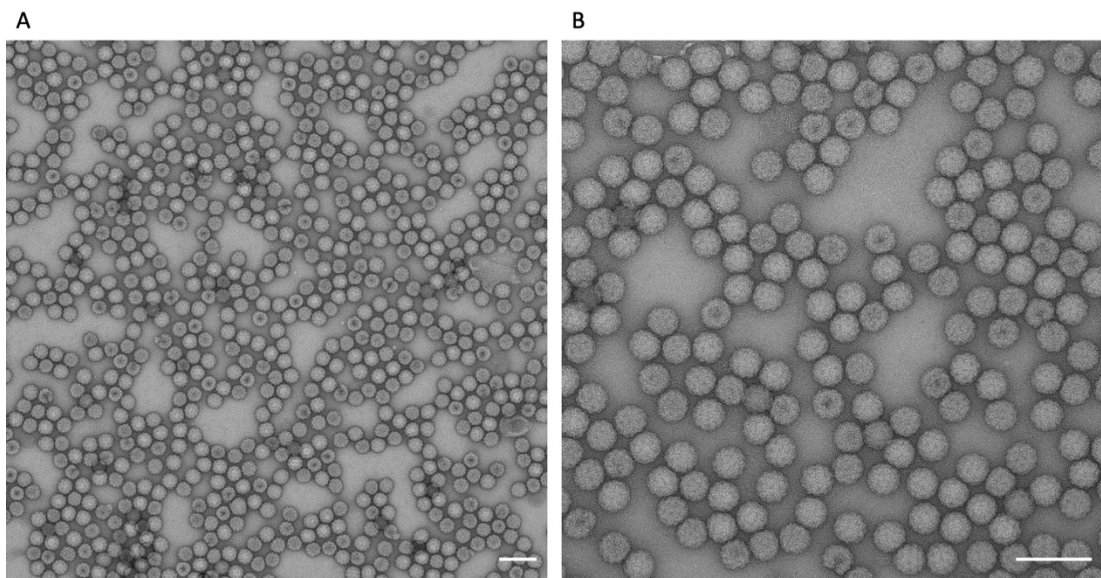


Figure 3.19 | NωV VLPs capsids extracted at pH 5.0 from plants. Sample stained with 2% (w/v) UA and visualized by TEM. There is a major population of NωV VLPs with an approximate size of ~42 nm that are compact, however, some particles might be porous as they presented stain penetration. Images of the same sample at different magnifications: 45,000 x (a) and 92,000 x (b). The scale bar is 100 nm.

3.2.4.3. *In vivo* maturation of the NwV VLPs

As it was shown in Figure 3.2, over time, maturation of NwV occurred inside the plants, which has been proposed as *in vivo* maturation of the VLPs. In Figure 3.3, using the sucrose gradients, it was possible to separate several populations of cleaved and uncleaved proteins. This suggested that capsids could be isolated directly from the plants without having to expose them to a pH 5.0 buffer. In order to separate them, sucrose, as described in Chapter 2, and iodixanol gradients (Brillault et al., 2017) were used. Using these procedures, it was possible to isolate mature NwV capsids despite carrying out the extraction at pH 7.6.

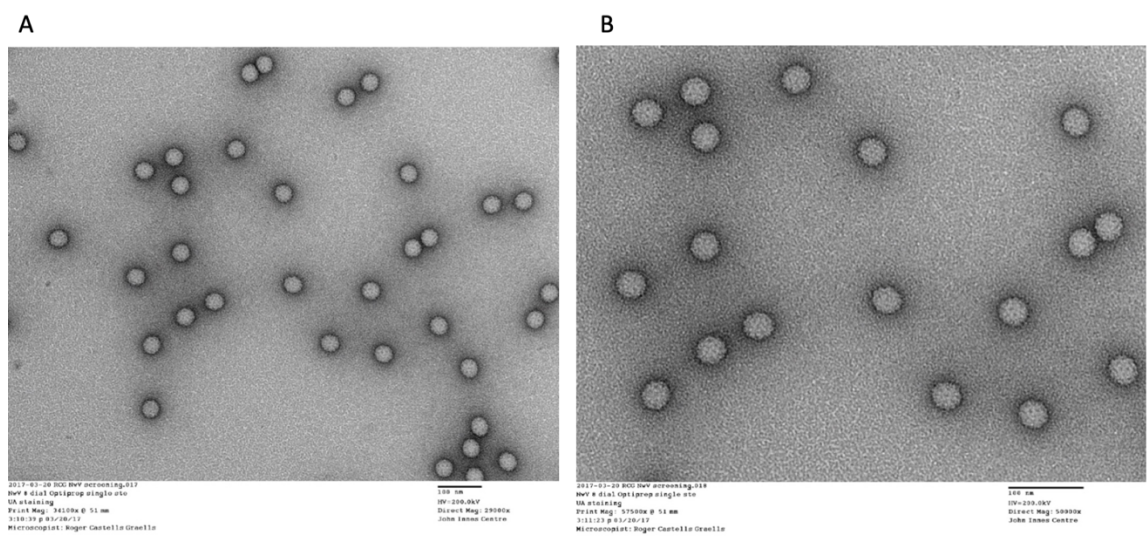


Figure 3.20 | NwV VLPs capsids matured in the plant and extracted at pH 7.6. Sample stained with 2% (w/v) UA and visualized by TEM. These particles matured *in vivo* and were extracted at pH 7.6. There is a major population of NwV VLPs with an approximate diameter of ~42 nm with the features of capsid VLPs. Images of the same sample at different magnifications: 29,000 x (a) and 50,000 x (b). A 100 nm scale bar is provided in the figure caption generated by the microscope software.

The TEM images in Figure 3.20 show particles with the features of matured particles as seen in matured particles produced in insect cells (Taylor et al., 2002). These demonstrated that NwV VLPs can be matured inside the plant and form capsids.

These particles were further studied with cryo-EM and the structures are described in Chapter 4.

Overall, it was observed that the NwV VLPs could achieve mature capsid characteristics when the particles were extracted using a pH 5.0 buffer or when they were matured inside the plant. However, if the particles were extracted as procapsids, when the pH was dropped *in vitro* they did not behave as expected. A fraction of these

capsids, generated *in vitro* from extracted procapsids, were misshapen, heterogeneous and more porous than the reported previously for insect cells (Taylor et al., 2002). These observations suggested that there could be some trouble with plants that was affecting the structure of the N ω V VLPs. In the following chapter, SAXS and cryo-EM were used to study the structural changes of the N ω V VLPs from plants.

Summary of section 3.2.4: Maturation at different times during the expression and purification of the N ω V VLPs can have an effect on their structure and properties. Additionally, the method of their extraction has also an effect, like seen in section 3.2.4.2 for the ones extracted at pH 5.0. Further experiments are required to understand their properties and one of their structures has been studied by cryo-EM in the following chapter.

3.3. Discussion

This chapter demonstrates the successful production and characterization of N ω V VLPs in plants. The ability of plants to assemble a complex virus like N ω V keeping its structural functionalities is remarkable. The precision demands of the maturation process of N ω V are huge as the residues that are associated with the autocatalysis are ~ 20 Å apart in the procapsid and need to move to the perfect positioning to allow the cleavage.

Plants have been used to make capsids of viruses which require processing of the precursor protein by a viral protease, such as cowpea mosaic virus and poliovirus (Marsian et al., 2017; Saunders et al., 2009). However, the production in plants of a VLP with autoproteolytic activity as N ω V, is unique. The maturation process requires high precision and the plant-produced particles display an outstanding fidelity of assembly and maturation that makes them a great candidate for further characterization studies and a broad range of applications. Furthermore, the liposome lysis experiments are particularly significant because demonstrate the biological functionality of the plant-produced N ω V VLPs. This lytic activity makes them a suitable candidate for the delivery of cargos across membranes, as it has been demonstrated in a previous study using the lytic peptide for the delivery of quantum dots into cells (Safi et al., 2017).

The autocatalytic cleavage of nonenveloped virus coat proteins is usually designed to take place in the extracellular environment, in order to avoid the release of membrane-active peptides inside the cell (Veesler and Johnson, 2012). However, in the plant-produced N ω V VLPs, the cleavage has been observed when the particles were still within the plant cells. This can be because the factor that induces the autocatalytic cleavage of the particles in plants is already present before their lysis. For example, it could be that the pH is reduced locally inside the cells and then the particles can cleave. However, it could also be that for N ω V, the cleavage could also naturally occur inside the cells when, for example, it encapsidates a certain amount of nucleic acid. It has been shown that to trigger the membrane-lytic activity of the particles, they need to be in the alkaline conditions of the extracellular environment of the mid-gut of the lepidopteran larvae (Domitrovic et al., 2012; Dow, 1992; Penkler et al., 2016). Therefore, these changes in pH could be a mechanism that the virus has evolved in order to allow the autocatalytic cleavage and avoid the release of active lytic peptides when it is still inside the cell.

Previous work on HaSV has demonstrated that the virions and VLPs of this virus, which is similar to N ω V, are resistant to temperatures up to 55°C, to pH values ranging from 3 to 11 and to the protease activity of the midgut lumen (Hanzlik and Gordon, 1997). Furthermore, studies were performed on N ω V and HaSV VLPs stability to proteases and it was found that the capsid is resistant to the protease activity for several hours (Bothner et al., 2005). Therefore, we believe that N ω V VLPs capsids could be a great tool for the delivery of drugs and other cargos, as they are resistant to a broad range of harsh conditions and they are easy to purify and produce in plants.

Overall this chapter establishes the early work for the production of N ω V VLP in plants and demonstrates the novel success at making N ω V VLP in plants where it is possible to have a well-established assembly and it is possible to achieve the structural details required for the maturation.

In the next chapter of this thesis I structurally characterize the plant-produced particles to better understand their architecture and find out if they preserve the same structure as the original virus.

Chapter 4

The trouble with plants¹

4.1. Introduction

One of the main goals of this thesis was to reveal the structural details of the maturation process of N ω V. In the previous chapter it was shown that the plant-produced N ω V VLPs are able to mature and have biological activity, which is remarkable considering the complexity of the maturation process. The yields were encouraging and sufficient to carry out further experiments. However, the maturation *in vitro* appeared to be heterogeneous and presented some difficulties from the structural point of view of particle assembly and maturation, as revealed by TEM. In this chapter, SAXS and cryo-EM analysis were performed in order to look at the structure of N ω V particles and their maturation mechanisms. Furthermore, the use of a non-cleavable mutant (N ω V N570T VLP) for the structural analysis, as an alternative to the N ω V WT VLPs, was explored.

¹ With reference to John Wyndham "Trouble with lichen".

4.2. Results

4.2.1 Cryo-EM of the plant-produced N ω V capsid VLP

The first step to determine if it was possible to generate, *in planta*, a particle able to complete the maturation process, was to look at the final product of the maturation, the capsid. The crystal structure of the capsid of N ω V was available from authentic virions (Helgstrand et al., 2004; Munshi et al., 1996). Therefore, it was possible to compare the two structures.

Cryo-EM grids of N ω V WT VLPs that had matured inside the plant and that were extracted at pH 7.6 were prepared using the process described in Chapter 2. These particles were expected to have the structure of the mature capsid (see section 3.2.4.3 from Chapter 3), as they were selected from the fraction of an iodixanol gradient that contained the β peptide. For this sample, the grid preparation and N ω V data acquisition were done by our collaborators, Dr. Emma Hesketh and Dr. Charlotte Scarff (Astbury Biostructure Laboratory, University of Leeds), on a FEI Titan Krios microscope (300 kV) with a Falcon III detector, with a final object sampling of 1.065 Å/pixel and a total dose of ~ 79.5 e/Å². The dose was fractioned across 59 frames during a 1.5 s exposure. The data acquisition reports for this dataset and all the others presented in this thesis are provided in Appendix 3.

For the processing of the data I used Relion 3.0 as mentioned in Chapter 2. I describe the most relevant steps and analysis in the following paragraphs.

The initial screening of the grids revealed that the particles were homogeneous and intact in the vitreous ice (see Figure 4.1).

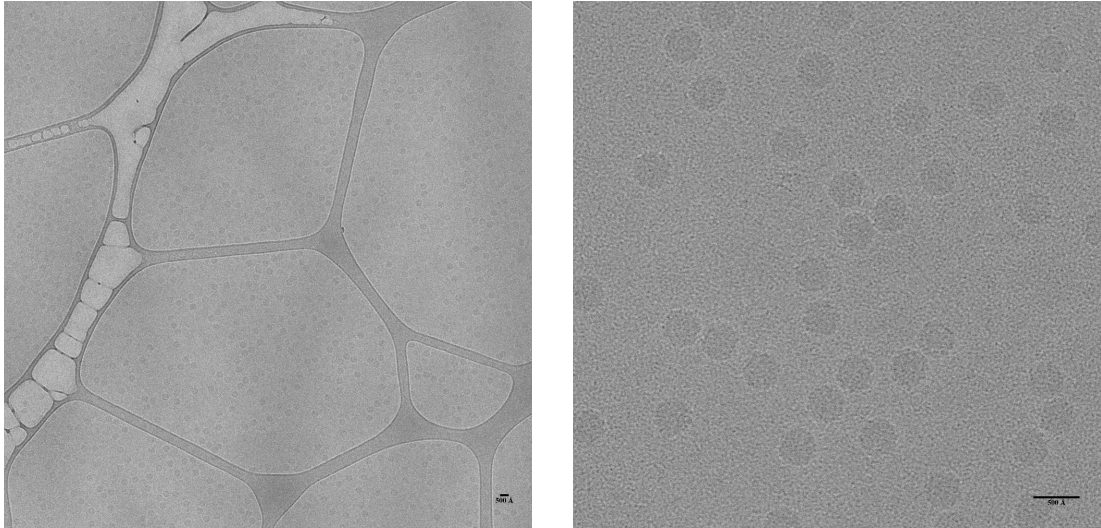


Figure 4.1 | Cryo-EM micrograph of N ω V WT capsid VLPs matured *in planta*. Two views of the sample in the cryo-EM grid (a, b). The distribution of the particles was homogeneous and the characteristics of the ice were ideal for data collection. Data acquisition: FEI Titan Krios EM (300 kV) with a Falcon III camera. The data was acquired at 1.065 Å/pixel. Scale bar = 500 Å.

The particles were picked from the micrographs using the automatic picking tool. The picked particles were then subject to several rounds of reference-free 2D classification, the particles that were in poor quality classes were removed after each round. The results suggested that the population was very homogeneous and most of the particles clustered in a few classes (see Figure 4.2).

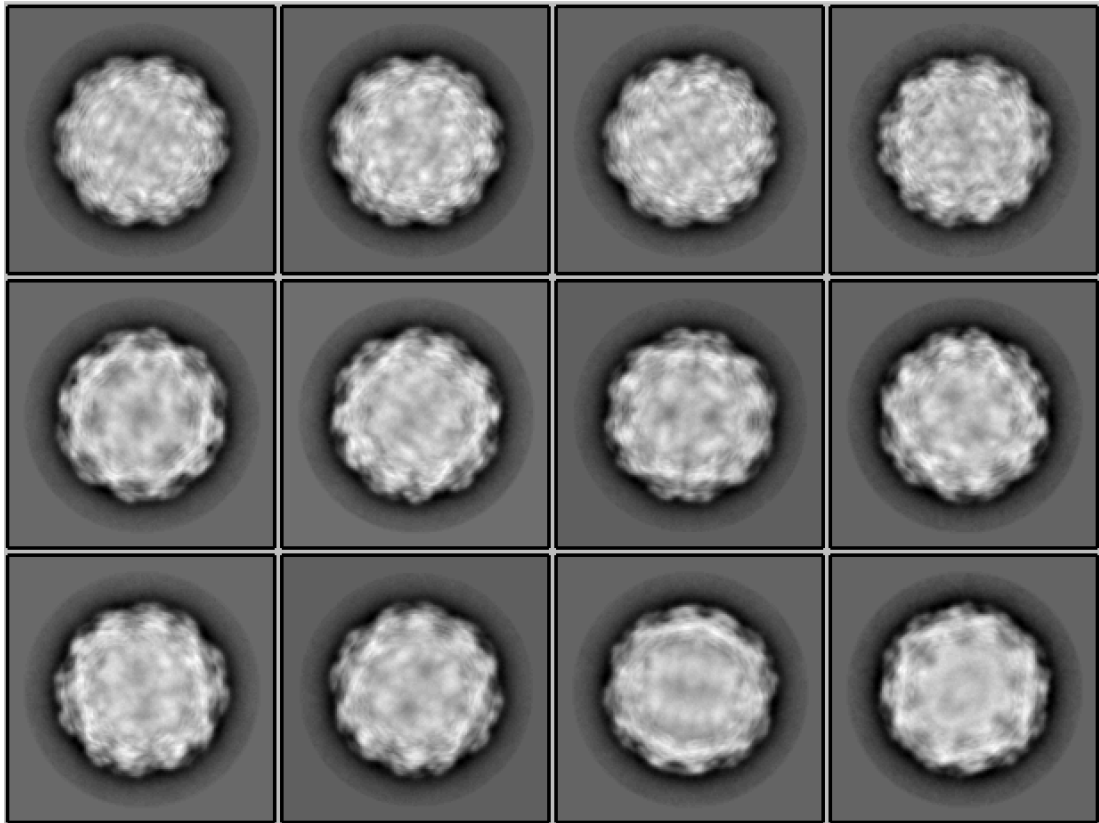


Figure 4.2 | Representative 2D averages of the N ω V WT capsid VLPs. Representative 2D classes averages of N ω V WT capsid VLPs, obtained from the 2D classification of the particles picked from the cryo-EM micrographs. The classes show different views, which depend on the orientation of the particle on the grid.

For the final reconstruction, 21,395 particles were employed to generate a structure at 3.04 Å resolution. After the post-processing, the final resolution estimates were determined based on the gold-standard Fourier shell correlation (FSC = 0.143) criterion (Scheres and Chen, 2012). I then performed per-particle defocus refinement and Bayesian polishing, improving the resolution of the structure to 2.7 Å, the highest resolution ever obtained for the N ω V capsid (see Figure 4.3). Local resolution calculations were performed using the RELION local resolution estimator (Scheres, 2012).

Many regions of the map, in the inner part of the capsid, reached higher resolution than the overall estimation according to the local resolution estimations (Figure 4.3). However, there are more disordered parts near the Ig domain on the outer surface, which can be correlated with additional flexibility of this area of the particle.

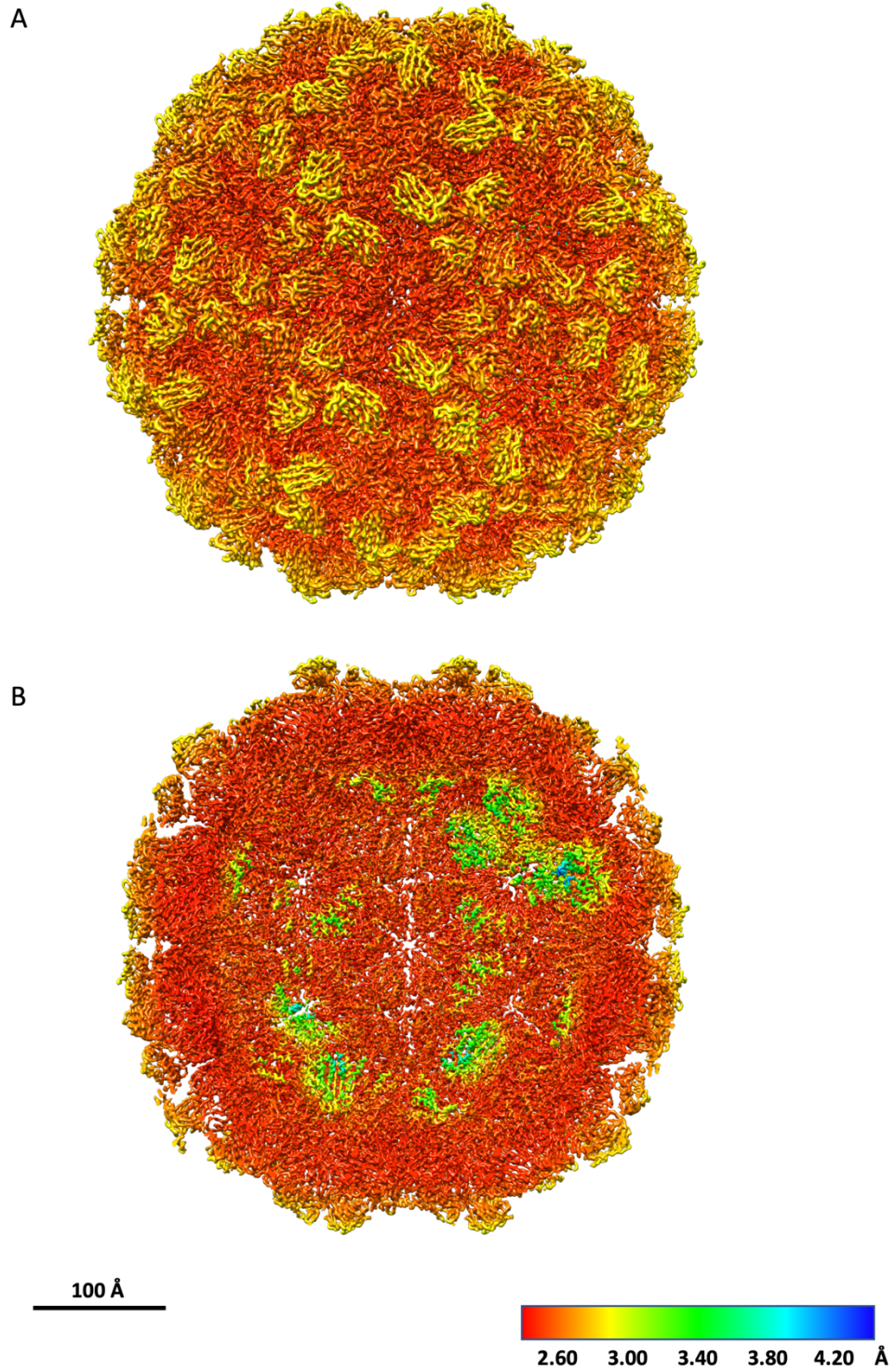


Figure 4.3 | 2.7 Å resolution structure of NwV capsid by cryo-EM. The 2.7 Å structure of NwV capsid is shown in full (a) and as cross section (b). The structure is coloured by resolution following local resolution analysis from red (2.60 Å) to blue (4.20 Å). Most parts of the structure are at higher resolution than 3 Å. Areas of the particles that can display higher flexibility such as the external Ig domains and the internal helical domain have a lower resolution, between 3 to 4 Å. The scale bar is 100 Å.

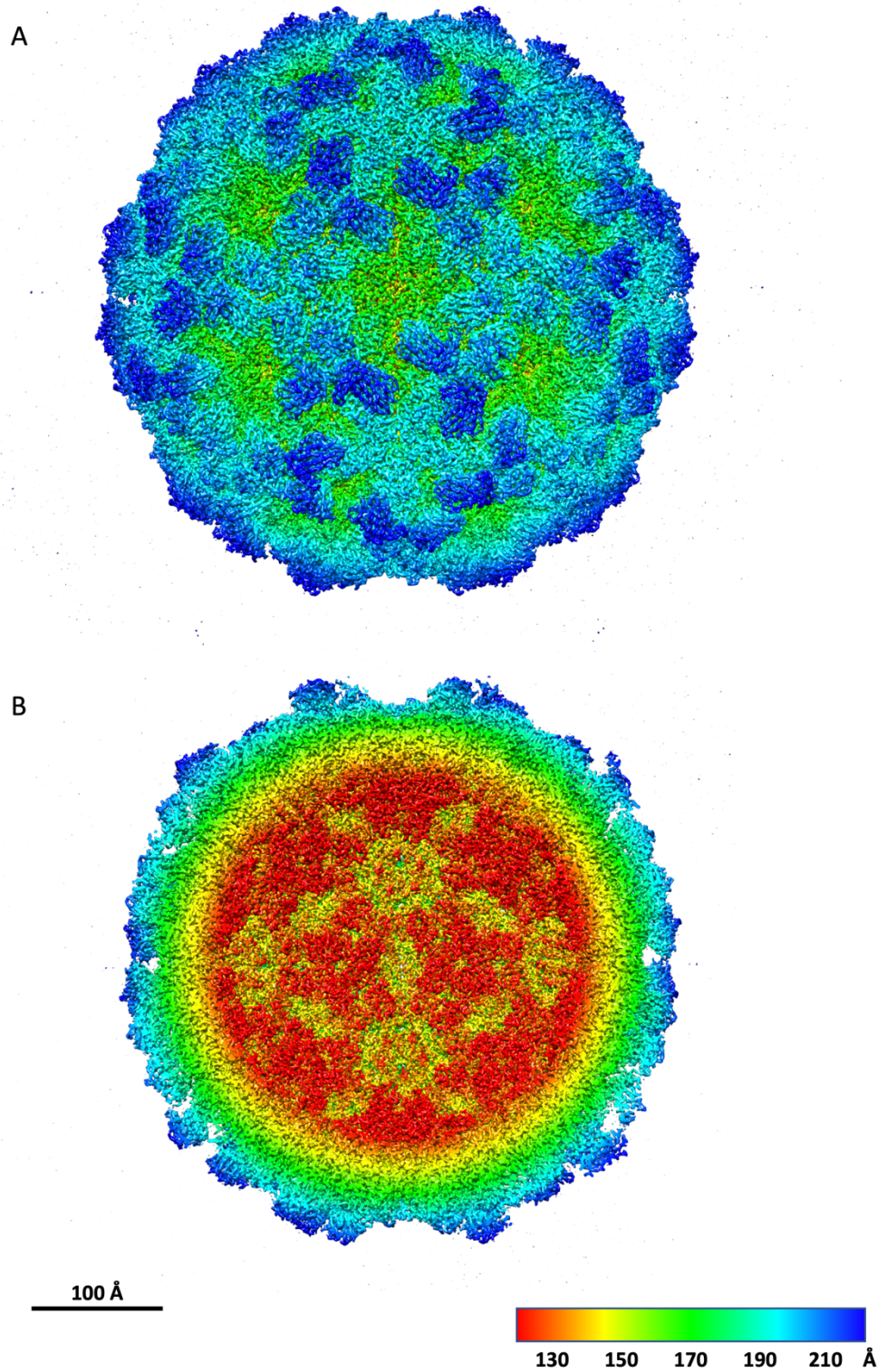


Figure 4.4 | Cryo-EM structure of N ω V capsid VLP coloured by radius. Two views of the 2.7 Å structure of N ω V capsid are shown; full particle (a) and cross section (b). The structures are coloured by radius from red (130 Å) to blue (210 Å). The scale bar is 100 Å.

The high-resolution data from the N ω V capsid structure (Figure 4.4) allowed identification of the secondary structure and also the side chains in some areas of the capsid. In the inside of the particle it was possible observe areas of the helical domains. The total area of helices was similar to that observed with the crystal structure, which was probably due to the fact that those are the structured parts of the helical domain. On the surface of the particle it was also possible to clearly distinguish the β -sheet density in the Ig domains of the N ω V coat proteins (see Figure 4.5). In the helical domain it was even possible to fit side chains in the α -helical density (Figure 4.6).

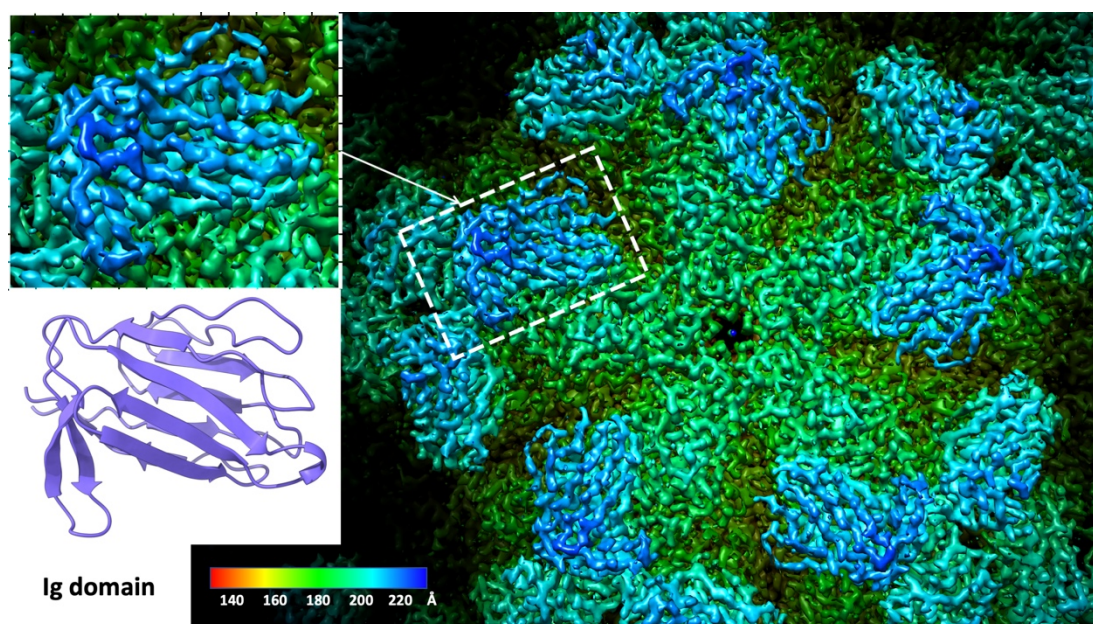


Figure 4.5 | View down a 5-fold axis of the N ω V capsid VLP cryo-EM structure. The Ig domains have β -sheets that can be resolved in this high-resolution structure (2.7 Å). One of the Ig domains is compared side by side with its ribbon model representation. The cryo-EM structure is coloured by radius from red (140 Å) to blue (220 Å).

The model building and analysis were carried out with the assistance of Prof. David Lawson from the John Innes Centre. The model for the capsid was generated by fitting the PDB structure 1OHF into the cryo-EM map and then doing several rounds of manual rebuilding in Coot (Emsley and Cowtan, 2004) and Real Space Refinement in Phenix (Adams et al., 2010; Afonine et al., 2018). Reconstructions were calculated with the imposition of strict icosahedral symmetry, such that each asymmetric unit (comprised of four protein chains) was considered to be identical. Thus, to simplify model building and to speed up refinement jobs, only the asymmetric unit was rebuilt and refined. The model was rebuilt with reference to the unsharpened map (from Relion

Refine3D) and the sharpened map (from Relion PostProcessing) as well as a locally sharpened map produced by Phenix Autosharpen. After the final Real Space Refinement job, the model consisting of 2,288 protein residues and 274 water molecules, had an overall real space cross correlation with the map of 0.88, and 95.5 % of the residues in the favoured region of the Ramachandran plot with only 0.5 % outliers. A preliminary model for the intermediate at pH 5.9 (details in Chapter 6) was generated using the capsid model as a starting point and then rebuilding it with Coot. Similarly, a preliminary model for the procapsid (see Chapter 5) was generated by fitting the model generated for the intermediate at pH 5.9 and rebuilding it in Coot. Due to time constraints, refinement of the latter two models was not completed. These three models have been used for the study of the conformational changes, the subunit trajectories and the formation of the cleavage site that are described in the following chapters.

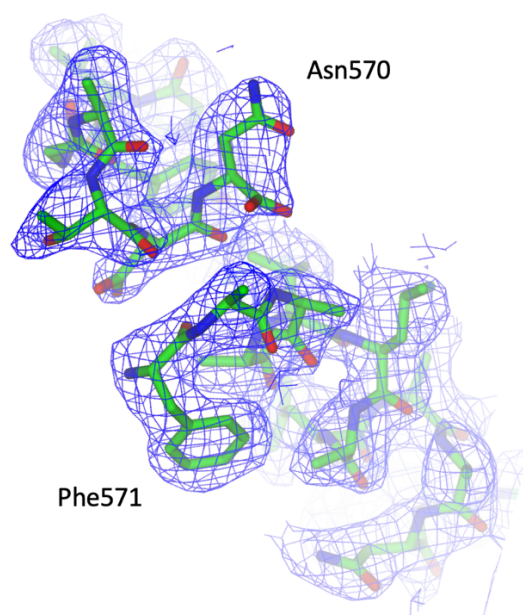


Figure 4.6 | View of the model build in the density map at the cleavage site. Cryo-EM density from the N ω V capsid with the model fitted to highlight the cleavage between residues Asn570-Phe571. Figure provided by D. Lawson.

This capsid structure demonstrated that the N ω V VLPs produced in plants undergo correct initial assembly that allows for the subsequent maturation and formation of the capsid structure (Figure 4.7). The model allowed us to see, in detail, features such as the conformational changes of the helical domains (Figure 4.8) and the formation of the helical bundle at the 5-fold axis, associated with the lytic peptides (Figure 4.9) (see more details in Chapter 6).

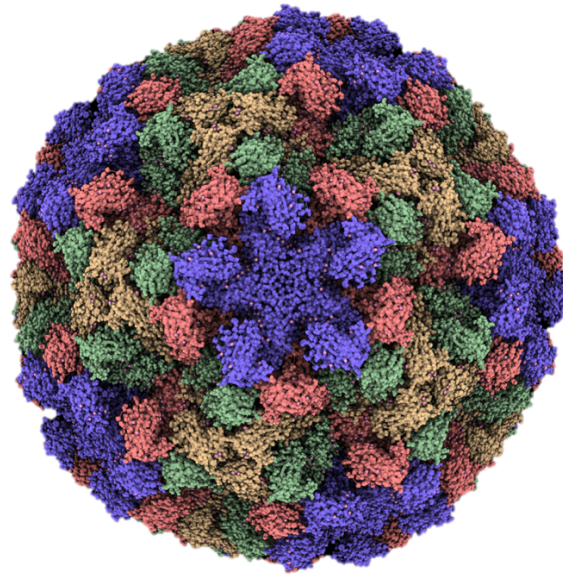


Figure 4.7 | Surface representation generated from the fitted model in the NwV WT capsid VLP cryo-EM map. The model was fitted and refined using as a reference the cryo-EM map presented in this section. Each one of the different colours represents one of the four subunits, A (blue), B (red), C (green) and D (yellow). This figure was produced with ChimeraX (Goddard et al., 2018).

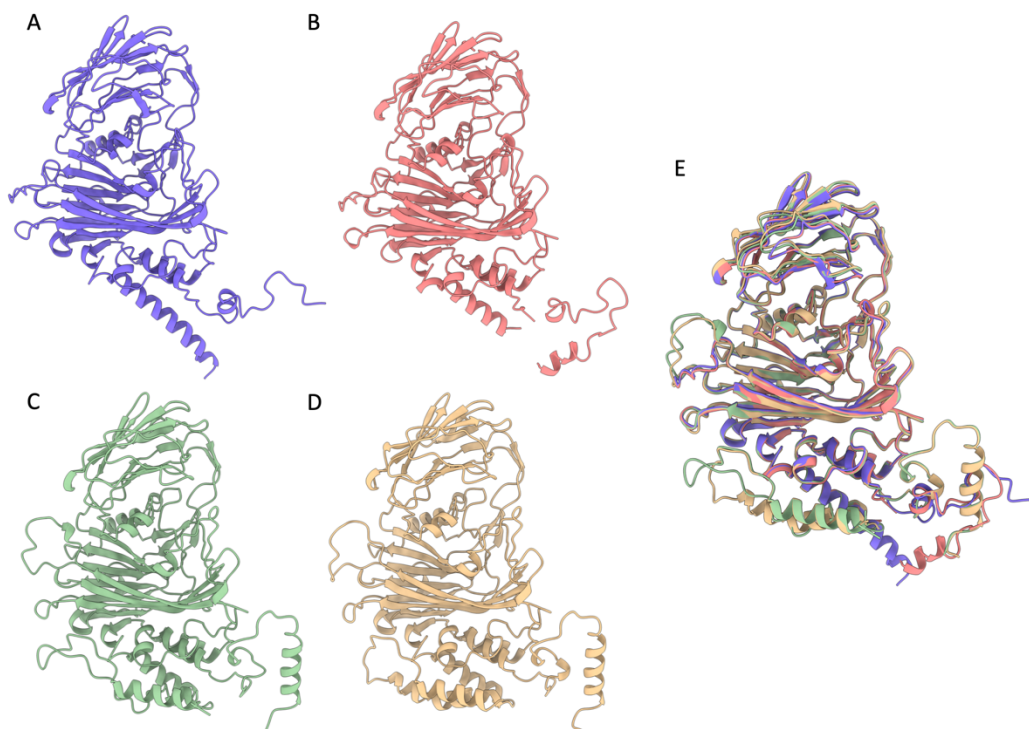


Figure 4.8 | Comparison of the structure from the quasi-equivalent subunits of NwV capsid. NwV capsid subunits (A-D) compared side-by-side and all four overlaid (E), shown by the colour scheme (A, blue; B, red; C, green; D, yellow). The internal helical domains present dramatic changes in their structure while the jellyroll and Ig domain remain similar in all the structures.

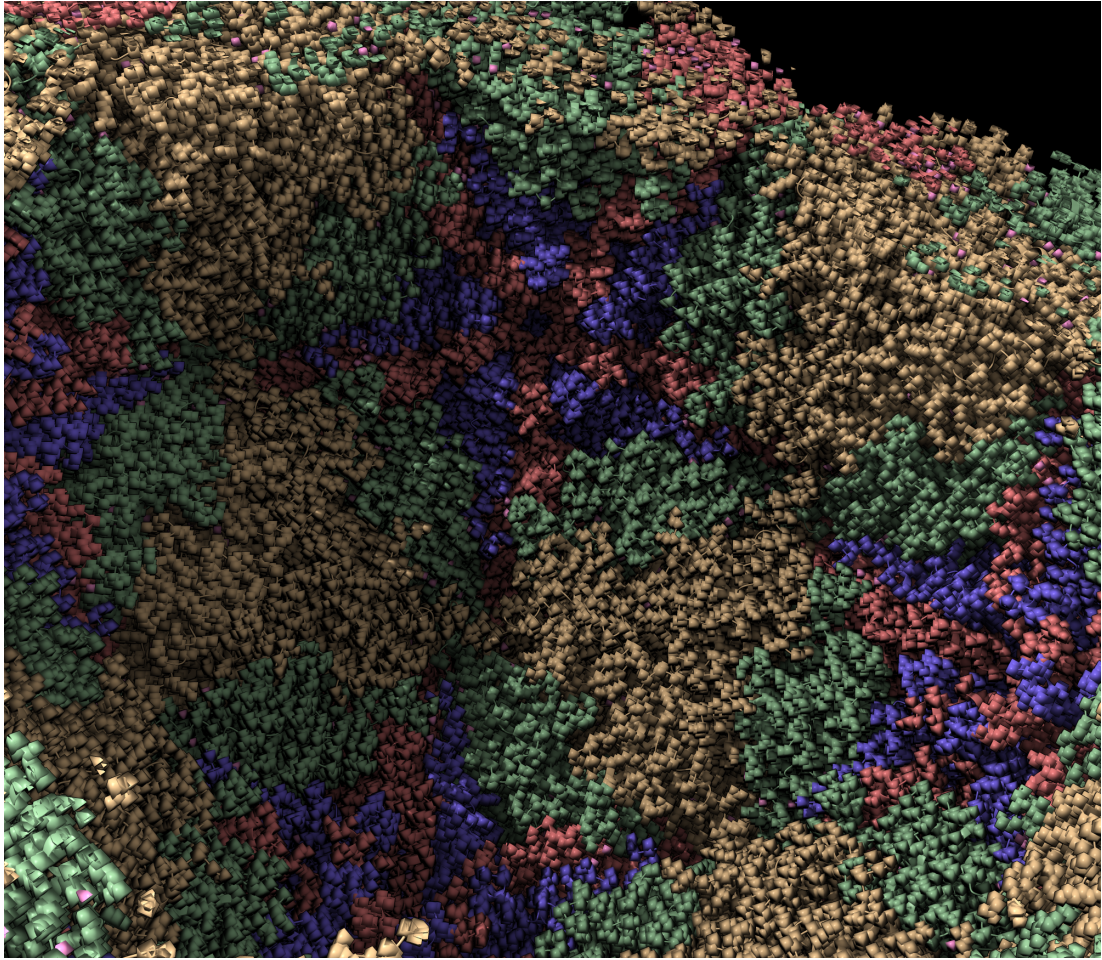


Figure 4.9 | Inside view of the atomic model of the N ω V capsid matured in plants. Surface representation of the model generated from the cryo-EM density map. Each one of the different colours represents one of the four subunits (A, B, C and D). At the 5-fold axis, it is possible to observe a channel formed by A (blue) and B (red) subunits. It has been proposed that at the 5-fold is where the lytic peptides (γ peptide) are released to allow the entry of the virus into the cells (Domitrovic et al., 2012). This figure was produced with ChimeraX (Goddard et al., 2018).

Summary of section 4.2.1: Plant-produced N ω V WT VLPs in the capsid form can be rapidly frozen for cryo-EM and are adequate samples for cryo-EM analysis. The cryo-EM structure of the capsid of N ω V presented in this chapter, at 2.7 Å, is the highest resolution structure available for N ω V capsids. It also demonstrated that plants are able to produce VLPs that can mature and form capsids with the same final structure as the authentic virion. Furthermore, this structure has been used as a reference to build the models for the cryo-EM structures that are presented in the following chapters.

4.2.2 RNA content in particles by cryo-EM

In the structure presented in the previous section, in addition to the protein density that allowed the generation of the 2.7 Å resolution cryo-EM density map, a significant amount of extra density was identified inside of the particle (see Figure 4.10). This density was weaker than that of the capsid and it was attributed to the RNA that the particles encapsidate. RNA analysis of NωV VLPs produced in insect cells demonstrated that such VLPs are able to package mainly cellular RNAs from the host (Routh et al., 2012). Therefore, the presence of RNA in the plant-produced particles is entirely feasible.

The RNA appeared as a concentric irregular shell of density (red density in Figure 4.10), in the centre of the particle, underneath the capsid proteins. In wild-type NωV virions this would correspond to single-stranded genomic RNA-1 and RNA-2; however, this structure is from a VLP transiently produced in plants, therefore this density cannot represent the genomic RNAs but rather can be ascribed to the mRNA for the NωV coat protein or random host RNAs.

Summary of section 4.2.2: Extra density inside the capsid of the virus could be attributed to RNA encapsidated by the particles. NωV VLPs produced in insect cells have been shown to contain mainly cellular RNAs from the host (Routh et al., 2012). In the cryo-EM structure presented in this section, the RNA density suggests that the nucleic acid is making contacts with particular areas of the internal structure of the capsid.

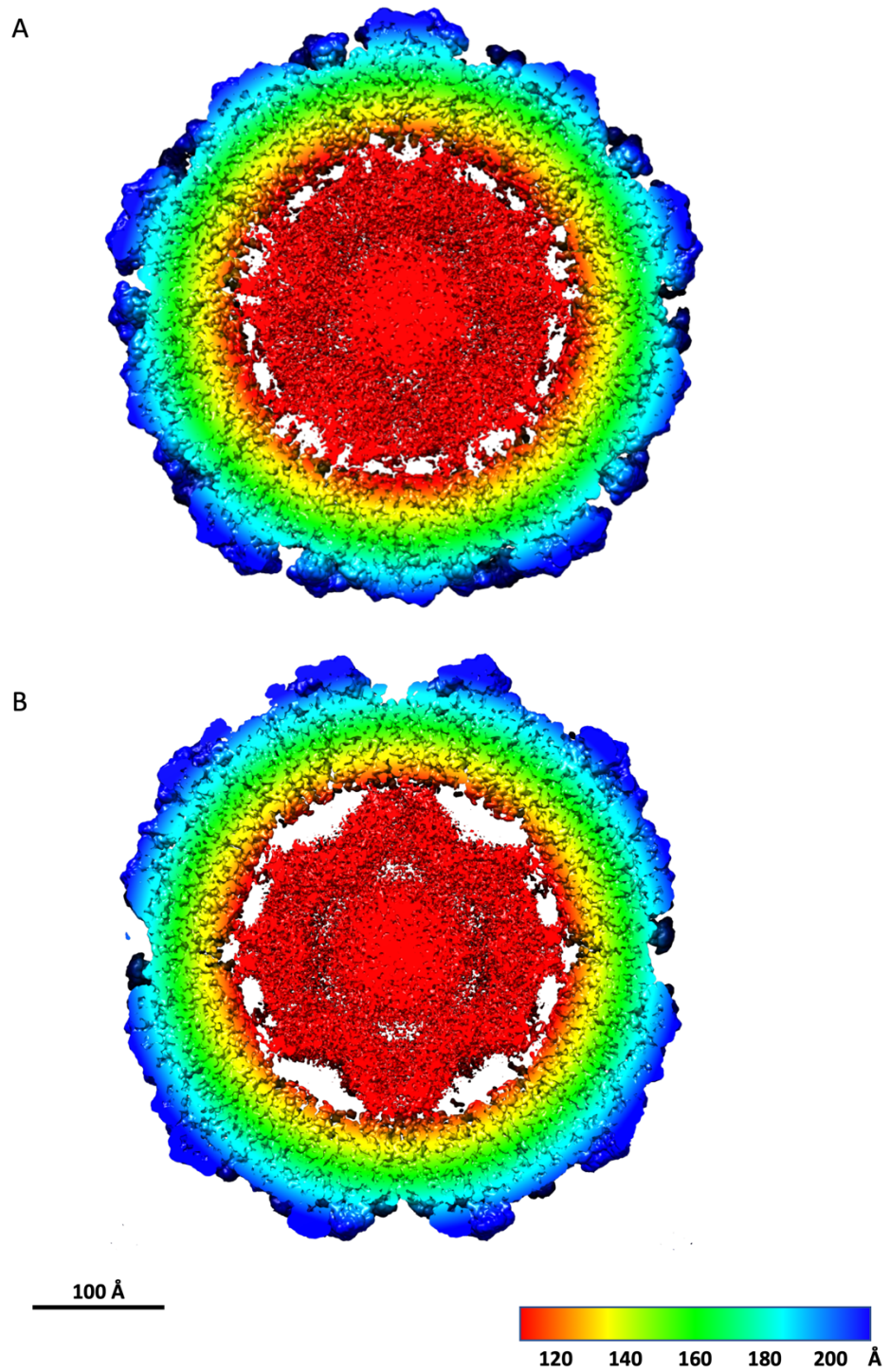


Figure 4.10 | Cross sections of the cryo-EM map of the NwV capsid VLP with RNA density. Two different views of the inside of the particles (a, b). The internal shell (red density) would correspond to the RNA packaged by the VLPs. The RNA density was weaker than the protein. The structure is coloured by radius from red (120 Å) to blue (200 Å). The scale bar is 100 Å.

4.2.3 Cryo-EM of the plant-produced N ω V procapsid VLP

The procapsid is the first assembly stage of N ω V, which undergoes large conformation changes during the maturation process (Canady et al., 2001; Matsui et al., 2009; Taylor et al., 2002). To be able to study the intermediate structures of the maturation process of N ω V, it was important to be first able to solve the structure of the procapsid and show that the particles were properly assembled.

Plant-produced procapsids (see Chapter 3, section 3.2.2) were used for the preparation of cryo-EM grids and the collection of a dataset. For this sample and the samples described in following sections of this chapter, the grid preparation and N ω V data acquisition, were done by our collaborator, Dr. Emma Hesketh on a FEI Titan Krios EM equipped with a Falcon III detector, with a final object sampling of 1.065 Å/pixel and a total dose of ~ 72 e/Å². The dose was fractionated across 49 frames during a 1.5 s exposure.

The initial screening of the grids revealed that there was heterogeneity within the particle population and that some particles appeared deformed and disassembled in the vitreous ice (see Figure 4.11).

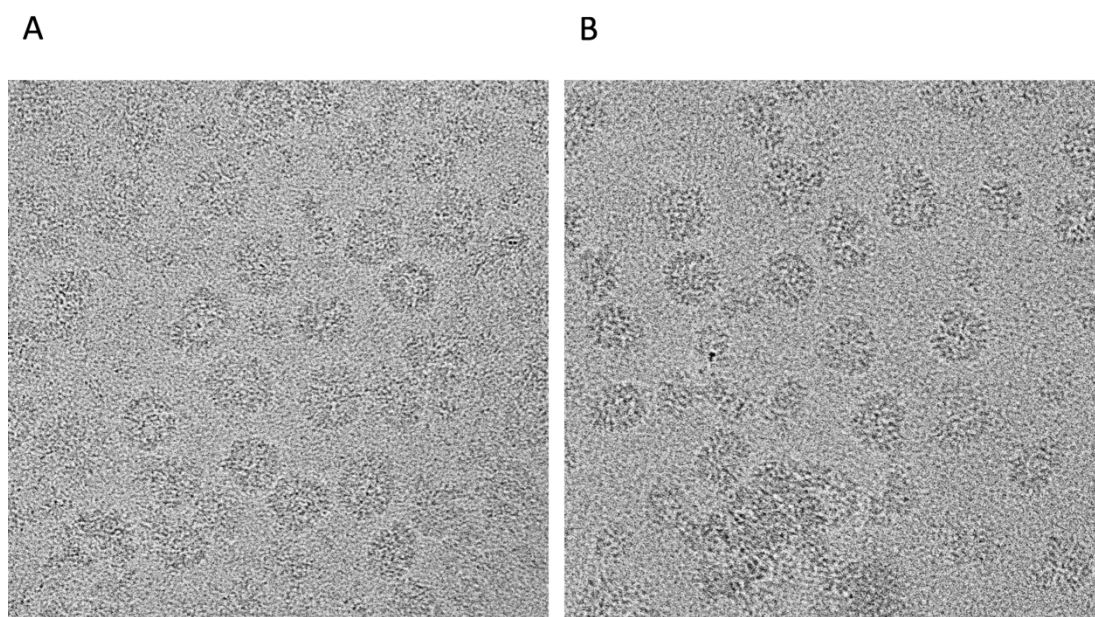


Figure 4.11 | Cryo-EM micrograph of N ω V procapsid VLPs. The particles were very heterogenous and some were disassembled. The concentration of particles from this sample suggested that it may be possible to isolate a population of intact particles using the data processing software. Data acquisition: Titan Krios with Falcon III, 1.065 Å/pixel, dose 72 e/Å².

After picking the particles from the micrographs using the automated picking tool, I carried out reference-free 2D classification of the particles. The 2D classes suggested that the population was heterogeneous; the particles were distributed across several classes and some of them corresponded to misshapen and broken particles (Figure 4.12).

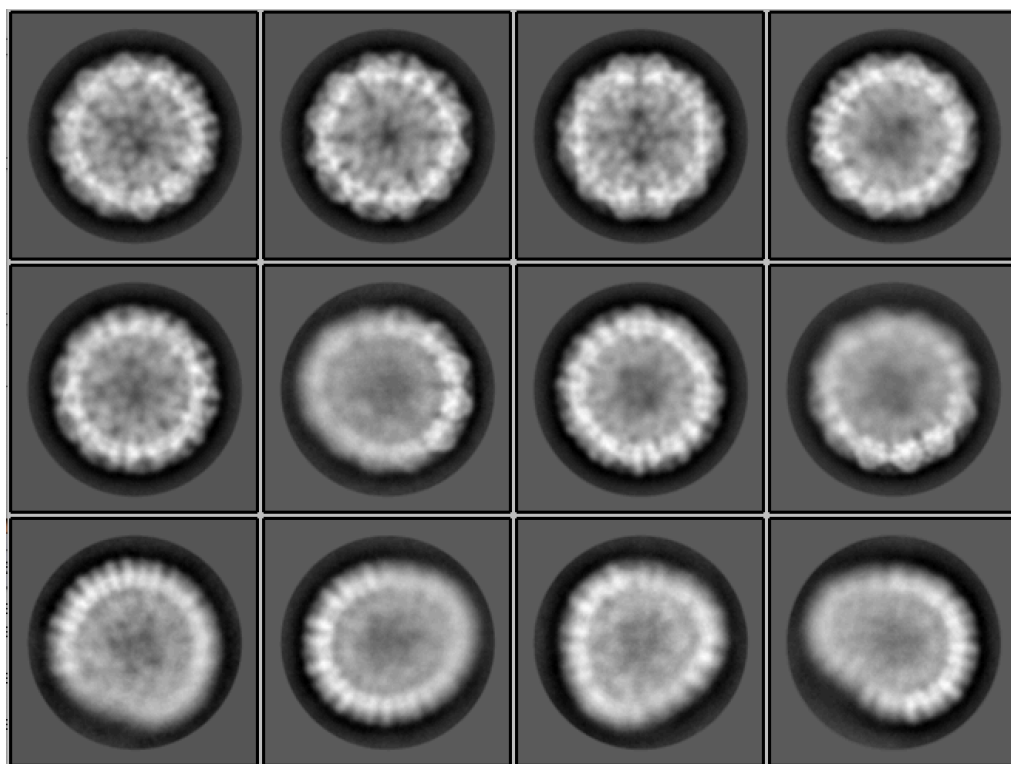


Figure 4.12 | Representative 2D averages of the NwV procapsid VLPs. The 2D classes show different views and populations of the VLPs. This sample is very heterogeneous with a large proportion of particles damaged or misassembled. Several rounds of 2D classification allowed the removal of the aberrant particles.

After the 3D classification and refinement steps, it was possible to obtain a cryo-EM reconstruction at 8.2 Å resolution (see Figure 4.13), which was very much lower than obtained with the mature capsids. This structure was a challenge as only 10% of the particles picked from the dataset were used for the reconstruction. Many of the particles were unstable in the cryo-EM grid, which frequently lead to disassembly or deformation of the particles. Furthermore, it looked like they were quite flexible. Further processing would be required and a new dataset might be able to increase the resolution of this structure (see further details in Chapter 5). As a preliminary structure, this result was very exciting as this cryo-EM structure showed the clear difference between the

procapsid and the capsid. Compared with the capsid structure, the procapsid had a larger volume, was more porous and the subunit contacts were more exposed. However, the resolution was too low to reconstruct the structure at a near-atomic level. This low resolution could be due to the intrinsic nature of the procapsids, as flexible structures present difficulties for structure determination.

Summary of section 4.2.3: It was possible to obtain a structure of the N ω V procapsid VLP produced in plants. The size of the particle and arrangement of the subunits was different compared to the capsid structure. The N ω V procapsid had a porous and flexible structure and the analysis of the cryo-EM micrographs revealed that the population was heterogeneous. The overall resolution obtained for this structure was of 8.2 Å.

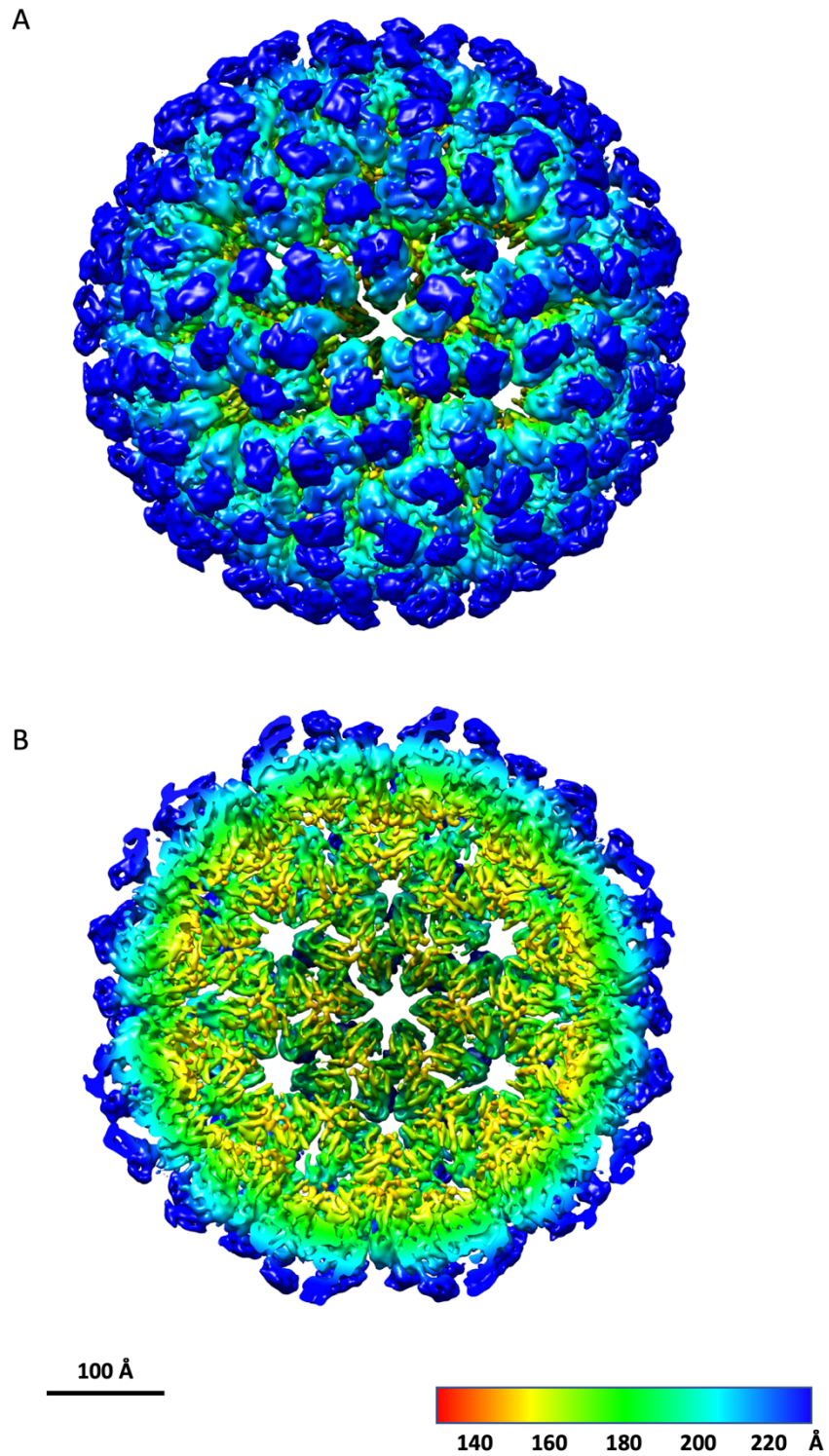


Figure 4.13 | 8.2 Å resolution structure of N ω V procapsid by cryo-EM. The 8.2 Å structure of N ω V is shown as a whole particle (a) and as cross section (b). The structure is coloured by radius from red (140 Å) to blue (220 Å). The scale bar is 100 Å.

4.2.4 Purification of N ω V N570T mutant VLPs expressed in plants

As homogeneous populations of procapsids are necessary to perform high-resolution structural studies, the idea of using cleavage-defective particles, which have the same morphology as the wild-type but do not undergo proteolysis, was explored. This mutant has the advantage that the quaternary structural changes that occur during maturation are reversible and can be controlled by the buffer conditions in which the particles are resuspended (Taylor et al., 2002).

Using site-directed mutagenesis, the pEAQ-*HT*-N ω V-WT was modified at position 570, replacing an asparagine for a threonine, giving rise to pEAQ-*HT*-N ω V-N570T. This mutation results in the production of the cleavage-defective mutant, N ω V N570T. The expression and purification of N ω V N570T particles were done in the same way as described in the previous chapter for N ω V WT particles.

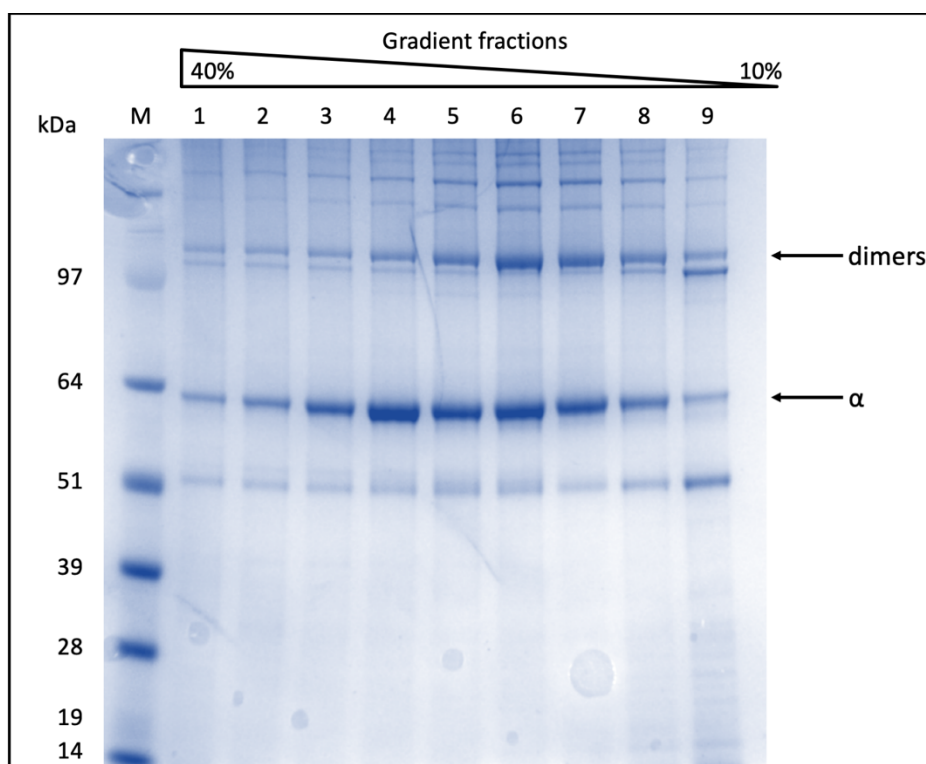


Figure 4.14 | Sucrose gradient step in the purification of N ω V N570T VLPs from *N. benthamiana*. SDS-PAGE gel displaying the profile of the fractions collected from a 10 to 40 % (w/v) sucrose gradient. The fractions were collected from the bottom of the tube, being the first collected fraction labelled as 1. For this sample, there is no presence of cleaved protein, which is the phenotype expected for this mutant coat protein. M = SeeBlue Plus 2 pre-stained protein standard.

The mutant N ω V N570T demonstrated that, in the absence of the cleavage site, there was no cleavage of the coat protein when this was extracted at pH 7.6 from plant leaves (see details in Chapter 2 and 3). However, the distribution of the protein across the gradient was similar to that observed for the N ω V WT sample (see in Chapter 3), suggesting that the sample was also structurally heterogeneous. It was expected that particles that compacted inside the plant cells would expand at pH 7.6; however, as shown in previous research (Taylor et al., 2002), this re-expansion may not happen at the same rate and in the same way for all the particles. Therefore, heterogeneity would be present within the particles but the population of procapsids was enriched.

Summary of section 4.2.4: It is possible to produce N ω V N570T VLPs in plants and purify them using the combination of sucrose cushions and gradients. Extracting the mutant VLPs in the same conditions as the N ω V WT VLPs, resulted in the absence of the cleavage, as was expected. However, the broad distribution across the gradient suggests that the population of particles is also structurally heterogeneous.

4.2.5 Dialysis of N ω V WT and N ω V N570T at low pH

At pH 7.6, N ω V VLPs are extracted in the procapsid form (without cleavage) (Agrawal and Johnson, 1995; Taylor et al., 2002). However, unexpectedly, in the previous chapter I showed that a population of the N ω V WT VLPs extracted from plants showed cleavage. This cleavage was not detected when N ω V N570T VLPs were expressed, as shown in the previous section, suggesting that the proteolysis was linked to the maturation process. At this point, however, it was not known what triggered the maturation of the N ω V WT particles inside the plant. In order to check that the WT and N570T particles were behaving as previously reported in low pH conditions (Taylor et al., 2002), I dialyzed purified procapsids at pH 7.6 (control) and at pH 5.0.

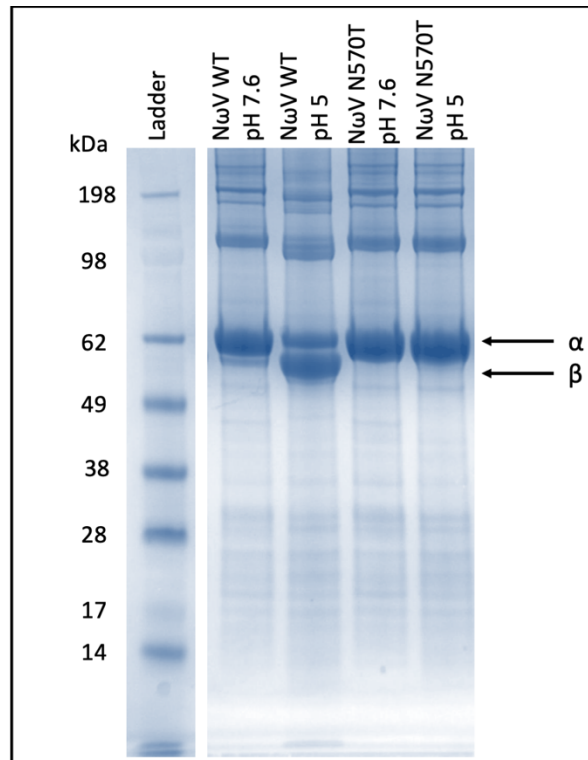


Figure 4.15 | Low pH triggers the cleavage for the N ω V WT coat protein but not for the N ω V N570T. Purified N ω V WT and N570T VLPs samples were dialyzed for 3 days at pH 7.6 and pH 5.0. The samples were run in an SDS-PAGE gel. The N ω V WT dialysed at pH 5.0 partially matured and it was possible to see the β peptide, while the N570T stayed as α peptide. Ladder = SeeBlue Plus 2 pre-stained protein standard.

At pH 5.0, the N ω V WT VLPs underwent the autoproteolytic cleavage in most of the coat proteins. However, a population of N ω V WT coat protein showed incomplete cleavage. This could be associated with particles that could not assemble properly and could not perform the cleavage in all the subunits or it could be also associated with variations in the RNA content of the particles or simply represent a fraction of the subunits not being able to cleave in the mature particles. N ω V N570T VLPs at pH 5.0 did not show cleavage, demonstrating that these particles could not undergo the autoproteolytic cleavage, as previously demonstrated with insect cells produced VLPs (Taylor et al., 2002).

Summary of section 4.2.5: For N ω V VLPs extracted from plants, low pH triggers the autoproteolytic cleavage in the N ω V WT VLPs but not in the N ω V N570T VLPs.

4.2.6 SAXS of the plant-produced N ω V WT and N ω V N570T VLPs

The following results have been produced in collaboration with Dr. Tsutomu Matsui, from the Stanford Synchrotron Radiation Lightsource (SSRL). The data presented in this section is presented with his kind permission.

Previous research showed that N ω V VLPs produced in insect cells can go through large-scale conformational changes when they are exposed to acidic conditions (pH 5.0), which also trigger an autocatalytic cleavage. These conformational changes can be studied with SAXS (Matsui et al., 2010a). We wanted to check if the N ω V VLPs produced in plants had a similar SAXS profile at different pH values. SAXS was a good approach as it provides information such as the diameter of the particles in solution, which was ideal as the large conformational changes of N ω V involve a reduction in the size of the particles.

Several samples of N ω V VLPs produced in plants, both WT and the N570T mutant, were sent to the SSRL to be analysed with SAXS, which allowed the determination of nanoparticle size distributions. The following figure shows a plot of the SAXS data for N ω V WT and N ω V N570T VLPs produced in plants. The particles were originally extracted at pH 7.6. For the SAXS experiments the VLPs were incubated at pH 7.6, 6.0 and 5.0 in order to look for the conformational changes (see Figure 4.16).

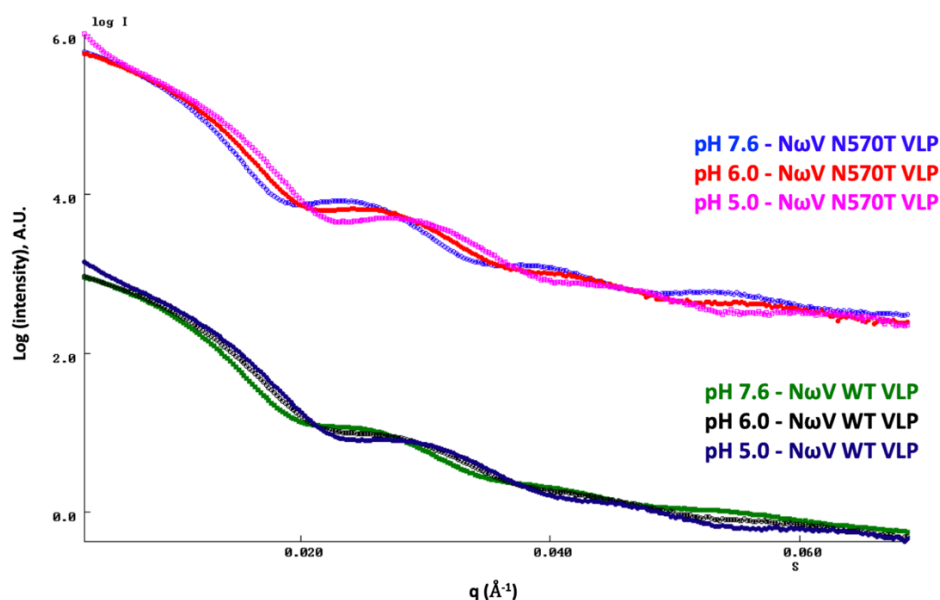


Figure 4.16 | SAXS profile of N ω V WT and N570T VLPs at different pHs. SAXS scattering curves of the N ω V VLPs incubated at different pHs. The pH and type of VLP are indicated in the legend of the plot, the colour of the text matches the colour of the plotted data that it represents. It was possible to observe a shift in the conformation of the particles at the different pHs. These shifts in the profiles were related with changes in the conformation of the particles.

The SAXS results from Figure 4.16 revealed that plant produced N ω V VLPs showed pH-dependent large conformational changes. This was very promising as it demonstrated that the plant-produced VLPs had similar maturation properties to those produced in insect cells. However, the lack of sharpness of the peaks suggested that there could be some heterogeneity and that those samples needed to be purer. These are much less distinct than those observed from the insect cell-produced N ω V VLPs (see section 5.1.4 from Chapter 5)

More details about the SAXS analysis carried for N ω V VLPs are provided in Chapter 5 where, using insect cell-produced VLPs, it is possible to see that the peaks are sharper and it is possible to clearly determine the conformational changes at different pHs.

Summary of section 4.2.6: Large conformational changes induced by a change in pH could be detected by SAXS using N ω V WT and N570T VLPs produced in plants. This demonstrated that the particles were dynamic and able to change shape and size. However, the SAXS profile suggested that there was heterogeneity, a hypothesis supported by the evidence presented in section 4.2.3. Alternatively, it could represent the presence of some uncharacterized impurity within the sample that was affecting the sharpness of the peaks.

4.2.7 Cryo-EM sample preparation of intermediates by pH change *in vitro*

The SAXS experiments demonstrated the ability of the plant-produced VLPs to undergo quaternary structural changes; however, they also suggested that the sample may be problematic regarding heterogeneity. To test this, I performed cryo-EM analysis on different stages of the maturation process of plant-produced N ω V VLPs generated by changing the pH to 6.0, 5.7 and 5.0 *in vitro*. The samples were initially kept at pH 7.6 and the pH was changed before the preparation of the grids. Two conditions were tested, the samples were frozen three minutes and 24 hours after changing the pH.

N ω V WT VLPs and N ω V N570T VLPs were tested for these preparations and in both cases, the screening of the cryo-EM grids revealed that the particles were mostly disassembled, aggregated or misshapen. This suggested that the maturation process was not being accomplished properly or that the freezing conditions used for the preparation of the cryo-EM grids were damaging the particles, which were not stable under those conditions. These results, together with the SAXS profiles presented in the previous section and the TEM results presented in the previous chapter, suggested that the study of the maturation process *in vitro* using plant-produced VLPs had limitations from a structural point of view. With the conditions tested for these experiments, no advantage of the particular use of N ω V WT or N ω V N570T VLPs was observed as both presented difficulties when frozen in the cryo-EM grids. In the following section, I explored the use of intermediates generated during the extraction. In chapters 5 and 6, I explore the use of insect cells to produce the N ω V VLPs to generate the intermediates for the cryo-EM analysis.

Summary of section 4.2.7: The generation of the different stages in the maturation process by changing the pH *in vitro* of N ω V procapsid VLPs, produced in plants, was not a suitable approach for the analysis of the structural changes by cryo-EM. The particles in the cryo-EM grids were heterogeneous with a major population of disassembled and aggregated particles.

4.2.8 Cryo-EM of the plant-produced N ω V intermediate VLP (pH 5.7)

The cryo-EM analysis of the plant-produced N ω V procapsid (see section 4.2.3), the results from SAXS and the cryo-EM tests from the previous section suggested that some of the maturation stages of the particles produced in plants had problems in terms of stability and homogeneity. On the other hand, when the particles were extracted as capsids, their structure closely resembled authentic virions (see section 4.2.1). These results suggested the possibility that if the particles were purified directly at the pH conditions for the intermediate rather than the procapsid, these particles might be more homogenous and it would be possible to solve their structure at a high resolution by cryo-EM.

To test this hypothesis I prepared N ω V VLPs at pH 5.7, which is in the range of pH values that allow the generation of intermediate structures (Matsui et al., 2010a). The protocol followed was the same as described in chapter 2 with the modification that the buffer used for the extraction, for the sucrose preparation and the resuspension of the particles is at pH 5.7, instead of pH 7.6. The composition of the pH 5.7 buffer was 100 mM MES, 250 mM NaCl, pH 5.7 and the pH was adjusted at room temperature. The idea was that if the particles have the same intermediate size they will all move in the same fraction of the gradient and if there were particles that were aberrant or that could not change conformation, those would be separated into different fractions. The particles obtained with this approach were first screened by TEM (see Figure 4.17). The images revealed a population of particles that were partially porous, as stain could penetrate and the increased homogeneity observed made the intermediate VLPs a good candidate to proceed with the cryo-EM analysis.

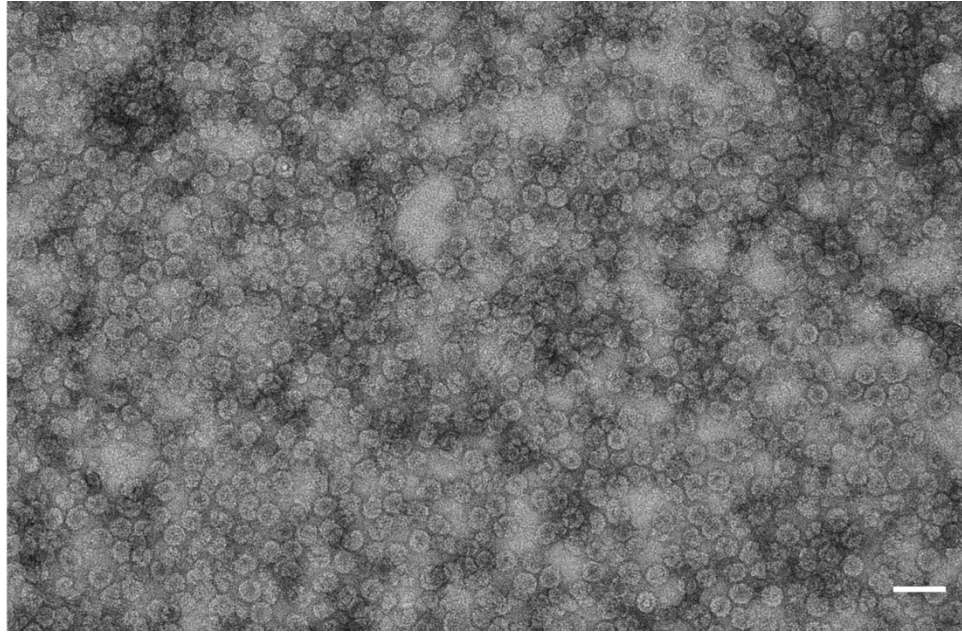


Figure 4.17 | TEM image of N ω V VLPs intermediates produced in plants and purified at pH 5.7. The particles were stained with 2% (w/v) UA and visualized by TEM. The VLPs have a mixture of shapes and some imperfections due to their flexibility and the effect of the stain. The diameter of the particles is ~42-50 nm. Scale bar is 100 nm. Image provided by Elaine Barclay.

These intermediate N ω V VLPs (pH 5.7) were prepared for cryo-EM (see details in Chapter 2). The data collection was done on a FEI Titan Krios EM (300 kV) equipped with a Falcon III detector, with a final object sampling of 1.065 Å/pixel and a total dose of ~62 e/Å². The dose was fractioned across 59 frames during a 1.5 s exposure.

Processing of the dataset was done with the Relion 2.1 and Relion 3.0 pipelines (Scheres, 2012; Zivanov et al., 2018). It was possible to see in the grids that there were good-looking particles as well as disassembled particles and others with a variety of shapes and sizes (Figure 4.18).

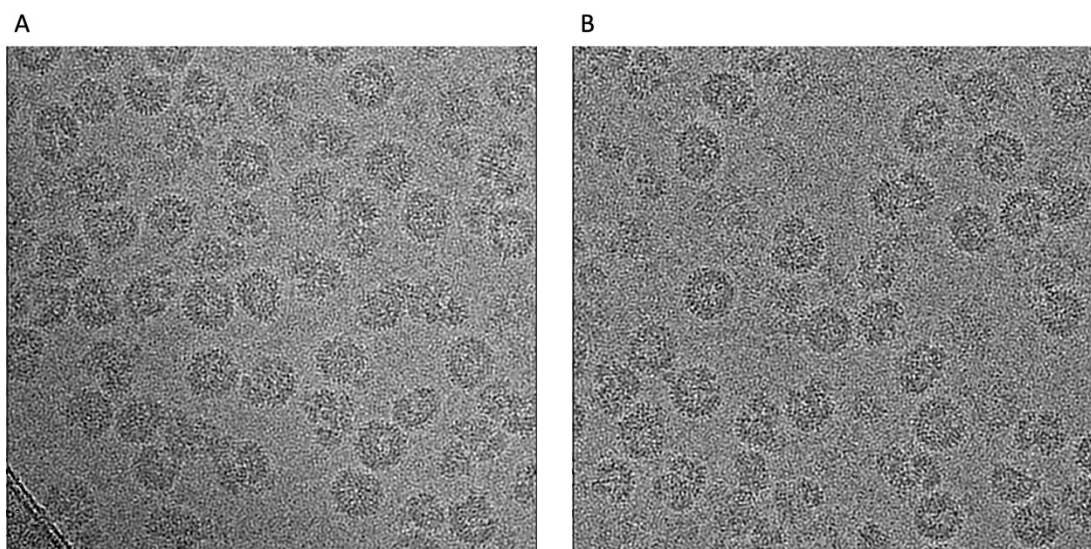


Figure 4.18 | Cryo-EM micrograph with N ω V intermediate pH 5.7 VLPs. This sample had a high concentration of particles but it was heterogeneous and some particles were broken and aberrant. Data acquisition: Titan Krios with Falcon III, 1.065 Å/pixel, dose 62 e-/Å².

Initial picking of the particles was done manually. The picked particles were used to generate 2D references for the automatic picking of the particles from the micrographs. The reference-free 2D classification of the picked particles showed that the population was heterogeneous; the particles were distributed across multiple classes and over 50% of them were misshapen or broken particles (Figure 4.19). After multiple rounds of 2D and 3D classification (Figure 4.20), the particles were separated in one population of particles that had a diameter of ~ 425 Å and was compact like the capsid structure (capsid-like intermediate) and in another one that had a diameter of ~ 455 Å and was slightly porous like the procapsid structure (procapsid-like intermediate). The two populations of particles were separately used for high-resolution 3D refinement and post-processing.

Two different cryo-EM structures were obtained from this intermediate pH 5.7 dataset. For the final reconstruction of the population of particles that had similar features to the capsid structure of N ω V, 6,658 particles were employed to generate a structure at 3.27 Å resolution (Figure 4.21). For the population of particles that was similar to, but smaller than, procapsid, 12,334 particles were employed to generate a structure at 6.95 Å resolution (Figure 4.21). For both structures the final resolution estimates were determined based on the gold-standard Fourier shell correlation (FSC = 0.143) criterion (Scheres and Chen, 2012).

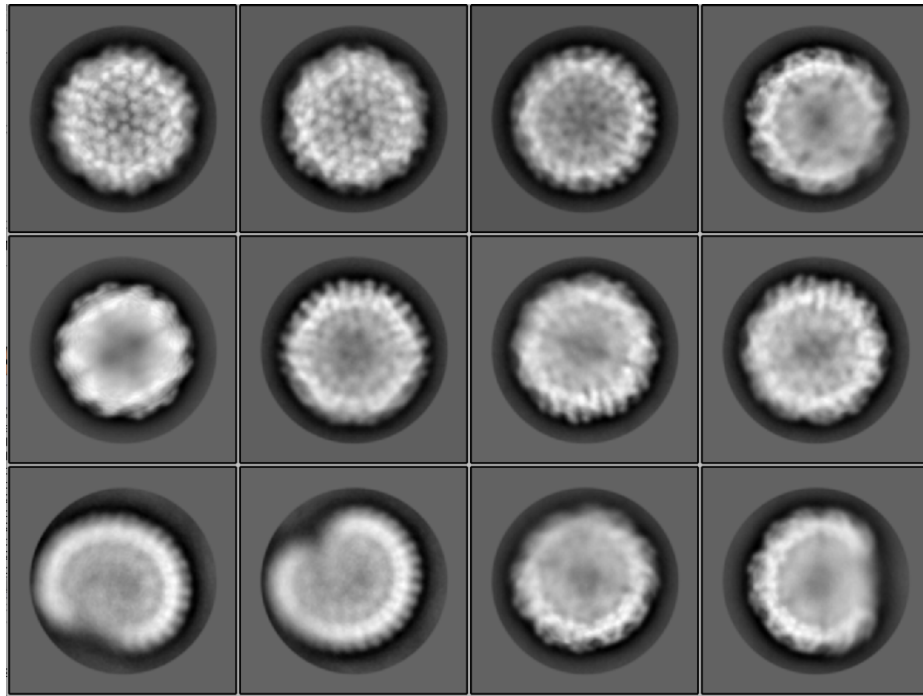


Figure 4.19 | 2D classification of the NwV pH 5.7 intermediate VLPs. The 2D classes show different views and populations of the VLPs. The first image in the second row, has features similar to those observed in the 2D classification of capsid particles. This sample is very heterogeneous with a large proportion of particles damaged or misassembled. Several rounds of 2D classification allowed the removal of the aberrant particles.

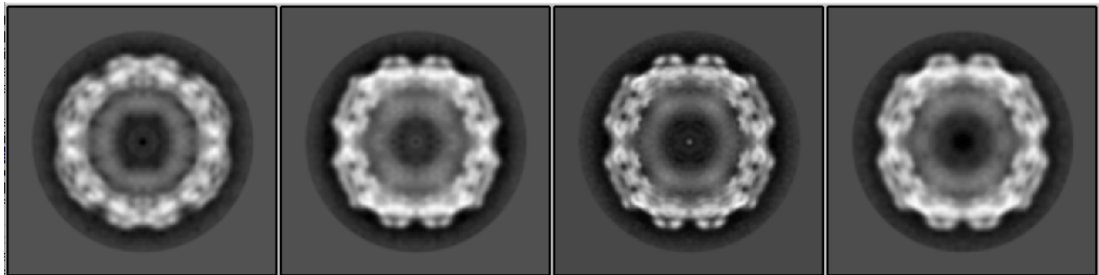


Figure 4.20 | 3D classes from the pH 5.7 dataset. The 3D classification shows that there is heterogeneity within the selected particles. From the 2D and 3D classifications it was possible to isolate two main populations of particles with distinctive features in their structure, such as different diameter (425 and 460 Å).

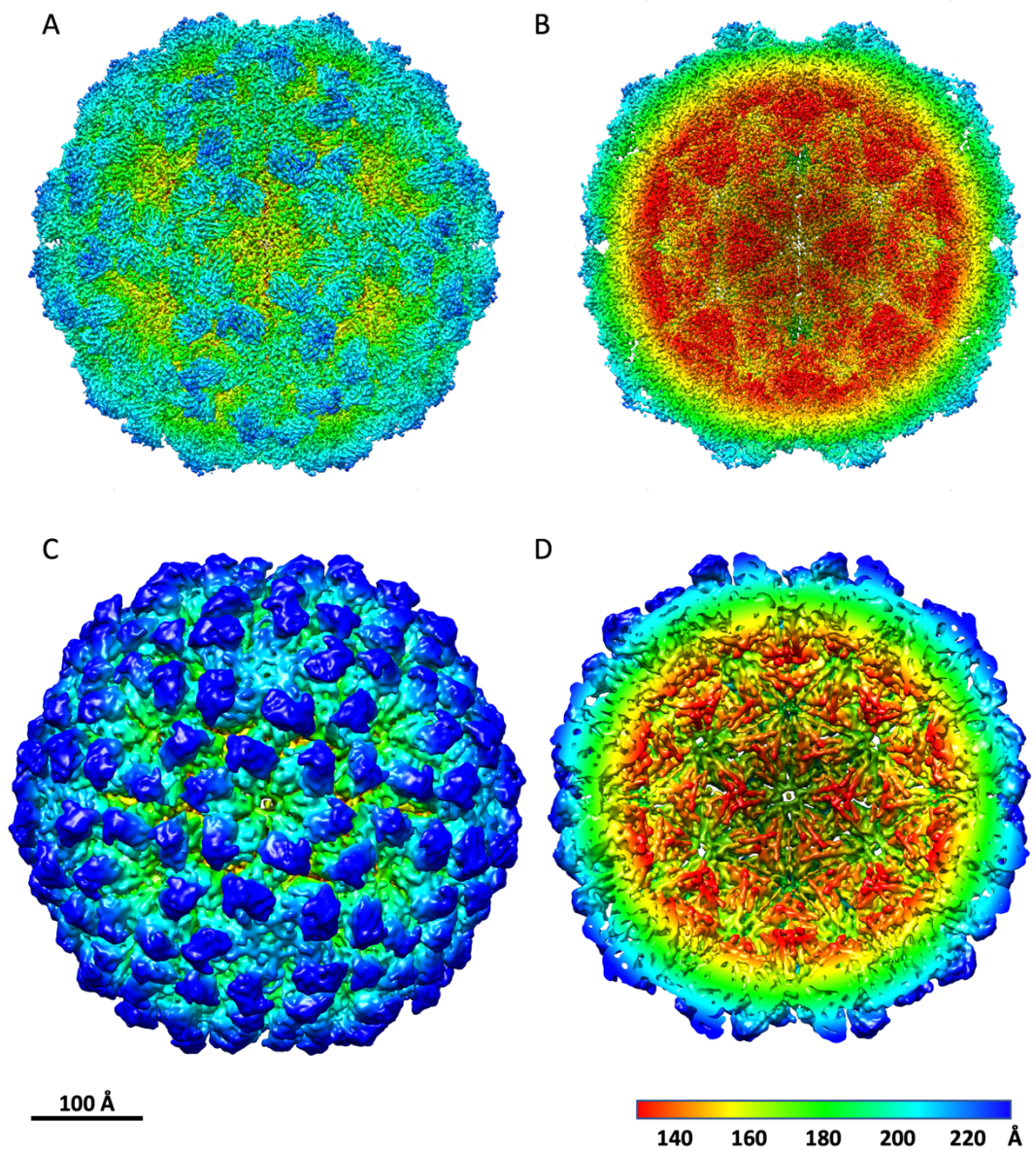


Figure 4.21 | Comparison of the cryo-EM structures of the NwV VLPs intermediates at pH 5.7. Cryo-EM structures of capsid-like intermediate at pH 5.7 (a, b) and procapsid-like intermediate at pH 5.7 (c, d). Two views are shown, full particle (a, c) and cross section (b, d). The structures are coloured by radius from red (140 Å) to blue (220 Å). The scale bar is 100 Å.

Regarding the origin of the capsid-like structure from this dataset, it could be from particles that had completed the maturation process during the incubation at this pH. On the other hand, it could be from particles that were already mature at the moment of the extraction and that copurified with the intermediate particles. Due to their higher stability, the capsids could have survived better the freezing conditions than the other intermediate structures and therefore their relative proportion could have been artificially enriched as they were not detected in the initial screenings by negative staining TEM (see Figure 4.17).

Summary of section 4.2.8: In this chapter, two cryo-EM structures have been obtained from N ω V VLPs extracted at pH 5.7. One structure was similar to capsid and was possible to obtain it at high-resolution (3.27 Å). The structure of the procapsid-like intermediate (6.95 Å) had a different diameter (460 Å) when compared to capsid (420 Å) and procapsid (480 Å). This was a significant milestone and demonstrated that it was possible to get detailed structural information from these transient states. However, as it has been described in the previous sections of this chapter, the plant-produced N ω V VLPs presented a heterogeneity and lack of stability that hampered the structural studies. Therefore, in the following two chapters it was explored the use of insect cells to get even higher resolution structures of the intermediates.

4.3. Summary of the cryo-EM structures obtained from plant-produced N ω V VLPs

In this chapter I have presented four cryo-EM structures of N ω V from three different datasets of samples produced in plants and extracted under different conditions (Figure 4.22). The capsid structure of plant-matured particles is very well defined at 2.7 Å. The procapsid structure is at 8.2 Å and provides interesting insights about the assembly and the initial stages in the maturation of N ω V; however, it is not at high enough resolution to be able to fit the secondary structure of the protein. The intermediate at pH 5.7 is at 6.95 Å for the procapsid-like structure. From the pH 5.7 dataset, I also obtained a capsid-like structure at 3.27 Å resolution. Though this was a significant achievement in its own right, I wanted to achieve near-atomic resolution for the procapsid and intermediates and it was clear that I could not get this with plant-expressed material. Therefore, I decided to explore the use of another system, insect cells, to produce N ω V VLPs.

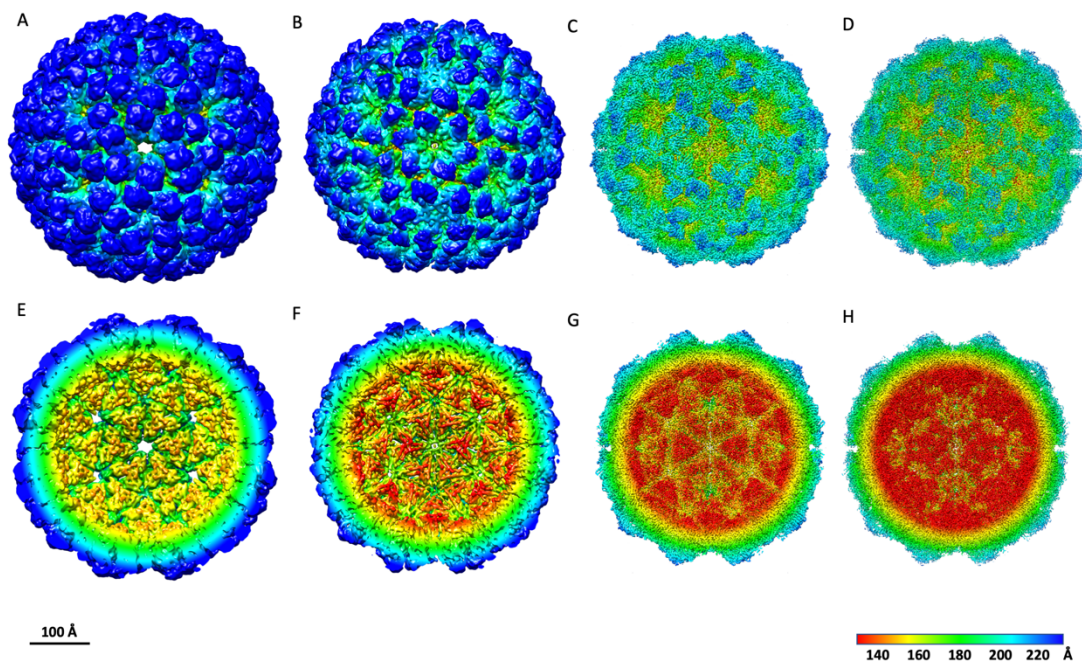


Figure 4.22 | Summary of the cryo-EM structures obtained from plant-produced N ω V VLPs. Procapsid (a, e), procapsid-like pH 5.7 intermediate (b, f), capsid-like pH 5.7 intermediate (c, g), capsid matured in plants (d, h). Two views are shown, full particle (a, b, c, d) and cross section (e, f, g, h). The structures are coloured by radius from red (140 Å) to blue (220 Å). The scale bar is 100 Å.

4.4. Comparison with the insect cells

The plant-produced capsid structure demonstrated that the initial assembly of the N ω V VLPs was likely to be correct and that the particles were able to undergo the fine process of maturation properly, as the structure of the final capsids closely resembled that of the previously reported crystal structure of authentic N ω V virions (Helgstrand et al., 2004; Munshi et al., 1996). However, the SAXS results and the procapsid and intermediate (pH 5.7) cryo-EM structures, suggested that the stages before the completion of the maturation were heterogeneous and the particles unstable. Therefore, we hypothesised that maybe during the extraction and the purification of the particles from the plants, some changes affecting the structure of the purified particles occurred, hampering the maturation process and the architecture of the resulting particles. Even though plants showed great promise for analysing some of the properties of the N ω V VLPs, as described in this thesis, they presented limitations for the structural studies.

To understand the issues, I compared the properties of the plant-produced particles with those produced insect cells (described in detail in Chapter 5).

4.4.1. Cross-linking and effect on the dynamics of N ω V VLPs

When comparing the SDS-PAGE and western blots obtained for N ω V VLPs produced in plants and insect cells, I observed extra high molecular weight bands (~120-140 kDa) only in the sample from the plant-expressed VLPs. As discussed in Chapter 3, section 3.2.1, these are hypothesized to be oligomers of the coat protein. The denaturing conditions used for all the VLPs were the same, therefore the formation of the oligomers was probably induced by the plants (Figure 4.23).

Plants have a broad repertoire of peroxidases that can be activated, for example, under stress conditions. Consequently, these peroxidases could be contributing to the crosslinking of some of the N ω V coat proteins that were then observed as dimers and higher structures in the protein gels. This observation had important implications because it could explain the maturation problems that the plant-produced N ω V VLPs faced when the pH was changed from neutral (pH 7.6) to acid (pH 5.0) in *in vitro* conditions after the initial extraction.

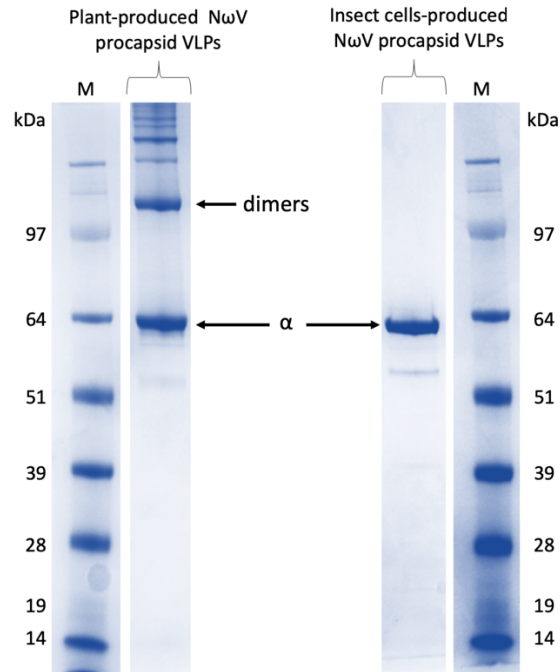


Figure 4.23 | Side by side comparison of N ω V WT VLPs produced in plants and insects. Comparison of plant- and insect cell-produced N ω V procapsid VLPs. Both samples were treated with the same denaturing conditions and were run in an SDS-PAGE gel, which was stained with InstantBlue. In both samples there is the presence of the full coat protein (α peptide). The oligomers, high molecular weight bands, are only present in the plant sample. M = SeeBlue Plus 2 pre-stained protein standard.

To further investigate the possible crosslinking induced by the plant, I incubated insect cell-produced N ω V VLPs with plant extracts and then analysed them by western blot using the polyclonal antibody against N ω V (see details in Chapter 2).

The particles were therefore incubated in plant material that had been extracted with the same buffer and conditions as used for the plant-produced VLPs. The time of the incubation was approximately the same as the time that it takes from the extraction to the separation of the VLPs from the plant material using the single sucrose cushion step (4 hours), which has been further described in Chapters 2 and 3.

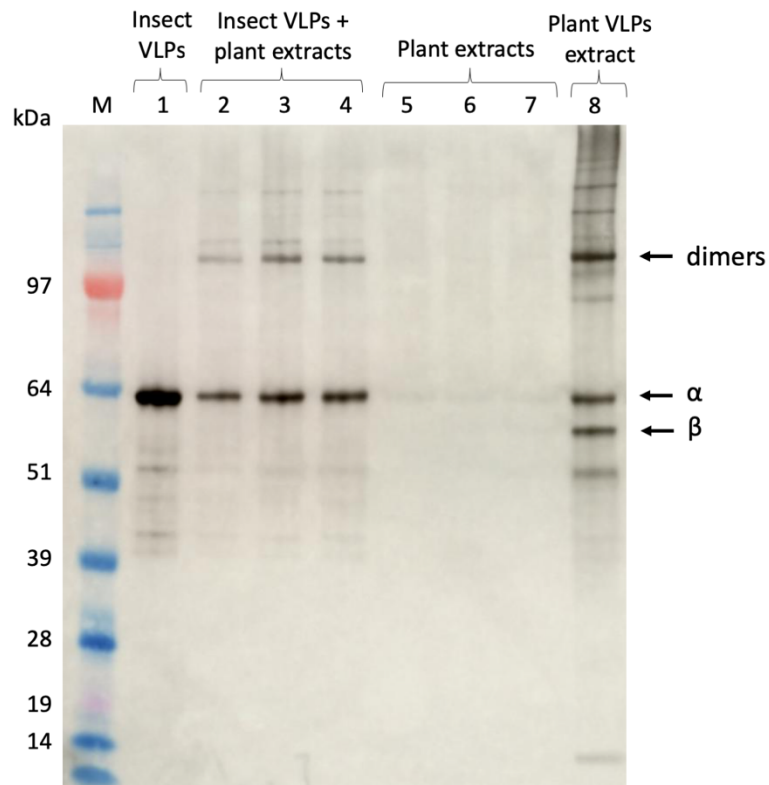


Figure 4.24 | Incubation of insect cell-produced N ω V WT VLPs with plant extracts. The western blot revealed that insect cell-produced N ω V VLPs incubated with different plant extracts, formed dimers that were not denatured when run in the SDS gel. In lanes 1 to 4, N ω V VLPs produced in insect cells were mixed with pH 7.6 buffer (1) or different plant extracts (2, 3 and 4). In lanes 5 to 7 are the same plant extracts used for lanes 2 to 4 but without the VLPs. These were the negative controls to check that the plant extracts did not cross react with the N ω V polyclonal antibodies used for the western blot. In lane 8 there is the plant extract from plants infiltrated with pEAQ-*HT*-N ω V-WT. In lane 8 it is possible to detect the α peptide, the β peptide, from the maturation that occurs in the plant (details in Chapter 3), and also the dimers. The plant extract in lanes 2 and 5 was from uninfiltrated plant leaves blended with pH 7.6 buffer. In lanes 3 and 6, the plant extract was from plants that were infiltrated with pEAQ-*HT*-EV and for lanes 4 and 7, with pEAQ-*HT*-GFP and in all cases, the plant material was blended with the pH 7.6 buffer. M = SeeBlue Plus 2 pre-stained protein standard.

The results from the western blot (see Figure 4.24) showed that the insect cell-produced VLPs incubated in the plant extract have additional high molecular bands (lanes 2 to 4), as observed for the plant-produced (lane 8). The negative controls (lanes 5 to 7), with only plant extracts without insect cell-produced VLPs, did not display N ω V-specific bands, indicating that this high molecular weight bands came from the insect cells particles. This suggested that there is a certain degree of crosslinking, which is not observed in the particles before the incubation (lane 1). These results strongly imply that some component from the plant cells induce the crosslinking of the N ω V coat proteins.

Varying the conditions of extraction using, for example, buffers at different pHs (5.0, 7.6, 10.0), did not make a significant difference, with the crosslinking being persistent in different tested extraction conditions. More conditions should be tested in order to try to find a combination that reduces the formation of these strong interactions in the plant-produced VLPs.

The experiments presented in this section suggested that the protein aggregates could be a product of crosslinking induced by peroxidases naturally occurring in the plant cells and that have been activated during the disruption of the cells in the protein extraction procedure. Furthermore, this crosslinking could also happen as a process of the cell decay as it has been observed in the time course experiments that crosslinking increases with time as well as the cleavage of the N ω V coat protein (see section 3.2.1).

This observation has not only implications for this project, but also for producing other VLPs in plants, as this crosslinking could affect the properties of the proteins and the assemblies. For N ω V, we propose that it affects the protein rearrangements necessary for the maturation, affecting the final assembly. Indeed, we observed that when the particles matured inside the plant cells or when the VLPs were extracted from the plant directly under acidic conditions, the particles displayed features similar to well-formed matured particles. Therefore, for these particles, their dynamics had not been hampered before the maturation completion. As the large conformational changes can be resolved in a few seconds when the particles are in acidic conditions, this suggested that probably the maturation was faster than the crosslinking. However, when the particles were extracted at neutral pH, then there was enough time for the crosslinking to happen and then a part of the population of particles was not suitable to successfully complete the maturation at a structural level.

Summary of section 4.4.1: This is the first result that demonstrates that extracts from plant cells can crosslink VLPs produced in insect cells. This crosslinking is also present in the plant-produced N ω V VLPs and together with the cryo-EM and SAXS results presented in the previous sections, it is hypothesised that it has effects in the dynamical properties of the particles. These covalent interactions may hamper the maturation process and avoid the correct formation of the different stages. These results imply that for structural biology studies, N ω V VLPs produced in insect cells, would be more suitable than the plant-produced. However, for other applications, these stronger interactions could have beneficial effects on the mechanics and stability of the particles. Further experiments would be needed to test and compare the rigidity and the resistance of plant- and insect cell-produced N ω V VLPs.

4.5. Discussion

This chapter started by presenting the cryo-EM experiments done to obtain the structure of N ω V capsid VLPs with the highest resolution reported so far (2.7 Å). This demonstrated that plants were able to produce N ω V assemblies that can mature towards capsids that resembled the structure of authentic virions. Extra density was detected inside the structure that was proposed to be RNA. Between the RNA shell and the capsid, several points of interaction were observed, especially in the areas away from the fivefold axis. This idea is supported by the fact that a previous study reported the encapsidation of RNAs by N ω V VLPs. Those VLPs had been produced in insect cells and their RNA content was 80 % attributed to host RNAs and 5 % to mRNA of the N ω V coat protein (Routh et al., 2012). Furthermore, RNA densities have been previously observed in other cryo-EM structures of insect viruses such as FHV (Dong et al., 1998) and also in plant viruses like CPMV (Hesketh et al., 2015) and BBSV (Lecorre et al., 2019). These last examples were of authentic virions; therefore, the observed density was of their genomic RNA.

Subsequently, I presented the cryo-EM structure of the procapsid form of the N ω V VLP. This structure provided new information regarding the quaternary structure of N ω V in the initial stages of the maturation process. It also demonstrated that it was possible to isolate procapsids from plants. These cryo-EM results, suggested that plant-produced particles could be a good system for the study of the maturation of N ω V as these particles were able to undergo large conformational changes. However, this view changed after exploring the structure of the intermediates using SAXS and cryo-EM. What was observed was that the generation *in vitro* of the different stages in the maturation process failed to provide suitable particles for high resolution cryo-EM analysis. The VLPs showed heterogeneity and had some problems including disassembly and aggregation. Despite the difficulties presented by the plant-produced particles, I was able to solve the structure of N ω V intermediates to moderate resolution. Their structures provide new insights in the maturation process but did not have sufficient resolution to fit in the secondary structure of the protein. However, this could be improved in the future, as new software may allow for the better classification and reconstruction of heterogeneous and flexible structures, which would improve their resolution.

Additional experiments, comparing the plant-produced VLPs with the ones produced in insect cells (more details in Chapter 5 and 6), revealed a trouble with plants as an

expression system. The cell content from the plants induced the formation of strong interactions between the subunits of N ω V, probably crosslinks, which were only observed when the particles were in contact with the plant extract. This was unexpected and provided new evidence for the limited dynamical properties of the plant-produced particles. For a system that relies on changes in the quaternary structure, strong interactions can hamper these changes and have detrimental effects in the maturation process of the virus and therefore in the production of the N ω V maturation movie. Given the fact that insect cells did not present this difficulty, using them to make the VLPs for the cryo-EM analysis was the next goal, which is presented in the following chapters.

Chapter 5

Back to the insects

5.1. Introduction

The aim of the research presented in this chapter was to produce N ω V VLPs and to establish the conditions necessary to produce homogeneous populations of particles representing the different stages of its maturation process. Instead of plants, which have been described in the previous chapters, the approach for this chapter was to use insect cells for the expression of the N ω V coat protein. This system has been already used for the production of numerous VLPs and has been proven to be effective for the production of N ω V VLPs (Agrawal and Johnson, 1995). The N ω V VLPs produced in insect cells were tested to determine the best conditions for their use in cryo-EM studies.

5.2. Results

5.1.1. Expression of N ω V WT coat protein in insect cells

In order to produce the N ω V VLPs in insect cells I followed the same procedures employed in previous publications (Domitrovic et al., 2012; Matsui et al., 2009). Briefly, the N ω V coat protein was overexpressed in insect cells using the pFast-Bac 1 vector containing the N ω V coat protein sequence, which was kindly provided by Tatiana Domitrovic (UFRJ). The particles were extracted from the insect cells at pH 7.6 and purified by running them through a sucrose cushion followed by a sucrose gradient (see Figure 5.1). Afterwards, the sucrose was removed and the particles concentrated using the Amicon® filters (see details in Chapter 2). The particles were stored at pH 7.6, as at this pH they remain in the procapsid stage and it is possible to obtain the other states by changing the pH and buffer conditions.

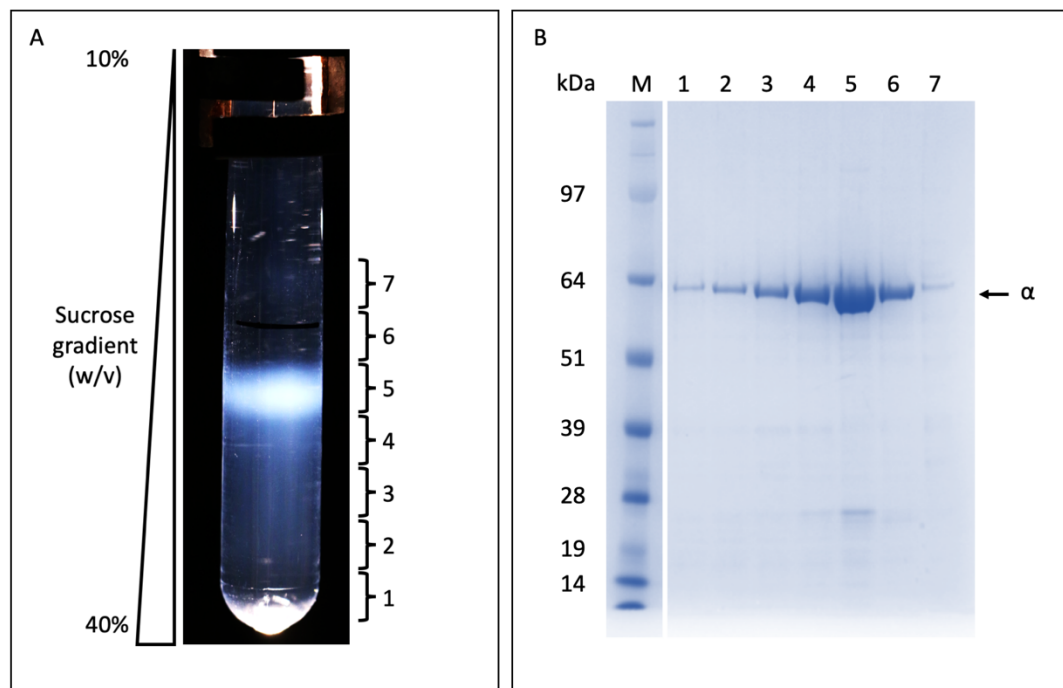


Figure 5.1 | Sucrose gradient step in the purification of N ω V VLPs produced in insect cells. After the sucrose cushion, the particles were loaded on top of a 10 - 40 % (w/v) sucrose gradient. The particles advanced in the gradient and by shining a light to the tube it was possible to observe an opalescent band, which corresponded to the accumulated VLPs. The gradient was fractionated from the bottom by making a hole to the tube (a). The collected fractions, indicated by numbers, were analysed by SDS-PAGE. A band of the appropriate size to be α peptide (around 70 kDa) was observed across the different fractions and a higher concentration was observed in fraction 5 (b).

The sucrose gradient allowed the purification and concentration of N ω V within a few fractions. The sample obtained from this step was mainly composed of N ω V coat protein and, as shown in the following sections, the purity and yield (20 - 40 mg/L) were ideal for the subsequent structural studies. The presence of the majority of the coat protein in the lower fractions of the gradient suggested that it was assembling in VLPs, because single subunits would usually accumulate in higher fractions of the gradient. The SDS-PAGE from Figure 5.1b also revealed that the coat protein migrated as one main band of around 70 kDa, with no sign of the autocatalytic cleavage seen in plants. The higher molecular weight bands found with the plant-produced VLPs described in the previous two chapters were not observed. This was a striking difference that suggested that the conformational changes required for the maturation process of N ω V would not be hampered by the cross-linking hypothesised to occur in the plant-produced VLPs as discussed in Chapter 4.

Summary of section 5.2.1: N ω V coat protein can be transiently expressed in insect cells. VLPs can be successfully purified by sucrose gradient centrifugation. When compared with plant-produced N ω V VLPs under the same denaturing conditions, the dimers seen with the plant-produced VLPs were not observed.

5.1.2. N ω V conformational changes under TEM

After successfully producing the N ω V coat protein in insect cells, I wanted to check if the VLPs assembled properly and if these were able to undergo the large conformational changes associated with changes of pH. One sample (at pH 7.6) was loaded in TEM grids and stained with 2 % (w/v) uranyl acetate. Another sample was prepared by dropping the pH of procapsid VLPs to pH 5.0 and incubating them at this new pH for 5 minutes before applying them to the TEM grid. It was anticipated that the change in pH would change the morphology and size of the particles as they are able to undergo the large conformational changes in a matter of seconds (Matsui et al., 2010a).

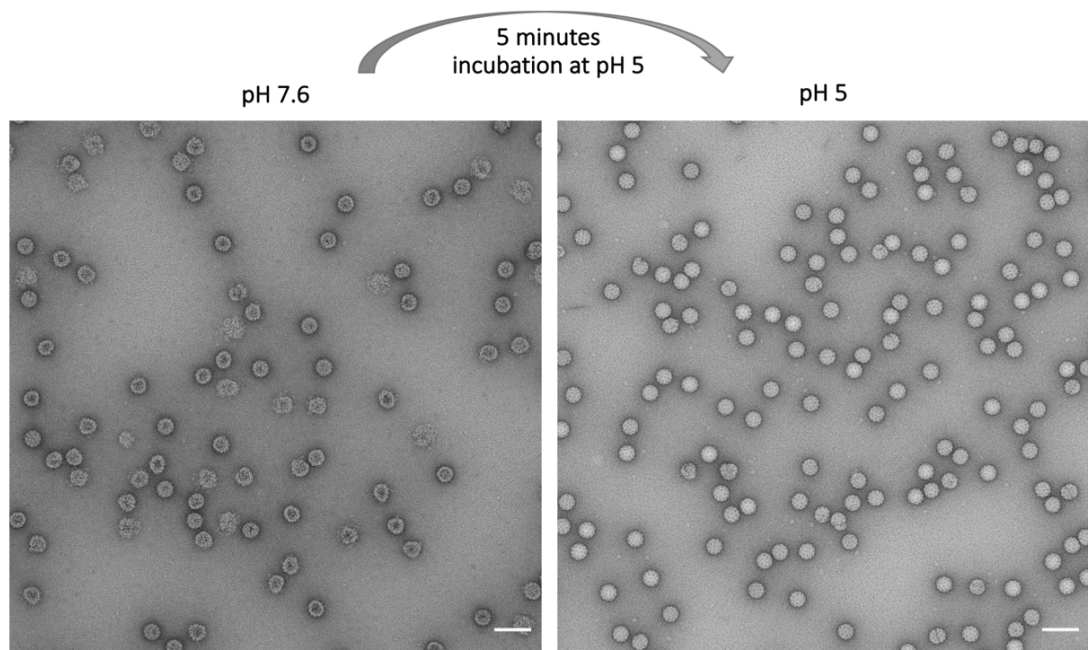


Figure 5.2 | TEM images of N ω V VLPs incubated pH 7.6, left, and at pH 5.0, right. The VLPs were stained with 2 % (w/v) UA. The procapsids (pH 7.6), left, were observed as porous and fragile and of an approximate diameter of ~48-50 nm. With the pH drop and transition to the capsid stage (pH 5.0), the particles became less porous, more homogeneous and of an approximate diameter of ~42 nm. Scale bar of 100 nm.

The TEM results demonstrated that the particles were able to change conformation and size with the pH of the buffer in which they were resuspended. The uranyl acetate staining can be harsh for some samples, for example when they are pH-sensitive, because it has a pH of 4.2 - 4.5. Some of the procapsids in the images looked damaged; this was expected to be produced by the staining and also because the nature of the procapsids, which are more flexible assemblies. Furthermore, procapsids are porous and it was possible to observe staining penetrating inside of the particles. On the other hand, the capsids had a more compact structure and the stain was not able to penetrate. These results were very encouraging and suggested that the particles produced in insect cells would be a good candidate for structural biology studies, including SAXS and cryo-EM.

Summary of section 5.2.2: N ω V coat proteins are able to assemble into VLPs that are able to undergo conformational changes when the pH is dropped. These characteristics suggested that they would be suitable candidates for cryo-EM studies.

5.1.3. Cryo-EM of the N ω V procapsid (pH 7.6): The initial assembly

N ω V undergoes a complex series of structural rearrangements during the maturation process. It starts as an expanded procapsid and it transitions to the compact capsid. Therefore, to be able to study the whole maturation process it was important to have high quality preparations of the procapsid that would be able to transition through the different stages and complete the maturation. It was already known that N ω V VLPs produced in insect cells could mature and form capsids that would structurally resemble authentic virions (Campbell et al., 2014; Helgstrand et al., 2004; Munshi et al., 1996); therefore we decided to start by studying the structure of the procapsid.

The procapsid is the first known structure that N ω V adopts after the complete assembly of the 240 subunits into particles. The assembly of the procapsid allows the formation of the T = 4 capsid as the N ω V subunits assemble in a near-reversible way that allows their proper arrangement and avoids kinetic traps (Katen and Zlotnick, 2009). It is possible to disassemble the procapsids using, for example, moderate salt concentrations. There is evidence suggesting that, when they are in solution, the subunits form dimers that then associate to form the spherical procapsid (Veesler and Johnson, 2012). Furthermore, between the basic N-terminal region of the subunits and the RNA there are electrostatic attractions but, at pH 7.6, there is also electrostatic repulsion among the negatively charged acidic residues distributed on the subunit interfaces contributing to the expanded state of the procapsid (Matsui et al., 2010a).

The structure of the insect cell-produced N ω V VLP procapsid at pH 7.6, was determined by cryo-EM. The grid preparation (see Chapter 2 for details) was done with the assistance of Dr. Emma Hesketh, who then set up the data collection. The particles were imaged using a FEI Titan Krios microscope equipped with a Falcon III detector, with a final object sampling of 1.065 Å/pixel and a total dose of 88.5 e/Å². The dose was fractioned across 59 frames during a 1.5. s exposure.

The micrographs (Figure 5.3) show that there were intact particles, suitable for the reconstructions. The data were analysed using the RELION 3.0 pipeline (Zivanov et al., 2018). To produce a template for automated particle picking, a small subset of particles was manually picked to calculate a set of reference-free 2D class-averages. These were used to pick 103,177 particles that were extracted and used as the input for the 2D classification.

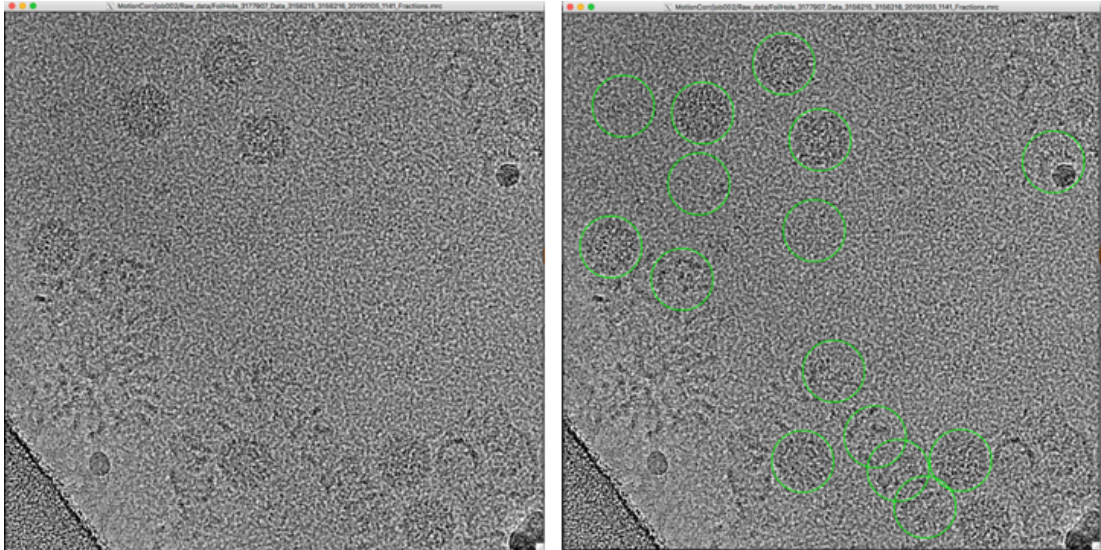


Figure 5.3 | Cryo-EM micrograph of N ω V procapsid VLPs. N ω V VLPs at pH 7.6 in vitreous ice (left image) and a set of N ω V VLPs at pH 7.6 selected to proceed with the processing (right image). The final particle picking was done with the autopicking option in Relion 3.0, which allowed fast picking of the thousands of particles in the micrographs. However, it was possible to observe that it also picked elements that were not particles. The following steps in the processing allowed for the classification of the particles and discarding of the other elements that are not of interest for the final reconstruction. The grids used had a thin layer of carbon that goes across the grid and favours the homogenous distribution of the particles. Therefore, these grids favoured the presence of the particles in the middle of the hole, because usually the particles had the tendency to go to the sides and stick to the carbon. Data acquisition: Titan Krios with Falcon III, 1.065 Å/pixel, dose 88.5 e/Å².

Those 2D classes that showed high-resolution features were selected (see Figure 5.4). In total, 34,532 particles were selected for the following steps of 3D classification, with icosahedral (I1) symmetry imposed (see Figure 5.5), and 3D refinement. For the final reconstruction, 11,955 particles were employed to generate a structure that after postprocessing was used to appropriately mask the model, estimate and correct for the B-factor (particle motion) of the maps. Using the ‘gold standard’ Fourier shell correlation (FSC = 0.143) criterion, the final resolution was determined to be 4.9 Å. Local resolution estimation was performed using RELION (Fernandez-Leiro and Scheres, 2017; Scheres, 2012) and revealed that some areas of the cryo-EM map, mainly on the inside of the particle, had a local resolution better than 4.5 Å (Figure 5.6).

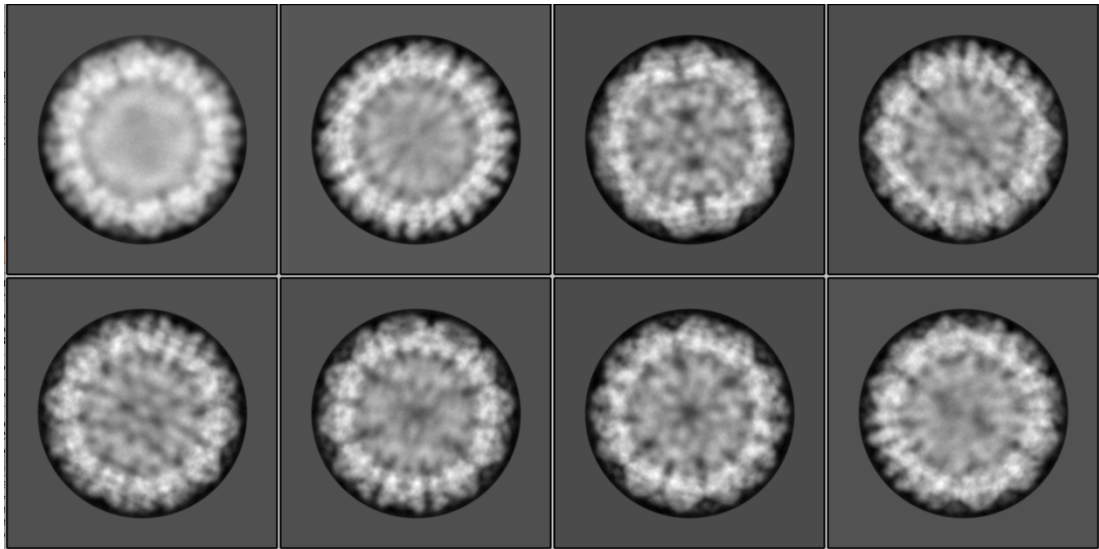


Figure 5.4 | 2D classes obtained in the 2D classification step of the NwV procapsid VLPs. Several rounds of 2D classification allowed the removal of disassembled and aberrant particles, together with other elements, like carbon, that were picked during the automated particle picking step. With the 2D classification it was possible to see the porosity of the particles and their round shape. These particles displayed more heterogeneity when compared with the capsids described in Chapter 4.

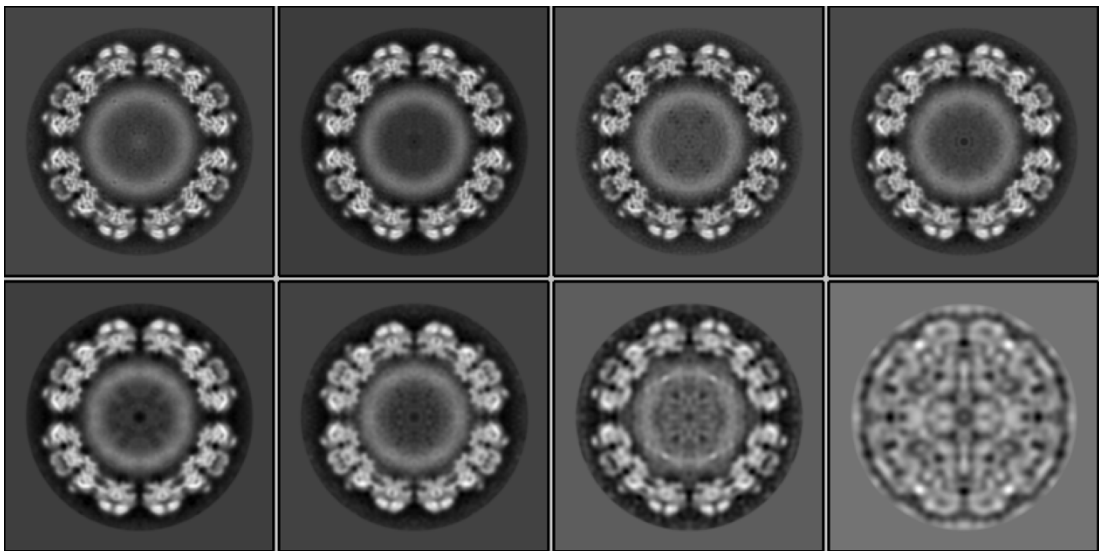


Figure 5.5 | 3D classification of the NwV procapsids VLPs. After the 2D classification, there was still heterogeneity in the population of particles remaining. The 3D classification allowed separation of different classes and the best, showing better structural features, were selected for the following refinement steps.

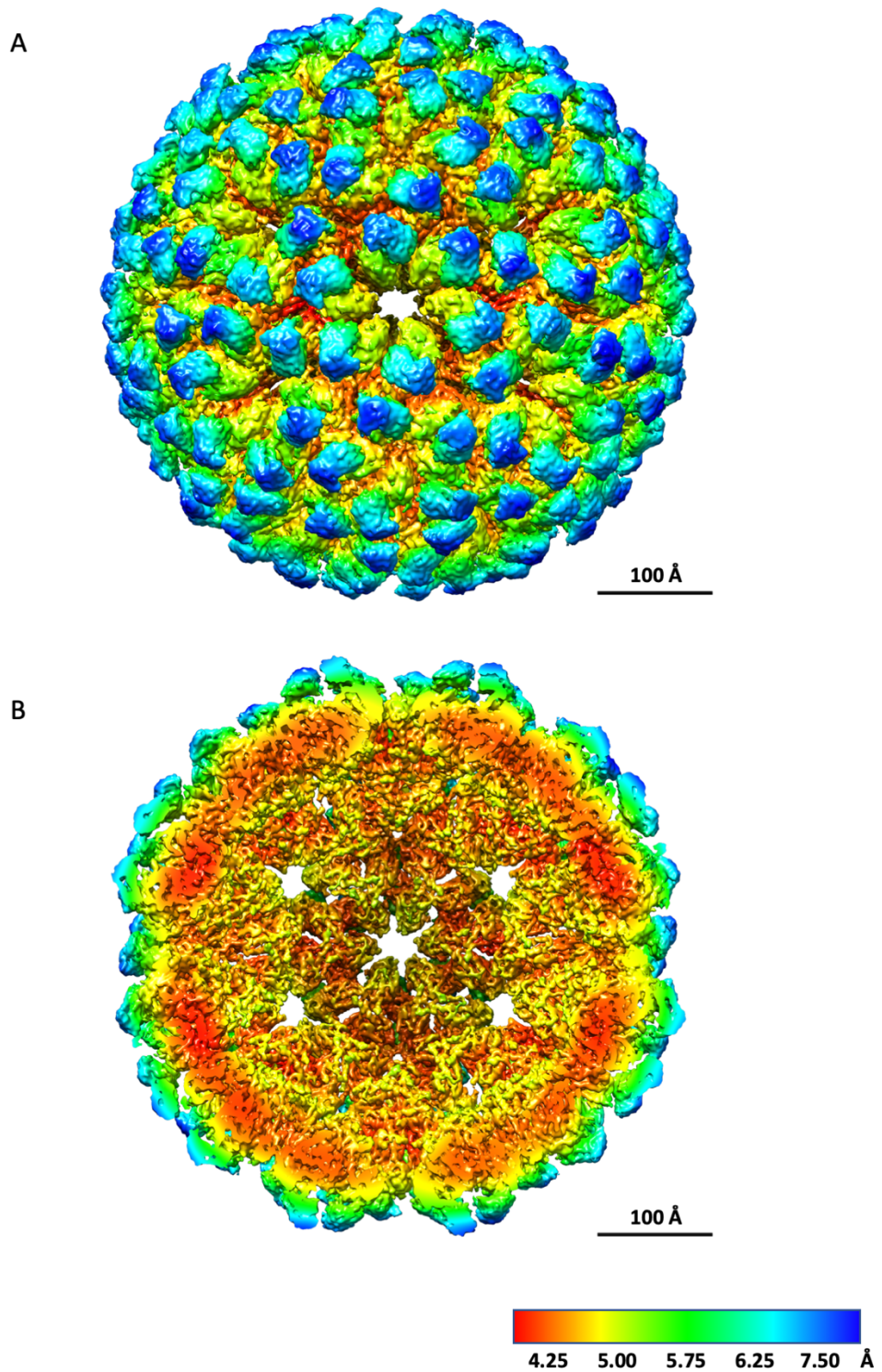


Figure 5.6 | 4.9 Å resolution structure of NwV procapsid VLP by cryo-EM. The 4.9 Å structure of NwV procapsid is shown in full (a) and as cross section. The structure is coloured by resolution following local resolution analysis from red (4.25 Å) to blue (7.50 Å) showing that the interior part of the particle was solved at higher resolution than the external Ig domains, which may be more flexible. The scale bar is 100 Å.

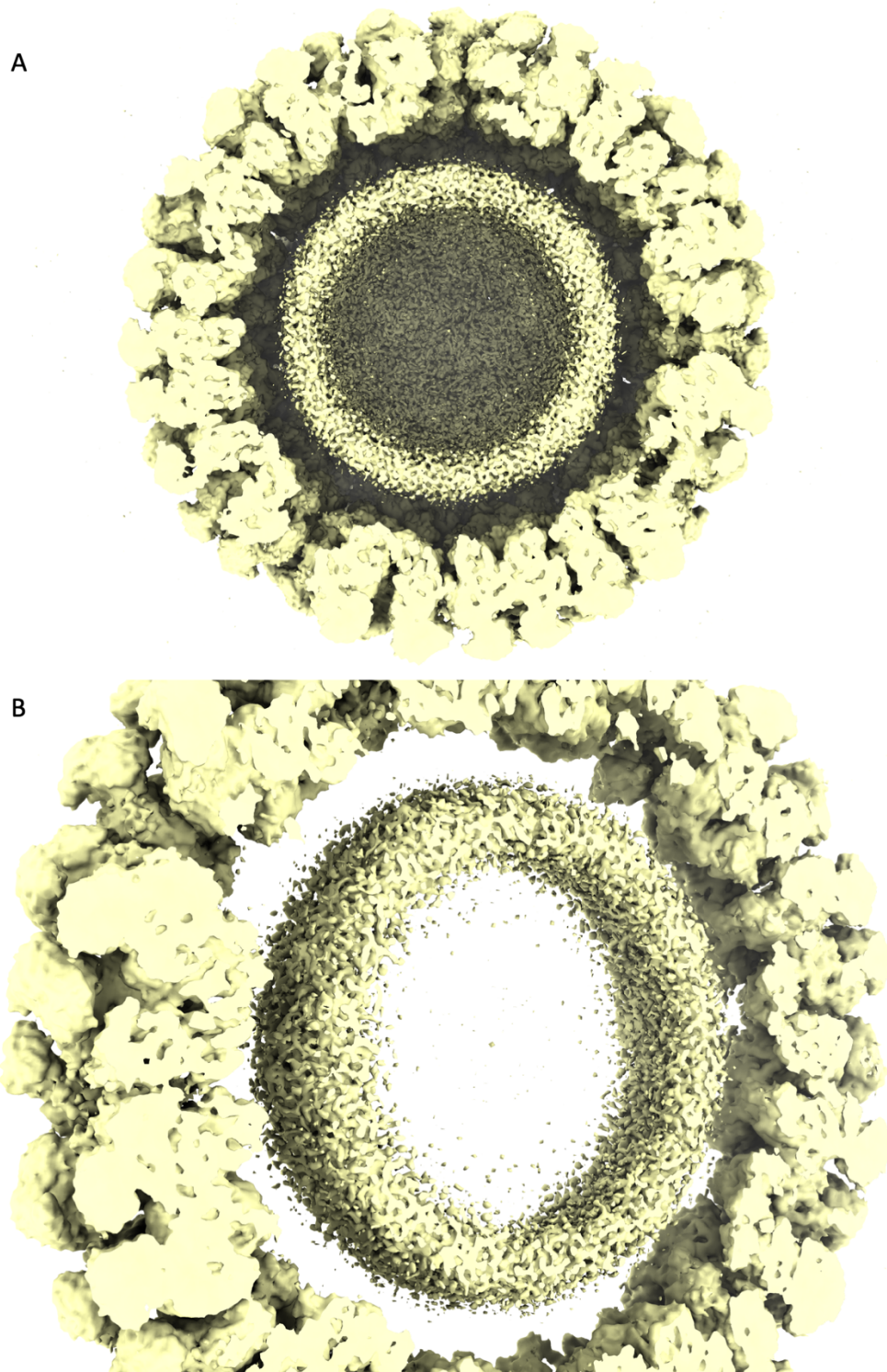


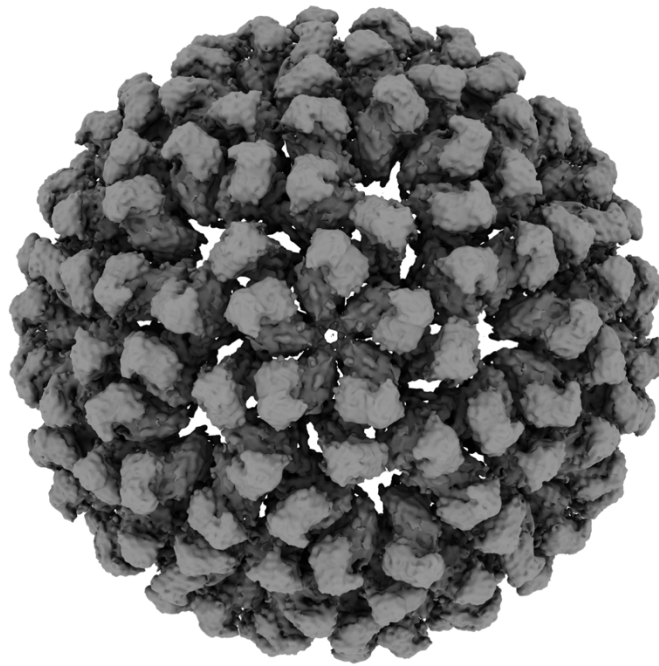
Figure 5.7 | Cryo-EM map of the N ω V procapsid displaying the protein and RNA shell densities. N ω V procapsid cross section view (a) and slice view (b) showing the protein density, outer shell, and the RNA density, inner ring. The RNA density does not show defined structure because this is cellular RNA, not genomic, required for assembly. Therefore, the particle packages many different sequences in multiple orientations that get blurred when averaged together by the reconstruction of the coat proteins.

From the cryo-EM structure of the procapsid it was possible to detect the presence of the packaged RNA, which is required for the assembly as the positive charge at the termini of the capsid protein needs the negative charged RNA to nucleate and start assembly. The RNA density was weaker than the protein, and did not show defined structure. The RNA packaged in N ω V VLPs produced in insect cells is cellular RNA from the host (Routh et al., 2012). Therefore, the particles package different RNA sequences in multiple orientations that get blurred by the reconstruction (Figure 5.7).

Additionally, different views of the structure revealed that it was very porous and that there were few surface contacts between the different subunits (Figure 5.8). The surface of the structure shows some degree of flexibility as it has lower resolution. The availability of a crystal structure for the capsid stage and the new model generated for capsid in the previous chapter, facilitated the interpretation of the map. The models for the subunits were built in the cryo-EM density map and refined in Coot (Figure 5.9). Applying icosahedral symmetry, it was then possible to build a model for the whole procapsid (Figure 5.10). The building of the model for the procapsid in the cryo-EM density map was done with the assistance of Prof. David Lawson, from the John Innes Centre. Additional details about the model building for the different cryo-EM maps are provided in Chapter 4.

With the models, it is possible to observe that the A, B, C and D subunits have a very similar fold (Figure 5.11), which is not the case for the mature capsid (see Chapter 4). In the capsid, the folds of the jellyroll and Ig domain are quite similar, however, the internal helical domains change dramatically. This suggests that initially all the subunits have the same conformation and then they acquire a different structure and specialize during the maturation process. This can be explained by the fact that as the pH decreases, the charge of the amino acids change. The electrostatic repulsion between the subunits, which is caused by the acidic residues, is reduced when the pH is lowered, as these residues become protonated and their negative charge is neutralized. The decrease in the electrostatic repulsion allows for the reduction in particle size and formation of the faceting expected for an icosahedral structure. These structural changes allow for formation of the cleavage site that is followed by the autocatalysis and the generation of the gamma peptide (Matsui et al., 2010a).

A



B

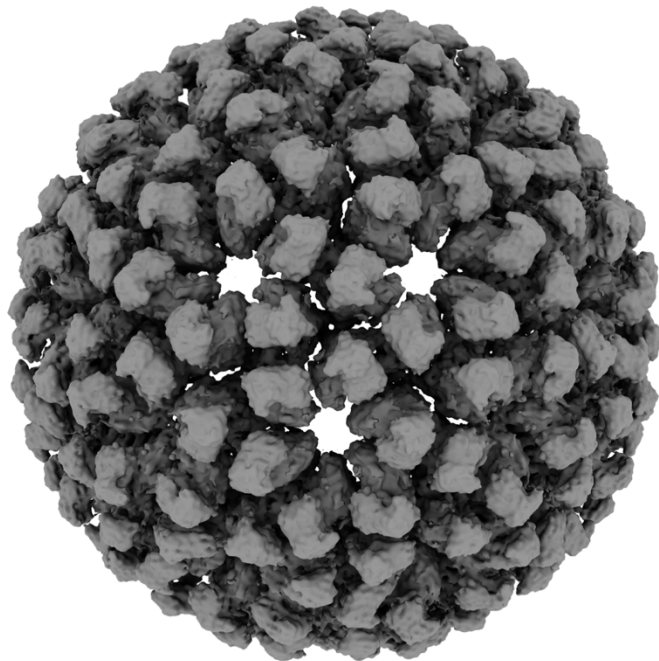


Figure 5.8 | Views of the N ω V procapsid cryo-EM structure to display the porosity of the particle. Different views looking at the 5-fold (a) and 3-fold (b) symmetry axis of the particle allow the identification of multiple pores located at the 6-axis.

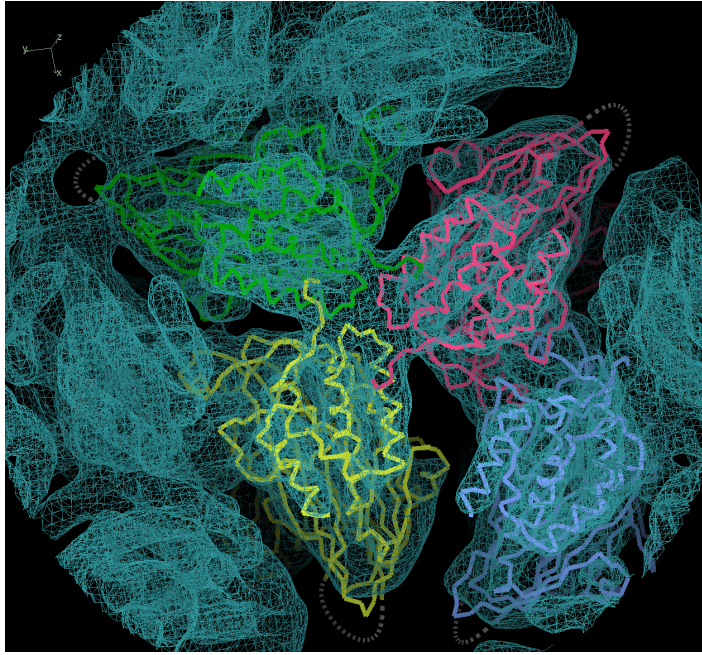


Figure 5.9 | Inside view of the cryo-EM density map of the N ω V procapsid VLP with a fitted model. Fitted chains in the cryo-EM map for subunits A (blue), B (red), C (green) and D (yellow). The internal helical domains of the subunits B, C and D are interacting and forming a trimer.

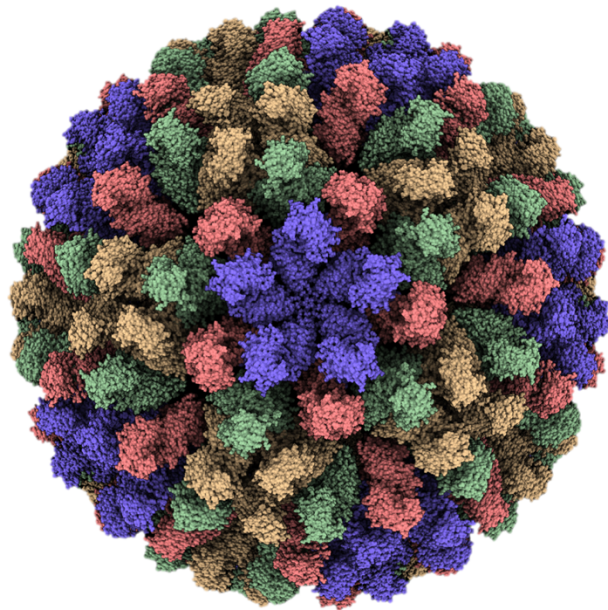


Figure 5.10 | Model generated from the fitted model in N ω V procapsid cryo-EM map. Model reconstruction using icosahedral symmetry (I1). Each one of the four subunits (A, B, C, D) that form the asymmetric unit are shown by the colour scheme.

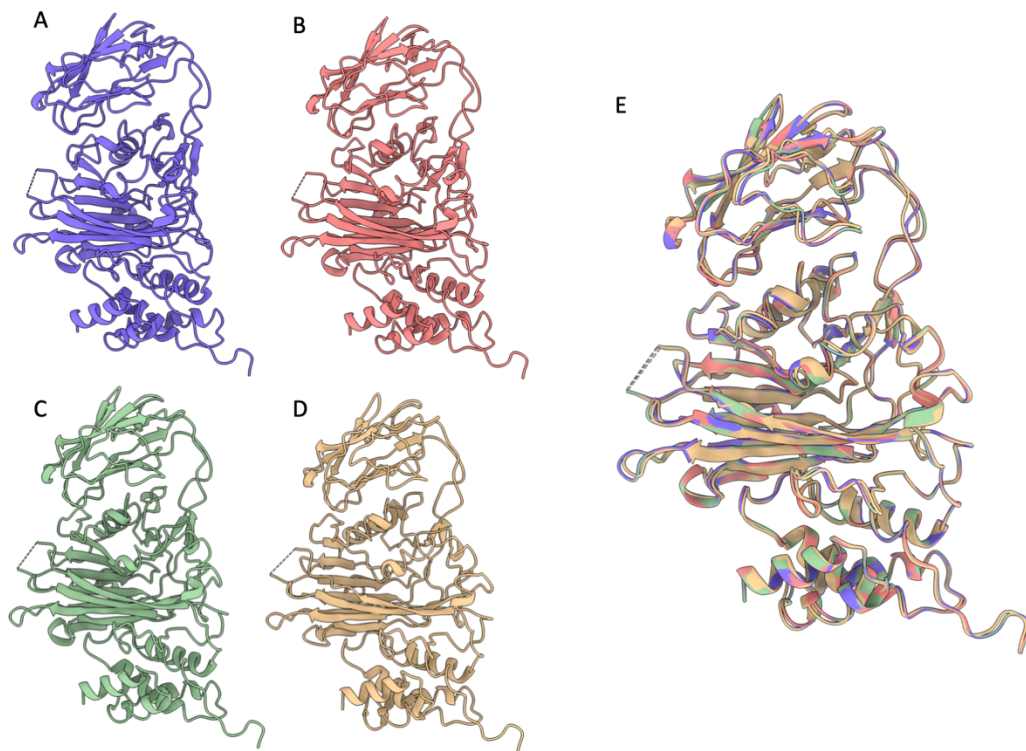


Figure 5.11 | Comparison of the structure from the subunits of N ω V procapsid. N ω V procapsid subunits (a-d) compared side-by-side and all four superimposed (e). The four subunits have a conserved structure and variations in the helical domains are indistinguishable.

In this section I have presented the highest resolution reported structure for the N ω V procapsid VLP (4.9 Å). This structure reveals key features and breaks new ground for the understanding of maturation driven by pH changes and associated electrostatics. A full analysis and comparison together with the other cryo-EM structures is provided in Chapter 6.

Summary of section 5.2.3: N ω V VLPs assemble into procapsids that can successfully be used for cryo-EM studies to produce high resolution structures. The cryo-EM structure of the N ω V procapsid revealed in this chapter has the highest resolution reported so far (4.9 Å) and allows resolution of key structural features such as the conservation of the same structure in the different subunits of the particle. This characteristic is totally different in the capsid, where the subunits specialise and achieve different conformations determined by their quaternary structure environments.

5.1.4. SAXS analysis to study the conformational changes of N ω V VLPs as a function of pH

Previous work (Matsui et al., 2010a) showed that the protonation of the acid interfaces of the N ω V subunits weakens the electrostatic repulsion between neighbouring subunits and triggers the compaction of the particle. This compaction happens through large conformational changes that end up with a size reduction of more than 50 Å in diameter between procapsid and mature particles. A broad range of different pH conditions was tested and it was found that the change in particle size is continuous overall. The mutant N ω V VLPs (described in Chapter 4), which are cleavage-defective, showed the same behaviour as the wild type for pH values between 7.6 and 6.0 (Matsui et al., 2010a). However, between pH values of 5.8 and 5.0 the mutant had a greater diameter compared with the wildtype, suggesting that the cleavage also contributes to the compaction of the particles (Matsui et al., 2010a). This previous research provided the groundwork to perform the experiments described in this section, which were essential in order to select the best conditions to study the structure of different N ω V intermediates by cryo-EM.

The SAXS experiments described in this chapter were performed by Tsutomu Matsui at the Stanford Synchrotron Radiation Lightsource (USA). In order to have exactly the same conditions for the cryo-electron microscopy experiments, I produced the N ω V VLPs and prepared the buffers for the experiments at the John Innes Centre and provided aliquots of them to T. Matsui to perform the SAXS experiments. After obtaining the SAXS results, I prepared the cryo-EM grids at the Astbury Centre, University of Leeds with Emma Hesketh. These cryo-EM grids (data presented in Chapter 6) were prepared using the same N ω V VLPs, buffers and conditions as used for the SAXS experiments. This combination was crucial in order to finely produce intermediates that sense variations in the environment.

To find the best conditions to isolate the intermediates a set of buffers between pH 7.6 to 5.0 were tested in the SAXS experiments. As maturation is time-dependent, two different time points were used (Figure 5.12). The scattering curves of the SAXS data from the N ω V VLPs incubate at different pHs (Figure 5.12), revealed that intermediate structures, of sizes smaller than procapsid but bigger than capsid, could be generated at pH values between 6.25 and 5.60. A close examination of the scattering curve (Figure 5.13) showed that there were three distinctive intermediates generated. The first intermediate was generated at pH 6.25, the second at either pH 6.00 or 5.90 and the third at either pH 5.75 or 5.60. This last one is further discussed in the following section, 5.1.5.

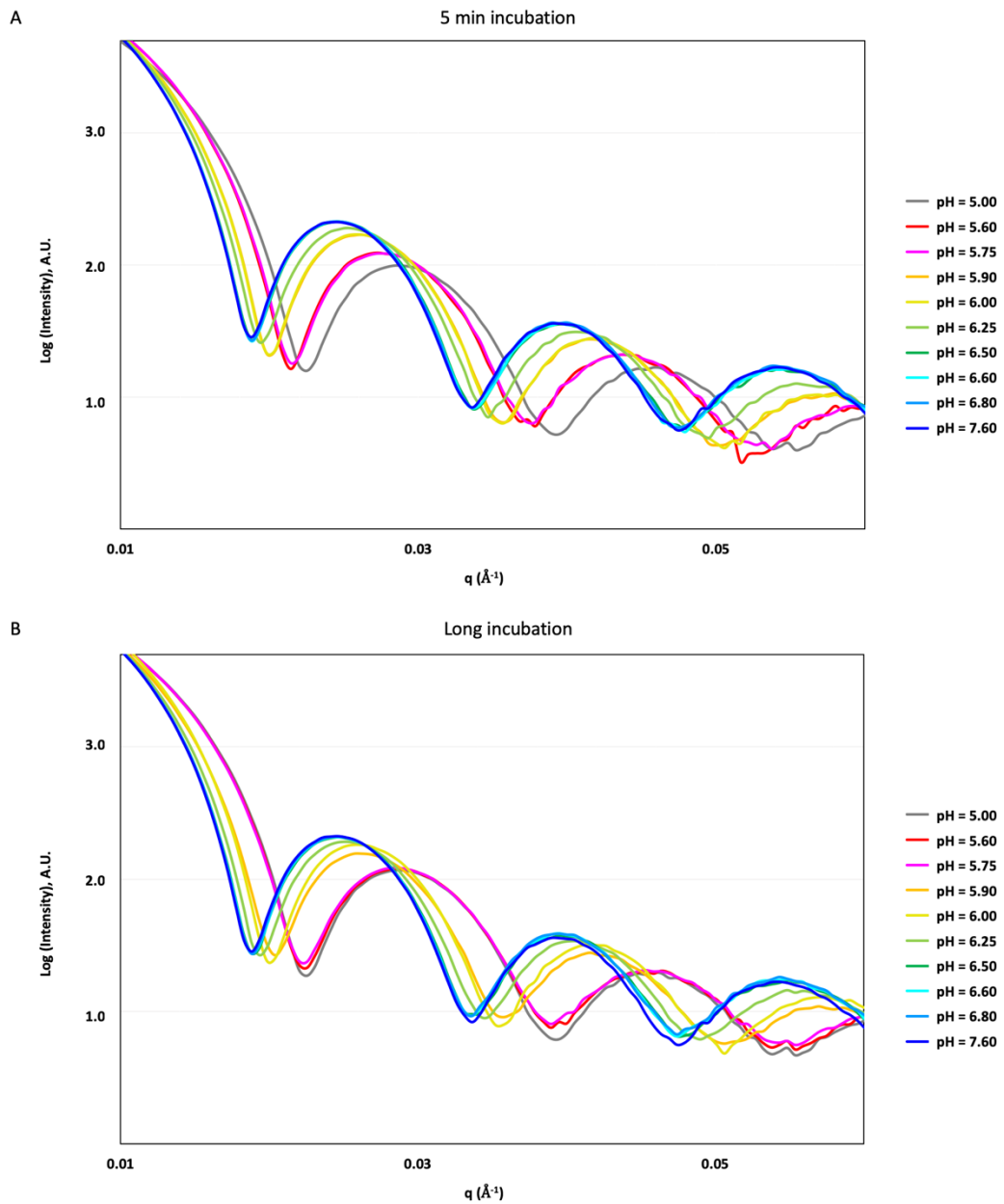


Figure 5.12 | Scattering curves of the SAXS data from NwV VLPs incubated at different pHs. The NwV VLPs were incubated at the intermediate pHs (pH 6.80 to pH 5.60) for 5 minutes (a) and for 7.5 to 9 hours (long incubation) (b); then they were analysed by SAXS. The SAXS profiles show that the particles form homogeneous populations of spherical structures, as expected for icosahedral VLPs. For some of the pH values there is a shift in the curves that corresponds to a reduction in size of the particles. The particles incubated at pH 6.80, 6.60 and 6.50 have the same profile as the procapsid, pH 7.6. This indicated that at these pHs there are no large conformational changes. In the scattering curve, the intensity (log scale) value is presented in the Y axis and the q (Å⁻¹), scattering angle value, in the X axis.

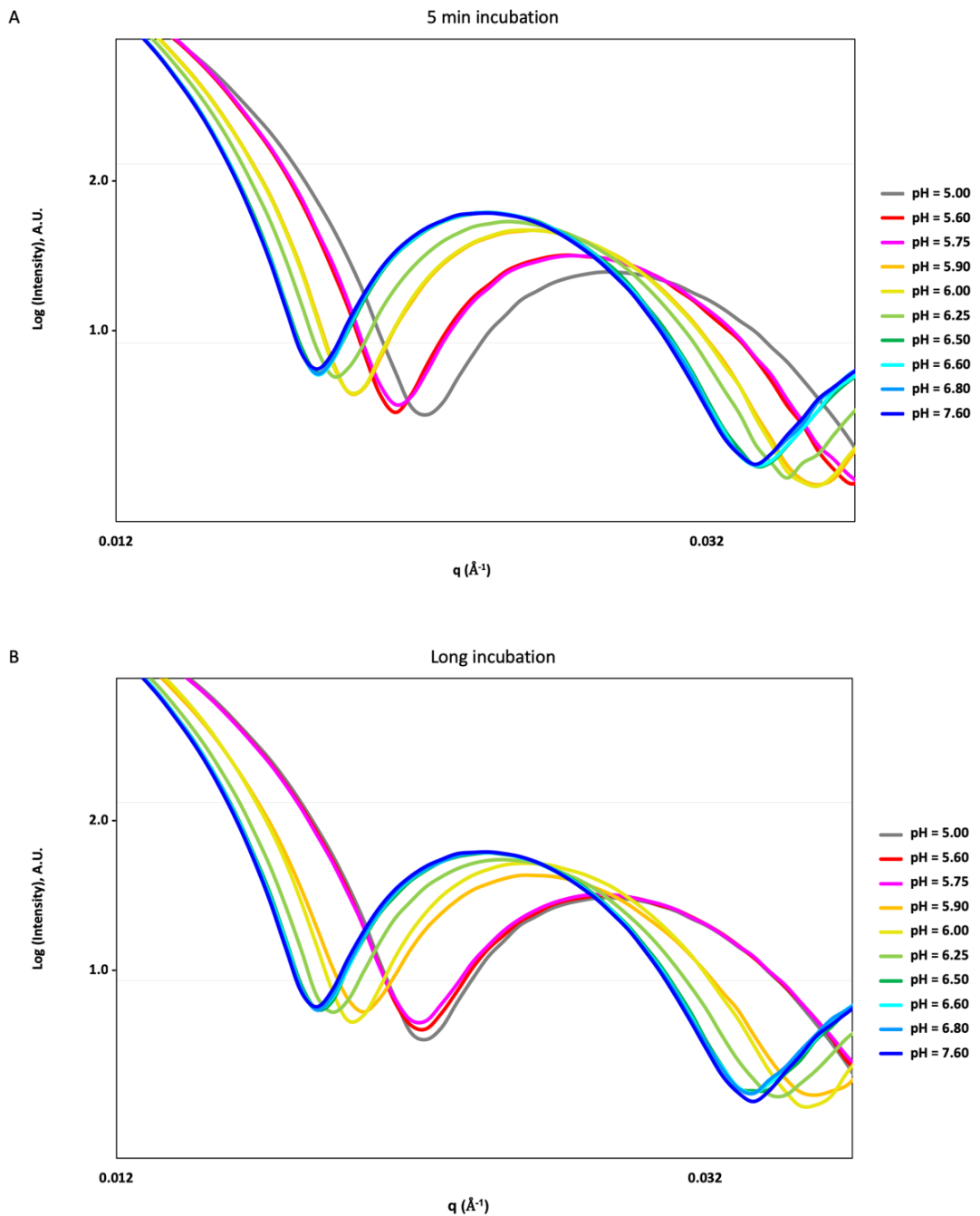


Figure 5.13 | Close view at the scattering curves of the SAXS data for NwV VLPs incubated at different pHs. The NwV VLPs were incubated at the intermediate pHs (pH 6.80 to pH 5.60) for 5 minutes (a) and for 7.5 to 9 hours (long incubation) (b); then they were analysed by SAXS. In this closer view of the scattering curve it is possible to determine that particles incubated at pH 6.25 form a population of a smaller diameter than procapsid, at pH 6.00 and 5.90 form a different population of smaller diameter than pH 6.25. These changes can be visualized with the shifts towards the right of the scattering curves. Incubation at pH 5.75 and 5.60 forms a population that changes size over time, this is discussed in detail in the following section 5.1.5. In the scattering curve the intensity (log scale) value is presented in the Y axis and the q (\AA^{-1}), scattering angle value, in the X axis.

5.1.5. The time-dependent pH 5.6 intermediate

The intermediates generated at pH 6.25, 6.00 and 5.90, had the same diameter at either short or long incubation at the particular pH. However, the particles incubated at pH 5.75 and 5.60 presented a shift in the scattering curves that was dependent on the incubation time. The diameter of the pH 5.60 intermediate particles, after a long-time incubation, was very similar to that of mature capsids, $\sim 410 \text{ \AA}$ (Figure 5.14). However, short incubations generated an intermediate that was $\sim 20 \text{ \AA}$ bigger in diameter than capsid (Figure 5.16). Therefore, for this intermediate it was necessary to have a short incubation before preparing the cryo-EM grids.

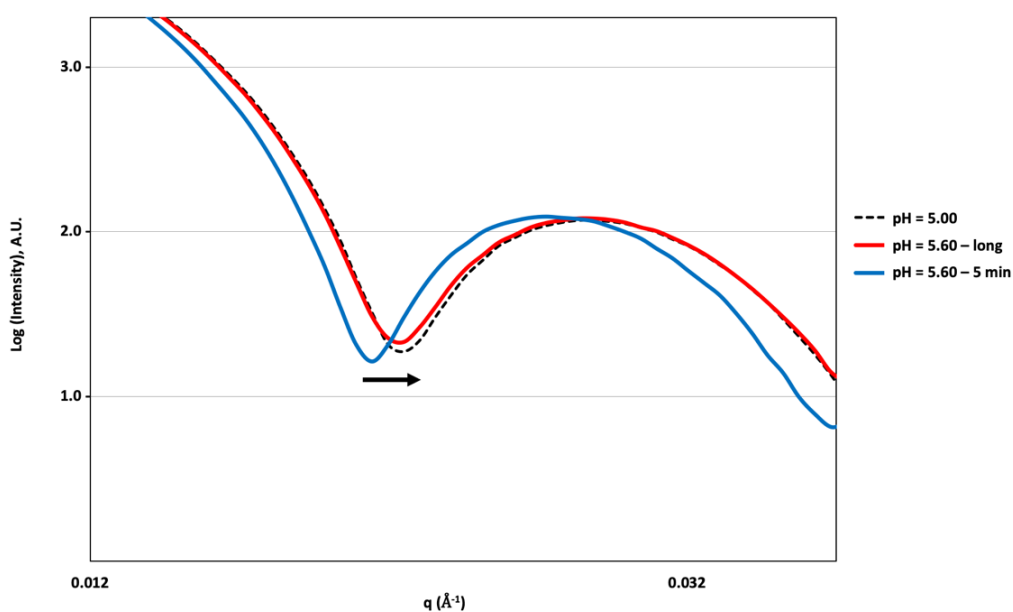


Figure 5.14 | Scattering curves of the SAXS data from NwV VLPs incubated at pH 5.60 for different times. Comparison of the scattering curve of the NwV VLPs incubated at pH 5.60 for short (5 minutes) and long times. There is a shift in the scattering curve and the particles incubated for a long time end up having a scattering curve that overlaps with the capsids. This suggested that the particles compacted to the capsid form if they were incubated at pH 5.6 for a long time. Therefore, to be able to isolate the intermediate at this pH, the incubation should be short, 5 minutes. In the scattering curve, the intensity (log scale) value is presented in the Y axis and the $q (\text{\AA}^{-1})$, scattering angle value, in the X axis.

5.1.6. The conditions for the intermediates to perform the cryo-EM studies

Overall, three different conditions were selected to study the N ω V intermediates. To obtain the first intermediate after starting the compaction of the procapsids (blue curve in Figure 5.16), the particles had to be incubated at pH 6.25 (green curve in Figure 5.15). The expected diameter of this intermediate was ~ 470 Å (Figure 5.16). To further compact the particles, the pH had to be reduced to pH 5.9 (orange curve in Figure 5.15). The expected size for this intermediate was ~ 450 Å (Figure 5.16) For both of these pH conditions, a long incubation was used to allow the particles to stabilize and increase the homogeneity of the population. On the other hand, for pH 5.6 (red curve in Figure 5.15), the incubation had to be short to generate an intermediate of ~ 435 Å, otherwise, the particles would compact to ~ 410 Å.

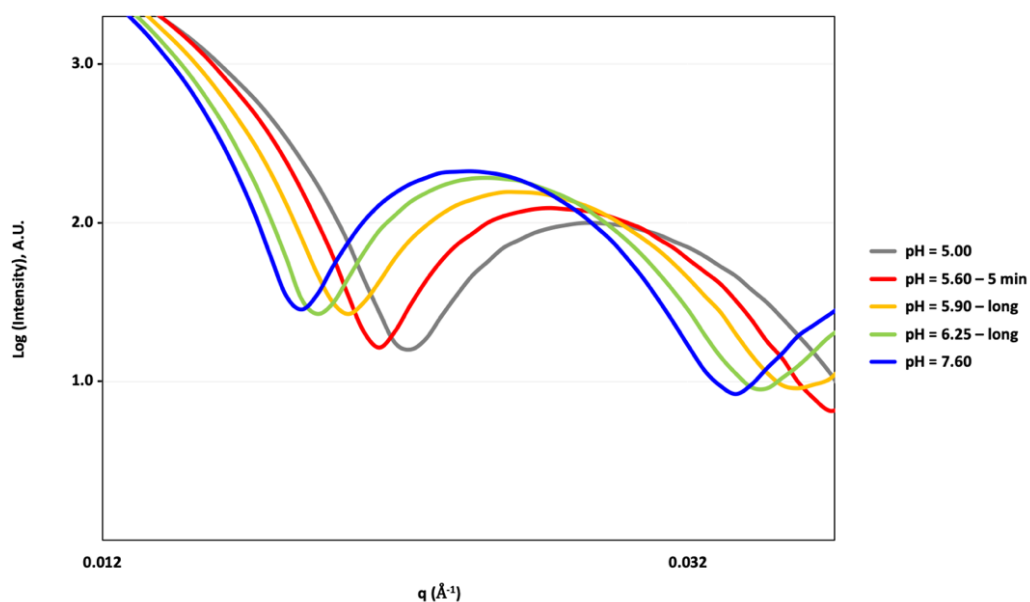


Figure 5.15 | Scattering curves of the SAXS data from the intermediates of N ω V VLPs. The SAXS results suggest that it is possible to obtain intermediates in the maturation process of N ω V. With these experiments it has been possible to pinpoint the best combination of conditions to be used in the cryo-EM analysis. In this figure are represented the results for the pH conditions to generate the intermediate to be analysed in cryo-EM (pH 5.60, 5.90 and 6.25). In the scattering curve, the intensity (log scale) value is presented in the Y axis and the q (\AA^{-1}), scattering angle value, in the X axis.

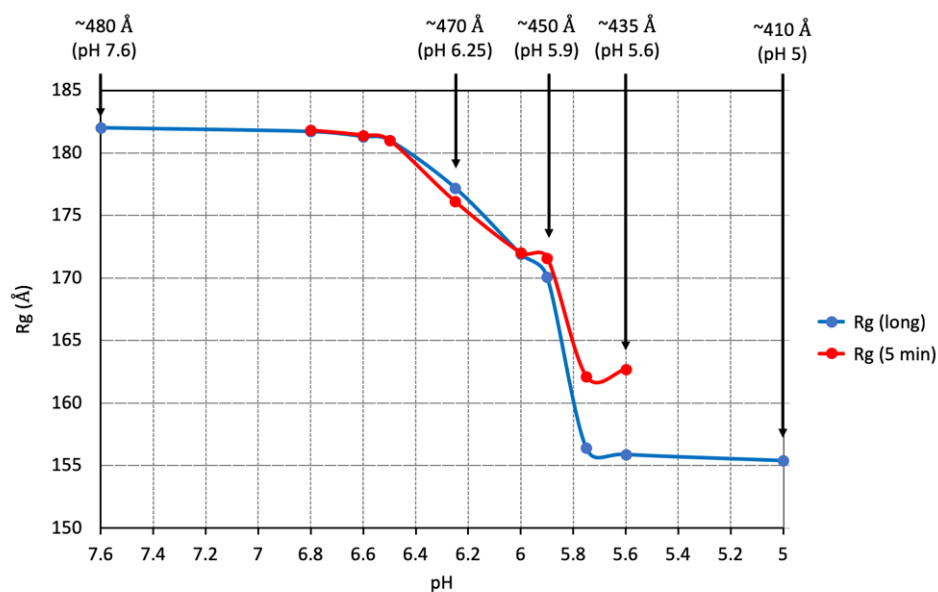


Figure 5.16 | Representation of the calculated diameters, from the SAXS data, for the N ω V VLPs at different pHs. In this plot the diameter of the particles, at each pH, for the long and short incubations, is compared. When the pH is between 7.6 and 5.9, the diameter of the particles remains constant over time. However, for pH 5.75 and 5.60, the diameter changes over time. The structures that are studied by cryo-EM in this thesis, to make the maturation movie of N ω V, are indicated with arrows.

5.3. Discussion

In this chapter I explored the use of insect cells to produce N ω V VLPs for structural biology analysis, including SAXS and cryo-EM. The presented work demonstrates that it is possible to obtain a cryo-EM structure for the N ω V procapsid at high enough resolution (4.9 Å) to reveal some features of the secondary structure from the N ω V subunits. The procapsid subunits (A, B, C, D) have a very similar tertiary structure. This was a striking result as the capsid subunits show major differences in the helical domain (see Chapter 4). These results agreed with the hypothesis that initially all the subunits have the same structure, as they have the same sequence. Then, the large conformational changes of the maturation process allow for specialization of the different subunits and their local environment induces changes in their structure. This is a major finding as it allows us to know the original arrangement of the subunits and to track the changes in the structure that are necessary to allow the maturation and start of the autoproteolysis.

Furthermore, using SAXS, the conditions for the isolation of homogeneous populations of the N ω V intermediates have been established. In the following chapter the structures of the three intermediates that were selected for the cryo-EM analysis are described. These structures finally allowed me to generate the first high-resolution movie of the process of N ω V maturation (see Chapter 6).

Chapter 6

N ω V, “the movie”

6.1. Introduction

The overall aim of this thesis was to elucidate the details of the maturation process of N ω V to near-atomic resolution by cryo-EM. In the previous chapters I have presented high resolution cryo-EM structures of the procapsid and the capsid, the initial and final structures of the maturation process. In this chapter I present the structures of six intermediates in the maturation process of N ω V, also revealed by cryo-EM. The conditions used for each of the stages were established in the previous chapter using SAXS. Furthermore, I compare the different structures and generate a model from them to explain the maturation process of N ω V and the large conformational changes involved in this complex process. At the end of this chapter, the structural data are combined to generate the “N ω V movie”. This movie is based on the high-resolution structures of the whole process of maturation and it reveals unique details of the programme contained within the structure of this extraordinary virus. Finally, this movie reveals how a single type of building block, the coat protein, is able to associate, change conformation and specialize to form N ω V particles, sophisticatedly programmed nanomachines.

6.2. Results

6.2.1. Cryo-EM structure of N ω V intermediate (pH 6.25): the initial stage of compaction

In Chapter 5 I presented the structure of the procapsid (pH 7.6) from insect cell-produced N ω V VLPs. The procapsid is the initial assembly complex and the starting point for the maturation process. I wished to understand how this initial assembly product was able to transition to more compact and robust structures during maturation. The SAXS results that I presented in the previous chapter provided information about the conditions necessary to generate the different intermediates of the maturation process. Those results suggested that the first intermediate in the maturation process that involved a conformation change was generated at pH 6.25. In this section I analyse the structure of this intermediate by cryo-EM.

To prepare the grids, N ω V procapsid VLPs, produced in insect cells, that had been stored in 10 mM Tris, 250 mM NaCl, pH 7.6 were mixed at a 1:1 ratio with 100 mM MES, 250 mM NaCl, pH 6.25 buffer. I prepared the mixture at room temperature and incubated it for 6 to 7 hours before the freezing step to allow for time for stabilization of the particles in the new conditions. The grids were prepared at room temperature to replicate the same conditions used for the SAXS experiments and then were frozen rapidly in liquid ethane to generate the vitreous ice.

The grid preparation (see Chapter 2 for details) was done with the assistance of Dr. Emma Hesketh, from the University of Leeds, who then set up the data collection using a FEI Titan Krios microscope with a Falcon III detector, with a final object sampling of 1.065 Å/pixel and a total dose of 50.4 e/Å². The dose was fractioned across 39 frames during a 1 s exposure (Figure 6.1).

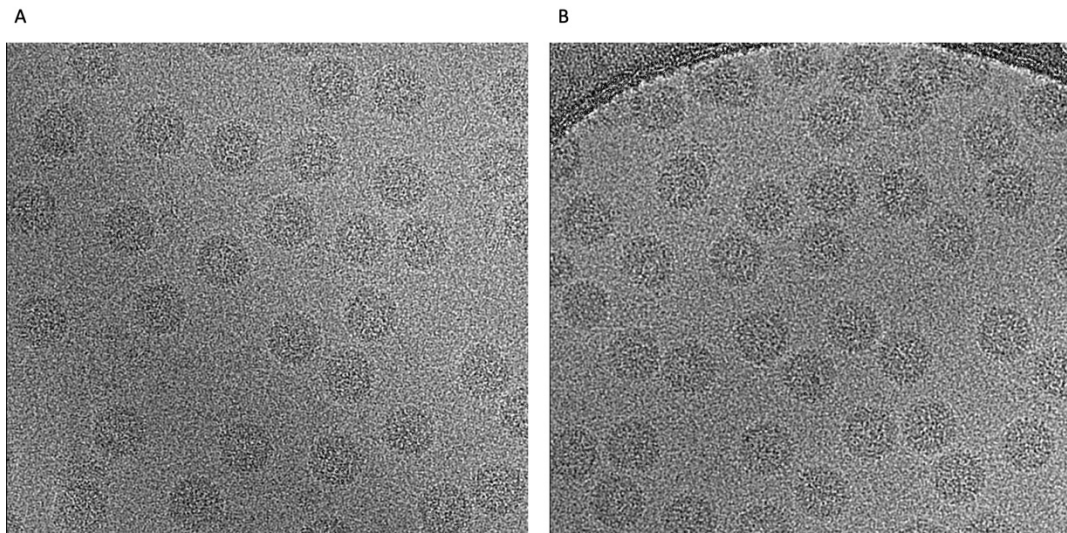


Figure 6.1 | Cryo-EM micrographs of N ω V VLPs at pH 6.25. Different views of the cryo-EM grid (a, b). The particles are well spread and they look intact and homogeneous. Data acquisition: FEI Titan Krios EM (300 kV) with a Falcon III camera. The data was acquired at 1.065 Å/pixel with a dose of 50.4 e/Å².

The cryo-EM data was processed using the Relion 3.0 pipeline (Scheres, 2012; Zivanov et al., 2018), described in Chapter 2, 4 and 5. Briefly, the initial picking of the particles was done with the Laplacian function and the picked particles were used to generate 2D classes to use as references to pick the particles from all the micrographs automatically. These automatically picked particles were then subject to several rounds of reference-free 2D classification using 50 classes over 25 iterations (Figure 6.2). This allowed particles erroneously picked during the automated particle picking to be removed and also to separate damaged particles. The 2D class averages allowed for the selection of 114,963 particles to take forward for the 3D structure determination.

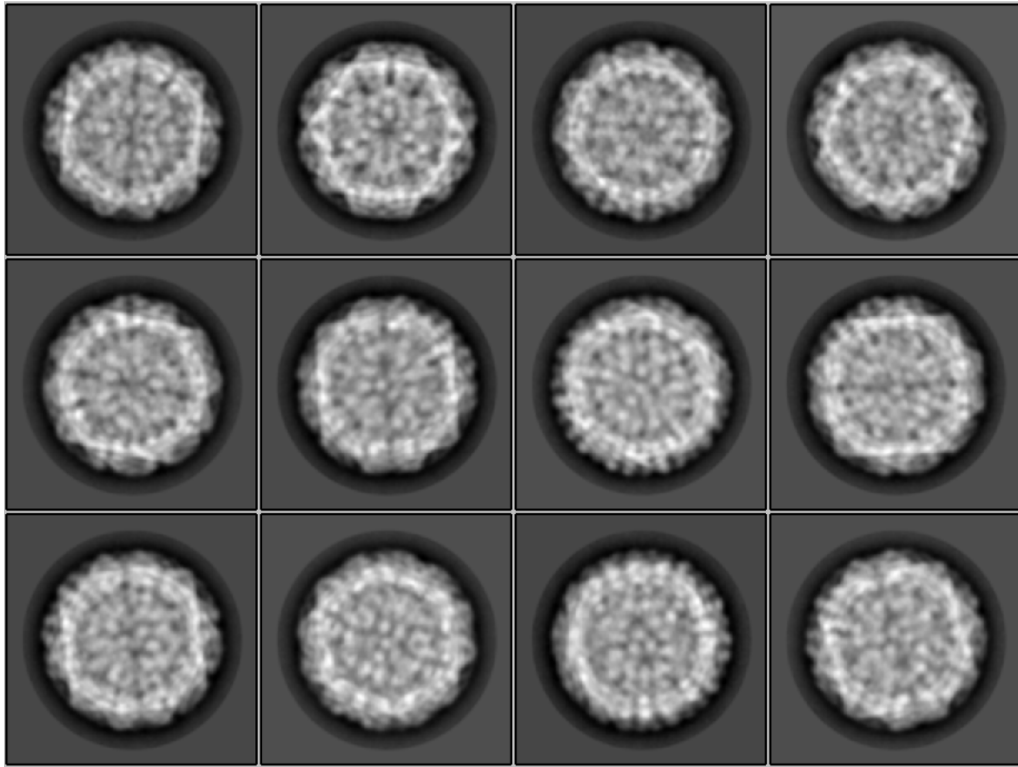


Figure 6.2 | Representative 2D classes averages of N ω V VLPs at pH 6.25. The 2D classes show different views of the N ω V VLPs and it is possible to see that it has a porous structure, as it was observed for the procapsids. Several rounds of 2D classification allowed the removal of disassembled and aberrant particles.

To further classify the particles and assess the dataset heterogeneity, I used unsupervised 3D classification with icosahedral symmetry (I1) imposed, splitting the particles into 6 classes (Figure 6.3). Three of the generated 3D structures, in total 84,649 particles, converged to a similar resolution and these were selected for further refinement. The high-resolution 3D structure refinement converged after 20 iterations. The final resolution was determined to be 4.8 Å, according to the ‘gold standard’ Fourier shell correlation criterion (FSC = 0.143) (Scheres and Chen, 2012). Local resolution estimation was performed using RELION (Fernandez-Leiro and Scheres, 2017; Scheres, 2012) and showed that some areas of the structure, mainly on the inside of the particle, had a resolution of nearly 4.25 Å (Figure 6.4).

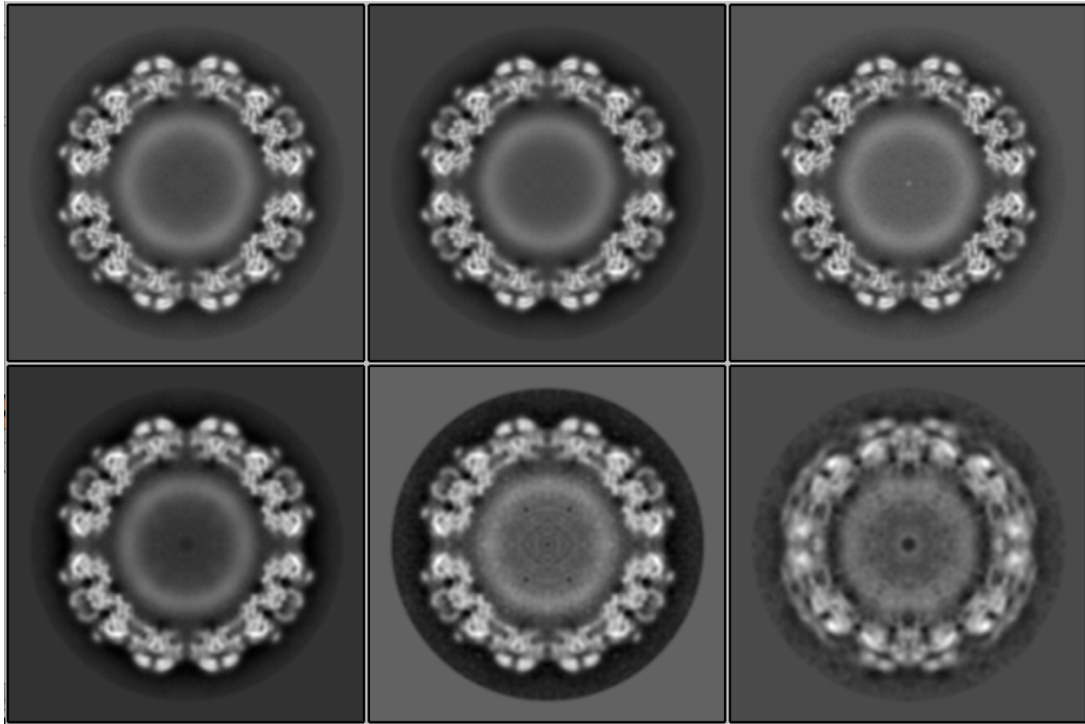


Figure 6.3 | 3D classes from the of N ω V VLPs at pH 6.25. The 3D classification allowed separation of different classes and the three best (top row), showing better structural features, were selected for the following refinement steps.

Overall, the pH 6.25 cryo-EM structure (Figure 6.4) resembled the structure of the procapsid presented in the previous chapter. One of the main differences is the reduction of ~ 10 Å in the diameter of the particle compared with the procapsid.

Summary of section 6.2.1: At pH 6.25 it is possible to obtain one population of particles with a diameter of 470 Å that, after the processing, provided a cryo-EM structure at 4.8 Å resolution. This represents the first intermediate in the maturation process of N ω V. The overall features of this intermediate structure are very similar to the procapsid, with a porous structure. The reduction in size can be attributed to changes in the electrostatic interactions between the subunits influenced by the reduction in pH.

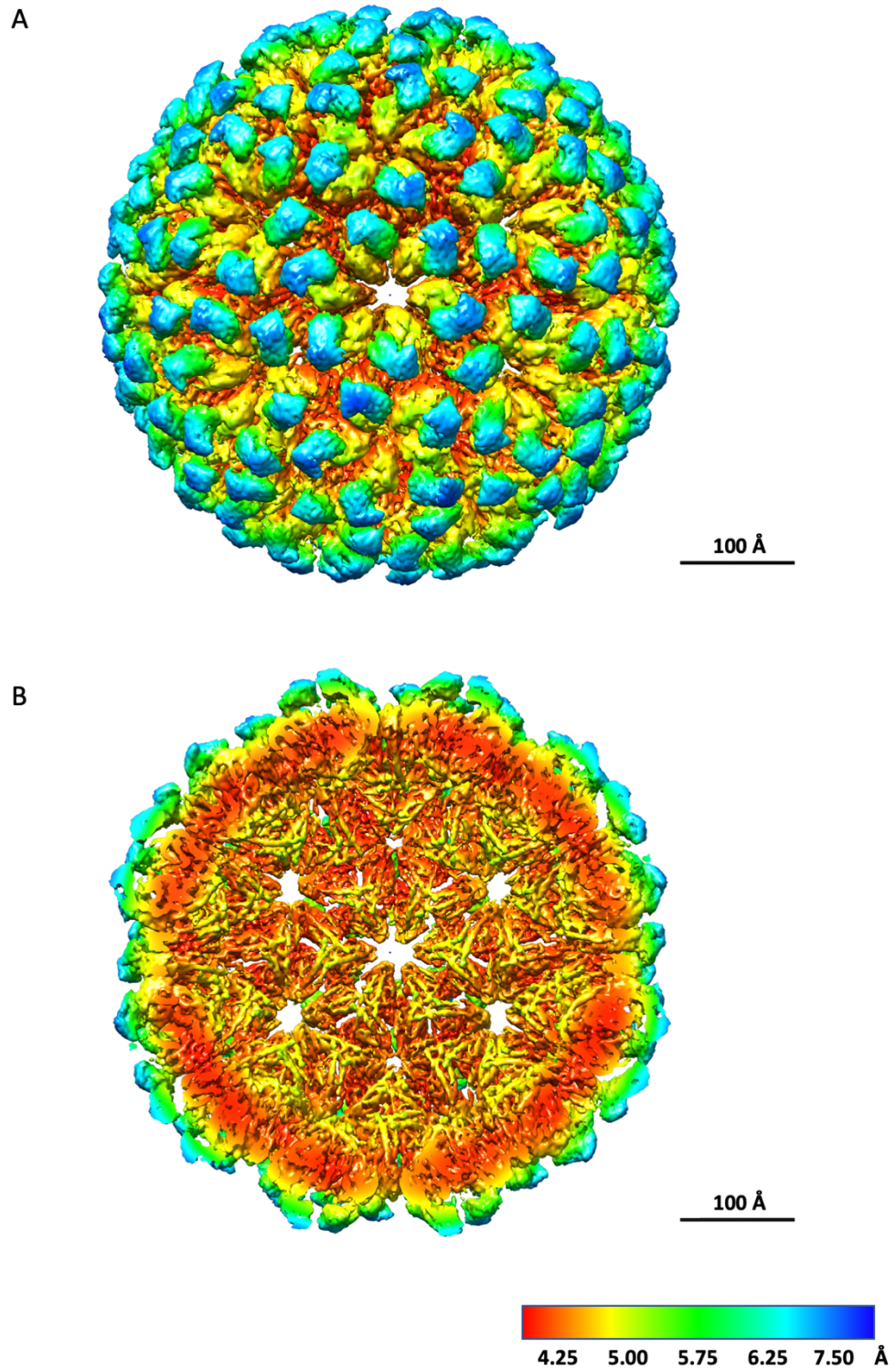


Figure 6.4 | 4.8 Å resolution structure of N ω V intermediate (pH 6.25) by cryo-EM. The 4.8 Å structure of N ω V is shown in full (a) and as cross section (b). The structure is coloured by resolution following local resolution analysis from red (4.25 Å) to blue (7.50 Å). The interior part of the particle was solved at higher resolution than the external Ig domains, in a similar way as with the procapsid structure. The scale bar is 100 Å.

6.2.2. Cryo-EM structure of N ω V intermediate (pH 5.9): half-way in the maturation

The SAXS results, presented in the previous chapter, suggested that the second distinctive intermediate in the maturation process was generated when the particles were incubated at pH 5.9. The estimated diameter of this intermediate, from SAXS analysis, was of 460 Å.

To prepare the grids, N ω V procapsid VLPs, produced in insect cells, that had been stored in 10 mM Tris, 250 NaCl mM, pH 7.6 were mixed at a 1:1 ratio with 100 mM MES, 250 mM NaCl, pH 5.9 buffer. In the same way as for the pH 6.25 sample, the mixture was incubated at room temperature for 6 to 7 hours before freezing the sample on the grid to allow time for stabilization of the particles in the new conditions.

The grid preparation (see Chapter 2 for details) was done with the assistance of Dr. Emma Hesketh, from the University of Leeds, who then set up the data collection using a FEI Titan Krios microscope with a Falcon III detector, with a final object sampling of 1.065 Å/pixel and a total dose of 46 e/Å². The dose was fractionated across 39 frames during a 1 s exposure (Figure 6.5).

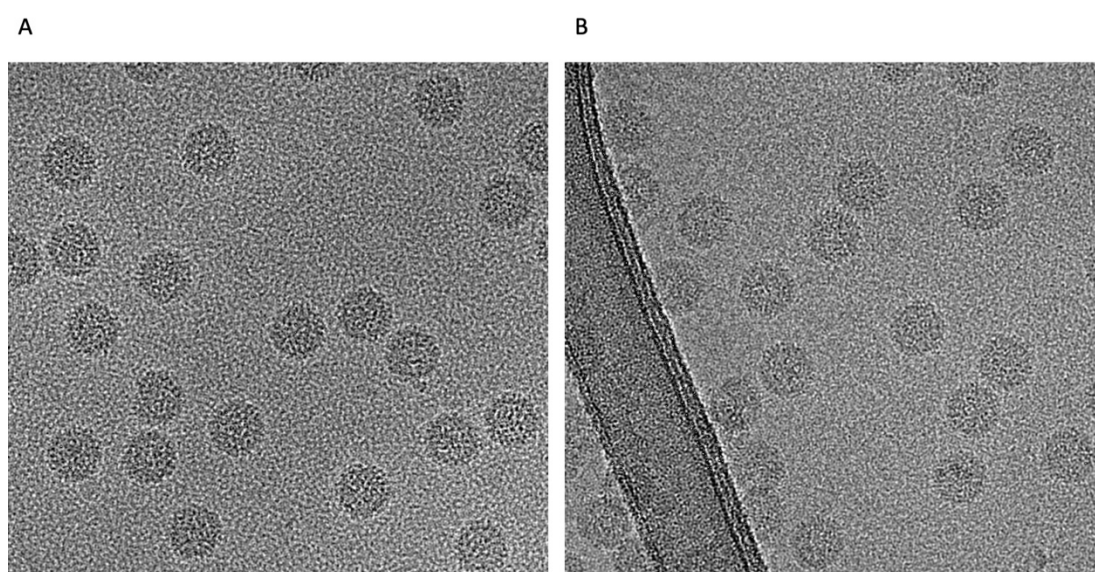


Figure 6.5 | Cryo-EM micrographs of N ω V VLPs at pH 5.9. Different views of the cryo-EM grid (a, b). The particles are well distributed in the vitreous ice and they look intact. The particles stick and aggregate usually in the regions where there is carbon (b). Data acquisition: FEI Titan Krios EM with a Falcon III camera, operating at 300 kV. The data was acquired at 1.065 Å/pixel with a dose of 46 e/Å².

The cryo-EM data was processed using the Relion 3.0 pipeline (Scheres, 2012; Zivanov et al., 2018), described in Chapter 2, 4 and 5. Briefly, the particles were automatically picked by using 2D classes as references. These references were generated from particles initially picked using the Laplacian function from RELION. The automatically picked particles were then subject to several rounds of reference-free 2D classification into 50-100 classes over 25 iterations (Figure 6.6). This allowed removal of particles erroneously picked during the automated particle picking and also to the separation of damaged particles. The 2D class averages allowed for the selection of 80,320 particles to take forward for the 3D structure determination.

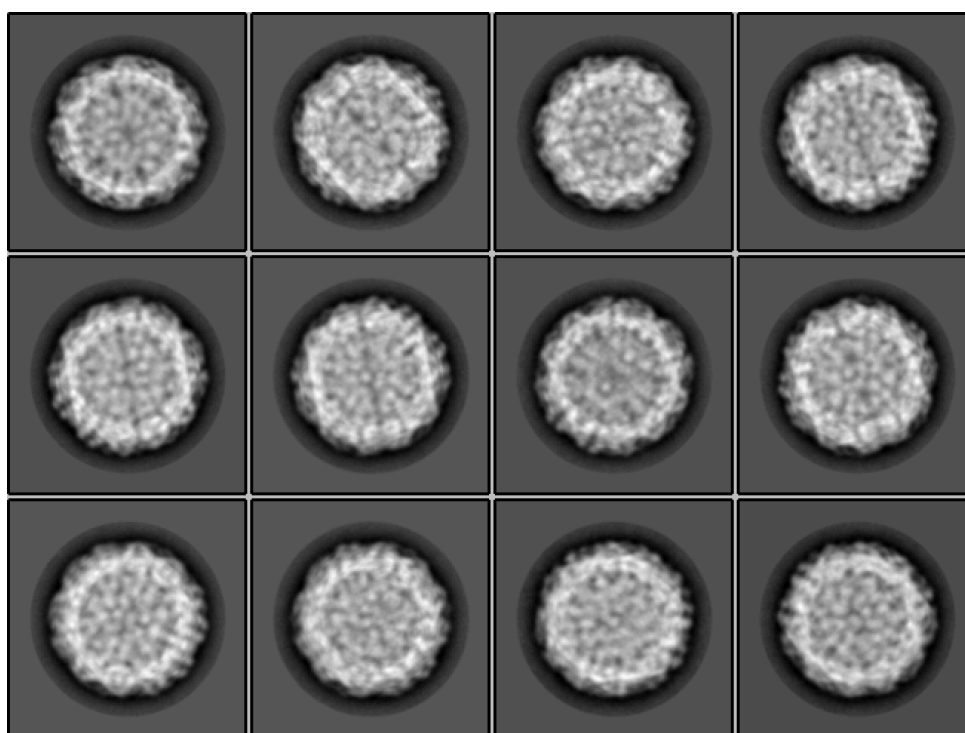


Figure 6.6 | Representative 2D classes averages of N ω V VLPs at pH 5.9. Multiple rounds of 2D classification allowed for the selection of 80,320 particles that were used for the following steps of 3D classification.

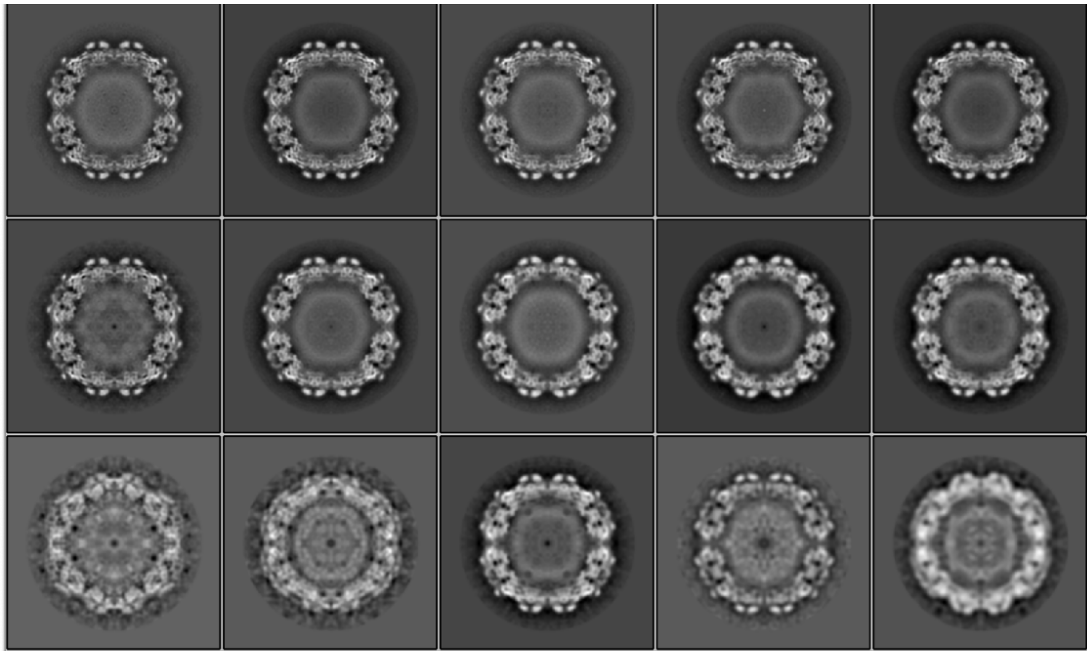


Figure 6.7 | 3D classes from the pH 5.9 dataset. The 3D classification shows that there is heterogeneity within the selected particles and allowed for their separation in multiple populations. Those with higher resolutions were selected and used for the refinement steps. Only half of the particles initially selected from the 2D classification were used for the final reconstruction (38,792 particles).

To further classify the particles and assess the dataset heterogeneity, I used unsupervised 3D classification with several rounds of icosahedral (I1) symmetry imposed (Figure 6.7). Further ‘clean-up’ was done by alignment-free 3D classification. For the high-resolution 3D structure refinement, 38,792 particles were used. The refinement converged after 26 iterations and the final resolution was determined to be 4.39 Å. The particles processed in this dataset were the sum of the 39 movie frames collected for each micrograph. Particles may move during the exposure to the electron beam from the microscope when the data is collected. It is possible to look at individual frames and correct the effect of particle movements between each frame, also known as particle polishing. Therefore, RELION’s particle polishing algorithm and CTF refinement (Zivanov et al., 2018) were used for all the particles used for the refinement. Then the particles were re-refined and the map improved to be 3.9 Å, according to the ‘gold standard’ Fourier shell correlation criterion (FSC = 0.143) (Scheres and Chen, 2012). The local resolution estimation tool in RELION was used to generate maps filtered by local resolution (Fernandez-Leiro and Scheres, 2017; Scheres, 2012). Some areas of the structure, mainly on the inside of the particle, had a resolution of nearly 3.5 Å (Figure 6.8).

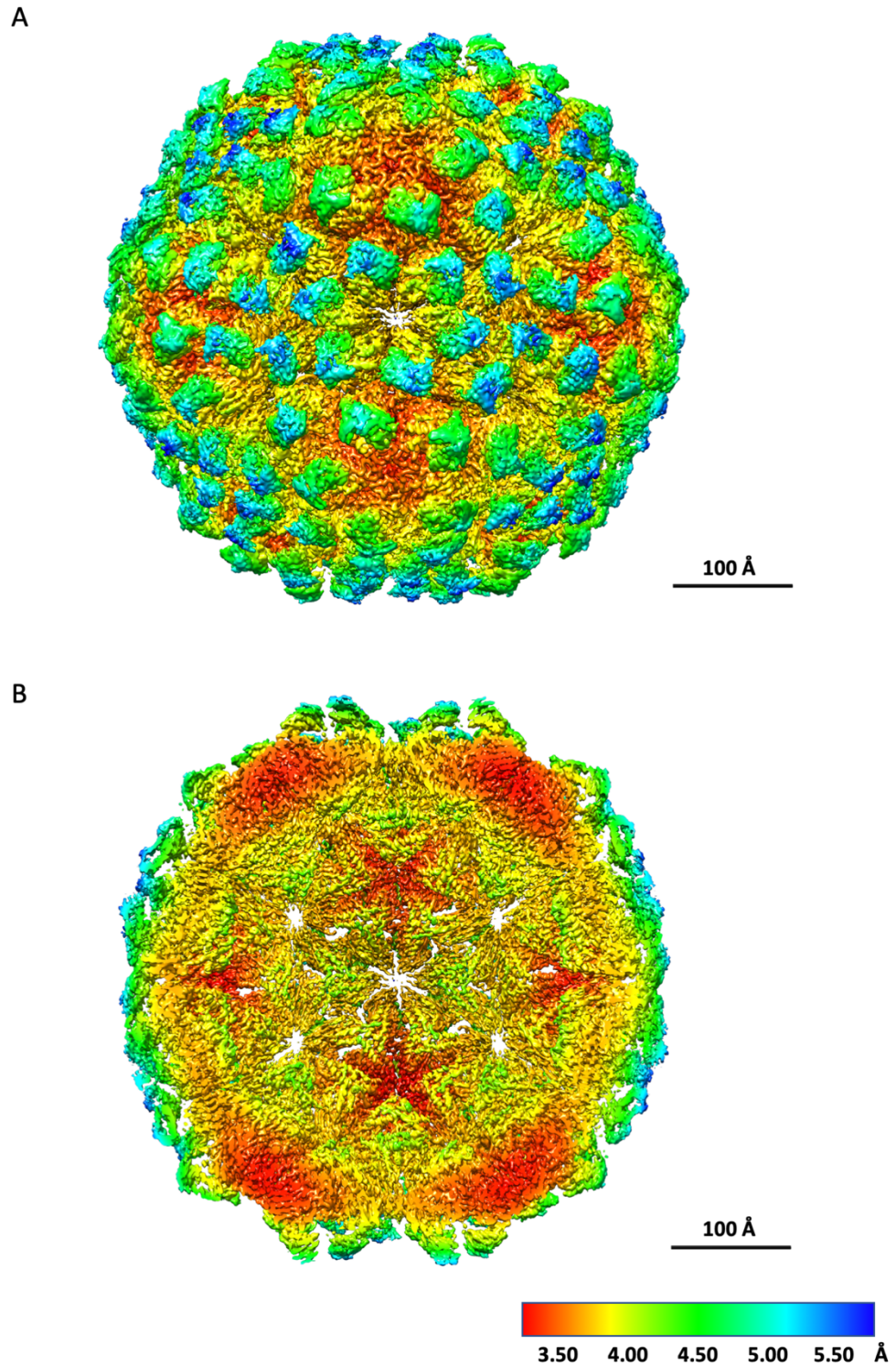


Figure 6.8 | 3.9 Å resolution structure of N ω V intermediate (pH 5.9) by cryo-EM. The 3.9 Å structure of N ω V is shown in full (a) and as cross section (b). The structure is coloured by resolution following local resolution analysis from red (3.50 Å) to blue (5.50 Å). The interior part of the 5-fold axis was solved at higher resolution than the external domains and the areas in the 6-fold axis. The scale bar is 100 Å.

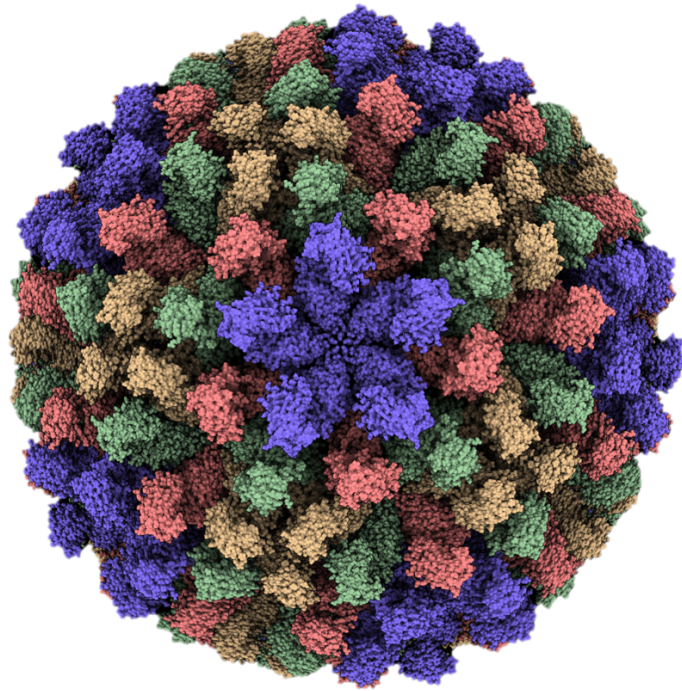


Figure 6.9 | Surface representation generated from the fitted model in the N ω V intermediate (pH 5.9) cryo-EM map. Model reconstruction of N ω V intermediate (pH 5.9) using icosahedral symmetry (I1). Each one of the four subunits that form the asymmetric unit are shown by the colour scheme.

The pH 5.9 cryo-EM structure (Figure 6.8) showed some of the features of the procapsid (Chapter 5) and the intermediate at pH 6.25, presented in the previous section, such as the pores in the shell and high exposure of the Ig domains. One of the main differences was the reduction of ~ 20 Å in the diameter of the particle, when compared with the procapsid. The higher resolution of this structure (3.9 Å), made it suitable for building a model in the cryo-EM density map, which was refined in Coot (Emsley and Cowtan, 2004). Applying icosahedral symmetry, it was then possible to build a model for the whole intermediate particle (Figure 6.9). The building of the model for the intermediate in the cryo-EM density map was done with the assistance of David Lawson. Additional details about the model building for the different cryo-EM maps are provided in Chapter 4. With this model, it is possible to observe that the structure of the jellyroll and Ig domain is conserved between the quasi-equivalent subunits. However, the internal helical domains, from N and C termini, show differences in their fold, especially in subunit A (Figure 6.10). The electrostatic repulsion between the subunits, which is caused by the acidic residues, is reduced when the pH is lowered and allows for the reduction in particle size and changes in the fold of the subunits. This intermediate

reveals the start of the structure differentiation and specialization that occurs during the maturation process. A comparison of the structure of the helical domains between different stages in the maturation process is presented in detail in this chapter.

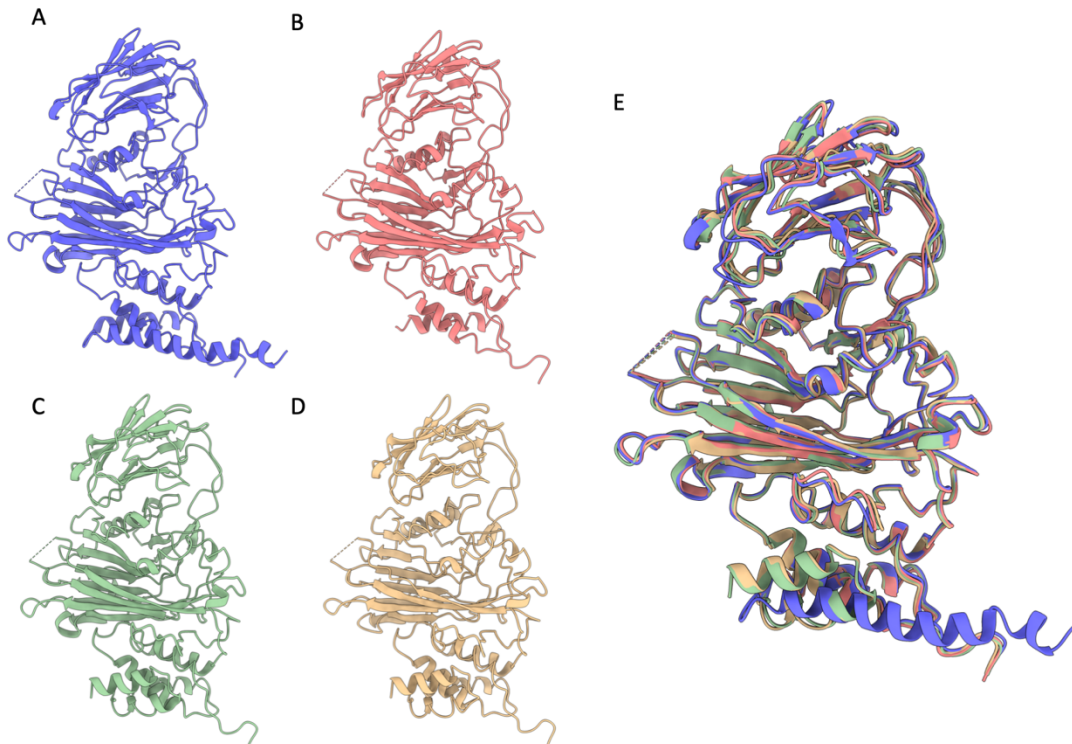


Figure 6.10 | Comparison of the structure from the quasi-equivalent subunits of N ω V intermediate (pH 5.9). N ω V intermediate (pH 5.9) subunits (a-d) compared side-by-side and all four overlaid (e), shown by the colour scheme. The jellyroll and Ig domain are similar in all the structures. The internal helical domains show changes in their structure, especially for the A subunit.

Summary of section 6.2.2: At pH 5.9 it was possible to isolate a main population of particles that, combined, generated a structure at 3.9 Å resolution. It was possible to distinguish the secondary structure of the coat protein and to fit the backbone of the protein in the cryo-EM density map. This structure shows slight changes in the structure of the helical domains, in different subunits, which increase in the later stages of the maturation.

6.2.3. Cryo-EM structure of N ω V intermediate (pH 5.6): formation of cleavage site and autoproteolysis start

The intermediates presented in this section were some of the most challenging to study due to their transitory nature. The SAXS experiments (see section 5.1.5) showed that at pH 5.6, the particles initially compact to a diameter of around ~ 435 Å. However, a long incubation period revealed that the particles became even more condensed over time at this pH and eventually reached the same size as the capsids (~ 410 Å). Therefore, in order to capture the intermediate before reaching the capsid size, the time for sample preparation had to be considered.

The grid preparation (see Chapter 2 for details) was done with the assistance of Dr. Emma Hesketh, from the University of Leeds, who then set up the data collection. To prepare the grids, N ω V procapsid VLPs, produced in insect cells, that had been stored in 10 mM Tris, 250 mM NaCl, pH 7.6 were mixed at a 1:1 ratio with 100 mM MES, 250 mM NaCl, pH 5.6 buffer. For this experiment, the incubation of the particles at pH 5.6 was carried out for five minutes before freezing the particles in the grid. In order to prepare all the grids with particles incubated for the same length of time, a fresh mixture was prepared each time and incubated for five minutes before preparing each grid. The data collection was done using a FEI Titan Krios microscope with a Falcon III detector, with a final object sampling of 1.065 Å/pixel and a total dose of 48.7 e/Å². The dose was fractionated across 39 frames during a 1 s exposure (Figure 6.11).

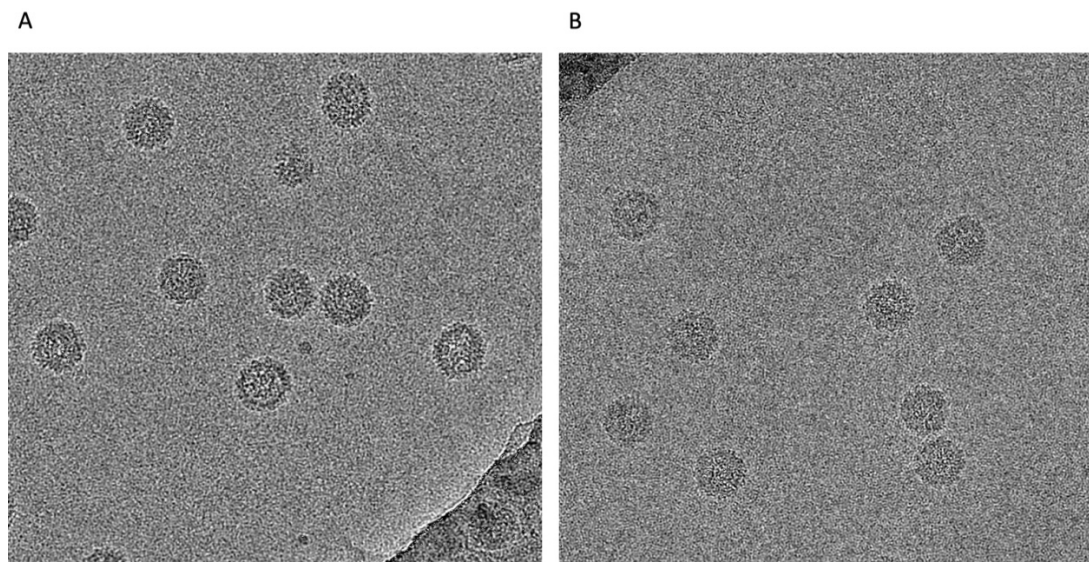


Figure 6.11 | Cryo-EM micrographs of N ω V VLPs at pH 5.6. Different views of the cryo-EM grid (a, b). The particles are well distributed but are heterogeneous, with particles of different sizes. Data acquisition: FEI Titan Krios EM (300 kV) with a Falcon III detector. Data acquired at 1.065 Å/pixel.

As previously, the cryo-EM data was processed using the Relion 3.0 pipeline (Scheres, 2012; Zivanov et al., 2018). In the early stages of the data processing I noticed that the population of particles from this sample was heterogeneous. The particles from this experiment were frozen in the middle of a transition to capture the intermediate state(s). Therefore, there could be variation in the dynamics of the particles within the population, with particles that matured and transitioned at different speeds. This caused the generation of the multiple conformations that are described in further detail in this section. These multiple structures were of great interest as they provided information about several conformational stages; however, this made the processing difficult and split the data into multiple classifications, which reduced the resolution of the structures, as they were each resolved using a smaller number of particles.

For the processing of this challenging dataset, briefly, a subset of particles was picked manually and was used to generate a reference for the automated picking of the particles from all the micrographs of the dataset. I used multiple rounds of reference-free 2D classification to select properly assembled particles (Figure 6.12). Within the 2D classes I noticed that the population was heterogeneous and I applied 3D classification in order to separate the different subpopulations of particles from the heterogeneous sample.

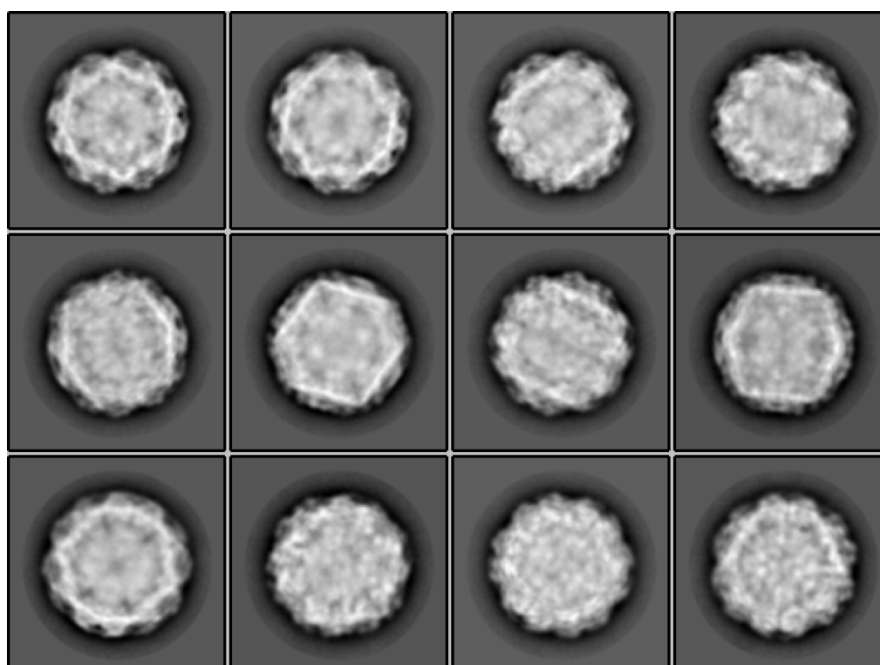


Figure 6.12 | Representative 2D classes averages of N ω V VLPs at pH 5.6. Multiple rounds of 2D classification allowed for the selection of 30,524 particles that were used for the following steps of 3D classification.

This dataset was the most heterogeneous of those analysed from the insect cell-produced VLPs and the particles presented differences in both flexibility and size. With the 3D classification (Figure 6.13) it was possible to select five distinctive populations that were classified by their differences in size. I solved the structures using the particles from the different populations. As there were differences in the properties and number of particles, each structure had a different resolution, in the range of ~ 4 to 8 \AA (Figure 6.14). Interestingly, the structure with the largest diameter in the pH 5.6 dataset had the same diameter as the pH 5.9 structure ($\sim 460 \text{ \AA}$). The structure with the smallest diameter from the pH 5.6 dataset had a similar diameter as the capsid ($\sim 420 \text{ \AA}$). Therefore, at these conditions it was possible to virtually isolate all the structures and the quaternary changes that occur between pH 5.9 and pH 5.0 in the last steps of the maturation (Figure 6.14).

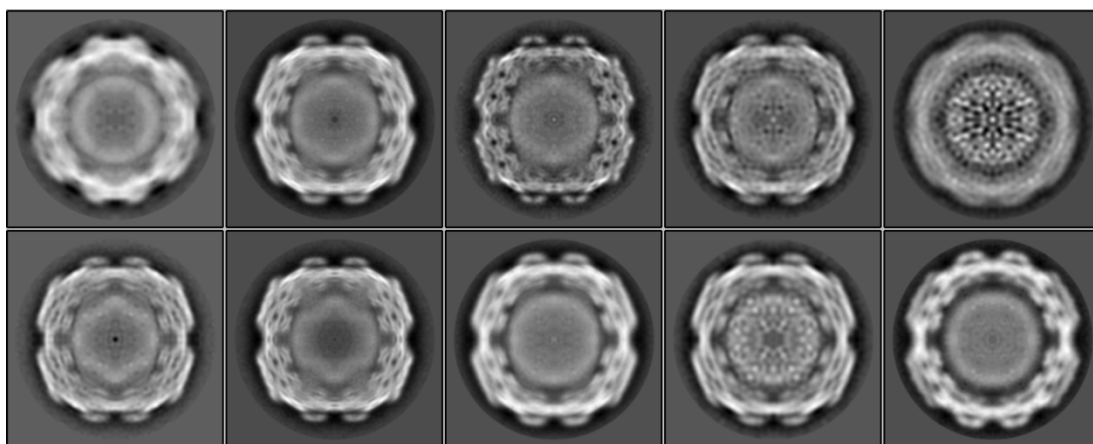


Figure 6.13 | 3D classes from the pH 5.6 dataset. The 3D classification shows that there is heterogeneity within the selected particles and allowed for their separation in multiple populations. Those with higher resolutions were selected and used for the refinement steps.

The current resolution (between 4.4 and 8.7 \AA) allows for the determination of large conformational changes in the structure of the particle, but it limits the building of a model for three of the structures. However, this is still work in progress and more data will be collected and processed for this pH but time did not permit this to be included in this thesis.

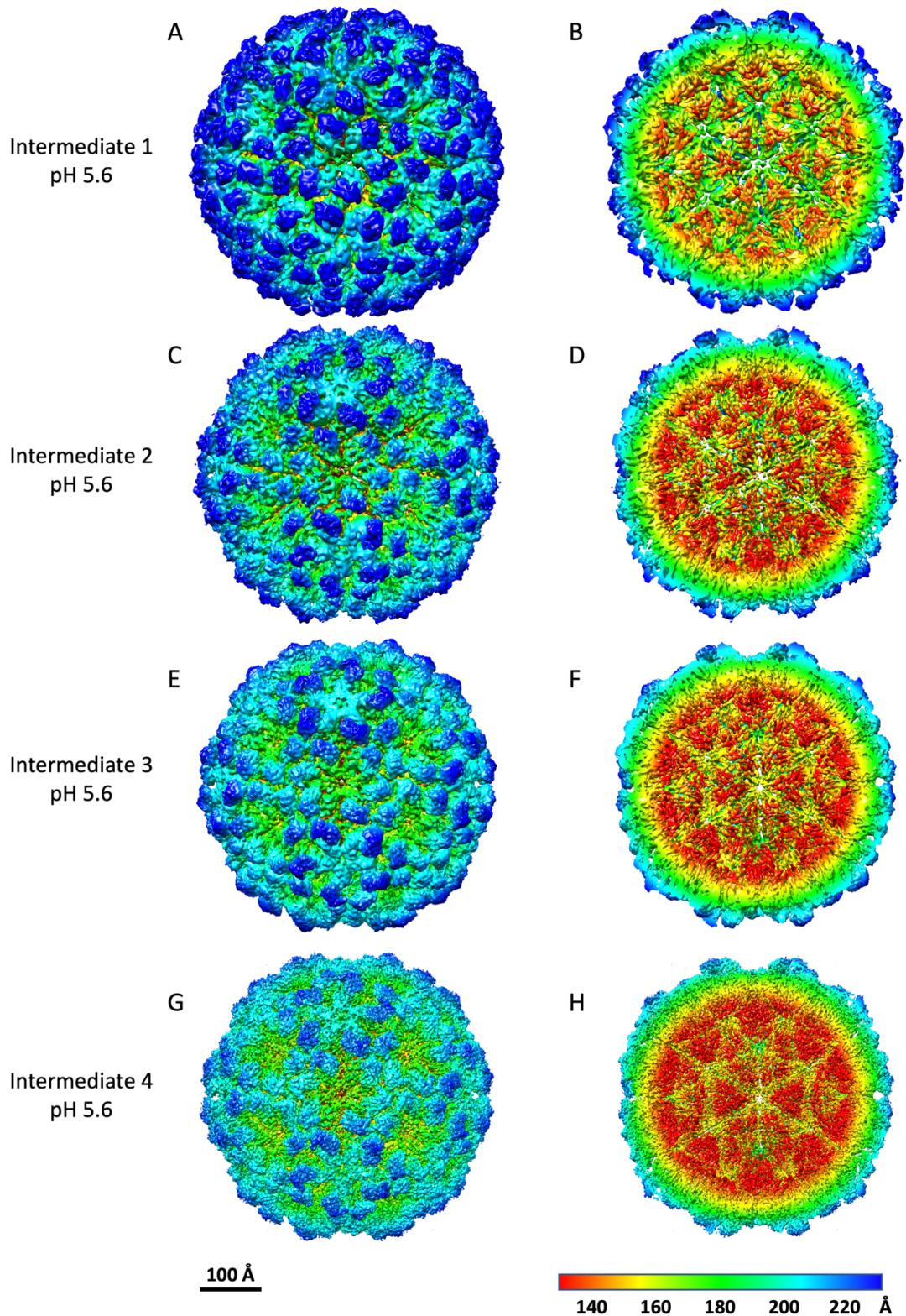


Figure 6.14 | Comparison of the four intermediate cryo-EM structures from N ω V VLPs at pH 5.6. The four structures intermediate 1 (a, b), 2 (c, d), 3 (e, f) and 4 (g, h) are in order, from bigger (a, b) to smaller (g, h) diameter. Two views are shown, full particle (a, c, e, g) and cross section (b, d, f, h). The structures are coloured by radius from red (140 Å) to blue (220 Å). The scale bar is 100 Å.

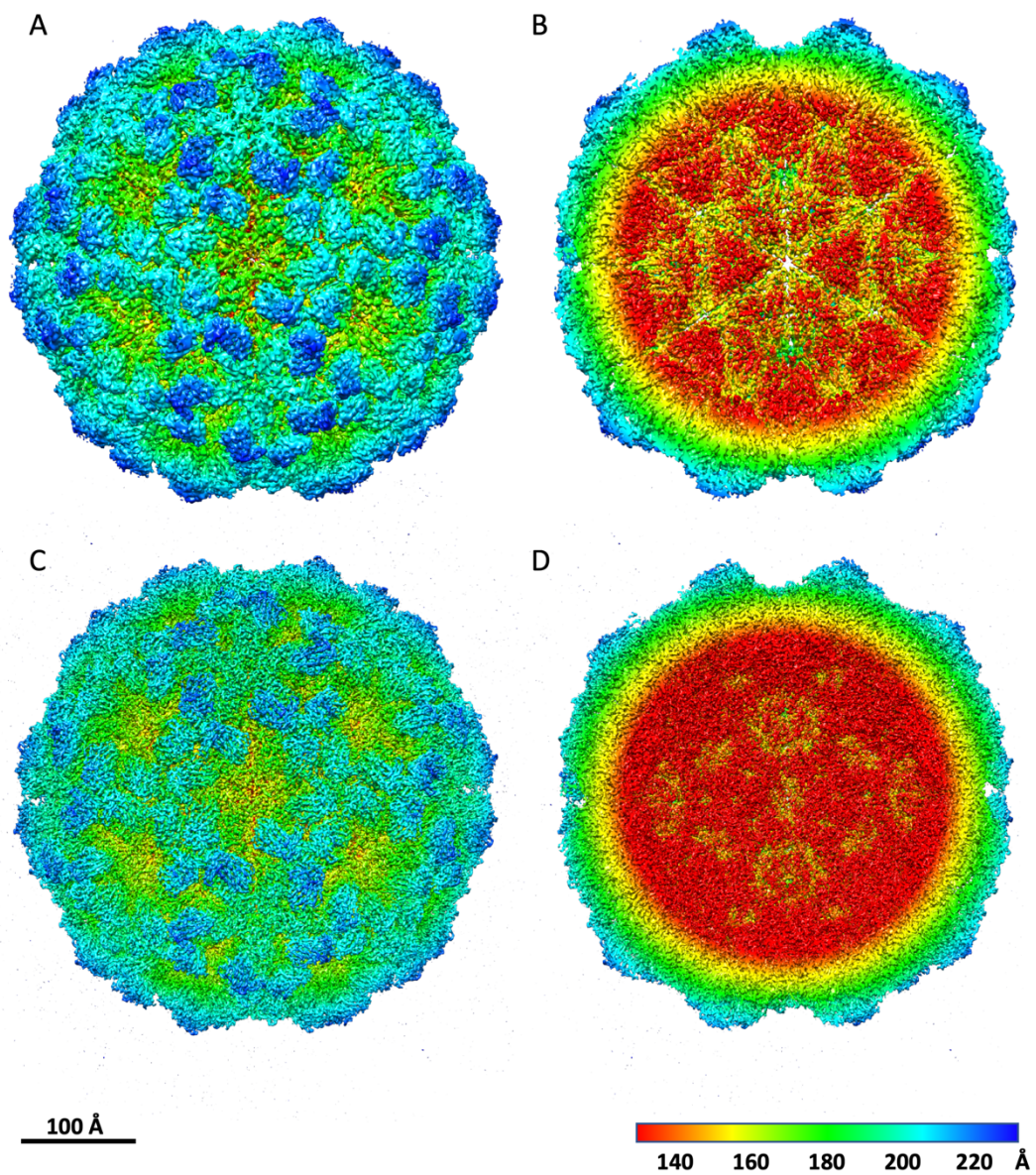


Figure 6.15 | Comparison of the cryo-EM structures of intermediate 4 at pH 5.6 and capsid N ω V VLPs. Cryo-EM structures of intermediate 4 at pH 5.6 (a, b) and capsid (c, d). Two views are shown, full particle (a, c) and cross section (b, d). The structures are coloured by radius from red (140 Å) to blue (220 Å). The scale bar is 100 Å.

At pH 5.6, intermediate 1 is the biggest of the four intermediates obtained at this pH, with a diameter of ~ 460 Å and a model could be produced at a resolution of 8.7 Å. It has a porous surface (Figure 6.14a) and it is very similar to the intermediate at pH 5.9 (see section 6.2.2). Intermediate 2, structures (c) and (d) from Figure 6.14, has a diameter of ~ 440 Å, a resolution of 7.3 Å, a less porous surface and the 5-fold axis is flatter when compared with intermediate 1. Intermediate 3, structures (e) and (f) from Figure 6.14, has a diameter of ~ 430 Å and a resolution of 5.5 Å. Intermediate 4, the smallest one from the dataset at pH 5.6, has a diameter of ~ 425 Å, which is very similar to the capsid structure (Figure 6.15), and a resolution of 4.4 Å. The surface from the intermediate 4 and the capsid are very similar, the apparent differences visible in Figure 6.15 are due to the resolution of the structures; Intermediate 4 is at 4.4 Å and capsid at 2.7 Å resolution. There is more density towards the centre of the particle in the capsid structure; this is probably because of the rearrangements in the helical domains that occur during the maturation process (more details in section 6.6).

Summary of section 6.2.3: At pH 5.6 it is possible to isolate four intermediates that have different diameters. One of these intermediates is nearly identical to that obtained at pH 5.9, but has been solved at lower resolution (8.7 Å). The smaller of the intermediates is similar to capsid in terms of diameter; however, the density in the interior is different and can be attributed to the rearrangements in the helical domains during the maturation. Further data and processing will probably provide an increase in resolution to be able to look at the autoproteolysis.

6.3. Summary of cryo-EM structures for the maturation movie

In this section I briefly summarize the information regarding the cryo-EM structures solved in this thesis. In total, 11 cryo-EM structures generated from 7 datasets were produced during the course of this thesis. This accounts for over 100 Tb of cryo-EM data collected and analysed during the processing.

These structures have different resolutions and characteristics. For the movie that is presented at the end of this chapter, I have used the datasets highlighted in green in Table 7.1 due to their resolution and distribution in the maturation process. The structures highlighted in blue have been used to make a model of the latest steps in the compaction of the particle at pH 5.6. The structures in grey are those where there is already a better resolution structure or that are still under analysis. In Table 7.1, the order of the listed structures is according to the pH at which the data were collected. Note that the capsid structure was imaged at pH 7.6 after maturation in the plant. *In vitro* maturation was achieved by lowering the pH to 5.0. Therefore, the capsid particles were imaged at a neutral pH, but they were equivalent to particles from insect cells matured by lowering the pH. Previous cryo-EM work on N ω V VLPs that were matured at pH 5.0 and then exposed to pH 8.0 showed that they preserved the same structure as N ω V authentic mature virions (Campbell et al., 2014). This data supports the results obtained for the *in planta* matured N ω V VLPs that displayed a capsid structure despite being kept at pH 7.6.

Table 7.1 | Summary of cryo-EM structures produced in this thesis.

Structure	pH	Resolution	Expression system
Procapsid	7.6	4.9 Å	Insect cells
Procapsid	7.6	8.2 Å	Plants
Capsid	7.6	2.7 Å	Plants
Intermediate pH 6.25	6.25	4.8 Å	Insect cells
Intermediate pH 5.9	5.9	3.9 Å	Insect cells
Intermediate pH 5.7- 1	5.7	7.0 Å	Plants
Intermediate pH 5.7- 2	5.7	3.3 Å	Plants
Intermediate pH 5.6 - 1	5.6	8.7 Å	Insect cells
Intermediate pH 5.6 - 2	5.6	7.3 Å	Insect cells
Intermediate pH 5.6 - 3	5.6	5.5 Å	Insect cells
Intermediate pH 5.6 - 4	5.6	4.4 Å	Insect cells

In the following sections I compare the different structures involved in the maturation process of N ω V (Figure 6.16). To visualize and quantify the conformational changes involved in the maturation process, the models built from the cryo-EM maps from procapsid, intermediate pH 5.9 and capsid, were used.

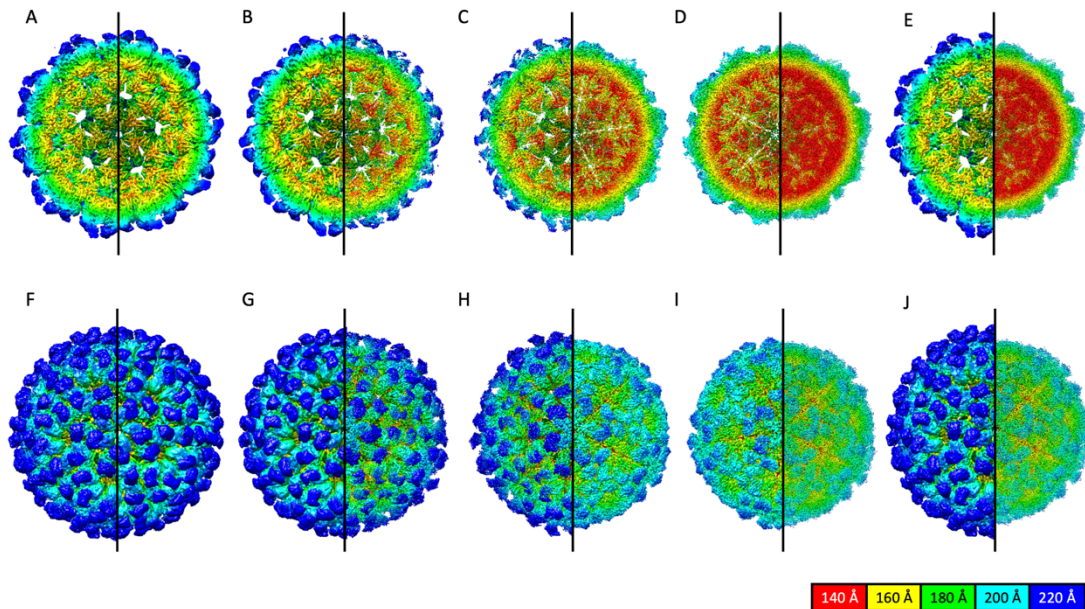


Figure 6.16 | Successive stages in the maturation of N ω V VLPs. Each particle structure is compared with the succeeding state in juxtapositions of sections of the respective cryo-EM density maps. (a, f) Procapsid on left (L) versus intermediate at pH 6.25 on right (R); (b, g) Intermediate at pH 6.25 (L) versus intermediate at pH 5.9 (R); (c, h) Intermediate at pH 5.9 (L) versus first intermediate from pH 5.6 (R); (d, i) Intermediate at pH 5.6 (L) versus capsid (R) and lastly, the endpoints; (e, j) Procapsid (L) versus capsid (R). Two views are shown, cross section (a, b, c, d, e) and full particle (f, g, h, i, j). The structures are coloured by radius from red (140 Å) to blue (220 Å).

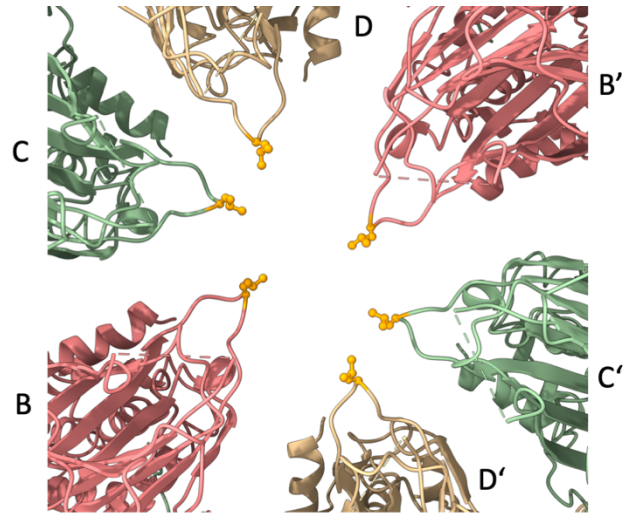
6.4. Analysis of the transitions at the 6- and 5-fold axis

The procapsid has a remarkably porous architecture that drastically changes during the maturation process, reaching a final compact particle. The pores were found in the 6-fold axis of the particle and it was observed that their diameter was reduced during the maturation process (Figure 6.17). In a loop that is pointing towards the centre of the 6-fold axis, the six copies of Leu254 that are initially far apart move towards the centre of the axis during the maturation. I measured the distance between the leucines in opposing subunits and I observed that initially the Leu254 residues that were closer were the ones from subunit B (red). At pH 5.9, the Leu254 from subunits C (green) and D (yellow) had approached by approximately 10 Å. Finally, in the capsid, all the subunits (B, C, D) were at similar distance, establishing close contacts between them (Figure 6.17). In subunit A, the same loop harbouring Leu254 established interactions with four other A subunits at the 5-fold axis. The distances between the subunits remain constant across the maturation process (Figure 6.18).

A - Procapsid

Distances between C α from
Leu254 of subunits:

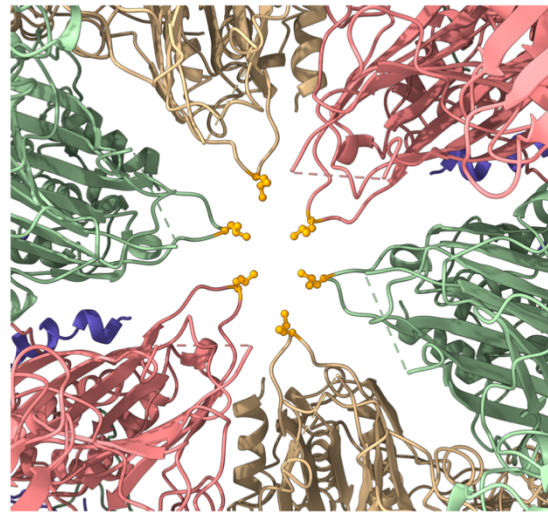
B – B': 16.4 Å
C – C': 24.3 Å
D – D': 29.6 Å



B - Intermediate (pH 5.9)

Distances between C α from
Leu254 of subunits:

B – B': 12.8 Å
C – C': 14.1 Å
D – D': 20.3 Å



C - Capsid

Distances between C α from
Leu254 of subunits:

B – B': 10.2 Å
C – C': 10.4 Å
D – D': 10.1 Å

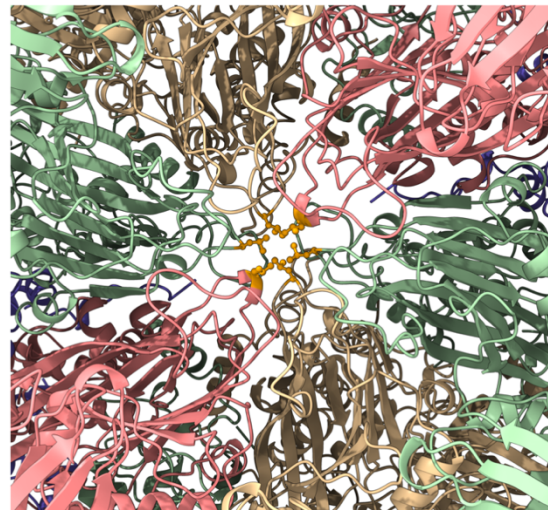
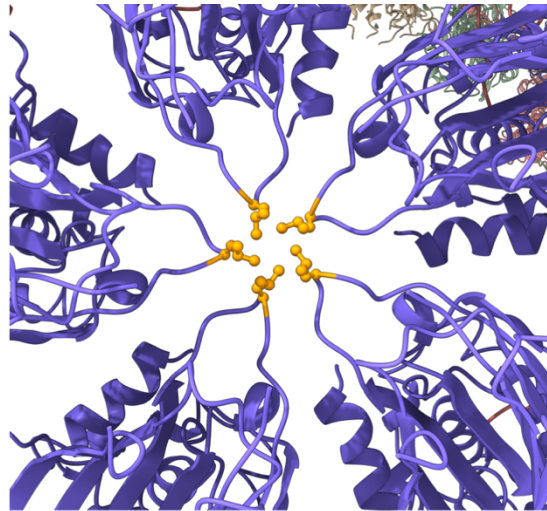


Figure 6.17 | 6-fold axis view from three maturation stages of N ω V VLPs. View of the 6-fold axis with the residue Leu254 highlighted in orange. As the maturation of the virus proceeds the particle compacts and the loops of the coat proteins come together, with the leucine establishing hydrophobic interactions in the capsid form.

A - Procapsid

Distances between C α from
Leu254 of subunits:

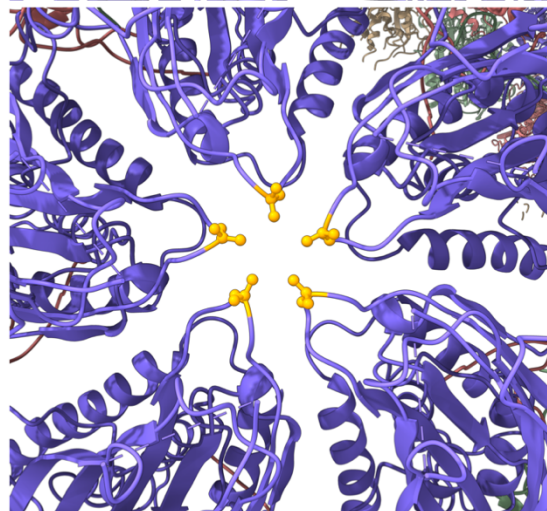
A - A (adjacent): 5.1 Å
A - A (opposite): 8.2 Å



B - Intermediate (pH 5.9)

Distances between C α from
Leu254 of subunits:

A - A (adjacent): 5.5 Å
A - A (opposite): 8.9 Å



C - Capsid

Distances between C α from
Leu254 of subunits:

A - A (adjacent): 4.8 Å
A - A (opposite): 7.8 Å

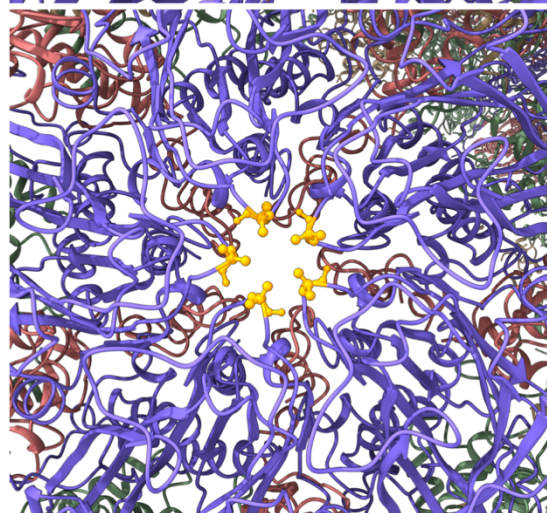


Figure 6.18 | 5-fold axis view from three maturation stages of NCoV VLPs. View of the 5-fold axis with the residue Leu254 highlighted in orange. During the maturation, the distances between the Leu254 of the A subunits stay practically constant.

6.5. Quaternary conformational changes to direct the maturation

In the previous section I showed that the interactions between the Leu254 residues of subunit A at the 5-fold axis remain constant across the maturation process. By analysing the trajectory of the subunit A during the maturation, it is possible to observe that it pivots about the 5-fold axis, keeping the interaction of the loop where Leu254 is located nearly constant (Figure 6.19).

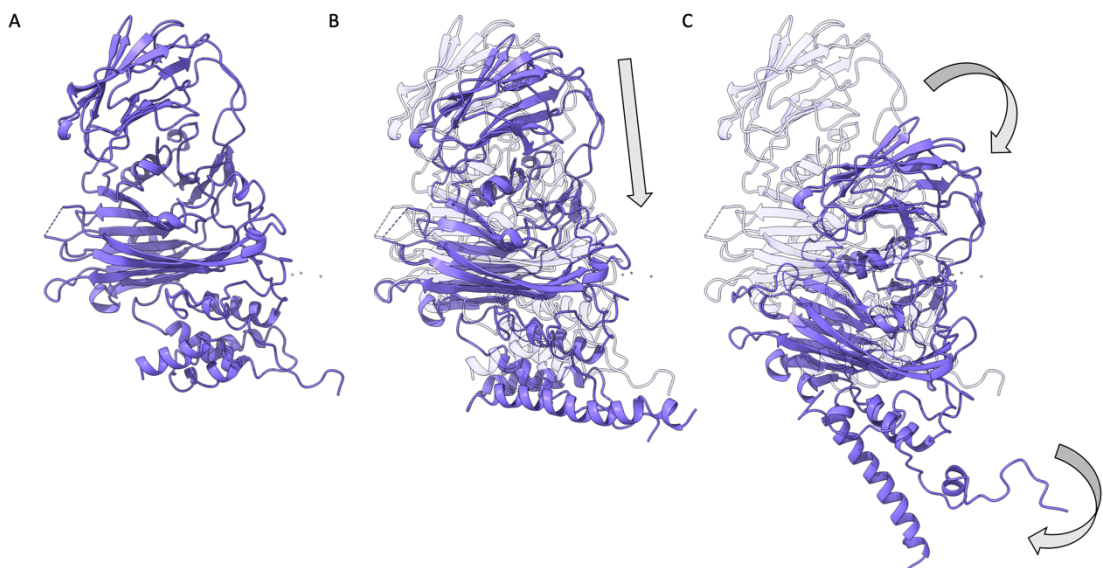


Figure 6.19 | Side view of the subunit A of N ω V across different points in the maturation. The structures of the procapsid (a), intermediate at pH 5.9 (b) and capsid (c) were superimposed to compare the movement and change in conformation of the subunit A. In figures (b) and (c), there is also the silhouette of the subunit A in the procapsid form (a), to facilitate the identification of the structural changes.

On the other hand, subunits B, C and D, move towards the centre of the particle in a linear mode with a slight rotation to accommodate closer interactions between them and to allow for the closure of the pores described in the previous section (Figure 6.20).

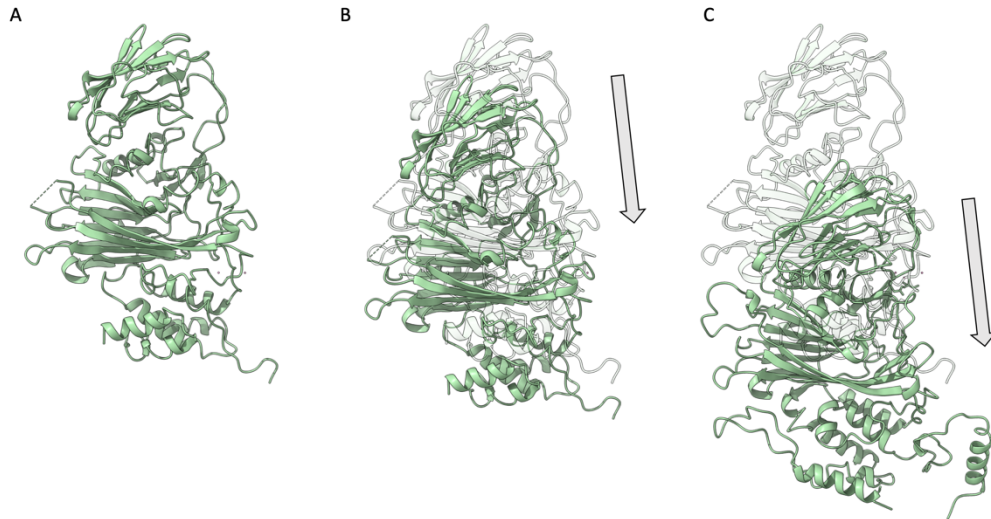


Figure 6.20 | Side view of the subunit C of NφV across different points in the maturation. The structures of the procapsid (a), intermediate at pH 5.9 (b) and capsid (c) were superimposed to compare the movement and change in conformation of the subunit C. In figures (b) and (c), there is also the silhouette of the subunit C in the procapsid form (a), to facilitate the identification of the structural changes.

6.6. The multiple roles of γ peptides: breaking and building bonds

The γ peptide is generated after the autoproteolytic event that occurs during the maturation process of N ω V. Before the cleavage, the residues that constitute the γ peptide are part of the C-terminal end of the α peptide, the full-length coat protein of N ω V (Canady et al., 2000). In this section I traced the movements and interactions that the residues of the γ peptide, which is part of the helical domain, establish during the maturation, before (procapsid and intermediate) and after the cleavage (capsid). Initially, the residues of the γ peptide form a chain with the same folding in all the four subunits (A, B, C, D); however, during maturation they differentiate, resulting in different conformations and interactions. Due to their different properties, the γ peptides of A and B subunits have some areas that become more disordered and that cannot be identified in the final structure (capsid). On the other hand, the helical domains from the N-terminal end of the α peptide are more disordered at the start of the maturation and become more visible towards the end.

The γ peptide residues from the trimer of D subunits (yellow), interact at the loop of 3-fold-related Glu590 residues in the procapsid (Figure 6.21, procapsid and intermediate). However, when the particle matures, that interaction is broken and Glu590 establishes new salt bridges, with Arg79 from the N-terminal region of the α peptide (Figure 6.21, capsid). Additionally, new hydrophobic interactions, not present in the procapsid, are established between the Pro615, Gly616, Leu617 and Leu618 of subunit D and subunit C (Figure 6.21, capsid).

On the other hand, the γ peptide residues from subunit A (blue), subunit B (red) and subunit C (green), initially also establish quasi-3-fold interactions at the loop harbouring the Glu590 (Figure 6.21, procapsid and intermediate), in the same way as the D subunits trimer. However, that interaction is broken when the maturation proceeds. In the capsid, Glu590 of subunit B makes a salt link with Arg79 from subunit C and Glu590 of subunit C makes the same interaction with Arg79 from subunit A (Figure 6.21, capsid). The γ peptide from subunit A forms a pentameric helical bundle with the same region from four other A subunits (Figure 6.21, capsid).

In conclusion, the γ peptide is very dynamic during the maturation and is able to break and establish new interactions. Initially, the γ peptide has the same conformation in all the subunits, but it differentiates in dissimilar ways for each subunit during maturation. Therefore, this peptide contributes to the quaternary conformational changes during the maturation and provides the lytic activity of the mature particles.

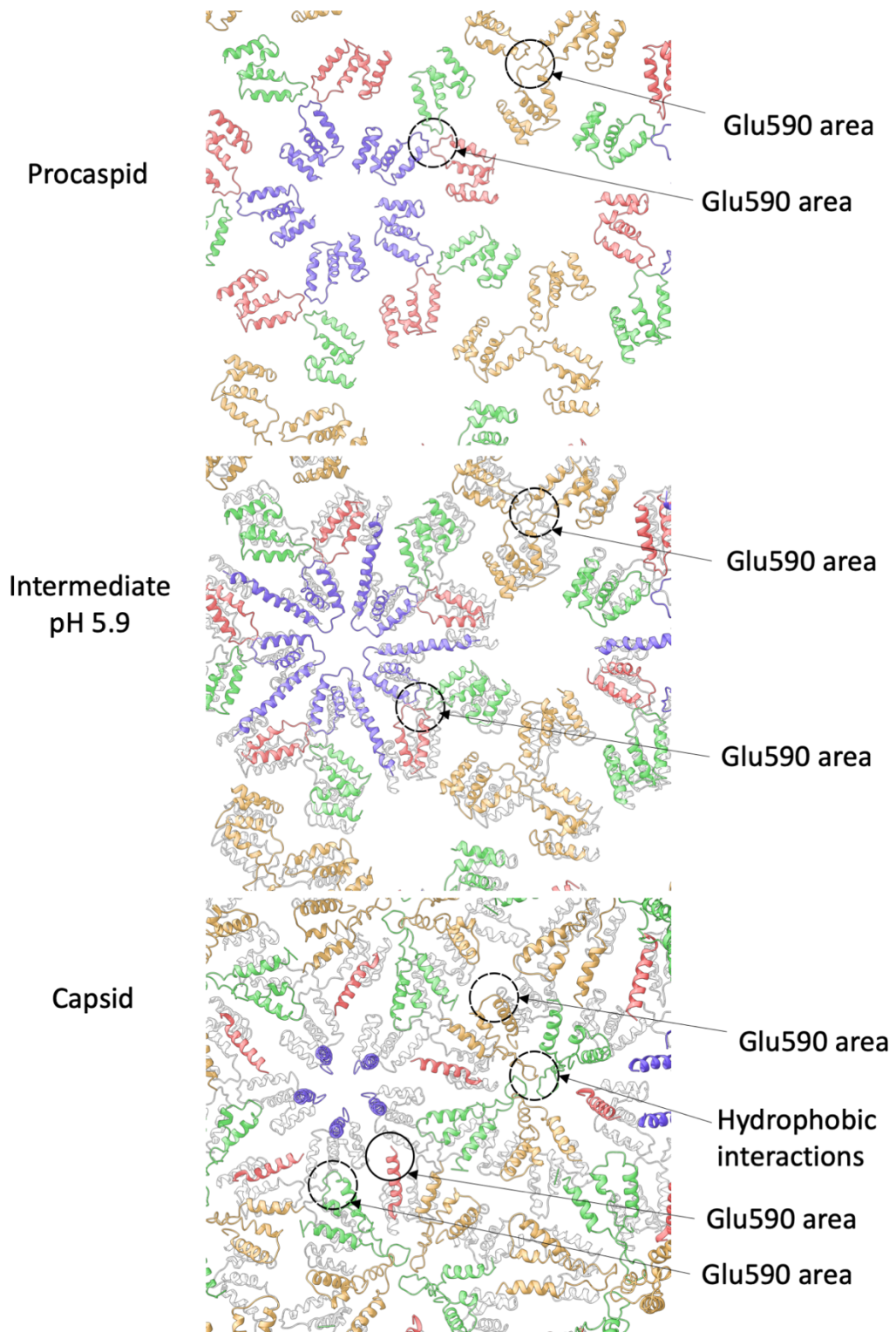


Figure 6.21 | Structure and distribution of the γ peptides in N ω V VLP. Inside view of the N ω V VLP, displaying only the γ peptides. The colouring used for each γ peptide corresponds to the subunit that it belongs to, A (blue), B (red), C (green) and D (yellow). Three structures are represented, procaspid, intermediate at pH 5.9 and capsid (in the last two, there is also the silhouette of the procaspid γ peptides to facilitate the identification of the structural changes).

6.7. Formation of the cleavage site

In the N ω V procapsid structure, the amino acids that form the cleavage site (Asn570 and Glu103) are separated by ~ 20 Å, with contributing residues Thr246 ~ 13 Å from the site and Lys521 ~ 15 Å (see Figure 6.22a). For the pH 5.9 intermediate, the four amino acids described maintain the same distances as in procapsid and the major changes in this intermediate are in the quaternary structure of the particle. In the capsid structure, when the cleavage site is formed and the autoproteolysis takes place, the distance between Asn570 and Glu103 is ~ 3 Å, with Thr246 ~ 3 Å and for Lys521 ~ 3 Å (see Figure 6.22b). These results suggest that in the capsid, these residues establish interactions, such as hydrogen bonds, that trigger the autoproteolytic event between residues Asn570-Phe571. However, the structure of the capsid is a view of the arrangement of the residues after the cleavage. The pH 5.6 intermediate, which is still under investigation, will provide further information regarding the formation of the cleavage site and the interactions that are established as the cleavage occurs. These changes in the distribution of the residues that participate in the cleavage, observed between the procapsid and the capsid, demonstrate that it is necessary for a change in the conformation of the protein to occur to initiate the cleavage. Therefore, the autoproteolysis is dependent on the large conformational changes of the particles, which are the result from the changes in the electrostatic interactions between the proteins induced by the change in pH.

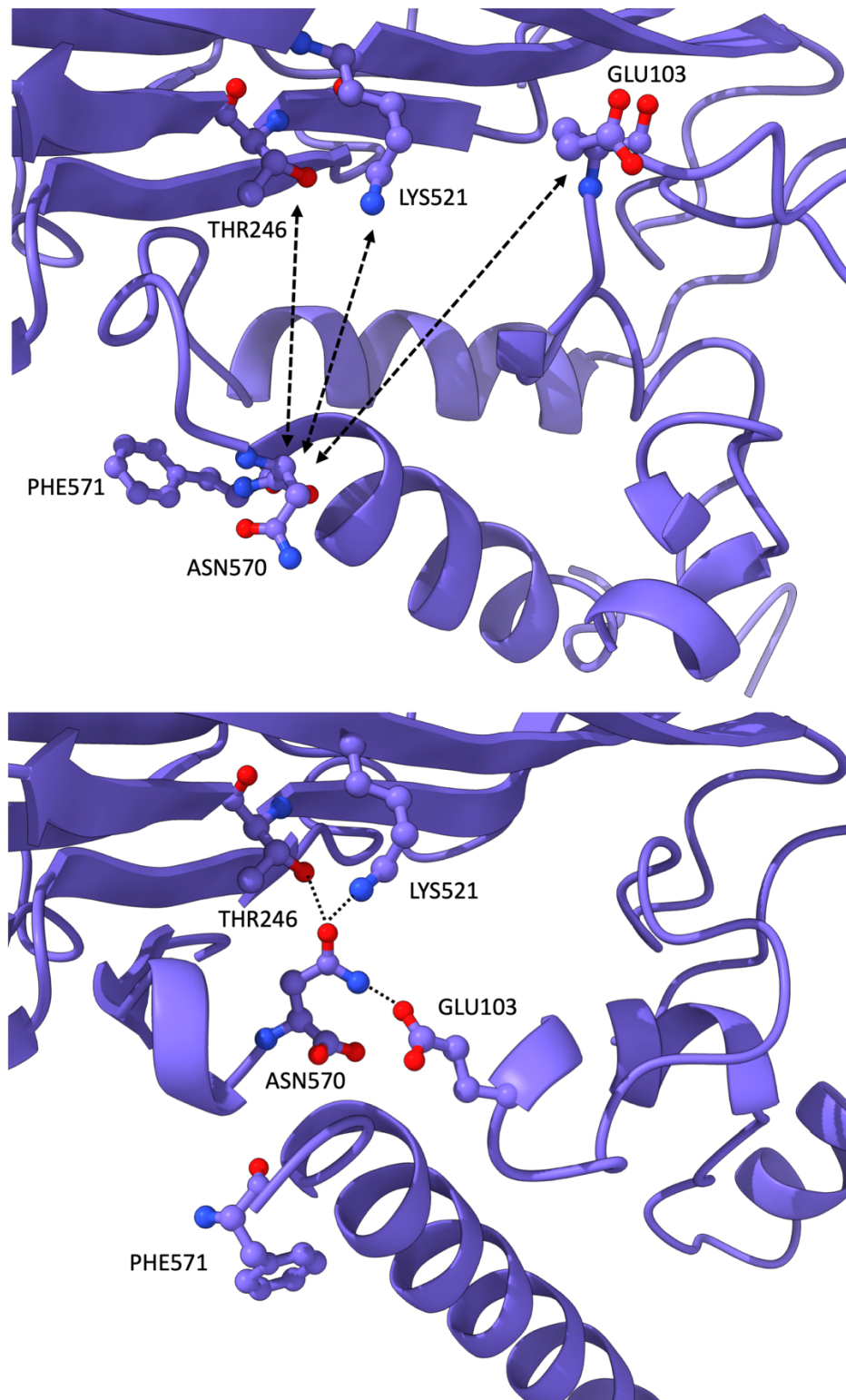


Figure 6.22 | Arrangement of the residues, from subunit A, that participate in the cleavage site in the procapsid and capsid N ω V VLP structures. In the procapsid (a) structure Glu103 and Asn570 are ~ 20 Å apart. During the maturation process they move in the three-dimensional space and end up at less than 3 Å and establish interactions. This structure suggests that the interaction with Glu103 contributes to the triggering of the autoproteolysis.

6.8. The movie of N ω V, a simple yet structurally sophisticated nanomachine

Viruses evolve to efficiently package the necessary information to ensure their perpetuation. In the case of N ω V, the processes of assembly, maturation and infection are encoded by a single coat protein. In this final section I present the “movie” of the maturation process of N ω V, generated by the combination of the cryo-EM structures presented in this thesis. The first time that I watched the movie, revealing the continuous transitions occurring across the maturation process, was one of the most exciting days of my PhD. It was incredible to see how a unique building block, the N ω V coat protein, assembled into a porous structure that was able to transition to a compact structure with different properties, by changing only the pH. Additionally, during this maturation process there was a specialization of the building blocks, which develop different structures and roles within the particle that are determined by their locations in the asymmetric unit, even though they all share the same amino acid sequence.

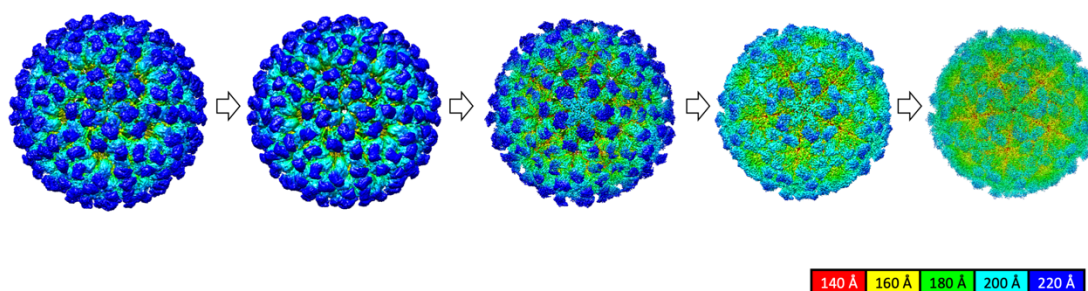


Figure 6.23 | N ω V, “the movie”. Cryo-EM structures from the different maturation steps representing the snapshots of the maturation movie. An actual movie showing the morphing between the different structures is provided in Appendix 4. Structures coloured by radius from red (140 Å) to blue (220 Å).

This maturation movie shows a fascinating mechanism that is encoded within the structure of the virus and is triggered under the right conditions allowing the virus to activate the auto-catalytic cleavage and to strengthen the capsid structure. The structures presented in this chapter are consistent with models generated from previous lower resolution data on N ω V (Canady et al., 2000). It is hypothesised that nearly identical dimers are able to assemble into a procapsid, where all the subunits have a similar fold. Changes in pH alter the charges of the amino acids and therefore the electrostatic interactions of the subunits, which lead to changes in the quaternary structure of the particle.

6.9. Discussion

In this chapter I have presented the structures of the intermediate stages of the maturation process of N ω V at a remarkably high resolution using cryo-EM, a unique achievement for this or any other eukaryotic virus. This data provides a wealth of information regarding the maturation mechanisms of this virus and, combined with the structures and results obtained in the previous chapters, it broadens the view in the field of virus maturation. To solve the cryo-EM structures presented in this thesis I have had to process over 100 Tb of cryo-EM data, which has been a herculean effort and has led to the generation of over ten structures from VLPs produced in insect cells and plants.

Cryo-EM is a fast-moving field with continuous developments in the tools and procedures used. The models that are presented in this thesis have been refined as far as has been possible within the time frame of the PhD. However, it is expected that further refinement will lead to improvements, as for some of the structures it is still not possible to properly fit the position of residues and side chains due to limitations in the resolution of the cryo-EM structures, which would benefit from additional data and processing time.

Overall, the cryo-EM structures presented in this thesis revealed that all the N ω V coat protein subunits have a similar overall structure when they form the procapsid; however, they specialize during the maturation process and adopt different conformations that depend on their quasi-equivalent position. This was striking, as for the same amino acid sequence the protein is able to achieve different final conformations that are directed by the environment in which the subunit sits within the architecture of the particle. Furthermore, it was observed that in the helical domains, mainly comprising the γ peptide, there were large conformational changes that contributed to the formation and breakage of interactions between residues. This modification in interactions can be associated with an increase in the stability of the structure of the particle and also with the repositioning of the γ peptides from some subunits, particularly the A subunit, to be in the ideal position to be finally released in order to lyse of membranes, as shown in Chapter 3.

Another outstanding finding has been the formation of the cleavage site and how the amino acids that contribute to the autoproteolytic cleavage start from positions distant from the active side in the initial stages of the maturation and then they form the active site. This suggested that the cleavage site was formed in the final stages in the maturation and that the amino acids participating in the cleavage possibly establish interactions, such as hydrogen bonds, that contribute to trigger the proteolysis.

Therefore, the autoproteolysis is directly linked with the large conformational changes of the particles, which can happen thanks to the variation in the charge of the amino acids induced by the change in pH.

Finally, the cryo-EM structures that I presented in this thesis can be combined and treated as frames to generate the maturation “movie”, as previously proposed by Kearney and Johnson, 2014. This exceptional movie reveals the large conformational changes that occur during the pH-dependent maturation process. In the initial intermediates, between pH 7.6 and 5.9, the changes are mainly related to changes in the electrostatic interactions between the subunits, which contribute to the compaction of the particle. In the final stages of the compaction, at pH 5.6 and below, there is further compaction of the particle and there are, importantly, major rearrangements in the tertiary structure of the subunits. These changes were mainly located in the helical domains, at the C- and N-terminal of the protein. They are involved in the closure of the pores at the 6-fold axis, with the formation of hydrophobic interactions between chains, and the formation of additional contacts that possibly conferred the higher stability of the capsid structure. Additionally, in these final stages there was the rearrangement of the residues that participate in the cleavage and that trigger the autoproteolysis. This mechanism is so precise that modifications in the interactions between the subunits, can have dramatic effects in the proper maturation of the particles. In chapters 3 and 4, comparisons of the N ω V VLPs produced in two different expression systems, insect cells and plants, showed reduction in the dynamics of the plant-produced VLPs, which hampered the completeness of the maturation process for some of the particles.

In conclusion, N ω V is a fascinating virus with a complex maturation mechanism that has been revealed in great detail in this thesis. This work provides the fundamental knowledge to better understand large conformational changes and architecture rearrangements in viruses. The N ω V maturation movie summarizes the structural information and is a great tool to visualize the dynamics and large conformation changes of N ω V, an elegantly programmed nanomachine.

Chapter 7

General discussion

Over the last two decades, N ω V has become one of the main models to study the maturation mechanisms of non-enveloped animal viruses (Kearney and Johnson, 2014; Veessler and Johnson, 2012). This virus presents multiple intermediate structures, which are part of the maturation process, that can be produced *in vitro* through changes in pH. It is possible to generate homogeneous populations of these intermediates, which show differences in the diameter of the particle, making N ω V a unique system to study maturation in a continuous way *in vitro* (Matsui et al., 2009, 2010a). However, at the start of this thesis there were no high-resolution structures available for the procapsid and intermediate structures, which limited the understanding of the maturation process. Fortunately, recent developments in the field of structural biology with the “resolution revolution” of cryo-EM (Kuhlbrandt, 2014) offered an opportunity to better understand the maturation mechanisms of this virus.

The main goal of this thesis was to elucidate the details of the N ω V maturation process using cryo-EM to solve the different intermediate structures to high resolution. In Chapter 3 and 4, I explored the use of plants to produce N ω V VLPs and use them for the structural studies. Despite having autoproteolytic and lytic activity, the plant-produced particles presented limitations in their dynamics that made the study of some structures of the maturation process difficult. I managed to obtain a near-atomic resolution structure for a N ω V capsid VLP matured *in planta*; however, it was not possible to generate and isolate homogenous populations of the different intermediates in the maturation process. Therefore, I determined low-resolution structures of the procapsid and intermediate structures. I decided to use insect cells as an alternative to plants, presented in Chapter 5, and I found that they were a better system to generate N ω V VLPs able to generate homogenous intermediate structures. I used cryo-EM to solve the structures of the procapsid and multiple intermediate stages that finally lead to the generation of a new high-resolution model of virus maturation, “the N ω V movie”, presented in Chapter 6. This movie provides new insights about the architecture and large conformational changes of viruses.

7.1. On the importance of having different expression systems

It is crucial to have stable and homogeneous particles to accurately solve and analyse their structure. This requires the correct expression system for each experiment or application. In this project, for the first time, a side by side comparison was made for N ω V VLPs produced in plants and in insect cells. Previously, the production of N ω V VLPs was achieved only using insect cells, however this expression system presents several limitations in terms of cost, possible contamination and ease of use that were thought to be overcome by using plants (Avesani et al., 2014). Plants have surged as a system with great potential for the production of VLPs for several applications (Lomonossoff and D'Aoust, 2016; Marsian and Lomonossoff, 2016). Despite the several advantages that plants provide as expression systems (presented in Chapter 1), they still require more research and development as they are developing technology, when compared with other expression systems. Although, during the course of this thesis, it was possible to produce N ω V VLPs in plants, limitations of this system for the goals of this thesis were identified. The experiments presented in Chapter 4, demonstrate that crosslinking occurs in particles from plants, which can impact the dynamics of the N ω V VLPs. As this project relied on the ability of the particles to smoothly transition through different structures, this restriction in the dynamics affected the structural studies.

In this thesis it has been shown that expression in plants can have some detrimental effects on some specific properties of the virus particles, such as the dynamics of maturation. If the enzymes involved can be identified, this could be addressed by genetically modifying the plants to make them more suitable platforms. The generation of *N. benthamiana* plants engineered to have reduced oxidation pathways with, for example the knockout of peroxidases involved in crosslinking, will allow the production of VLPs with more stability or to maintain key structural and dynamic features. Modification of the production system could be achieved using genetic engineering techniques like CRIPR-Cas9, which have already been successfully used in plants (Belhaj et al., 2015; Wu et al., 2019). Furthermore, there is a rising interest from companies that realise the potential of plants for the production of pharmaceuticals and other biological products of interest (Lomonossoff and D'Aoust, 2016). More research and investment in this technology will facilitate the production of VLPs with desired properties and may resolve problems encountered in the present work regarding properties of the N ω V VLPs.

7.2. Maturation in the original host

From *N. capensis* larvae it is usually only possible to isolate particles with the cleaved form of the coat protein of N ω V, the mature capsids (Hendry et al., 1985). Probably this is due to the fact that the extractions were performed at the late stages in the infection of the larvae. In order to identify the uncleaved coat protein (α peptide), a time-course experiment could be performed. After starting the infection of the larvae, samples could be collected every a few hours in order to have snapshots of the infection progression and reveal the moment when the coat protein is produced and when it starts to mature. However, this may be difficult as the infection is not synchronized across the different cells of the natural host.

In this thesis, when the N ω V VLPs were produced in plants, I observed that the particles showed more cleavage the longer they stayed in the plant. These results were unexpected, because with insect cells, the particles are isolated only in the procapsid form (Agrawal and Johnson, 1995; Canady et al., 2000). This *in planta* maturation of the VLPs could be due to an acidification of the environment where the particles accumulate or, it has been hypothesized, that it could be also due to the effect of accumulated, naturally acidic, RNAs within the particles.

7.3. The role of RNA in N ω V maturation

The results described in Chapter 4 demonstrate that the N ω V VLPs produced in plants contain RNA. The cryo-EM structures of the N ω V procapsid and capsid showed evidence of an internal density that can be attributed to bulk RNA density. Previous research with nodaviruses has shown that quasi-equivalent regions of the same coat protein established different interactions with the RNA (Cheng et al., 1994). Therefore, further processing and analysis of N ω V cryo-EM structures may provide more information about the interactions of the RNA with the subunits. This would help to understand the roles that RNA may have in the maturation process.

VLPs have proven to be a useful tool for studying the maturation process of N ω V providing high resolution models of the different intermediates. However, it is important to remember that this is a mimic of the original process and the absence of viral RNA can have an effect on the process. Previous research demonstrated that structurally identical particles had different properties in solution due to the presence or absence of the viral RNA (Bothner et al., 1999). Hence, the structures obtained can resemble at a nearly-

atomic level the maturation process but some of the properties of the particles may differ from the original virions. N ω V VLPs are one of the most accurate models of virus maturation that have so far been obtained *in vitro*. However, to have a full view of the mechanism it would be necessary to study it completely *in vivo*. The question remains as to how the subunits are initially assembled to form the procapsid. It is still not clear if they wrap around the RNA as subunits or small aggregates thereof or if they form an initial protein assembly complex and then RNA gets inside the protein shell through the pores of the procapsid that have been described in this thesis. With the improvements in cryo-EM tomography, which allows the visualisation of molecular structures in their native environment, it may be possible to examine this in the future (Hutchings and Zanetti, 2018).

7.4. The maturation of the N ω V movie

The cryo-EM structures presented in this thesis required the use of 25 litres of insect cell cultures, ~500 plants and the preparation of cryo-EM grids and the collection of data during a three-year period. Additionally, the processing of micrographs and generation of cryo-EM density maps required more than two years of computational analysis involving 100 terabytes of data. Cryo-EM is a fast-evolving field due to the continuous developments in hardware and software experienced over the past years (Kuhlbrandt, 2014; Nogales and Scheres, 2015; Smith and Rubinstein, 2014). For the N ω V project, the processing is still ongoing as more data is being acquired for some of the structures. Additionally, new data processing tools are being tested to improve the resolution of the structures and gain additional detail. Therefore, the data presented in this thesis is a snapshot (Figure 7.1) of a movie that it is still maturing and evolving.

The current resolutions (2.7 to 4.9 Å) of the main cryo-EM structures of N ω V VLPs studied in this thesis are sufficient to understand the large conformational changes and the mechanisms of residues involved in key processes such as the formation of the cleavage site and the closure of the pores at the 6-fold axis. An improvement in resolution, especially for the pH 5.6 intermediates, will provide further information regarding the autoproteolysis, such as subtle differences in the four subunits in the icosahedral asymmetric unit, and the bonds established by side chains, which may have important roles in the architecture of the intermediates but that are difficult to resolve due to their highly dynamic properties.

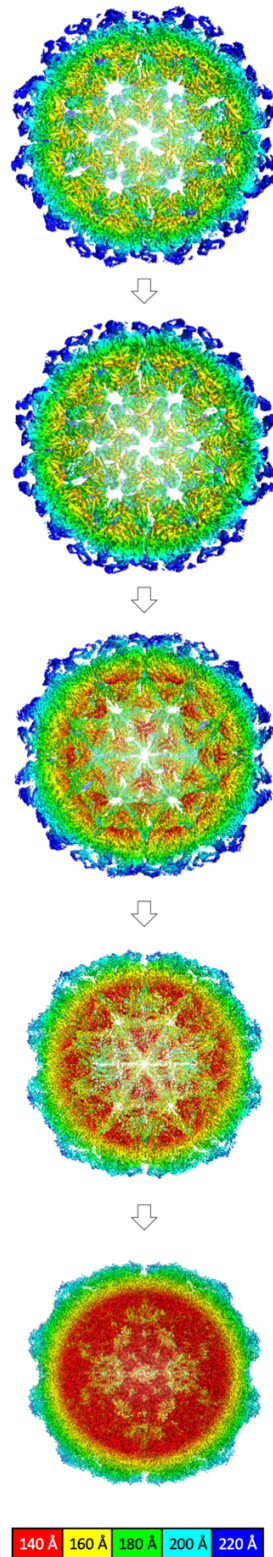


Figure 7.1 | The NσV movie structure snapshots.

Summary of the cryo-EM structures from the maturation process of NσV. The box in the bottom indicates the colour scheme used, the values indicate the distance, in Å, from the centre of the particle at which each colour starts.

7.5. $N\omega V$ conformational changes: a model to design and engineer nanomachines

There is remarkable diversity of protein assemblies in nature providing scaffolds, including fibres, tubes, and cages, that can be used for a wide range of applications in nanotechnology and biomedicine (Pieters et al., 2016; Steele et al., 2017). The characterization of these supramolecular protein assemblies has provided the structural and functional information necessary to engineer and repurpose these proteins for the development of new properties and tools in synthetic biology, materials science, vaccine development and drug delivery (Aumiller et al., 2018; Edwardson et al., 2018; Howorka, 2011). This structural knowledge has also contributed to the computational redesign of small proteins, transforming them into building blocks able to self-assemble and generate new cages with different geometries (Hsia et al., 2016; King et al., 2012, 2014; Lai et al., 2012; Malay et al., 2019; Padilla et al., 2001). Some of these new assemblies resemble virus-like symmetric particles and have been optimized for features such as stability at high temperatures, the ability to load cargoes of interest and catalysis by enzymatic reactions (Cristie-David et al., 2019; Sasaki et al., 2017). Recently, it has been possible to produce computationally designed icosahedral particles able to encapsidate their own mRNA genome (Butterfield et al., 2017). Furthermore, Terasaka et al. (2018), engineered a nonviral protein to build artificial virus-like nucleocapsids that are also able to encapsulate and protect their own full-length RNA genome. These last examples show remarkable “bottom up” approaches to the design of new synthetic nanoparticles that resemble viruses.

Despite the efforts described above to design and build new protein assemblies and viruses (Butterfield et al., 2017; Cristie-David et al., 2019; King et al., 2012; Malay et al., 2019), it is still a challenge to develop dynamic assemblies with the ability to control their size and shape over time. Dynamic nanoparticles will open the door to a new range of applications that require continuous changes in their structure, like nanomachines. A recent study has shown pH-inducible conformational changes in proteins that were designed *de novo*. These tuneable proteins were able to transition to different conformations, as naturally occurs with some proteins in response to environmental changes. The advantage of this approach was that the changes could be controlled and modified through the design of the protein, providing a wide range of new versatile proteins (Boyken et al., 2019). However, there is also a need for dynamic structures at

the scale of complex protein assemblies like viruses, where tens and hundreds of proteins work in a coordinated manner.

It is important to note that the N ω V maturation mechanisms revealed in this thesis open the door for the development of a new range of protein assemblies that can undergo large-conformational changes and that can be controlled at a nearly atomic level. Therefore, N ω V has a great potential to be a model for the development of versatile and precise supramolecular nanomachines. Some of its components, like the gamma peptide, have already been used for the delivery of quantum dots into cells directly through the plasma membrane which has great potential for further biotechnology applications (Safi et al., 2017). The movie of the maturation process provides a toolkit for the engineering and design of a new generation of nanomachines that are able to self-assemble and change within complex biological environments.

7.6. Final conclusion

In this thesis I presented high-resolution cryo-EM structures of the different maturation stages of N ω V VLPs. These structures are a wonderful new resource for facilitating understanding of virus maturation and to develop new nanodevices.

The biophysical analysis of the different states in the maturation process of N ω V allowed us to build a movie, comprising cryo-EM density maps at 2.7 to 4.9 Å, of the large-conformational changes that this virus goes through during its maturation. Near-atomic models of the coat proteins in the context of the whole virus particle were generated, providing a unique understanding of virus maturation driven by pH changes and associated electrostatics. This has strengthened our knowledge of the structural organization and maturation mechanism within the tetra virus family. This model can be extrapolated to other systems, highlighting the importance of the precise folding of the proteins to drive complex particle and chemical changes. It also illustrates the ability of a unique protein chain to specialize and adopt different conformations determined by their quaternary structure environments. In conclusion, N ω V is a fascinating system to study dynamics and virus maturation. This thesis provides the basis to fully understand this complex mechanism with a broader view on the intermediate structures and conformational changes that take place in N ω V, a unique programmed nanomachine.

References

- Abad-Zapatero, C., Abdel-Meguid, S.S., Johnson, J.E., Leslie, A.G.W., Rayment, I., Rossmann, M.G., Suck, D., and Tsukihara, T. (1980). Structure of southern bean mosaic virus at 2.8 Å resolution. *Nature* *286*, 33–39.
- Adams, P.D., Afonine, P.V., Bunkóczi, G., Chen, V.B., Davis, I.W., Echols, N., Headd, J.J., Hung, L.-W., Kapral, G.J., Grosse-Kunstleve, R.W., et al. (2010). PHENIX: a comprehensive Python-based system for macromolecular structure solution. *Acta Crystallogr. D Biol. Crystallogr.* *66*, 213–221.
- Adrian, M., Dubochet, J., Lepault, J., and McDowell, A.W. (1984). Cryo-electron microscopy of viruses. *Nature* *308*, 32–36.
- Afonine, P.V., Poon, B.K., Read, R.J., Sobolev, O.V., Terwilliger, T.C., Urzhumtsev, A., and Adams, P.D. (2018). Real-space refinement in *PHENIX* for cryo-EM and crystallography. *Acta Crystallogr. Sect. Struct. Biol.* *74*, 531–544.
- Agrawal, D.K., and Johnson, J.E. (1992). Sequence and analysis of the capsid protein of *Nudaurelia capensis* ω virus, an insect virus with T = 4 icosahedral symmetry. *Virology* *190*, 806–814.
- Agrawal, D.K., and Johnson, J.E. (1995). Assembly of the T = 4 *Nudaurelia capensis* ω virus capsid protein, post-translational cleavage, and specific encapsidation of its mRNA in a baculovirus expression system. *Virology* *207*, 89–97.
- Alushin, G.M., Lander, G.C., Kellogg, E.H., Zhang, R., Baker, D., and Nogales, E. (2014). High-resolution microtubule structures reveal the structural transitions in $\alpha\beta$ -tubulin upon GTP hydrolysis. *Cell* *157*, 1117–1129.
- Amunts, A., Brown, A., Bai, X., Ll acer, J.L., Hussain, T., Emsley, P., Long, F., Murshudov, G., Scheres, S.H.W., and Ramakrishnan, V. (2014). Structure of the yeast mitochondrial large ribosomal subunit. *343*, 1485–1489.
- Arntzen, C. (2015). Plant-made pharmaceuticals: from ‘Edible Vaccines’ to Ebola therapeutics. *Plant Biotechnol. J.* *13*, 1013–1016.
- Aumiller, W.M., Uchida, M., and Douglas, T. (2018). Protein cage assembly across multiple length scales. *Chem. Soc. Rev.* *47*, 3433–3469.
- Avesani, L., Merlin, M., Gecchele, E., Capaldi, S., Brozzetti, A., Falorni, A., and Pezzotti, M. (2014). Comparative analysis of different biofactories for the production of a major diabetes autoantigen. *Transgenic Res.* *23*, 281–291.
- Azizgolshani, O., Garmann, R.F., Cadena-Nava, R., Knobler, C.M., and Gelbart, W.M. (2013). Reconstituted plant viral capsids can release genes to mammalian cells. *Virology* *441*, 12–17.
- Bai, X., McMullan, G., and Scheres, S.H.W. (2015). How cryo-EM is revolutionizing structural biology. *Trends Biochem. Sci.* *40*, 49–57.
- Bajaj, S., Dey, D., Bhukar, R., Kumar, M., and Banerjee, M. (2016). Non-enveloped virus entry: Structural determinants and mechanism of functioning of a viral lytic peptide. *J. Mol. Biol.* *428*, 3540–3556.

- Bally, J., Jung, H., Mortimer, C., Naim, F., Philips, J.G., Hellens, R., Bombarely, A., Goodin, M.M., and Waterhouse, P.M. (2018). The Rise and Rise of *Nicotiana benthamiana*: A plant for all reasons. *Annu. Rev. Phytopathol.* *56*, 405–426.
- Banerjee, M., and Johnson, J.E. (2008). Activation, exposure and penetration of virally encoded, membrane-active polypeptides during non-enveloped virus entry. *Curr. Protein Pept. Sci.* *9*, 16–27.
- Banerjee, M., Khayat, R., Walukiewicz, H.E., Odegard, A.L., Schneemann, A., and Johnson, J.E. (2009). Dissecting the functional domains of a nonenveloped virus membrane penetration peptide. *J. Virol.* *83*, 6929–6933.
- Belhaj, K., Chaparro-Garcia, A., Kamoun, S., Patron, N.J., and Nekrasov, V. (2015). Editing plant genomes with CRISPR/Cas9. *Curr. Opin. Biotechnol.* *32*, 76–84.
- Bergh, Ø., Børsheim, K.Y., Bratbak, G., and Heldal, M. (1989). High abundance of viruses found in aquatic environments. *Nature* *340*, 467–468.
- Bloomer, A.C., Champness, J.N., Bricogne, G., Staden, R., and Klug, A. (1978). Protein disk of tobacco mosaic virus at 2.8 Å resolution showing the interactions within and between subunits. *Nature* *276*, 362–368.
- von Borries, B., Ruska, E., and Ruska, H. (1938). Bakterien und Virus in Übermikroskopischer Aufnahme. *Klin. Wochenschr.* *17*, 921–925.
- Bothner, B., Schneemann, A., Marshall, D., Reddy, V., Johnson, J.E., and Siuzdak, G. (1999). Crystallographically identical virus capsids display different properties in solution. *Nat. Struct. Biol.* *6*, 114–116.
- Bothner, B., Taylor, D., Jun, B., Lee, K.K., Siuzdak, G., Schlutz, C.P., and Johnson, J.E. (2005). Maturation of a tetra virus capsid alters the dynamic properties and creates a metastable complex. *Virology* *334*, 17–27.
- Boyken, S.E., Benhaim, M.A., Busch, F., Jia, M., Bick, M.J., Choi, H., Klima, J.C., Chen, Z., Walkey, C., Mileant, A., et al. (2019). De novo design of tunable, pH-driven conformational changes. *Science* *364*, 658–664.
- Brillault, L., Jutras, P.V., Dashti, N., Thuenemann, E.C., Morgan, G., Lomonosoff, G.P., Landsberg, M.J., and Sainsbury, F. (2017). Engineering recombinant virus-like nanoparticles from plants for cellular delivery. *ACS Nano* *11*, 3476–3484.
- Brooks, E.M., Gordon, K.H.J., Dorrian, S.J., Hines, E.R., and Hanzlik, T.N. (2002). Infection of its lepidopteran host by the *Helicoverpa armigera* stunt virus (Tetraviridae). *J. Invertebr. Pathol.* *80*, 97–111.
- Butterfield, G.L., Lajoie, M.J., Gustafson, H.H., Sellers, D.L., Nattermann, U., Ellis, D., Bale, J.B., Ke, S., Lenz, G.H., Yehdego, A., et al. (2017). Evolution of a designed protein assembly encapsulating its own RNA genome. *Nature* *552*, 415–420.
- Campbell, M.G., Kearney, B.M., Cheng, A., Potter, C.S., Johnson, J.E., Carragher, B., and Veesler, D. (2014). Near-atomic resolution reconstructions using a mid-range electron microscope operated at 200kV. *J. Struct. Biol.* *188*, 183–187.
- Canady, M.A., Tihova, M., Hanzlik, T.N., Johnson, J.E., and Yeager, M. (2000). Large conformational changes in the maturation of a simple RNA virus, *Nudaurelia capensis* ω virus (NωV). *J. Mol. Biol.* *299*, 573–584.

- Canady, M.A., Tsuruta, H., and Johnson, J.E. (2001). Analysis of rapid, large-scale protein quaternary structural changes: time-resolved X-ray solution scattering of Nudaurelia capensis ω virus (N ω V) maturation. *J. Mol. Biol.* *311*, 803–814.
- Caspar, D.L. (1980). Movement and self-control in protein assemblies. Quasi-equivalence revisited. *Biophys. J.* *32*, 103–138.
- Caspar, D.L.D., and Klug, A. (1962). Physical principles in the construction of regular viruses. *Cold Spring Harb. Symp. Quant. Biol.* *27*, 1–24.
- Castells-Graells, R., Lomonosoff, G.P., and Saunders, K. (2018). Production of Mosaic Turnip Crinkle Virus-Like Particles Derived by Coinfiltration of Wild-Type and Modified Forms of Virus Coat Protein in Plants. In *Virus-Derived Nanoparticles for Advanced Technologies: Methods and Protocols*, C. Wege, and G.P. Lomonosoff, eds. (New York, NY: Springer New York), pp. 3–17.
- Chen, Z., Stauffacher, C., Li, Y., Schmidt, T., Bomu, W., Kamer, G., Shanks, M., Lomonosoff, G., and Johnson, J. (1989). Protein-RNA interactions in an icosahedral virus at 3.0 Å resolution. *Science* *245*, 154–159.
- Cheng, R.H., Reddy, V.S., Olson, N.H., Fisher, A.J., Baker, T.S., and Johnson, J.E. (1994). Functional implications of quasi-equivalence in a T=3 icosahedral animal virus established by cryo-electron microscopy and X-ray crystallography. *Structure* *2*, 271–282.
- Christian, P.D., Murray, D., Powell, R., Hopkinson, J., Gibb, N.N., and Hanzlik, T.N. (2005). Effective control of a field population of *Helicoverpa armigera* by using the small RNA virus *Helicoverpa armigera* stunt virus (Tetraviridae: Omegatetravirus). *J. Econ. Entomol.* *98*, 1839–1847.
- Cressey, D., and Callaway, E. (2017). Cryo-electron microscopy wins chemistry Nobel. *Nature* *550*, 167–167.
- Cristie-David, A.S., Chen, J., Nowak, D.B., Bondy, A.L., Sun, K., Park, S.I., Banaszak Holl, M.M., Su, M., and Marsh, E.N.G. (2019). Coiled-coil-mediated assembly of an icosahedral protein cage with extremely high thermal and chemical stability. *J. Am. Chem. Soc.* *141*, 9207–9216.
- Czapar, A.E., and Steinmetz, N.F. (2017). Plant viruses and bacteriophages for drug delivery in medicine and biotechnology. *Curr. Opin. Chem. Biol.* *38*, 108–116.
- D'Aoust, M.-A., Lavoie, P.-O., Couture, M.M.-J., Trépanier, S., Guay, J.-M., Dargis, M., Mongrand, S., Landry, N., Ward, B.J., and Vézina, L.-P. (2008). Influenza virus-like particles produced by transient expression in *Nicotiana benthamiana* induce a protective immune response against a lethal viral challenge in mice. *Plant Biotechnol. J.* *6*, 930–940.
- Domitrovic, T., Matsui, T., and Johnson, J.E. (2012). Dissecting Quasi-Equivalence in Nonenveloped Viruses: Membrane Disruption Is Promoted by Lytic Peptides Released from Subunit Pentamers, Not Hexamers. *J. Virol.* *86*, 9976–9982.
- Domitrovic, T., Movahed, N., Bothner, B., Matsui, T., Wang, Q., Doerschuk, P.C., and Johnson, J.E. (2013). Virus assembly and maturation: Auto-regulation through allosteric molecular switches. *J. Mol. Biol.* *425*, 1488–1496.
- Dong, X.F., Natarajan, P., Tihova, M., Johnson, J.E., and Schneemann, A. (1998). Particle polymorphism caused by deletion of a peptide molecular switch in a quasiequivalent icosahedral virus. *J. VIROL* *72*, 10.
- Dow, J. (1992). pH gradients in lepidopteran midgut. *J. Exp. Biol.* *172*, 355.
- Dubochet, J., Chang, J.-J., Freeman, R., Lepault, J., and McDowell, A.W. (1982). Frozen aqueous suspensions. *Ultramicroscopy* *10*, 55–61.

- Earl, L.A., and Subramaniam, S. (2016). Cryo-EM of viruses and vaccine design. *Proc. Natl. Acad. Sci.* *113*, 8903–8905.
- Edwardson, T.G.W., Mori, T., and Hilvert, D. (2018). Rational engineering of a designed protein cage for siRNA delivery. *J. Am. Chem. Soc.* *140*, 10439–10442.
- Emsley, P., and Cowtan, K. (2004). Coot: model-building tools for molecular graphics. *Acta Crystallogr. Sect. D* *60*, 2126–2132.
- Fang, Q., Zhu, D., Agarkova, I., Adhikari, J., Klose, T., Liu, Y., Chen, Z., Sun, Y., Gross, M.L., Van Etten, J.L., et al. (2019). Near-atomic structure of a giant virus. *Nat. Commun.* *10*, 388.
- Fernandez-Leiro, R., and Scheres, S.H.W. (2017). A pipeline approach to single-particle processing in *RELION*. *Acta Crystallogr. Sect. Struct. Biol.* *73*, 496–502.
- Flint, J., Racaniello, V.R., Rall, G.F., and Skalka, A.M. (2015). *Principles of Virology* (ASM Press).
- Fraenkel-Conrat, H., and Williams, R.C. (1955). Reconstitution of active tobacco mosaic virus from its inactive protein and nucleic acid components. *Proc. Natl. Acad. Sci.* *41*, 690.
- Fraenkel-Conrat, H., Singer, B., and Williams, R.C. (1957). Infectivity of viral nucleic acid. *Biochim. Biophys. Acta* *25*, 87–96.
- French, T.J., Marshall, J.J., and Roy, P. (1990). Assembly of double-shelled, viruslike particles of bluetongue virus by the simultaneous expression of four structural proteins. *J. Virol.* *64*, 5695.
- Ghilarov, D., Stevenson, C.E.M., Travin, D.Y., Piskunova, J., Serebryakova, M., Maxwell, A., Lawson, D.M., and Severinov, K. (2019). Architecture of microcin B17 synthetase: An octameric protein complex converting a ribosomally synthesized peptide into a DNA gyrase poison. *Mol. Cell* *73*, 749–762.
- Gierer, A., and Schramm, G. (1956). Infectivity of Ribonucleic Acid from Tobacco Mosaic Virus. *Nature* *177*, 702–703.
- Goddard, T.D., Huang, C.C., Meng, E.C., Pettersen, E.F., Couch, G.S., Morris, J.H., and Ferrin, T.E. (2018). UCSF ChimeraX: Meeting modern challenges in visualization and analysis: UCSF ChimeraX Visualization System. *Protein Sci.* *27*, 14–25.
- Goodin, M.M., Zaitlin, D., Naidu, R.A., and Lommel, S.A. (2008). *Nicotiana benthamiana*: Its History and Future as a Model for Plant–Pathogen Interactions. *Mol. Plant. Microbe Interact.* *21*, 1015–1026.
- Grace, T.D.C., and Mercer, E.H. (1965). A new virus of the saturniid *Antheraea eucalypti* Scott. *J. Invertebr. Pathol.* *7*, 241–244.
- Hanzlik, T.N., and Gordon, K.H.J. (1997). The Tetraviridae. In *Advances in Virus Research*, K. Maramorosch, F.A. Murphy, and A.J. Shatkin, eds. (Academic Press), pp. 101–168.
- Harrison, S.C., Olson, A.J., Schutt, C.E., Winkler, F.K., and Bricogne, G. (1978). Tomato bushy stunt virus at 2.9 Å resolution. *Nature* *276*, 368–373.
- Helgstrand, C., Munshi, S., Johnson, J.E., and Liljas, L. (2004). The refined structure of *Nudaurelia capensis* ω Virus reveals control elements for a T = 4 capsid maturation. *Virology* *318*, 192–203.
- Hendry, D., Hodgson, V., Clark, R., and Newman, J. (1985). Small RNA viruses co-infecting the pine emperor moth (*Nudaurelia cytherea capensis*). *J. Gen. Virol.* *66*, 627–632.

- Hershey, A.D., and Chase, M. (1952). Independent functions of viral protein and nucleic acid in growth of bacteriophage. *J. Gen. Physiol.* *36*, 39–56.
- Hesketh, E.L., Meshcheriakova, Y., Dent, K.C., Saxena, P., Thompson, R.F., Cockburn, J.J., Lomonosoff, G.P., and Ranson, N.A. (2015). Mechanisms of assembly and genome packaging in an RNA virus revealed by high-resolution cryo-EM. *Nat. Commun.* *6*, 10113.
- Hesketh, E.L., Meshcheriakova, Y., Thompson, R.F., Lomonosoff, G.P., and Ranson, N.A. (2017). The structures of a naturally empty cowpea mosaic virus particle and its genome-containing counterpart by cryo-electron microscopy. *Sci. Rep.* *7*, 539.
- Hesketh, E.L., Saunders, K., Fisher, C., Potze, J., Stanley, J., Lomonosoff, G.P., and Ranson, N.A. (2018). The 3.3 Å structure of a plant geminivirus using cryo-EM. *Nat. Commun.* *9*, 2369.
- Hoekema, A., Hirsch, P.R., Hooykaas, P.J.J., and Schilperoort, R.A. (1983). A binary plant vector strategy based on separation of vir- and T-region of the *Agrobacterium tumefaciens* Ti-plasmid. *Nature* *303*, 179–180.
- Hogle, J., Chow, M., and Filman, D. (1985). Three-dimensional structure of poliovirus at 2.9 Å resolution. *Science* *229*, 1358–1365.
- Hosur, M.V., Schmidt, T., Tucker, R.C., Johnson, J.E., Gallagher, T.M., Selling, B.H., and Rueckert, R.R. (1987). Structure of an insect virus at 3.0 Å resolution. *Proteins Struct. Funct. Genet.* *2*, 167–176.
- Howorka, S. (2011). Rationally engineering natural protein assemblies in nanobiotechnology. *Curr. Opin. Biotechnol.* *22*, 485–491.
- Hsia, Y., Bale, J.B., Gonen, S., Shi, D., Sheffler, W., Fong, K.K., Nattermann, U., Xu, C., Huang, P.-S., Ravichandran, R., et al. (2016). Design of a hyperstable 60-subunit protein icosahedron. *Nature* *535*, 136–139.
- Hutchings, J., and Zanetti, G. (2018). Fine details in complex environments: the power of cryo-electron tomography. *Biochem. Soc. Trans.* *46*, 807–816.
- Ilca, S.L., Sun, X., El Omari, K., Kotecha, A., de Haas, F., DiMaio, F., Grimes, J.M., Stuart, D.I., Poranen, M.M., and Huiskonen, J.T. (2019). Multiple liquid crystalline geometries of highly compacted nucleic acid in a dsRNA virus. *Nature* *570*, 252–256.
- Johnson, J.E. (2010). Virus particle maturation: insights into elegantly programmed nanomachines. *Curr. Opin. Struct. Biol.* *20*, 210–216.
- Johnson, J.E. (2013). Confessions of an icosahedral virus crystallographer. *Microscopy* *62*, 69–79.
- Johnson, J.E., and Chiu, W. (2000). Structures of virus and virus-like particles. *Curr. Opin. Struct. Biol.* *10*, 229–235.
- Jung, J., Grant, T., Thomas, D.R., Diehnelt, C.W., Grigorieff, N., and Joshua-Tor, L. (2019). High-resolution cryo-EM structures of outbreak strain human norovirus shells reveal size variations. *Proc. Natl. Acad. Sci.* *116*, 12828–12832.
- Kadri, A., Wege, C., and Jeske, H. (2013). In vivo self-assembly of TMV-like particles in yeast and bacteria for nanotechnological applications. *J. Virol. Methods* *189*, 328–340.
- Katen, S., and Zlotnick, A. (2009). Chapter 14 The Thermodynamics of Virus Capsid Assembly. In *Methods in Enzymology*, (Elsevier), pp. 395–417.
- Kausche, G.A., Pfankuch, E., and Ruska, H. (1939). Die Sichtbarmachung von pflanzlichem Virus im Übermikroskop. *Naturwissenschaften* *27*, 292–299.

- Kearney, B., and Johnson, J. (2014). Assembly and Maturation of a T = 4 Quasi-Equivalent Virus Is Guided by Electrostatic and Mechanical Forces. *Viruses* 6, 3348–3362.
- Kendrew, J.C., Dickerson, R.E., Strandberg, B.E., Hart, R.G., Davies, D.R., Phillips, D.C., and Shore, V.C. (1960). Structure of myoglobin: A three-dimensional fourier synthesis at 2 Å resolution. *Nature* 185, 422–427.
- Kimanius, D., Forsberg, B.O., Scheres, S.H., and Lindahl, E. (2016). Accelerated cryo-EM structure determination with parallelisation using GPUs in RELION-2. *ELife* 5, e18722.
- King, N.P., Sheffler, W., Sawaya, M.R., Vollmar, B.S., Sumida, J.P., Andre, I., Gonen, T., Yeates, T.O., and Baker, D. (2012). Computational design of self-assembling protein nanomaterials with atomic level accuracy. *Science* 336, 1171–1174.
- King, N.P., Bale, J.B., Sheffler, W., McNamara, D.E., Gonen, S., Gonen, T., Yeates, T.O., and Baker, D. (2014). Accurate design of co-assembling multi-component protein nanomaterials. *Nature* 510, 103–108.
- Kretzschmar, T., Aoustin, L., Zingel, O., Marangi, M., Vonach, B., Towbin, H., and Geiser, M. (1996). High-level expression in insect cells and purification of secreted monomeric single-chain Fv antibodies. *J. Immunol. Methods* 195, 93–101.
- Kruger, D., Schneck, P., and Gelderblom, H. (2000). Helmut Ruska and the visualisation of viruses. *The Lancet* 355, 1713–1717.
- Kuhlbrandt, W. (2014). The Resolution Revolution. *Science* 343, 1443–1444.
- Lai, Y.-T., Cascio, D., and Yeates, T.O. (2012). Structure of a 16-nm Cage Designed by Using Protein Oligomers. *Science* 336, 1129–1129.
- Lawson, D.M., Artymiuk, P.J., Yewdall, S.J., Smith, J.M.A., Livingstone, J.C., Treffry, A., Luzzago, A., Levi, S., Arosio, P., Cesareni, G., et al. (1991). Solving the structure of human H ferritin by genetically engineering intermolecular crystal contacts. *Nature* 349, 541–544.
- Lecorre, F., Lai-Kee-Him, J., Blanc, S., Zeddani, J.-L., Trapani, S., and Bron, P. (2019). The cryo-electron microscopy structure of Broad Bean Stain Virus suggests a common capsid assembly mechanism among comoviruses. *Virology* 530, 75–84.
- Lee, L., and Wang, Q. (2006). Adaptations of nanoscale viruses and other protein cages for medical applications. *Nanomedicine Nanotechnol. Biol. Med.* 2, 137–149.
- Lee, K.K., Gan, L., Tsuruta, H., Hendrix, R.W., Duda, R.L., and Johnson, J.E. (2004). Evidence that a local refolding event triggers maturation of HK97 bacteriophage capsid. *J. Mol. Biol.* 340, 419–433.
- Leong, H.S., Steinmetz, N.F., Ablack, A., Destito, G., Zijlstra, A., Stuhlmann, H., Manchester, M., and Lewis, J.D. (2010). Intravital imaging of embryonic and tumor neovasculature using viral nanoparticles. *Nat. Protoc.* 5, 1406–1417.
- Liu, H., Jin, L., Koh, S.B.S., Atanasov, I., Schein, S., Wu, L., and Zhou, Z.H. (2010). Atomic structure of human adenovirus by cryo-EM reveals interactions among protein networks. *Science* 329, 1038–1043.
- Liu, Y., Hill, M.G., Klose, T., Chen, Z., Watters, K., Bochkov, Y.A., Jiang, W., Palmenberg, A.C., and Rossmann, M.G. (2016). Atomic structure of a rhinovirus C, a virus species linked to severe childhood asthma. *Proc. Natl. Acad. Sci.* 113, 8997–9002.
- Liu, Y., Gonen, S., Gonen, T., and Yeates, T.O. (2018). Near-atomic cryo-EM imaging of a small protein displayed on a designed scaffolding system. *Proc. Natl. Acad. Sci.* 115, 3362–3367.

- Liu, Y., Huynh, D.T., and Yeates, T.O. (2019a). A 3.8 Å resolution cryo-EM structure of a small protein bound to an imaging scaffold. *Nat. Commun.* *10*, 1864.
- Liu, Y.-T., Jih, J., Dai, X., Bi, G.-Q., and Zhou, Z.H. (2019b). Cryo-EM structures of herpes simplex virus type 1 portal vertex and packaged genome. *Nature* *570*, 257–261.
- Lomonosoff, G.P. (2018). So what have plant viruses ever done for virology and molecular biology? In *Advances in Virus Research*, (Elsevier), pp. 145–162.
- Lomonosoff, G.P., and D'Aoust, M.-A. (2016). Plant-produced biopharmaceuticals: A case of technical developments driving clinical deployment. *Science* *353*, 1237–1240.
- Lomonosoff, G.P., and Evans, D.J. (2014). Applications of plant viruses in bionanotechnology. In *Plant Viral Vectors*, K. Palmer, and Y. Gleba, eds. (Berlin, Heidelberg: Springer Berlin Heidelberg), pp. 61–87.
- Lustig, A., and Levine, A.J. (1992). One hundred years of virology. *J. Virol.* *66*, 4629.
- Ma, J.K.-C., Drake, P.M.W., and Christou, P. (2003). The production of recombinant pharmaceutical proteins in plants. *Nat. Rev. Genet.* *4*, 794–805.
- Malay, A.D., Miyazaki, N., Biela, A., Chakraborti, S., Majsterkiewicz, K., Stupka, I., Kaplan, C.S., Kowalczyk, A., Piette, B.M.A.G., Hochberg, G.K.A., et al. (2019). An ultra-stable gold-coordinated protein cage displaying reversible assembly. *Nature* *569*, 438–442.
- Maree, H.J., van der Walt, E., Tiedt, F.A.C., Hanzlik, T.N., and Appel, M. (2006). Surface display of an internal His-tag on virus-like particles of *Nudaurelia capensis* ω virus (N ω V) produced in a baculovirus expression system. *J. Virol. Methods* *136*, 283–288.
- Marsian, J., and Lomonosoff, G.P. (2016). Molecular pharming — VLPs made in plants. *Curr. Opin. Biotechnol.* *37*, 201–206.
- Marsian, J., Fox, H., Bahar, M.W., Kotecha, A., Fry, E.E., Stuart, D.I., Macadam, A.J., Rowlands, D.J., and Lomonosoff, G.P. (2017). Plant-made polio type 3 stabilized VLPs—a candidate synthetic polio vaccine. *Nat. Commun.* *8*, 245.
- Marsian, J., Hurdiss, D.L., Ranson, N.A., Ritala, A., Paley, R., Cano, I., and Lomonosoff, G.P. (2019). Plant-Made Nervous Necrosis Virus-Like Particles Protect Fish Against Disease. *Front. Plant Sci.* *10*, 880.
- Masavuli, M.G., Wijesundara, D.K., Torresi, J., Gowans, E.J., and Grubor-Bauk, B. (2017). Preclinical development and production of virus-like particles as vaccine candidates for Hepatitis C. *Front. Microbiol.* *8*, 2413.
- Matsui, T., Lander, G., and Johnson, J.E. (2009). Characterization of large conformational changes and autoproteolysis in the maturation of a T=4 virus capsid. *J. Virol.* *83*, 1126–1134.
- Matsui, T., Tsuruta, H., and Johnson, J.E. (2010a). Balanced electrostatic and structural forces guide the large conformational change associated with maturation of T = 4 virus. *Biophys. J.* *98*, 1337–1343.
- Matsui, T., Lander, G.C., Khayat, R., and Johnson, J.E. (2010b). Subunits fold at position-dependent rates during maturation of a eukaryotic RNA virus. *Proc. Natl. Acad. Sci.* *107*, 14111–14115.
- McMullan, G., Faruqi, A.R., Clare, D., and Henderson, R. (2014). Comparison of optimal performance at 300keV of three direct electron detectors for use in low dose electron microscopy. *Ultramicroscopy* *147*, 156–163.

Mettenleiter, T.C., Kielian, M., and Roossinck, M.J. (2018). Preface to Volume 100: History and Looking Forward. In *Advances in Virus Research*, (Elsevier), pp. 15–24.

Metz, S.W., Gardner, J., Geertsema, C., Le, T.T., Goh, L., Vlak, J.M., Suhrbier, A., and Pijlman, G.P. (2013). Effective Chikungunya virus-like particle vaccine produced in insect cells. *PLoS Negl. Trop. Dis.* 7, e2124.

Moelling, K. (2012). Are viruses our oldest ancestors? *EMBO Rep.* 13, 1033–1033.

Munshi, S., Liljas, L., Cavarelli, J., Bomu, W., McKinney, B., Reddy, V., and Johnson, J.E. (1996). The 2.8 Å structure of a T=4 Animal virus and its implications for membrane translocation of RNA. *J. Mol. Biol.* 261, 1–10.

Nogales, E., and Scheres, S.H.W. (2015). Cryo-EM: A unique tool for the visualization of macromolecular complexity. *Mol. Cell* 58, 677–689.

Odegard, A.L., Kwan, M.H., Walukiewicz, H.E., Banerjee, M., Schneemann, A., and Johnson, J.E. (2009). Low Endocytic pH and Capsid Protein Autocleavage Are Critical Components of Flock House Virus Cell Entry. *J. Virol.* 83, 8628–8637.

van Oers, M.M., Pijlman, G.P., and Vlak, J.M. (2015). Thirty years of baculovirus-insect cell protein expression: from dark horse to mainstream technology. *J. Gen. Virol.* 96, 6–23.

Padilla, J.E., Colovos, C., and Yeates, T.O. (2001). Nanohedra: Using symmetry to design self assembling protein cages, layers, crystals, and filaments. *Proc. Natl. Acad. Sci.* 98, 2217–2221.

Pei, X.Y., Dendooven, T., Sonnleitner, E., Chen, S., Bläsi, U., and Luisi, B.F. (2019). Architectural principles for Hfq/Crc-mediated regulation of gene expression. *ELife* 8, e43158.

Penkler, D.L., Jiwaji, M., Domitrovic, T., Short, J.R., Johnson, J.E., and Dorrington, R.A. (2016). Binding and entry of a non-enveloped T=4 insect RNA virus is triggered by alkaline pH. *Virology* 498, 277–287.

Perutz, M.F., Rossmann, M.G., Cullis, A.F., Muirhead, H., Will, G., and North, A.C.T. (1960). Structure of hæmoglobin: A three-dimensional Fourier synthesis at 5.5-Å resolution, obtained by X-Ray analysis. *Nature* 185, 416–422.

Peyret, H. (2015). A protocol for the gentle purification of virus-like particles produced in plants. *J. Virol. Methods* 225, 59–63.

Peyret, H., and Lomonosoff, G.P. (2013). The pEAQ vector series: the easy and quick way to produce recombinant proteins in plants. *Plant Mol. Biol.* 83, 51–58.

Peyret, H., and Lomonosoff, G.P. (2015). When plant virology met *Agrobacterium*: the rise of the deconstructed clones. *Plant Biotechnol. J.* 13, 1121–1135.

Peyret, H., Gehin, A., Thuenemann, E.C., Blond, D., El Turabi, A., Beales, L., Clarke, D., Gilbert, R.J.C., Fry, E.E., Stuart, D.I., et al. (2015). Tandem fusion of Hepatitis B core antigen allows assembly of virus-like particles in bacteria and plants with enhanced capacity to accommodate foreign proteins. *PLOS ONE* 10, e0120751.

Pieters, B.J.G.E., van Eldijk, M.B., Nolte, R.J.M., and Mecinović, J. (2016). Natural supramolecular protein assemblies. *Chem. Soc. Rev.* 45, 24–39.

du Plessis, L., Hendry, D.A., Dorrington, R.A., Hanzlik, T.N., Johnson, J.E., and Appel, M. (2005). Revised RNA2 sequence of the tetravirus, *Nudaurelia capensis* ω virus (NωV). *Arch. Virol.* 150, 2397–2402.

- Putnam, C.D., Hammel, M., Hura, G.L., and Tainer, J.A. (2007). X-ray solution scattering (SAXS) combined with crystallography and computation: defining accurate macromolecular structures, conformations and assemblies in solution. *Q. Rev. Biophys.* *40*, 191–285.
- Rawlings, N.D., Barrett, A.J., and Bateman, A. (2011). Asparagine peptide lyases: A seventh catalytic type of proteolytic enzymes. *J. Biol. Chem.* *286*, 38321–38328.
- Roosien, J., Belsham, G.J., Ryan, M.D., King, A.M.Q., and Vlak, J.M. (1990). Synthesis of foot-and-mouth disease virus capsid proteins in insect cells using baculovirus expression vectors. *J. Gen. Virol.* *71*, 1703–1711.
- Rosenberg, Y., Sack, M., Montefiori, D., Forthal, D., Mao, L., -Abanto, S.H., Urban, L., Landucci, G., Fischer, R., and Jiang, X. (2013). Rapid high-level production of functional HIV broadly neutralizing monoclonal antibodies in transient plant expression systems. *PLoS ONE* *8*, e58724.
- Rossmann, M.G., and Johnson, J.E. (1989). Icosahedral RNA virus structure. *Annu. Rev. Biochem.* *58*, 533–569.
- Rossmann, M.G., Arnold, E., Erickson, J.W., Frankenberger, E.A., Griffith, J.P., Hecht, H.-J., Johnson, J.E., Kamer, G., Luo, M., Mosser, A.G., et al. (1985). Structure of a human common cold virus and functional relationship to other picornaviruses. *Nature* *317*, 145–153.
- Routh, A., Domitrovic, T., and Johnson, J.E. (2012). Host RNAs, including transposons, are encapsidated by a eukaryotic single-stranded RNA virus. *Proc. Natl. Acad. Sci.* *109*, 1907–1912.
- de Ruiter, M.V., Klem, R., Luque, D., Cornelissen, J.J.L.M., and Castón, J.R. (2019). Structural nanotechnology: three-dimensional cryo-EM and its use in the development of nanoplatforms for *in vitro* catalysis. *Nanoscale* *11*, 4130–4146.
- Ruska, E. (1987). The Development of the Electron Microscope and of Electron Microscopy (Nobel Lecture). *Angew. Chem. Int. Ed. Engl.* *26*, 595–605.
- Ruskin, R.S., Yu, Z., and Grigorieff, N. (2013). Quantitative characterization of electron detectors for transmission electron microscopy. *J. Struct. Biol.* *184*, 385–393.
- Safi, M., Domitrovic, T., Kapur, A., Zhan, N., Aldeek, F., Johnson, J.E., and Mattoussi, H. (2017). Intracellular Delivery of Luminescent Quantum Dots Mediated by a Virus-Derived Lytic Peptide. *Bioconjug. Chem.* *28*, 64–74.
- Sainsbury, F., and Lomonosoff, G.P. (2008). Extremely high-level and rapid transient protein production in plants without the use of viral replication. *Plant Physiol.* *148*, 1212–1218.
- Sainsbury, F., Thuenemann, E.C., and Lomonosoff, G.P. (2009). pEAQ: versatile expression vectors for easy and quick transient expression of heterologous proteins in plants. *Plant Biotechnol. J.* *7*, 682–693.
- Sainsbury, F., Sack, M., Stadlmann, J., Quendler, H., Fischer, R., and Lomonosoff, G.P. (2010). Rapid transient production in plants by replicating and non-replicating vectors yields high quality functional anti-HIV antibody. *PLoS ONE* *5*, e13976.
- Sasaki, E., Böhringer, D., van de Waterbeemd, M., Leibundgut, M., Zschoche, R., Heck, A.J.R., Ban, N., and Hilvert, D. (2017). Structure and assembly of scalable porous protein cages. *Nat. Commun.* *8*, 14663.
- Saunders, K., Sainsbury, F., and Lomonosoff, G.P. (2009). Efficient generation of cowpea mosaicvirus empty virus-like particles by the proteolytic processing of precursors in insect cells and plants. *Virology* *393*, 329–337.

- Scheres, S.H.W. (2012). RELION: Implementation of a Bayesian approach to cryo-EM structure determination. *J. Struct. Biol.* *180*, 519–530.
- Scheres, S.H.W., and Chen, S. (2012). Prevention of overfitting in cryo-EM structure determination. *Nat. Methods* *9*, 853–854.
- Sirohi, D., Chen, Z., Sun, L., Klose, T., Pierson, T.C., Rossmann, M.G., and Kuhn, R.J. (2016). The 3.8 Å resolution cryo-EM structure of Zika virus. *Science* *352*, 467–470.
- Smith, M.T.J., and Rubinstein, J.L. (2014). Beyond blob-ology. *Science* *345*, 617–619.
- Speir, J.A., and Johnson, J.E. (2008). Tetraviruses. In *Encyclopedia of Virology*, (Oxford: Elsevier), pp. 27–37.
- Speir, J.A., Taylor, D.J., Natarajan, P., Pringle, F.M., Ball, L.A., and Johnson, J.E. (2010). Evolution in Action: N and C Termini of Subunits in Related T = 4 Viruses Exchange Roles as Molecular Switches. *Structure* *18*, 700–709.
- Steele, J.F.C., Peyret, H., Saunders, K., Castells-Graells, R., Marsian, J., Meshcheriakova, Y., and Lomonosoff, G.P. (2017). Synthetic plant virology for nanobiotechnology and nanomedicine. *Wiley Interdiscip. Rev. Nanomed. Nanobiotechnol.* *9*, e1447.
- Steven, A.C., Heymann, J.B., Cheng, N., Trus, B.L., and Conway, J.F. (2005). Virus maturation: dynamics and mechanism of a stabilizing structural transition that leads to infectivity. *Curr. Opin. Struct. Biol.* *15*, 227–236.
- Suttle, C.A. (2007). Marine viruses — major players in the global ecosystem. *Nat. Rev. Microbiol.* *5*, 801–812.
- Tan, Y.Z., Aiyer, S., Mietzsch, M., Hull, J.A., McKenna, R., Grieger, J., Samulski, R.J., Baker, T.S., Agbandje-McKenna, M., and Lyumkis, D. (2018). Sub-2 Å Ewald curvature corrected structure of an AAV2 capsid variant. *Nat. Commun.* *9*, 3628.
- Taylor, D.J. (2005). Folding and particle assembly are disrupted by single-point mutations near the autocatalytic cleavage site of Nudaurelia capensis virus capsid protein. *Protein Sci.* *14*, 401–408.
- Taylor, D.J., Krishna, N.K., Canady, M.A., Schneemann, A., and Johnson, J.E. (2002). Large-scale, pH-dependent, quaternary structure changes in an RNA virus capsid are reversible in the absence of subunit autoproteolysis. *J. Virol.* *76*, 9972–9980.
- Terasaka, N., Azuma, Y., and Hilvert, D. (2018). Laboratory evolution of virus-like nucleocapsids from nonviral protein cages. *Proc. Natl. Acad. Sci.* *115*, 5432–5437.
- Theze, J., Bezier, A., Periquet, G., Drezen, J.-M., and Herniou, E.A. (2011). Paleozoic origin of insect large dsDNA viruses. *Proc. Natl. Acad. Sci.* *108*, 15931–15935.
- Thuenemann, E.C., Meyers, A.E., Verwey, J., Rybicki, E.P., and Lomonosoff, G.P. (2013). A method for rapid production of heteromultimeric protein complexes in plants: assembly of protective bluetongue virus-like particles. *Plant Biotechnol. J.* *11*, 839–846.
- Tomasicchio, M., Venter, P.A., H. J. Gordon, K., N. Hanzlik, T., and Dorrington, R.A. (2007). Induction of apoptosis in *Saccharomyces cerevisiae* results in the spontaneous maturation of tetravirus procapsids in vivo. *J. Gen. Virol.* *88*, 1576–1582.
- Urakawa, T., Ferguson, M., Minor, P.D., Cooper, J., Sullivan, M., Almond, J.W., and Bishop, D.H.L. (1989). Synthesis of immunogenic, but non-infectious, poliovirus particles in insect cells by a baculovirus expression vector. *J. Gen. Virol.* *70*, 1453–1463.

- Veesler, D., and Johnson, J.E. (2012). Virus maturation. *Annu. Rev. Biophys.* *41*, 473–496.
- Veesler, D., Quispe, J., Grigorieff, N., Potter, C.S., Carragher, B., and Johnson, J.E. (2012). Maturation in action: CryoEM study of a viral capsid caught during expansion. *Structure* *20*, 1384–1390.
- Veesler, D., Ng, T.S., Sendamarai, A.K., Eilers, B.J., Lawrence, C.M., Lok, S.M., Young, M.J., Johnson, J.E., and Fu, C.Y. (2013). Atomic structure of the 75 MDa extremophile *Sulfolobus* turreted icosahedral virus determined by CryoEM and X-ray crystallography. *Proc. Natl. Acad. Sci.* *110*, 5504–5509.
- Walter, C.T., Tomasicchio, M., Hodgson, V., Hendry, D.A., Hill, M.P., and Dorrington, R.A. (2008). Characterization of a succession of small insect viruses in a wild South African population of *Nudaurelia cytherea capensis* (Lepidoptera: Saturniidae). *South Afr. J. Sci.* *104*, 147–152.
- Wang, G., Porta, C., Chen, Z., Baker, T.S., and Johnson, J.E. (1992). Identification of a Fab interaction footprint site on an icosahedral virus by cryoelectron microscopy and X-ray crystallography. *Nature* *355*, 275–278.
- Wolf, M., Garcea, R.L., Grigorieff, N., and Harrison, S.C. (2010). Subunit interactions in bovine papillomavirus. *Proc. Natl. Acad. Sci.* *107*, 6298–6303.
- Wu, C.-H., Adachi, H., De la Concepcion, J.C., Castells-Graells, R., Nekrasov, V., and Kamoun, S. (2019). A CRISPR/Cas9 mediated 53 kb deletion of the NRC4 gene cluster of tomato does not affect bacterial flagellin-triggered immunity. *BioRxiv*.
- Zhang, X., Settembre, E., Xu, C., Dormitzer, P.R., Bellamy, R., Harrison, S.C., and Grigorieff, N. (2008). Near-atomic resolution using electron cryomicroscopy and single-particle reconstruction. *Proc. Natl. Acad. Sci.* *105*, 1867–1872.
- Zheng, S.Q., Palovcak, E., Armache, J.-P., Verba, K.A., Cheng, Y., and Agard, D.A. (2017). MotionCor2: anisotropic correction of beam-induced motion for improved cryo-electron microscopy. *Nat. Methods* *14*, 331–332.
- Zimran, A., Brill-Almon, E., Chertkoff, R., Petakov, M., Blanco-Favela, F., Munoz, E.T., Solorio-Meza, S.E., Amato, D., Duran, G., Giona, F., et al. (2011). Pivotal trial with plant cell-expressed recombinant glucocerebrosidase, taliglucerase alfa, a novel enzyme replacement therapy for Gaucher disease. *Blood* *118*, 5767–5773.
- Zivanov, J., Nakane, T., Forsberg, B.O., Kimanius, D., Hagen, W.J., Lindahl, E., and Scheres, S.H. (2018). New tools for automated high-resolution cryo-EM structure determination in RELION-3. *ELife* *7*, e42166.
- Zlotnick, A. (2003). Are weak protein–protein interactions the general rule in capsid assembly? *Virology* *315*, 269–274.

Acronyms and abbreviations

Cryo-EM	Cryo-electron microscopy
CPMV	Cowpea mosaic virus
DNA	Deoxyribonucleic acid
dpi	Days post infiltration
EV	pEAQ- <i>HT</i> empty vector control
FHV	Flock house virus
HaSV	<i>Helicoverpa armigera</i> stunt virus
HT	HyperTrans
kDa	kilodalton
LC	Lead citrate
LCC	Large conformational change
MW	Molecular weight
MWCO	Molecular weight cut-off
NωV	<i>Nudaurelia capensis</i> omega virus
OD₆₀₀	Optical density at 600 nm
PCR	Polymerase chain reaction
PDB	Protein data bank
pEAQ	Easy and quick plasmid
PrV	Providence virus
RdRp	RNA-dependent RNA polymerase
RNA	Ribonucleic acid
SAXS	Small angle X-ray scattering
SDS-PAGE	Sodium dodecyl sulphate polyacrylamide gel electrophoresis
ssRNA	Single-stranded RNA
TEM	Transmission electron microscope
UA	Uranyl acetate
VLP	Virus-like particle
WT	Wild-type

Appendix 1 – Table of primers

The following table lists the DNA primers used for colony PCR, cloning and sequencing.

Name	Sequence (5' to 3')	Tm (°C)	Purpose
C1	AACGTTGTCAGATCGTGCTTCGGCACC	63	Colony PCR and sequencing of inserts between the 5'UTR and 3'UTR of pEAQ- <i>HT</i>
C3	CTGAAGGGACGACCTGCTAAACAGGAG	63	Colony PCR and sequencing of inserts between the 5'UTR and 3'UTR of pEAQ- <i>HT</i>
NwV_N570T_fwd	GTGTGTACGGTGCAACCGATACCTTCGC TGCTGCAGTTTCTGC	72	Site-directed mutagenesis to generate N570T mutant
NwV_N570T_rev	GCAGAAACTGCAGCAGCGAAGGTATCGG TTGCACCGTACACAC	72	Site-directed mutagenesis to generate N570T mutant
Seq_NwV_N570T_fwd	GGTGTGACCAATGTGAATACTCC	55	Sequencing of N570T mutant
Seq_NwV_N570T_rev	CCTGATTAGCAAGTCCGGTAGC	57	Sequencing of N570T mutant
RCG1-fwd-seq-pFastBac1	GGATTATTCATACCGTCCCACCATC	58	Sequencing insert in pFastBac1
RCG2-rev-seq-pFastBac1	CGGATCTCCTAGGCTCAAGC	56	Sequencing insert in pFastBac1
RCG3-fwd-seq-NwVmiddleCP	CTGATTACAGGCTGACCTACAAG	55	Sequencing from middle of NwV coat protein sequence codon optimized for plants
pUC/M13 Forward	CCCAGTCACGACGTTGTAACACG	57	PCR recombinant bacmid
pUC/M13 Reverse	AGCGGATAACAATTCACACAGG	54	PCR recombinant bacmid

Appendix 2 – Sequences

Start codons are highlighted in **green**, stop codons are highlighted in **red**.

Sequence utilised in this work: N ω V coat protein sequence codon-optimised for the expression in *N. benthamiana*.

ATGGATAGCAACAGCGCTTCTGGTAAGAGAAGGTCTAGGAACGTGAGGATCGCTGC
TAACACTGTGAATGTGGCTCCTAAGCAGAGACAGGCTAGAGGTAGAAGGGCTTGTCTAGGG
CTAACAAACATCGATAACGTGACCGCTGCTGCTCAAGAGCTTGGTCAATCTCTGGATGCTAAC
GTGATCACCTTCCCTACCAATGTGGCTACCATGCCTGAGTTTAGGTCTTGGGCTAGGGGTAA
GCTGGATATCGATCAGGATAGCATCGGTTGGTATTTCAAGTACCTGGATCCTGCTGGTGCTA
CCGAATCTGCTAGAGCTGTTGGTGAGTACAGCAAGATCCCTGATGGTCTGGTGAAGTTCTCT
GTGGATGCTGAGATCAGAGAGATCTACAACGAAGAGTGCCCTACCGTGCCGATGCTTCTAT
TCCTCTTGATGGTGCTCAGTGGTCCCTGTCCATTATCAGCTACCCTATGTTTCAGGACCGCTTA
CTTCGCTGTGGCTAATGTGGATAACAAAGAAATCAGCCTGGATGTGACCAACGATCTGATCG
TGTGGCTTAACAACCTGGCTTCTTGGAGGGATGTGGTGGATTCTGGTCAGTGGTTCGCTTTC
TCTGATGATCCTACCTGGTTCGTGAGGATTAGGGTGTTCATCCTACCTACGATCTGCCTGA
TCCTACTGAGGGTTGCTTAGGACCGTGTCTGATTACAGGCTGACCTACAAGAGCATTACCT
GCGAGGCTAACATGCCTACCCTTGTGGATCAGGGATTCTGGATTGGTGGTCACTACGCTTTC
ACCCCTATTGCTACTACTCAGAACGCAGTTGAGGGTAGCGGTTTCGTGCATCCTTTCAATGT
TACCAGGCCAGGTATTGCTGCTGGTGTGACTCTTACTTGGGCTTCTATGCCTCCTGGTGGTT
CTGCTCCTTCTGGTGATCCTGCTTGGATTCCCTGATTCTACCACTCAGTTCAGTGGAGGCATG
GTGGTTTTTGATGCTCCTACAGGTGTGATTACCTACCCATCCCTAGGGTTACACCATGCAG
TACTTCGATAACCACTACCAACGAGTGGAAACGGTTTCGCTAACCCCTGATGATGTGGTGACCTT
TGGTCAAACAGGTGGTGCTGCTGGAACCTAACGCTACCATTACTATTACCGCTCCTACCGTGA
CCCTTACCATTCTTGCTACCACTACTAGCGCTGCAAATGTGATCAACTTTAGGAACCTGGAT
GCAGAGACTACCGCTGCTTCTAACAGGTCTGAAGTTCCTCTTCCCTCCTCTGACATTCGGTCA
ACTGCTCCTAACAAACCCTAAGATTGAGCAGACCCTGGTGAAGGATACCCTGGGATCTTACCT
TGTGCACTCCAAGATGAGGAACCCTGTGTTCCAATTGACCCCTGCTTCTAGCTTCGGTGCTA
TCTCTTTCACCAACCCTGGTTTTCGATAGGAACCTTGGATCTGCCAGGTTTTCGGAGGTATCAGG
GATAGCCTTGATGTGAACATGTCTACCGCTGTGTGCCACTTCAGAAGCCTGTCTAAGTCTTG
CAGCATCGTGACTAAGACCTACCAAGGTTGGGAGGGTGTGACCAATGTGAATACTCCTTTCG
GTCAGTTCGCTCACTCTGGTCTGCTTAAGAACGATGAGATTCTGTGCCTGGCTGATGATCTG
GCTACTAGGCTTACTGGTGTGTACGGTGCAACCGATAACTTCGCTGCTGCAGTTTCTGCTTT
CGCAGCAAACATGCTTACCAGCGTGTGAAGTCTGAGGCTACCACCTCTGTGATCAAAGAGT
TGGGTAACCAGGCTACCGGACTTGCTAATCAGGGTTTTGGCTAGACTTCTGGACTGCTGGCT
TCAATCCCTGGTAAGATTGCTGCTAGGGTTAGGGCTAGAAGGGATAGAAGAAGGGCTGCTA
GGATGAACAACAAC**TAG**

Sequence utilised in this work: N ω V coat protein sequence from the pFastBac1 vector used for the insect cells expression.

ATG GACAGTAACTCAGCCTCCGGTAAGCGACGATCCCGCAATGTGCGGATTGCAGCC
AACACCGTCAACGTCGCTCCGAAGCAACGCCAAGCACGCGGCCGCGAGCCTGTTACGTGCC
AACAAATCGACAATGTCACTGCCGCAGCTCAGGAACTCGGCCAATCTCTTGACGCAAACGT
TATTACCTTCCCAACCAATGTTGCAACCATGCCCGAATCCCGTAGCTGGGCGCGTGGTAAAC
TTGACATCGACCAGGACTCCATTGGTTGGTACTTTAAATACCTCGACCCTGTGGCGCCACG
GAGTCCGCTCGTGCCGTGAGTACTCCAAAATACCTGACGGCCTCGTCAAATTTTCTGT
CGACGCCGAGATAAGAGAGATATAACAATGAGGAGTGCCCTACCGTCTCCGACGTTCTATAC
CACTGGACGGCGCCCAATGGAGCTTGTCTATCATCTCCTACCCTATGTTTCGCACTGCTTACT
TTGCTGTGCGAACGTGGATAATAAGGAGATATCCCTTGACGTCACGAACGATCTTATCGTT
TGGCTTAACAATCTCGCTAGTTGGCGTGACGTTGTTGATAGCGGACAGTGGTTCGCTTTTTTC
GGACGACCCGACTTGGTTCGTCCGCATTCGTGTGCTACACCCACATACGATCTTCCTGATCC
GACCGAGGGCTTACTTCGTACGGTCTCCGACTACCGACTTACTTATAAGTCGATAACTTGTG
AGGCTAACATGCCACGCTCGTTGACCAGGGATTTGGATCGGAGGACATTACGCTCTCACT
CCGATCGCCACCACAGAATGCGGTTGAGGGTTCGGGTTTTGTGCACCCTTCAACGTCAC
CCGACCGGGTATCGCAGCGGGTGTACCCTCACTGGGCGTCAATGCCGCCGGGTGGCAGTG
CTCCGTCCGGTGATCCTGCTTGGATACCCGATTCCACCACGCAGTTCAGTGGCGTCATGGAG
GTTTTGACGCTCCACCGCGTCATCACTTATACTATCCCGGAGGCTACACCATGCAATACT
TTGACACTACCACGAATGAATGGAATGGGTTTGCCAATCCAGATGACGTGGTTACATTCCGGC
CAAATGGTGGTGGCGCCGGAACAAACGCCACCATTACGATCACTGCACCTACTGTTACTCT
CACCATTCTCGCCACGACCCTTCTGCTGCTAACGTCATTAACCTTCCGGAATTTGGACGCTGA
AACTACCGCTGCTTCTAATCGCAGTGAAGTGCCTCTGCCGCCTCTAACTTTTGGTCAAACGTC
GCCGAACAACCCGAAGATTGAACAGACTCTCGTCAAGGACACTTTGGGTTCCATACCTTGAC
ATAGCAAGATGCGCAACCCGGTTTTCCAACCTCACGCCTGCATCTTCTTTTGGCGCCATCAGTT
TCACGAATCCCGGGTTTGACCGCAACCTCGATCTTCCTGGTTTTGGCGGCATACGTGACTCCC
TTGATGTCAACATGTCCACCGCTGTGTGCCATTTTCGTTCTTTGTCTAAGTCATGTTCTATT
GTCACCTAAGACGTACCAAGGTTGGGAAGGTGTTACTAATGTTAACACCCCTTTTGGTCAATT
TGCTCACAGCGGGCTGCTCAAGAATGACGAGATTCTTTGCCTTGACAGACGACTTAGCTACTC
GTCTTACAGGCGTTTATGGTGGGACGGATAATTTTGCTGCTGCGGTCTCCGCTTTCGCCGCA
AATATGCTCACTTCGCTTGAAGTGGGAAGCTACCCTTACGTTATTAAGAGCTCGGCAA
CCAAGCTACTGGACTTGCCAACCGGGCCTTGCCCGTTTACCGGGTCTTCTTGCCTCGATACC
GGGCAAAATTGCTGCACGTGTCCGCGCTAGACGTGACCGTCGACGTGCTGCACGAATGAACA
ATAATT

Appendix 3 – Cryo-EM data acquisition reports

Data acquisition report

Date: 06 June 2017- NwV Capsid



Hardware	
Microscope	Krios1
Detector (mode)	F3 (integrating)
Accelerating voltage (ke-V)	300
Pixel size (Å)	1.065
Data acquisition parameters	
Nominal magnification	75000x
Spot size	4
Illuminated area	1.30 μm
Dose	
Square pixel (Å ²)	1.13
Dose per physical pixel per second	60
Dose per Å ² /sec	53
Exposure time (seconds)	1.5
Total dose (e/Å ²)	79.5
Number of fractions	59
Dose per fraction (e/Å ²)	1.35
EPU parameters	
Defocus range (- μm)	-0.8 to -3
Autofocus	Every 8 μm
Drift measurement	NA
Delay after stage shift	5s
Delay after image shift	NA
Exposures per hole	NA
Apertures (size in microns)	
C1	2000
C2	70
C3	2000
Objective	100

General information

Physical pixel size of Falcon III: 14 μm

Physical pixel size of K2: 5 μm

Cs of microscope: 2.7 mm

Data acquisition report

Date: 22 September 2017 – NwV Procapsid



Hardware	
Microscope	Krios1
Detector (mode)	F3 (integrating)
Accelerating voltage (ke-V)	300
Pixel size (Å)	1.065
Data acquisition parameters	
Nominal magnification	75000x
Spot size	4
Illuminated area	1.3
Dose	
Square pixel (Å ²)	1.13
Dose per physical pixel per second	54
Dose per Å ² /sec	48
Exposure time (seconds)	1.5
Total dose (e/Å ²)	72
Number of fractions	49
Dose per fraction (e/Å ²)	1.46
EPU parameters	
Defocus range (-µm)	-0.7, -1, -1.3, -1.6, -1.9, -2.2, -2.5, -2.7
Autofocus	Every 15µm using objective
Drift measurement	NA
Delay after stage shift	10
Delay after image shift	NA
Exposures per hole	NA – 1.7 µm spacing
Apertures (size in microns)	
C1	2000
C2	70
C3	2000
Objective	100

General information

Physical pixel size of Falcon III: 14 µm

Physical pixel size of K2: 5 µm

Cs of microscope: 2.7 mm

Data acquisition report

Date: 03 July 2018- NwV pH 5.7



Hardware	
Microscope	Krios1
Detector (mode)	F3 (integrating)
Accelerating voltage (ke-V)	300
Pixel size (Å)	1.065
Data acquisition parameters	
Nominal magnification	75000x
Spot size	5
Illuminated area	1.3
Dose	
Square pixel (Å ²)	1.13
Dose per physical pixel per second	47
Dose per Å ² /sec	42
Exposure time (seconds)	1.5
Total dose (e/Å ²)	62
Number of fractions	59
Dose per fraction (e/Å ²)	1.05
EPU parameters	
Defocus range (-µm)	-0.5, -1, -1.5, -2, -2.5
Autofocus	Every 10
Drift measurement	
Delay after stage shift	5
Delay after image shift	5
Exposures per hole	na
Apertures (size in microns)	
C1	2000
C2	70
C3	2000
Objective	100

General information

Physical pixel size of Falcon III: 14 µm

Physical pixel size of K2: 5 µm

Cs of microscope: 2.7 mm

Data acquisition report

Date: 04 January 2019 – NwV Procapsid



Hardware	
Microscope	Krios1
Detector (mode)	F3 (integrating)
Accelerating voltage (ke-V)	300
Pixel size (Å)	1.065
Data acquisition parameters	
Nominal magnification	75000x
Spot size	5
Illuminated area	1.3
Dose	
Square pixel (Å ²)	1.13
Dose per physical pixel per second	67
Dose per Å ² /sec	59
Exposure time (seconds)	1.5
Total dose (e/Å ²)	88.5
Number of fractions	59
Dose per fraction (e/Å ²)	1.5
EPU parameters	
Defocus range (-µm)	-0.7, -2.5
Autofocus	Every 10 µm using objective
Drift measurement	Once per grid square 0.05nm/s
Delay after stage shift	5s
Delay after image shift	NA
Exposures per hole	lacey
Apertures (size in microns)	
C1	2000
C2	70
C3	2000
Objective	100

General information

Physical pixel size of Falcon III: 14 µm

Physical pixel size of K2: 5 µm

Cs of microscope: 2.7 mm

Data acquisition report

Date: 08 April 2019- NwV – pH 5.6



Hardware	
Microscope	Krios1
Detector (mode)	F3 (integrating)
Accelerating voltage (ke-V)	300
Pixel size (Å)	1.065
Data acquisition parameters	
Nominal magnification	75000x
Spot size	4
Illuminated area	1.35
Dose	
Square pixel (Å ²)	1.13
Dose per physical pixel per second	55
Dose per Å ² /sec	48.7
Exposure time (seconds)	1
Total dose (e/Å ²)	48.7
Number of fractions	39
Dose per fraction (e/Å ²)	1.2
EPU parameters	
Defocus range (-µm)	-0.8, -1, -1.5, -2, -2.5
Autofocus	Every 10µm
Drift measurement	0.05nm/s every grid square
Delay after stage shift	5
Delay after image shift	5
Exposures per hole	6
Apertures (size in microns)	
C1	2000
C2	70
C3	2000
Objective	100

General information

Physical pixel size of Falcon III: 14 µm

Physical pixel size of K2: 5 µm

Cs of microscope: 2.7 mm

Data acquisition report

Date: 17 May 2019- NwV – pH 6.25



Hardware	
Microscope	Krios1
Detector (mode)	F3 (integrating)
Accelerating voltage (ke-V)	300
Pixel size (Å)	1.065
Data acquisition parameters	
Nominal magnification	75000x
Spot size	4
Illuminated area	1.35
Dose	
Square pixel (Å ²)	1.13
Dose per physical pixel per second	57
Dose per Å ² /sec	50.4
Exposure time (seconds)	1
Total dose (e/Å ²)	50.4
Number of fractions	39
Dose per fraction (e/Å ²)	1.3
EPU parameters	
Defocus range (-µm)	-0.8, -1, -1.2, -1.4, -1.6, -1.8, -2, -2.2
Autofocus	Every 10µm
Drift measurement	NA lacey grids
Delay after stage shift	5
Delay after image shift	5
Exposures per hole	NA lacey grids
Apertures (size in microns)	
C1	2000
C2	70
C3	2000
Objective	100

General information

Physical pixel size of Falcon III: 14 µm

Physical pixel size of K2: 5 µm

Cs of microscope: 2.7 mm

Data acquisition report

Date: 12 July 2019- NwV – pH 5.9



Hardware	
Microscope	Krios1
Detector (mode)	F3 (integrating)
Accelerating voltage (ke-V)	300
Pixel size (Å)	1.065
Data acquisition parameters	
Nominal magnification	75000x
Spot size	4
Illuminated area	1.35
Dose	
Square pixel (Å ²)	1.13
Dose per physical pixel per second	52
Dose per Å ² /sec	46
Exposure time (seconds)	1
Total dose (e/Å ²)	46
Number of fractions	39
Dose per fraction (e/Å ²)	1.18
EPU parameters	
Defocus range (-µm)	-0.7, -1, -1.3, -1.6, -1.9, -2.2
Autofocus	Every 10µm
Drift measurement	NA
Delay after stage shift	10
Delay after image shift	NA
Exposures per hole	NA
Apertures (size in microns)	
C1	2000
C2	70
C3	2000
Objective	100

General information

Physical pixel size of Falcon III: 14 µm

Physical pixel size of K2: 5 µm

Cs of microscope: 2.7 mm

Appendix 4 – Movies

On the accompanying USB:

Chapter 6:

Movie showing the maturation of N ω V:

Maturation_N ω V_movie.mp4

Movie showing the maturation of N ω V from inside the particle looking at the 5-fold axis:

Maturation_N ω V-inside-5-fold-view.mp4

Movie showing the maturation of N ω V from inside the particle looking at the 6-fold axis:

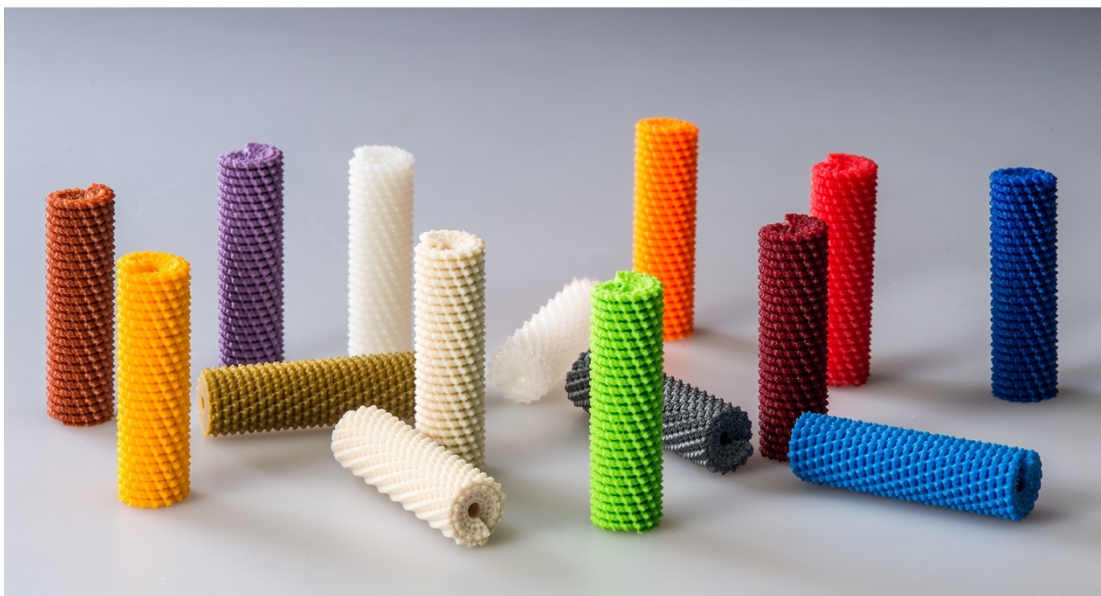
Maturation_N ω V-inside-6-fold-view.mp4

Appendix 5 – 3D printing

During the course of the PhD I got the opportunity to use 3D printing technologies to build 3D models of viruses, molecules and laboratory tools thanks to the support of the OpenPlant Fund. I have printed over 1000 models that are being used for scientific and educational purposes. The following images, taken by Andrew Davis from the Photography Department at JIC, show some of these models:



Picture A: Models of, from left to right, sulfobolus turreted icosahedral virus, Zika virus, *Nudaurelia capensis* omega virus, turnip crinkle virus, poliovirus, cowpea mosaic virus and satellite tobacco necrosis virus. The models in this picture are in the same scale to appreciate the differences in size and structure.



Picture B: Multiple models of tobacco mosaic virus in different colours to represent the applications that these viruses can have in nanotechnology.



Picture C: Side view of tobacco mosaic virus model.



Picture D: Side view of *Ageratum* yellow vein virus model.

Appendix 6 – Publications

Papers produced during the course of the PhD:

Steele, J.F.C., Peyret, H., Saunders, K., Castells-Graells, R., Marsian, J., Meshcheriakova, Y., and Lomonossoff, G.P. (2017). Synthetic plant virology for nanobiotechnology and nanomedicine: Synthetic plant virology for nanobiotechnology and nanomedicine. *Wiley Interdiscip. Rev. Nanomed. Nanobiotechnol.* 9, e1447.

Work conducted during first rotation of the PhD in the Lomonossoff lab:

Castells-Graells, R., Lomonossoff, G.P., and Saunders, K. (2018). Production of mosaic turnip crinkle virus-like particles Derived by coinfiltration of wild-type and modified forms of virus coat protein in plants. In *Virus-derived nanoparticles for advanced technologies: Methods and Protocols*, C. Wege, and G.P. Lomonossoff, eds. (New York, NY: Springer New York), pp. 3–17.

Work conducted during third rotation of the PhD in the Kamoun Lab:

Wu, C.-H., Adachi, H., De la Concepcion, J.C., Castells-Graells, R., Nekrasov, V., and Kamoun, S. (2019). A CRISPR/Cas9 mediated 53 kb deletion of the NRC4 gene cluster of tomato does not affect bacterial flagellin-triggered immunity. *BioRxiv*.